UNIVERSITÉ DE STRASBOURG

École doctorale
Physique, chimie-physique
ED 182
Université de Strasbourg

ÉCOLE DOCTORALE de Physique et Chimie-Physique – ED 182

Institut de Physique et Chimie des matériaux de Strasbourg

THÈSE présentée par :

Arvind Arun Dev

soutenue le : **15 Juillet 2022**

pour obtenir le grade de : **Docteur de l'université de Strasbourg**

Discipline/ Spécialité : Physique de la matière condensée

Flow mechanics in magnetically confined liquid tubes.

THÈSE dirigée par :

M. Bernard DOUDIN	Professeur, Université de Strasbourg
M. Thomas M. Hermans	Professeur, Université de Strasbourg

RAPPORTEURS :

Mme. Nora Dempsey	Directrice de Recherches, CNRS, Institut Néel
M. Jaap Den Toonder	Professeur, Eindhoven University of Technology

AUTRES MEMBRES DU JURY :

Mme. Wiebke Drenckhan	Directrice de Recherches, CNRS, Institut Charles Sadron

न चोर हार्यं न च राज हार्यं न भ्रातृ भाज्यं न च भारकारि |
व्ययं कृते वर्धत एव नित्यं विद्याधनं सर्वधन प्रधानम् ||

Elle ne peut être arrachée par un voleur, ni par le roi ou les gouvernements, ni divisée entre les frères et sœurs, et n’est pas lourde à porter. Si elle est dépensée quotidiennement, elle ne cesse de croître, la richesse de la connaissance est la richesse la plus précieuse entre toutes.

Cannot be snatched away by a robber, and cannot be snatched away by the king or governments, cannot be divided amongst the siblings, and not heavy to carry. If spent daily, it always keeps growing, the wealth of knowledge is the most precious wealth amongst everything.

Mécanique de l'écoulement dans des tubes liquides à confinement magnétique

Arvind Arun Dev*,†

†*Le Département des objets magnétiques à l'échelle nanométrique (DMONS) Institut de Physique et Chimie des Mat'eriaux de Strasbourg, UMR 7504 CNRS-UdS, 67034 Strasbourg, France*

‡*Université de Strasbourg, CNRS, ISIS, UMR 7140, 67000 Strasbourg, France*

E-mail: arvind.dev@ipcms.unistra.fr

Résumé

Le magnétisme et la mécanique des fluides sont deux domaines essentiels de la physique, et les phénomènes qui leur sont liés peuvent être observés dans la vie quotidienne, des appareils électroniques dans la cuisine aux machines IRM à l'hôpital. En fait, le champ magnétique terrestre qui protège la vie sur terre est généré dans son noyau externe par le mouvement de liquides en fusion. L'interaction entre la mécanique des fluides et le magnétisme est donc ancrée dans le noyau de la planète sur laquelle nous marchons, où un petit champ magnétique est généré par une énorme sphère, la Terre. Avec l'avènement des techniques de microfabrication, la miniaturisation a été utilisée pour créer des micro- (nano)aimants et des circuits microfluidiques. Un exemple de matériau technique où le magnétisme et la mécanique des fluides se rencontrent est le ferrofluide, composé de particules ferromagnétiques de 10 nm de diamètre stabilisées dans un fluide porteur comme une huile hydrocarbonée ou même de l'eau. Dans notre étude, nous utilisons la combinaison d'un champ magnétique avec des ferrofluides pour créer un canal

fluide permettant l'écoulement d'un liquide non magnétique avec des propriétés uniques telles que la réduction de la traînée, l'écoulement parfait, l'interface souple adaptée au pompage sans frottement, la stabilisation de dynamiques d'écoulements complexes, l'imitation de conduits souples dans la nature comme les vaisseaux sanguins du corps humain, le transport de cellules biologiques délicates, la bio-impression de liquides non-newtoniens. Nous utilisons plusieurs techniques expérimentales : l'imagerie par contraste d'absorption aux rayons X, la microscopie à fond clair, la microscopie à fluorescence, la vélocimétrie par suivi de particules, pour obtenir des données expérimentales étayées par des solutions théoriques et numériques, afin de démontrer la science qui sous-tend notre recherche sur les canaux liquides confinés magnétiquement.

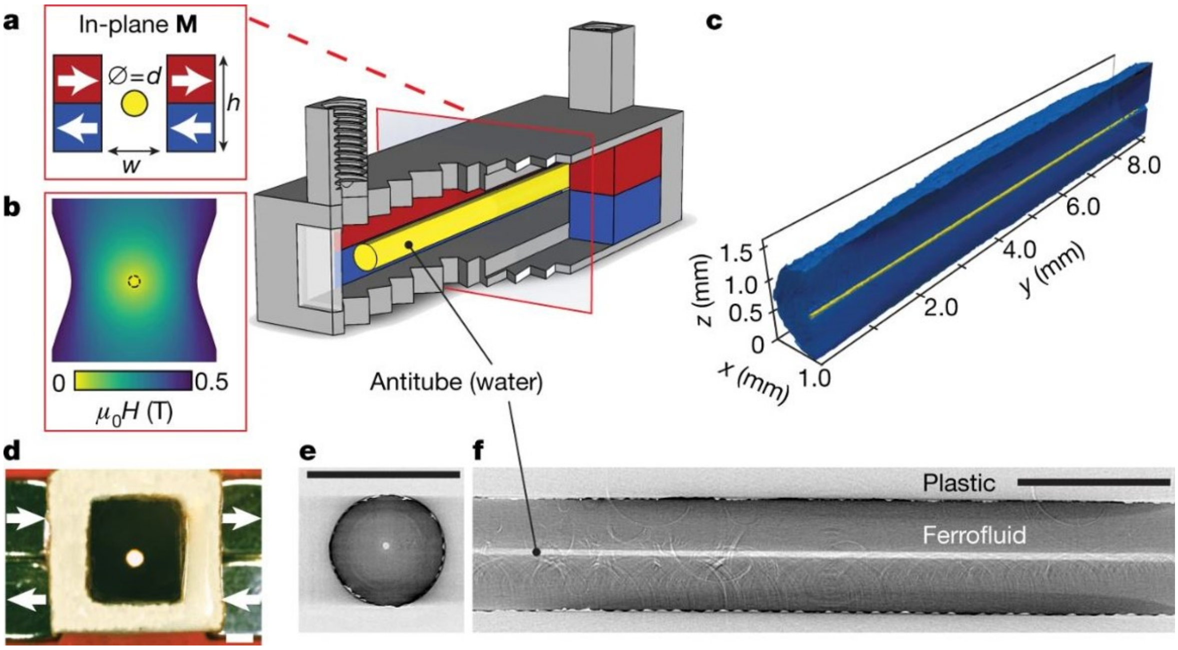

Figure 1: a, Encapsulation magnétique. a. Des aimants permanents (rouge, bleu) dans une configuration quadripolaire dans le plan créent une zone de faible champ au centre, où un antitube d'eau (jaune) est stabilisé à l'intérieur d'un liquide magnétique non miscible (blanc). b. Tracé des contours du champ magnétique. c, Reconstruction tomographique aux rayons X synchrotron d'un antitube d'eau (jaune) de 81 µm de diamètre, entouré de ferrofluide (bleu). d, Vue d'extrémité optique d'un antitube d'eau dans un ferrofluide. e, Coupe transversale de la vue d'extrémité aux rayons X à partir des données tomographiques à $y = 4$ mm. f, Coupe transversale de la vue latérale aux rayons X à partir des données tomographiques à $x = 1$ mm. Barres d'échelle (noir/blanc),2mm de.[1]

Les parois solides qui délimitent le circuit constituent un problème majeur dans les canaux liquides classiques. La paroi solide entraîne une friction du fluide ou une traînée visqueuse hydrodynamique. Pour limiter les dommages causés par le cisaillement des cellules biologiques, l'agrégation et la sédimentation dans les flux importants sur le plan médical, comme le sang à travers les tubes et les artères,[2] la réduction de la traînée visqueuse est essentielle. Permettre le contrôle de la traînée est également clé dans l'étude de la réponse des cellules cancéreuses[3] et des virus.[4] Une solution évidente pour réduire la traînée visqueuse consiste à éviter le contact avec les solides et à créer un canal d'écoulement dont les parois sont constituées d'air (surface libre) ou de liquide. Mais une surface libre ou une interface liquide-liquide est très instable et la stabilité de l'interface liquide- liquide constitue un problème classique en mécanique des fluides, ou instabilité de Plateau-Rayleigh (PRI). Cependant, il est possible d'éviter complètement la paroi solide en utilisant une paroi liquide magnétique, comme le montre la Fig.1 . Elle tire parti du champ magnétique externe créé par un agencement spécifique de (quatre aimants illustrés sur la Fig.1 a logés dans un circuit imprimé en 3D. Les flèches blanches montrent la direction de magnétisation des aimants permanents qui génèrent un champ magnétique entre les aimants nul au centre et augmentant radialement (Fig.1 b). Lors de l'insertion d'une quantité limitée de ferrofluide, les forces magnétiques attirent le ferrofluide près de l'aimant en gardant le centre encapsulant un liquide diamagnétique. Une image utilisant la tomographie à rayons X 3D montrée dans la Fig.1 c et une image optique montrée dans la Fig.1 d illustrent de concept. La partie centrale claire est le liquide piégé ou 'antitube' (eau) et l'encapsulation plus sombre est le ferrofluide. La Fig.1 e et la Fig.1 f montrent les images de radiographie aux rayons X. Notez que les fluides sont statiques sur la Fig.1 et que la taille de l'antitube dépend de l'équilibre entre les pressions magnétique et de Laplace. Des antitubes d'un diamètre aussi petit que 10 μm peuvent être réalisés expérimentalement, avec des diamètres inférieurs possibles par des choix appropriés des propriétés des fluides. Afin d'étudier la réduction de la traînée, les conditions dynamiques ou les conditions d'écoulement doivent être étudiées. Des séries d'expériences ont été réalisées avec plusieurs combinaisons différentes de ferrofluides et de liquides visqueux antitubes. La Fig.2 montre le schéma de la mesure de la chute de pression au moyen de capteurs de pression P1 et P2. La cavité imprimée en 3D (D, Fig.2 a) est d'abord remplie avec le liquide non magnétique, lentement remplacé par l'injection du ferrofluide avec comme résultat une stabilisation de l'antitube. Celui-ci absorbe moins les rayons X

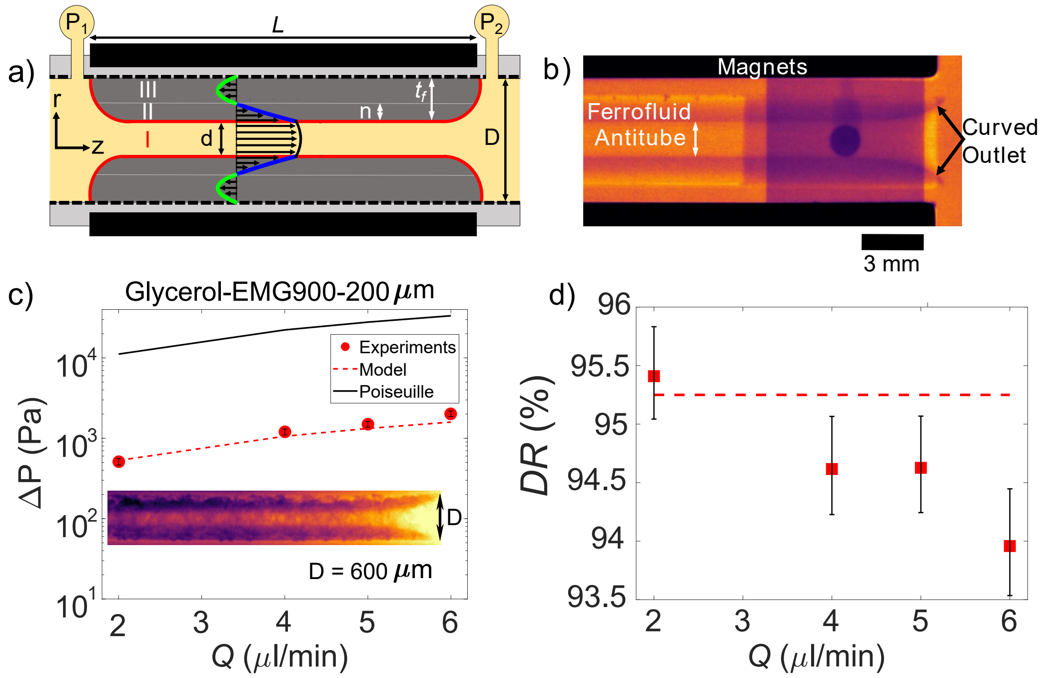

Figure 2: a) Montage expérimental pour la mesure de la pression différentielle (P1, P2). Un antitube de diamètre d à l'intérieur d'une cavité rigide de diamètre D est représenté avec un profil de vitesse suivant l'hypothèse d'un modèle à 2 fluides et 3 régions. La ligne rouge entre le ferrofluide et l'antitube représente l'interface liquide-liquide. b) Image de contraste par absorption de rayons X du circuit fluidique, à l'intérieur d'une cavité entourée d'aimants. Le liquide central plus clair qui s'écoule (antitube) est entouré d'un ferrofluide immiscible plus sombre. c) Chute de pression en fonction du débit pour un antitube de 200 μm de diamètre, avec un encart montrant l'image aux rayons X près de la sortie (la partie centrale claire est l'antitube). Les marqueurs sont les expériences, la ligne continue est un modèle d'écoulement de Poiseuille de diamètre d, et la ligne pointillée est la prédiction du modèle détaillé dans le texte ci-dessous. d) Réduction correspondante de la traînée par rapport à l'écoulement de Poiseuille. Le rapport de viscosité entre le liquide transporté et le ferrofluide est η_r=11.[5]

que le ferrofluide, ce qui donne une image avec une région centrale claire entourée de deux bandes plus sombres (Fig.2 b)). En haut et en bas de l'image se trouvent les aimants qui sont opaques aux rayons X à cette épaisseur, et apparaissent comme deux régions noires, séparées du ferrofluide par le support imprimé en 3D presque invisible. La Fig.2 c) montre la chute de pression mesurée en fonction du débit de glycérol (Sigma Aldrich) circulant dans le ferrofluide EMG900 (FerroTech) (marqueurs). Cette différence de pression est de plus d'un ordre de grandeur inférieur à celle attendue pour un écoulement de Poiseuille dans un canal solide de diamètre équivalent (200 ± 6 μm). Ceci illustre l'intérêt d'avoir un liquide cylindrique en écoulement confiné par une interface liquide plutôt que par des parois solides. La réduction de la perte de charge est mieux décrite par le facteur de friction sans dimension, f . Pour un fluide de densité ρ, la perte de charge mesurée ΔP résultant d'un débit Q à travers un tube de diamètre d et de longueur L est liée au facteur de friction expérimental par.[6]

$$f_{exp} = \frac{\pi^2 \Delta P d^5}{8 \rho Q^2 L} \tag{1}$$

Le facteur de réduction de la traînée DR est alors défini comme suit[7]

$$DR = \frac{f_P - f_{exp}}{f_P} \times 100 \tag{2}$$

qui est le pourcentage de variation du facteur de friction mesuré f_{exp} par rapport au facteur f_p sous le même débit qui suit la loi de Poiseuille. A la limite d'une paroi solide, $f_p = 64/\mathrm{Re}$ où le nombre de Reynolds $\mathrm{Re} = \frac{\rho U d}{\eta}$ est défini pour un diamètre d, une densité ρ , une viscosité η et la vitesse moyenne U correspondant au débit Q. En raison de l'interface liquide-liquide, les conditions limites de vitesse nulle aux parois du liquide transporté (interface anti-tube- ferrofluide) ne s'appliquent pas, et l'écart par rapport à la loi de Poiseuille entraîne une réduction de la traînée hydrodynamique. La Fig.2 d) montre la réduction expérimentale de la traînée (marqueurs) basée sur les équations 1 et 2 et sur les données de la Fig.2 c), avec des valeurs atteignant 95.5 %. Cette réduction de la traînée suggère une grande vitesse à l'interface liquide-liquide, cependant limitée expérimentalement dans l'imagerie du profil de vitesse avec un canal d'écoulement lubrifié cylindrique par la non-transparence du ferrofluide. Pour surmonter ce problème, nous avons conçu un arrangement magnétique tel que le ferrofluide inséré forme une lubrification à la limite des deux côtés, en gardant la direction normale (direction de la lumière incidente) exempte de ferrofluide. En utilisant la vélocimétrie par suivi de particules (PTV), nous avons montré un profil d'écoulement presque idéal (à profil de vitesse constant) dans l'antitube. Les expériences ont été réalisées avec du glycérol (η = 1.1 Pa.s) comme liquide d'écoulement et divers ferrofluides APGE32 (η = 1.7 Pa.s), EMG905 (η = 0.005 Pa.s) de ferrotech et un ferrofluide biocompatible (η = 0.144 Pa.s) de Qfluidics, de sorte que le rapport de viscosité η_r entre le liquide d'écoulement et le liquide d'encapsulation peut couvrir trois ordres de grandeur. La Fig.3 a) montre les schémas de l'installation d'imagerie. La Fig.3 b) et la Fig.3 c) montrent le canal microfluidique avant et après l'insertion du ferrofluide. La Fig.3 d) montre l'image agrandie en champ clair de la région d'intérêt pour les mesures de PTV. La profondeur de champ à ce grossissement est de 3 μm, ce qui est inférieur au diamètre des particules. Cela permet d'enregistrer des images avec une contribution minimale des particules hors focale (en dessous ou au-dessus du plan d'imagerie). Les images sont enregistrées à l'aide d'une caméra à haute vitesse. Le temps d'exposition est de 400 μs. La Fig.3 e) montre un exemple d'écoulement avec des particules, analysé pour obtenir le profil de vitesse. La Fig.4 montre le profil de vitesse analytique et expérimental utilisant les mesures μPTV analysées avec un code maison. Les marqueurs sont expérimentaux et les lignes sont le profil de vitesse analytique prédit. Les lignes noires correspondent à l'écoulement de Poiseuille, les lignes rouges à l'écoulement dans l'antitube, les lignes vertes et bleues au ferrofluide. Les erreurs correspondent à l'écart-type des vitesses mesurées sur 10000 séquences d'images. L'antitube se situe entre-entre y/d= [- 0.5 0 .5]. L'écoulement de Poiseuille montre qu'aux parois y/d = 0.5 et y/d = -0.5 , la vitesse d'écoulement est nulle. Les repères expérimentaux de la Fig.4 a) montrent que pour η_r = 0.65 avec APGE32 comme ferrofluide, la vitesse de paroi est significativement plus élevée que zéro, 60% de la vitesse maximale, et est bien prédite par le modèle analytique. La vitesse de la paroi atteint presque 85%. de la vitesse maximale pour η_r = 7.64 comme on le voit sur la Fig.4 b) pour un ferrofluide biocompatible. L'environnement ferrofluide est légèrement asymétrique pour η_r = 0.65 avec t_{ft} = 0.43 mm. Pour η_r = 7.64, le profil est symétrique. Après avoir compris la dynamique de l'écoulement, il

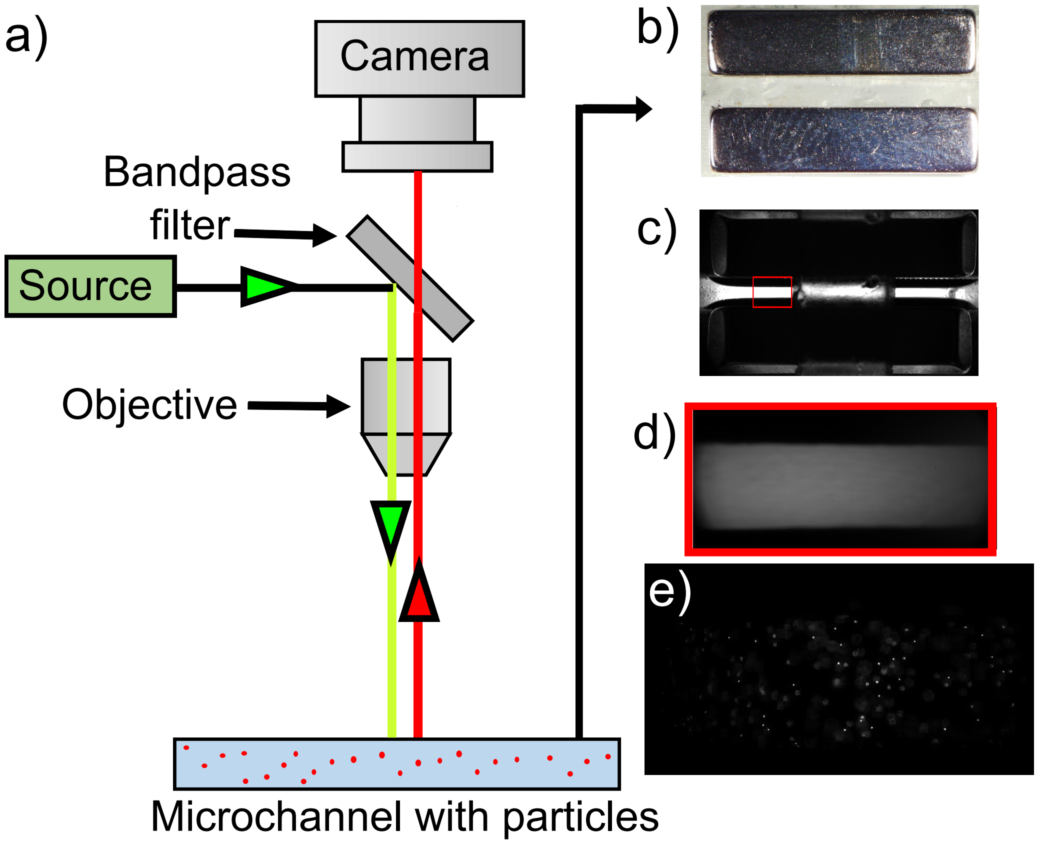

Figure 3: Montage expérimental. a) Système optique pour les mesures de PTV, b) Canal microfluidique sans ferrofluide, c) Canal microfluidique avec ferrofluide, d) Image à fond clair de la région d'intérêt sous microscope, e) Exemple de microcanal avec particules.

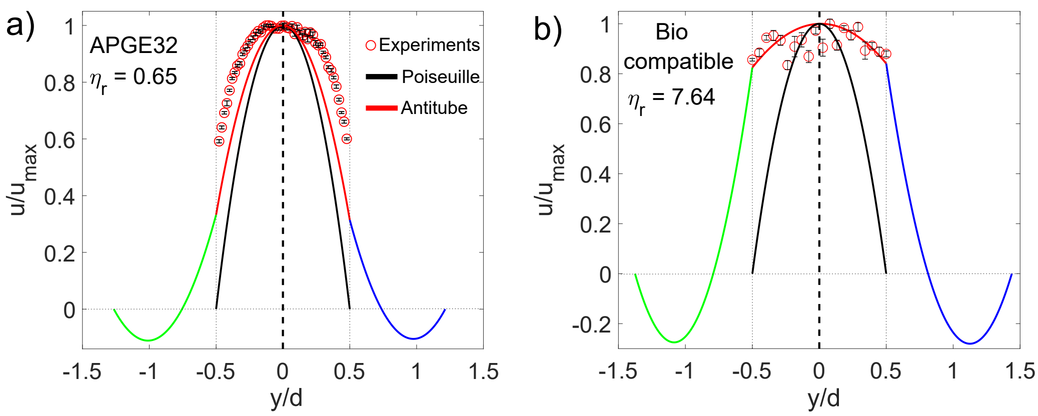

Figure 4: Comparaison des profils de vitesse. Les lignes sont analytiques et les marqueurs sont expérimentaux. La ligne noire représente l'écoulement de Poiseuille, la ligne rouge la solution de l'équation de Stokes dans l'anti-tube, les lignes verte et bleue dans le ferrofluide, a) pour le ferrofluide APGE32 avec un rapport de viscosité $\eta_r = 0.65$ et b) pour le ferrofluide biocompatible avec $\eta_r = 7.64$.

reste à comprendre la physique de la réponse d'une interface d'écoulement magnétique-non magnétique, plus précisément son comportement élastique apparent en réponse à un écoulement sous pression. Nous concentrons notre attention plus spécifiquement sur sa déformation sous un écoulement variable. Le couplage entre les contraintes magnétiques et visqueuses donne lieu à une échelle de longueur de déformation (l_d) qui régit la forme de l'interface déformée. Différentes combinaisons de contraintes magnétiques et visqueuses peuvent être représentées par un seul paramètre l_d (Fig.5 a) donné par

$$l_d = \left[\frac{\eta_f Q W L}{\mu_0 M_s M_r \beta_0}\right]^{\frac{1}{5}} \tag{3}$$

Où η_f est la viscosité du ferrofluide, M_s et M_r sont l'aimantation de saturation du ferrofluide et l'aimantation rémanente des aimants permanents, μ_0 est la perméabilité magnétique, W et L sont la distance entre les paires d'aimants et la longueur du canal d'écoulement, Q est le débit de l'antitube et β_0 est le facteur de réduction de la traînée pour un antitube non déformé (à Q = 0). Ce concept peut être étendu aux microfluidiques souples et stables, Fig.5 b) (Glycérol-APGE32, η_r = 0.65, Q = 100 μL/min, d_{min} =0,5 mm), Fig.5 c) (Glycérol-EMG900, η_r= 11, Q = 10 μL/min, d_{min} = 96 $\pm$6 μm). Au-delà des tubes cylindriques, des formes souples complexes peuvent être créées. La forme de l'instabilité de Plateau-Rayleigh (PRI)[8,9] à l'interface liquide-liquide peut être imitée et stabilisée sous écoulement. La Fig.5 d) montre le disposit if avec les aimants permanents appropriés et le champ magnétique créé entre les aimants, les flèches blanches indiquant la direction de l'aimantation. L'espace entre les aimants est rempli de glycérol (η_g =1.1 Pa.s , Sigma Aldrich). En introduisant le ferrofluide (Ferrotech) entre les aimants, un tube liquide se forme avec une partie centrale plus claire (glycérol) et une encapsulation plus foncée (ferrofluide), suivant ainsi le champ magnétique et stabilisant une forme de mode PRI pour le glycérol (Fig.5 e), Q = 0 μL/min). Avec un écoulement (Q = 75 μL/min) de gauche à droite, l'antitube se déforme et à l'arrêt de l'écoulement, il retrouve la forme il avait avant l'écoulement (Q

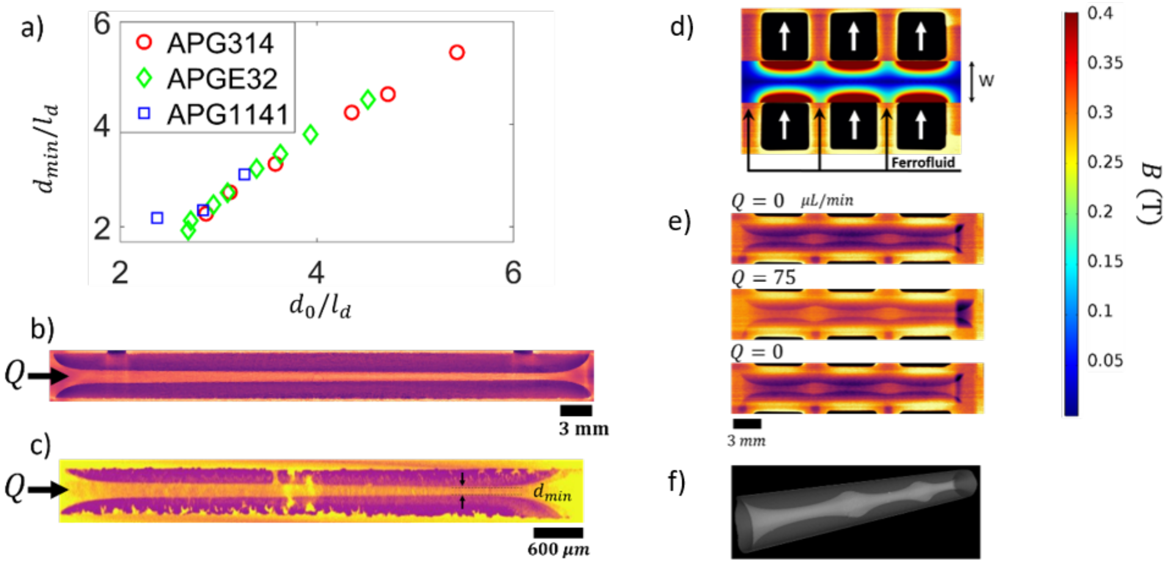

Figure 5: Diamètre expérimental normalisé non déformé d_0/l_d et diamètre minimal après déformation, d_{min}/l_d pour tous les cas inférieurs à Q_c. l_d est l'échelle de longueur de déformation. b) Buse de liquide avec Glycérol-APGE32, d_{min}=0.5 mm, W = 6 mm, c) Buse de liquide avec Glycérol-EMG900 (η_r=10), d_{min} = 96 ±6 μm, W = 0.9 mm. W est la distance entre la paire d'aimants, d) Conception des aimants et champ magnétique pour stabiliser une forme de mode d'instabilité de Plateau-Rayleigh, W = 3.5 mm est la distance entre les aimants, e) Forme de mode PRI stable avant l'écoulement (Q = 0 μL/min), pendant l'écoulement (Q = 75 μL/min) et après l'écoulement (Q = 0 μL/min), f) Tomographie 3D aux rayons X de la forme de mode PRI sous écoulement, glycérol dans le ferrofluide APGE32, avec un rapport de viscosité η_r=0.65.

= 0 μL/min), comparez les trois figures de la Fig.5 e), la Fig.5 f) montrant une image de tomographie à rayons X en 3D. La forme est stable car les contraintes magnétiques sont nettement plus importantes que la pression de Laplace et la gravité. Cette approche pourrait éventuellement être utilisée pour imiter des formes complexes dans la nature, par exemple des petites veines qui ne sont pas de section circulaire.

En conclusion, l'encapsulation magnétique d'un canal d'écoulement liquide conduit à une réduction de la traînée des liquides visqueux à travers des tubes cylindriques de type liquide-dans-liquide où le liquide de confinement est maintenu en place par un champ magnétique quadrupolaire. Nos résultats montrent que des réductions de traînée atteignant 99% peuvent être obtenues en exploitant la vitesse non nulle d'un liquide visqueux à son interface avec le liquide encapsulant. La réduction de la friction est quantifiée par une renormalisation du nombre de Reynolds par un facteur β qui dépend du rapport de viscosité et des dimensions géométriques du canal fluide. Les microcanaux à faible friction pourraient être bénéfiques pour les applications microfluidiques existantes, à condition qu'ils soient non magnétiques (diamagnétiques ou à faible susceptibilité magnétique), ce qui est le cas le plus fréquent rencontré dans la nature. Nous envisageons qu'au-delà des applications de réduction de la traînée, ces microcanaux confinés magnétiquement puissent également être utilisés comme système modèle pour étudier l'écoulement de biomatériaux utilisés pour préparer des produits pharmaceutiques. Les cellules biologiques souffrent des interfaces solides et des cellules délicates s'abîment à l'endroit d'une forte contrainte de cisaillement,[10] particulièrement dans les microcanaux. Les microcanaux confinés magnétiquement présentent une grande longueur de glissement accordable et donc un cisaillement accordable dans le microcanal, qui pourrait être exploité pour transporter des cellules biologiques délicates ainsi que pour étudier les cellules dans un environnement à faible cisaillement. Le remplacement d'une paroi de confinement solide par une paroi liquide ouvre de nouvelles perspectives, en particulier dans le contexte du transport de biomatériaux et de déplacements de micro-organismes.[11] En effet, au-delà de la dynamique de l'écoulement, le processus microbien fondamental de chimiotaxie est également affecté par la présence de cisaillement dans l'écoulement.[12] Notre compréhension du profil d'écoulement et de la mécanique de l'écoulement pourrait avoir un impact et améliorer la compréhension fondamentale de la motilité bactérienne et de la santé cellulaire, et peut-être fournir une solution pour le transport à faible cisaillement de cellules délicates, permettant d'imiter l'environnement de cisaillement du monde biologique. En outre, au-delà des tubes liquides droits, des structures d'écoulement complexes peuvent être stabilisées à des échelles de longueur millimétriques et microfluidiques pour imiter les bio-interfaces souples. Notre compréhension pourrait ouvrir la voie à la création d'une microfluidique (ultra)douce avec des parois liquides stables pour des applications technologiques et biologiques. L'immiscibilité et la réactivité chimique du liquide transporté et du ferrofluide encapsulé pourraient être déterminantes pour décider de l'adéquation de cette méthode au transport d'huiles, d'émulsions, de boues et de gouttelettes. Dans le transport biologique, où le transport à cisaillement réduit pourrait être d'une grande importance, la biocompatibilité du ferrofluide avec le biomatériau est un facteur limitant. Compte tenu de la grande banque de ferrofluides en cours de développement à partir de différents liquides de base comme le kérosène, le krytox, l'huile minérale et même l'eau, les conditions ad-hoc requises pour le transport de fluides sont à portée de main, avec des premiers tests encourageants. De plus, avec des diamètres d'antitube aussi petits que 10 μm déjà réalisables,[1] des rapports d'épaisseur de ferrofluide/ diamètre de l'antitube de l'ordre de 100 sont possibles. Les gradients de force le long de la direction de l'écoulement peuvent également renforcer la stabilité du ferrofluide contre le cisaillement, ouvrant la voie à des applications fluidiques à haute vitesse et à faible viscosité.

References

(1) Dunne, P.; Adachi, T.; Dev, A. A.; Sorrenti, A.; Giacchetti, L.; Bonnin, A.; Bourdon, C.; Mangin, P. H.; Coey, J. M. D.; Doudin, B.; Hermans, T. M. Liquid flow and control without solid walls. *Nature* **2020**, *581*, 58–62.

(2) Reinke, W.; Gaehtgens, P.; Johnson, P. C. Blood viscosity in small tubes: effect of shear rate, aggregation, and sedimentation. *American Journal of Physiology-Heart and Circulatory Physiology* **1987**, *253*, H540–H547.

(3) Mitchell, M. J.; King, M. R. Computational and Experimental Models of Cancer Cell Response to Fluid Shear Stress. *Frontiers in Oncology* **2013**, *3*, 44.

(4) Grein, T. A.; Loewe, D.; Dieken, H.; Weidner, T.; Salzig, D.; Czermak, P. Aeration and Shear Stress Are Critical Process Parameters for the Production of Oncolytic Measles Virus. *Frontiers in Bioengineering and Biotechnology* **2019**, *7*, 78.

(5) Dev, A. A.; Dunne, P.; Hermans, T. M.; Doudin, B. Fluid Drag Reduction by Magnetic Confinement. *Langmuir : the ACS journal of surfaces and colloids* **2022**,

(6) Karatay, E.; Haase, A. S.; Visser, C. W.; Sun, C.; Lohse, D.; Tsai, P. A.; Lammertink, R. G. H. Control of slippage with tunable bubble mattresses. *Proceedings of the National Academy of Sciences* **2013**, *110*, 8422–8426.

(7) Watanabe, K.; Udagawa, Y.; Udagawa, H. Drag reduction of Newtonian fluid in a circular pipe with a highly water-repellent wall. *Journal of Fluid Mechanics* **1999**, *381*, 225–238.

(8) Utada, A. S.; Fernandez-Nieves, A.; Stone, H. A.; Weitz, D. A. Dripping to Jetting Transitions in Coflowing Liquid Streams. *Phys. Rev. Lett.* **2007**, *99*, 094502.

(9) Haefner, S.; Benzaquen, M.; Bäumchen, O.; Salez, T.; Peters, R.; Mcgraw, J.; Jacobs, K.; Raphael, E.; Dalnoki-Veress, K. Influence of Slip on the Plateau-Rayleigh Instability on a Fibre. *Nature communications* **2015**, *6*.

(10) Blaeser, A.; Duarte Campos, D.; Puster, U.; Richtering, W.; Stevens, M.; Fischer, H. Controlling Shear Stress in 3D Bioprinting is a Key Factor to Balance Printing Resolution and Stem Cell Integrity. *Advanced healthcare materials* **2015**, *5*.

(11) Berke, A. P.; Turner, L.; Berg, H. C.; Lauga, E. Hydrodynamic Attraction of Swimming Microorganisms by Surfaces. *Phys. Rev. Lett.* **2008**, *101*, 038102.

(12) Guasto, J. S.; Rusconi, R.; Stocker, R. Fluid Mechanics of Planktonic Microorganisms. *Annual Review of Fluid Mechanics* **2012**, *44*, 373–400.

Acknowledgements

First and foremost, I heartily thank my academic supervisors, Prof. Bernard Doudin and Prof. Thomas M. Hermans, for their continuous support and scientific discussions throughout my Ph.D. journey. I owe them for my improved scientific temperament, analytical capabilities and confidence. Beyond academics, Prof. Doudin is very caring in person, and I am deeply touched by his support, especially during the tough COVID times. I remember troubling Prof. Doudin with the news that I got a big electricity bill, and he spoke to the authorities on my behalf. Prof. Hermans's trust and encouragement have molded me into a complete person. Prof. Hermans jokingly introduced me to some liquid (to drink, of course), saying it was an apple juice (it was good). I enjoyed this level of comfort throughout my Ph.D., and hence I consider myself lucky and blessed to have had supervisors who supported me to grow personally and professionally.

Apart from my supervisors, I am grateful to Dr. Dunne for his constructive suggestions throughout the Ph.D. and scientific training on my Ph.D. topic. Dr. Dunne's patient explanations set the tone of my research perfectly from 1st year itself. I also thank Dr. Anna Oleshkevych for being there as a manager for all our scientific-nonscientific planning. She was also a part of our beamtime experiments at PSI Switzerland, which was a great help in difficult times. I thank Dr. Anne Bonnin from PSI for helping and training in X-ray tomography. I would also like to take this opportunity to thank Prof. Andrejs Cēbers and Dr. Guntars Kitenbergs for hosting me in the MMML lab at, university of Latvia. Meaningful discussions with Prof. Cēbers have helped me refine my understanding of the research problem. I also thank Prof. Eberhard Bodenschatz, Dr. Isabella Guido and Gholamhossein bagheri for allowing me to work at Max Planck Institute for dynamics and self-organisation, Gottingen, Germany. Dr. Bagheri's support and involvement in the experiments were of utmost importance for our research. We also thank Prof. Gauthier , Antonie Egele and Damien Favier for allowing me to work with the X-Ray tomography setup.

Though the list of academic people I have to thank will be never-ending. However, I would like to remember and thank Prof. P. M. Ardhapurkar from MCOE Shegaon, India, Prof. M. D. Atrey from IIT Bombay and Prof. S. Vanapalli from the University of Twente, The Netherlands. Because of the trio, I entered the research field, was motivated and somehow traveled to Europe for my higher studies. I also remember my friends Abhishek Purandare , Prachi Bagave and Shreyasi Pathak for their great company when I arrived in Europe.

I am also thankful to Véronique Wernher, Catherine Bonnin and Jérôme ROBERT for their support in IPCMS.

Now let me begin the big list of people who are my family in Strasbourg. Jinu Kurian, my colleague for four years. Jinu has been there throughout my Ph.D., witnessing the ups and downs. I thank him for all his support, suggestions, teasing, joining me in restaurants, and for making my Ph.D. studies more lively. The only complaint is that he never displayed his cooking skills and kept it secret despite being friends for four years. Aleena Joseph and Dr. Krishnaprasad Maity joined the group later; however, very soon, we became a *fantastic four* group. Aleena, the master planner, joined two years later but knew everything from administrative details to trip planning. She helped where I should have helped her, with tax filing or details about university courses. I thank her for all her support and especially for planning the hiking or any group event, which took the stress away, if there was any. Dr. Maity or *KP* and I were considered the two older adults in the group who liked old songs. KP is an excellent tabla (instrument) player, and we had a fun musical party with him. It was undoubtedly a pleasure to discuss music and science with him.

I would also like to thank my neighbors Cynthia and Timothee. With Cynthia, I discussed literature and a wide range of topics from history to economics and with Timothee, I tried to learn some French. I had a great time with them trying different cuisine, which helped normalize life after the COVID confinement.

I also thank my friends for their immense contribution towards the weekend plans. I thank Deeksha, Vineesha, Anjana, Raj, Christeena, and the new colleagues Ankita, Jose, Gyandeep, Shubhradip, Tanushree, and Satakshi (Pandey Ji) for the great food which reminded me of my home.

I also had beautiful interactions with people in Hermans lab. I thank Florencia, Anastasia, Serena, Alessandra, George, Chungfeng, Michi, Alvaro, Caroline, Thomas, Lucas, Reza and Dr. Nishant Singh for his valuable suggestions.

Apart from the friends in Strasbourg, I would also like to thank Swapnil Shri Vasudevravji Dhule, Saurabh Shri Sambhajiraoji Pawar and Vishakha Shri Jaikrishnaji More from India who despite the distance were always close and provided continuous mental support and suggestions in the personal life.

My family's support, trust and love are unmatchable. Thanking them with words is so less. My father and mother, Arun Vyankatesh Dev and Veena Dev, have always stood by my side in all my decisions, whether coming to Europe for my master's or continuing as a Ph.D. student. I will always be indebted to them. The level of confidence they showed in me has

always encouraged me and kept me positive in tough times. I remember when I was frustrated with a job after my Bachelor's in engineering and explained to my parents my plan to leave the job and continue in studies. It feels now that that was a tough decision and a turning point in life. Only my parent's willpower, love and trust gave me the strength to continue my studies. Because of my parents' blessings, I have been able to perform when required. Apart from them, if there is one person I can not thank enough is my younger brother Surya Kant Kumar Dev. He stayed with and supported parents in the hard COVID times and in general when they needed it. It was because of him, I could focus completely on the Ph.D. and my worries of my family was taken care of and I didnot feel any pressure. He is very patient even when I could not find enough time for him, he is a great support. Though I am his funding agency for fun stuff from last few years, it always feels less. Anything for him.

I see that my Ph.D. has been supported by so many people in one or the other way. It is indeed a group task that was accomplished with the help of teachers, family and friends. I once again thank everyone from the bottom of my heart for their support…

Contents

List of Figures

List of Tables

List of Abbreviations

PDMS	**Poly-dimethyl siloxane**
MSC	**Mesenchymal stem cells**
RBC's	**Red blood cells**
SEM	**Scanning electron microscope**
LIS	**Liquid infused interafces**
PIV	**Particle image velocimetry**
PTV	**Particle tracking velocimetry**
PRI	**Plateau-Rayleigh instability**
FIS	**Ferrofluid infused surface**
CFD	**Computational fluid dynamics**
AFM	**Atomic force microscopy**
CTAB	**Cetyltrimethylammonium bromide**
NaSal	**Sodium salicylate**

List of Symbols

b	slip length	[m]
f	friction factor	[]
k	wave number	[m]
l_d	deformation length scale	[m]
l_s	length scale with surface tension	[m]
M	Magnetisation	[Am]
P	Pressure	[Nm^{-2}]
Q	Flow rate	[$\mathrm{m}^3\mathrm{s}^{-1}$]
R	radius of liquid tube	[m]
T	Time period	[s]
u	velocity	[ms^-1]
u_m	average velocity	[ms^-1]
u_{max}	maximum velocity	[ms^-1]
W	distance between magnets	[m]
α	Pressure drop improvement ratio	[]
β	drag reduction parameter	[]
β_0	approximated drag reduction parameter	[]
$\dot{\gamma}$	shear rate	[s^-1]
γ	surface tension	[Nm^-1]
ϵ	amplitude of perturbation	[m]
ζ	asymmetric coverage factor	[]
η	viscosity	[Pa s]
η_f	viscosity of ferrofluid	[Pa s]
η_r	viscosity ratio	[]
κ	curvature	[m^-1]
λ	wavelength	[m]
ρ	density	[kgm^{-3}]
τ	shear stress	[Nm^{-2}]

τ_d	relaxation time	[s]

Dedicated to aaji, my grandmother

Usha Vinayak Fadnavis (1942-2007)

Chapter 1

Introduction

Magnetism and fluid mechanics are the two key areas of physics with related phenomena found in daily life, ranging from electronic devices in kitchen to MRI machines in hospitals. In fact earth's magnetic field, essential to preserve life on earth, is generated in earth's outer liquid core due to motion of molten liquids. Hence, the interaction between fluid mechanics and magnetism is enshrined in the core of the very planet we walk upon, with small magnetic field generated by a huge ball. We will highlight here the fluid mechanics and magnetism concepts that are pertinent to our work.

1.1 Fluid mechanics

Fluid mechanics is extremely broad in human experience, it forms the basis of functioning life forms[1], settlement and flourishing of civilizations, disease transmission[2], and cutting edge technological advancements, to give a few examples. It includes flow of water in river to flow of blood in human arteries. In this context, we limit our discussion on fluid mechanics, that describes flow through channels. The two scientists credited for pushing forward their mathematical and physical understanding were Gotthilf Heinrich Ludwig Hagen (1797-1884) and Jean Léonard Marie Poiseuille (1797-1869).
In Newtonian mechanics, the steady flow of incompressible viscous fluids is described by the Navier-Stokes equation. In cylindrical coordinates, the steady axisymmetric momentum equation of fluid flow is given by

$$\rho u \frac{\partial u}{\partial z} = -\frac{\partial P}{\partial z} + \eta \left[\frac{1}{r} \frac{\partial}{\partial r} \left(r \frac{\partial u}{\partial r} \right) \right] \tag{1.1}$$

In the low Reynolds number (Re) limit, where $Re = \frac{\rho U d}{\eta}$ is the ratio of inertia force to viscous force for a flow of fluid with density ρ, viscosity η, average velocity U through a diameter d, pressure gradient $\frac{\partial P}{\partial z}$. In the limit $Re < 1$, the inertial term (left side of the equation) can be

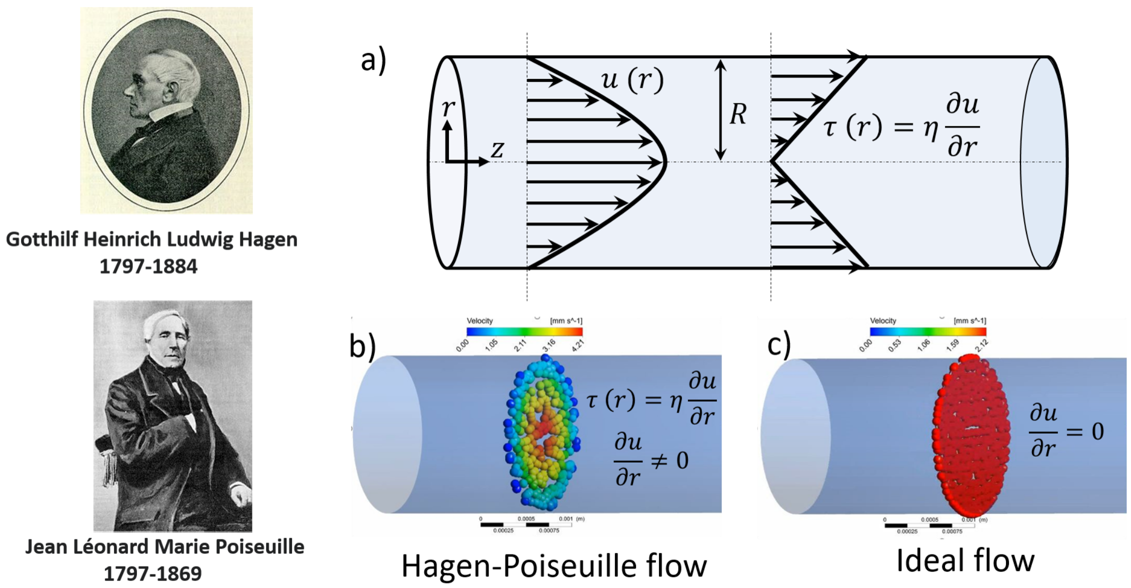

FIGURE 1.1: Poiseuille flow and ideal flow. a) Flow through a cylindrical tube of radius R, u(r) is velocity profile and $\tau(r)$ is shear stress, b) Hagen-Poiseuille flow showing maximum velocity (red) at the center of flow and zero velocity at the wall, velocity gradient is non-zero, c) Ideal flow with zero velocity gradient, frictional flow or plug flow. r and z are radial and axial co-ordinate. η is the viscosity of the flowing liquid.

neglected, which leads to the Stokes equation given by

$$0 = -\frac{\partial P}{\partial z} + \eta \left[\frac{1}{r} \frac{\partial}{\partial r} \left(r \frac{\partial u}{\partial r} \right) \right] \tag{1.2}$$

The solution of Stokes equation with no-slip boundary conditions

$$u = 0, \;\; at \;\; r = \pm R \tag{1.3}$$

at the solid confining wall gives the Hagen-Poiseuille flow equation, describing a steady and incompressible laminar flow through a duct. Fig.1.1 a) shows the resulting parabolic velocity profile $u(r)$ in a cylindrical tube given by

$$u(r) = -\frac{1}{4\eta} \frac{\partial P}{\partial z} \left(R^2 - r^2 \right) \tag{1.4}$$

and the shear stress ($\tau(r)$) is given by

$$\tau(r) = \eta \frac{\partial u}{\partial r} \tag{1.5}$$

Integrating Eq.1.4 over the cross section of flow and assuming a linear pressure gradient $\frac{\partial P}{\partial z} = \frac{\Delta P}{L}$, the pressure drop through a duct of length L is given by

$$\Delta P = \frac{8\eta L Q}{\pi R^4} \tag{1.6}$$

Eq.1.6 provides a design principle for flow through solid wall tubes (Fig.1.1 b)). The Hagen-Poiseuille flow and hence consequently Eq.1.6 is applicable for viscous dominated flow, therefore particularly in the field of microfluidics where $Re < 1$.

1.2 Microfluidics

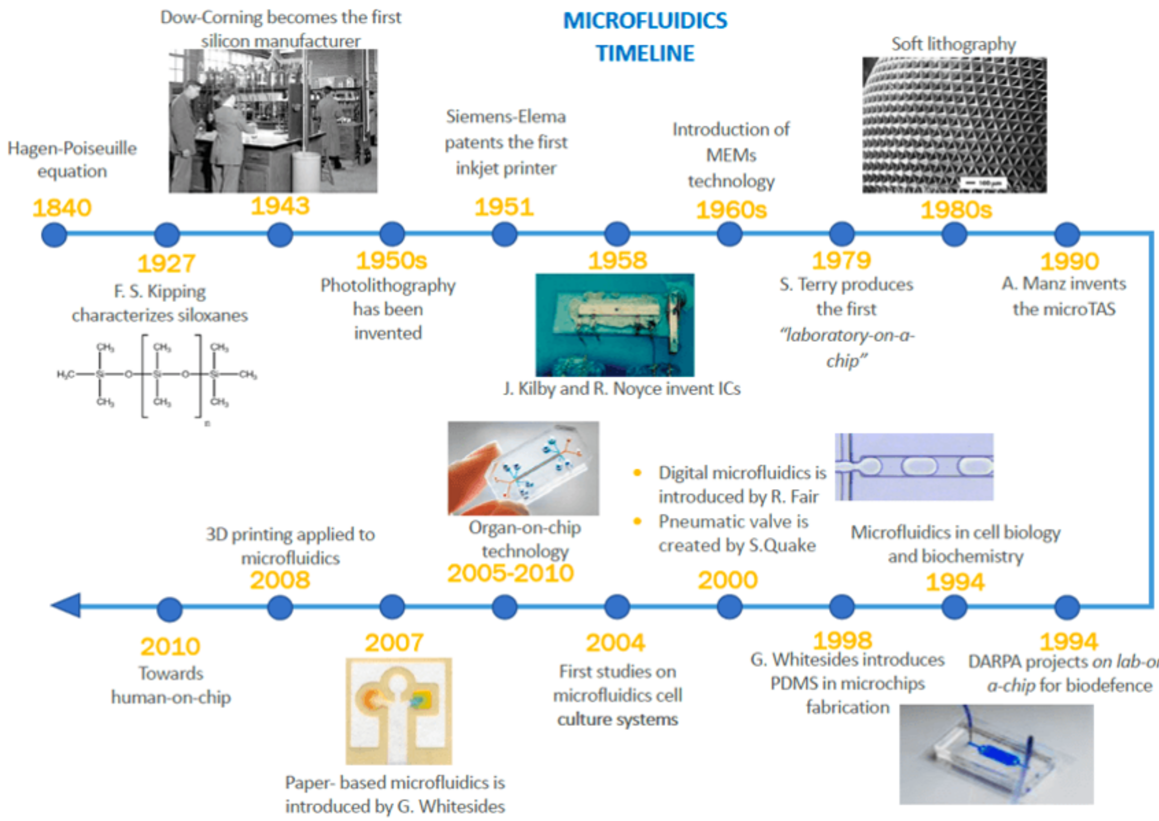

FIGURE 1.2: Microfluidics timeline. Source: Elveflow

With the fundamental understanding of flow mechanics in the 19^{th} century and the advent of new manufacturing techniques in the 20^{th} century, the pursuit of miniaturization lead to the field of microfluidics. A timeline of development of microfluidics is presented in Fig.1.2. It started with the introduction of silicon and development of photo-lithography technique. However it was only after the introduction of soft lithography (1980s) techniques that microfluidics became of interest for bio-applications. In soft lithography, elastomeric soft molds are used to transfer shape and hence make it possible to form micro-channels easily. The process of soft lithography[3] accelerated after the introduction of poly-dimethyl siloxane (PDMS) as the soft elastomer by G. Whitesides. The ease in microfabrication lead to the development of digital microfluidics where external field (electric-field) is applied in a microchannel to control the fluid behavior. Furthermore, microfluidics became increasingly popular to mimic biological organ behavior and with 3D printing advances, microfluidic channel with reduced size and design complexity can be realized.

Today microfluidics is a growing multi billion dollar industry. The pandemic of Covid-19 has further boosted the microfluidics[4] industry and rightly so. Microfluidics has been used to detect the virus and in general it is also used in drug delievery and discovery. Fig.1.3 a) shows some major applications of microfluidics[5]. Fig.1.3 b) shows the steady growth of microfluidics market with major applications. Point of care diagnostics for human is the most value generating business followed by tools development for pharma industry and clinical diagnostics. This shows the growing demand and importance of microfluidics providing solutions for life science.

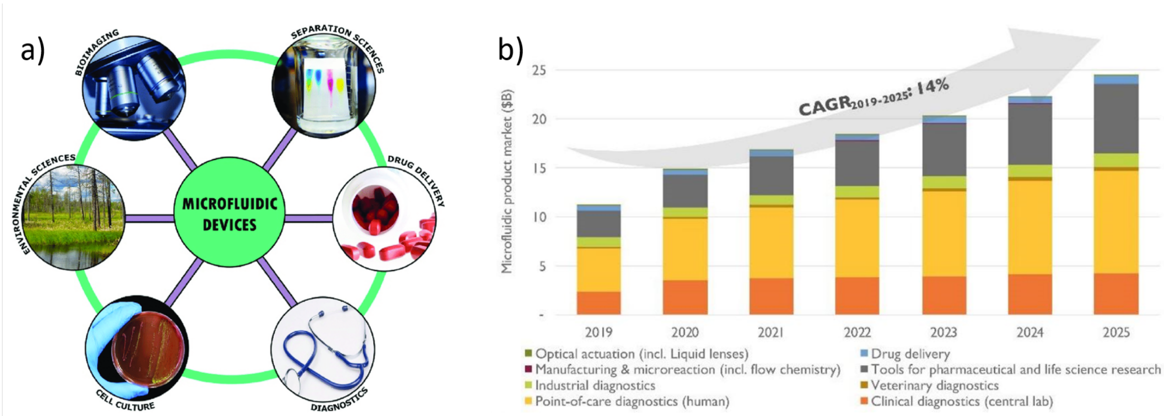

FIGURE 1.3: Growing microfluidics applications[5] and market

However, despite of decades of research there are still fundamental limitations with fluid mechanics, with significant impact on microfluidics. A key bottleneck is the no slip boundary condition at the bounding wall (Eq.1.3). As discussed, the zero wall velocity condition implicit in the Hagen-Poiseuille flow leads to large shear stress or pressure drop. Shear stress increases linearly over the cross section of a tube, from zero at the center to a maximum at the wall (Fig.1.1 a)). This viscous shear stress is extremely important to consider while designing flow systems, especially for biological materials that can experience shear damage. Fig.1.4 shows some applications where controlling shear stress is crucial. In a very basic application of pumping through a microneedle, a viscous fluid offers higher resistance

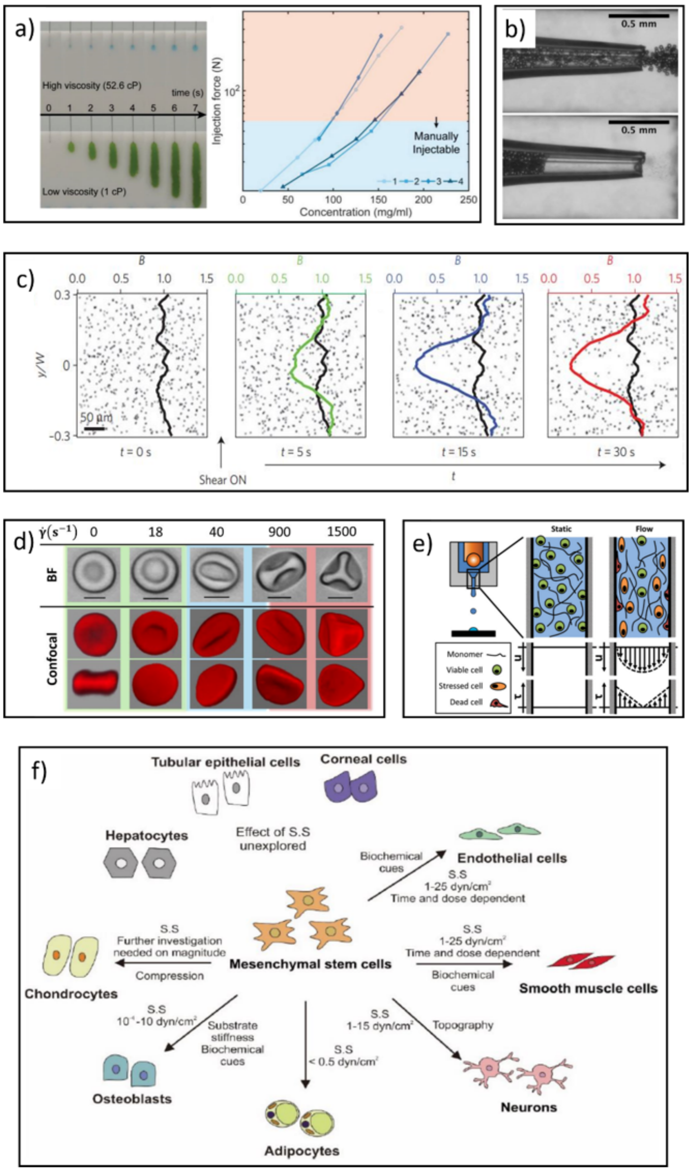

FIGURE 1.4: Effect of shear stress in microfluidics. a) Flow of low viscosity and comparatively high viscosity solution, highly concentrated drugs goes beyond human pumping limit[6], b) Jamming of PMMA particle suspension on increasing the particle concentration in a tapered capillary[7], c) Trapping of bacteria in the high shear region due to application of shear rate, bacteria distribution shown over time, black line is initial distribution and other coloured lines show temporal evelution of the bacterial population[8], d) Morphology change of red blood cells (RBC) on increasing the shear stress which is one of the reason for shear thinning of blood[9] , e) Schematic of bio-printing with biological cells, large shear stress at the nozzle unavoidable and bio-cells at different location in a flow nozzle experience different shear stress which might kill the cells near wall[10] , f) Differentiation of Mesenchymal stem cells (MSC) into various lineages due to shear stimulation along with bio and chemical stimulations[11]

(due to large shear stress). Fig.1.4 a) shows flow of two fluids with different viscosities, with the larger viscosity one difficult to pump[6]. In medical fluids, highly concentrated biological drug may be essential in developing new treatment protocols. However, the pumping force required increases with the concentrations of the fluid and may go beyond manual injection limits[6]. This offer serious limitations in micro medical needles which often handle fluids with variable concentration. Another very important issue with microfluidics related to large shear stress is clogging while flowing microparticle laden fluid. Fig.1.4 b) shows flow (top) and clogging (bottom) of a tapered glass capillary for a flow in liquid loaded with PMMA microparticles[7]. Clogging occurs when the volume fraction of particles increase beyond a critical limit $\phi > \phi_m$. Tapered capillaries are important as they form a micro-nozzle used for precise delivery, however with the decrease in diameter, the shear stress as well as the fraction of particle in a cross section increases and clogging becomes a major issue.

Beyond flow limitations, the biological world also responds to the shear stress in fluids. One of the many example is the trapping of bacteria in a high shear region[8]. It was observed that when a shear rate/shear stress is applied to a population of bacteria in the microchannel, a redistribution of the population takes place and the bacterias are trapped near the wall. Fig.1.4 c) shows series of temporal images (from left to right) with a bacterial solution in a microchannel. At $t = 0$, no flow is applied and hence there is no applied shear stress, the black line shows the random distribution of B. subtilis cells before shear. At $t > 0$, with the black line is drawn for reference, it can be seen that the cells are depleted from the central location and migrate to the walls. Hence controlling the shear profile in a microchannel could give access to tuning the bacterial density in a microchannel.

Blood's main components, the RBCs (red blood cells) change their morphology in response to shear stress[9]. Fig.1.4 d) shows the change in morphology of RBCs with increasing shear stress using bright field microscopy (BF) and confocal microscopy. At low shear rate ($\dot{\gamma}(s^{-1})$ < 10), RBC retain their biconcavity and look like discocytes. With increase in shear stress (10< $\dot{\gamma}$ < 40) RBC show a highly deformed stomatocytes and at high shear stress (900< $\dot{\gamma}$ < 1500) forms a polylobed cells (trilobe and hexalobe). The change in morphology in response to shear stress is strongly related to the reduction in viscosity of the blood. The deformability and stressing of the cells could also have adverse effect on cell health, for example in bioprinting[10] (Fig.1.4 e)), which is in growing demand for tissue engineering. Here a required nozzle is required which increases the shear stress and cells near the wall experiencing large shear stress might die. Mesenchymal stem cells (MSCs) are important for regenerative medicine applications. The MSC's differentiate into various lineages like chondrocyte, hematopoietic or endothelial cells with biophysical, biochemical or mechanical stimuli[11]. Shear stress (mechanical stimuli) could be used for the differentiation of

MSC's into liver, kidney and corneal tissue lineage cells. Fig.1.4 f) summarizes some of the effect of shear stress in MSC's differentiation. It is important to tune the shear stress along with other stimuli for in-vitro differentiation. Noting the widespread necessity of controlling shear stress, it is important to develop scientific techniques to tune the shear rate/shear stress and understand the underlying physical phenomena.

1.3 Control of viscous drag

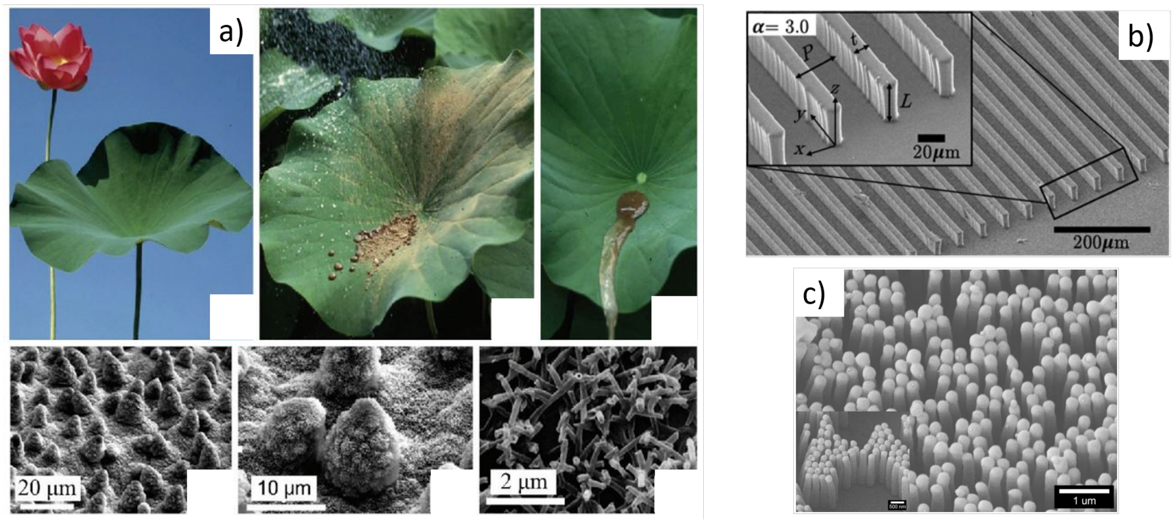

FIGURE 1.5: Nature inspired micro and nano structured surface. a) Lotus leaf with self cleaning properties[12], microscopic view at different magnification show the structured surface, b) PDMS microscopic lamalle[13], P is the pitch and t is the thickness of the structure, c) Circular metallic nano-pillars[14].

Shear stress is proportional to viscocity (η) and velocity gradient ($\frac{\partial u}{\partial r}$). Since η is a material property, the possibility to tailor the shear stress is by acting on $\frac{\partial u}{\partial r}$. The aim is to control shear stress and possibly move from finite shear flow to ideal flow with no shear shown by Fig.1.1 b) and Fig.1.1 c) respectively. Nature guides and provide a pathway for this through a number of examples like low drag property of plant leaves, butterfly wings and shark skin[15]. The most documented phenomena is termed as Lotus effect[16]. A Lotus leaf does not wet and acts as hydrophobic, low resistance and self cleaning surface[12] (Fig.1.5 a)). The phenomena has been observed from centuries in different part of the world with references of Lotus leaves found in philosophical discussions[17]. It is probably only after the advancement in the high magnification imaging that the material explanation was provided.

A lotus leaf exibit a micro structured surface with micro protrusions, as illustrated by the scanning electron microscope (SEM) image at different magnifications in Fig.1.5 a). The microstructures has been mimicked to form micro and nanostructured surfaces[12]. Fig.1.5

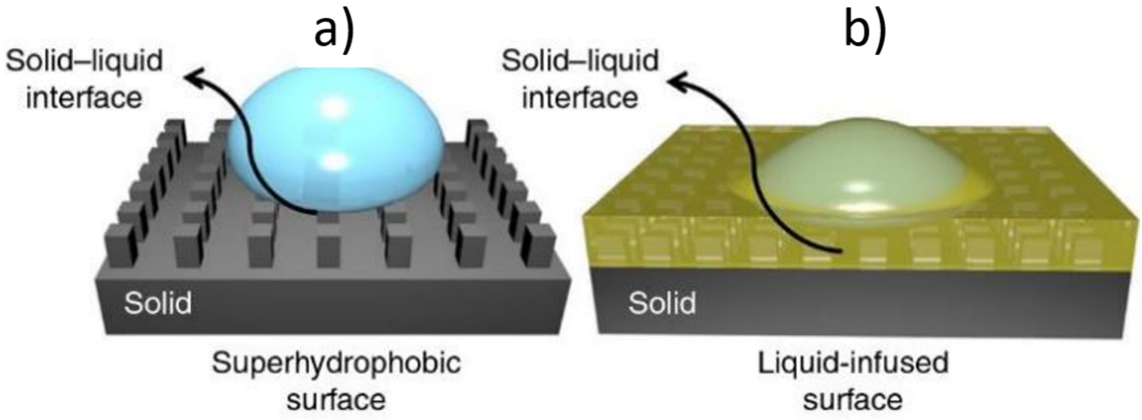

FIGURE 1.6: Liquid infused surfaces. a) air between structures, b) liquid between structure[18]

b) and Fig.1.5 c) shows two designs, a microstructured surface with stripes[13] and cylindrical nanostructures[14] respectively. The development of techniques to mimic the structured surface provide the capability of reducing viscous drag. When a drop is placed on the lotus leaf, air pockets are formed between the protrusions and the drop sits on this protrusions[18] (Fig.1.6 a)) which result in minimal solid contact, limiting the no-slip boundary condition and facilitating easy movements of the drop. Further advances include replacing the air pockets by an immiscible liquid and forming a liquid infused surface[18] (Fig.1.6 b)), this provides additional benefits of tuning drag by varying the viscosity of the infused liquid[19].

1.4 Drag measurement techniques

Drag or shear measurement methods can be classified as indirect method and direct method. Indirect methods involve measuring the quantities like pressure drop and shear force whereas a direct method involves measuring the velocity profile of flow. Fig.1.7 shows the indirect and direct method used for structured surface and related studies compiled[20].

1.4.1 Pressure drop measurements

In pressure drop vs. flow rate method, a known flow rate Q is set and a differential pressure is measured across length L. The pressure drop thus obtained is compared with the expected pressure drop over a flat solid surface. The deviation in the pressure drop quantifies the drag reduction (DR). For a flow over a modified surface, the DR is given by[21]

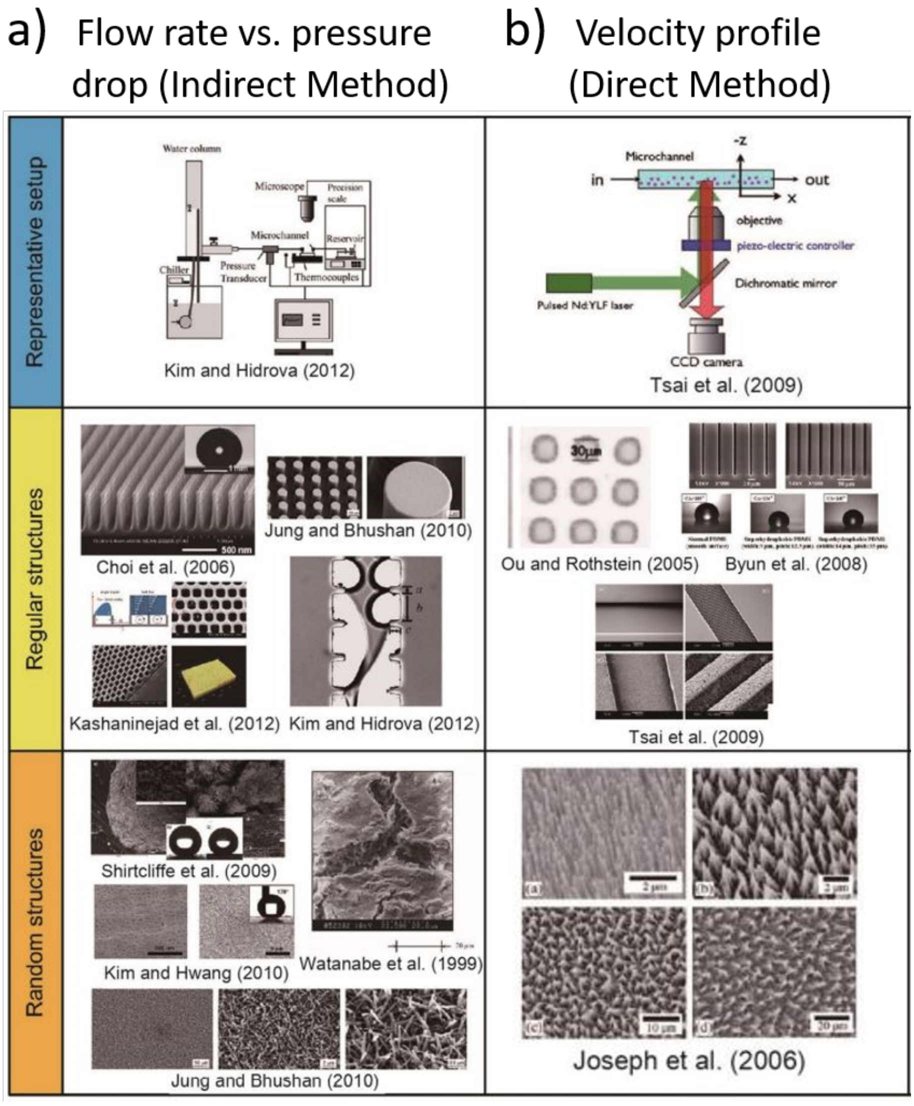

FIGURE 1.7: Drag reduction methods on structured surfaces: direct and indirect measurement methods[20]

$$DR = \frac{\Delta P - \Delta P_{SS}}{\Delta P} \times 100 \tag{1.7}$$

where ΔP is the pressure drop measured on a flat solid surface and ΔP_{SS} is the pressure drop measured on structured surface. Note that the flow over a flat solid surface assumes no slip boundary condition whereas in structured surface, the introduction of liquid-air interface overcomes the no-slip condition and result in drag reduction. Fig.1.7 a) shows examples of surface designs for drag reduction purposes from the literature. Drag reduction is studied mostly by modifying open surfaces by means of structuring at microscopic scale.

Fig.1.8 a) shows a schematic for liquid infused surface[21]. The lubricating liquid (yellow) is infused in the structured surface and the flow of transported liquid (blue) is expected to have a velocity profile (red profile) with non zero velocity at the liquid-liquid interface. Pressures are measured at two ports located near inlet and outlet separated by a distance L.

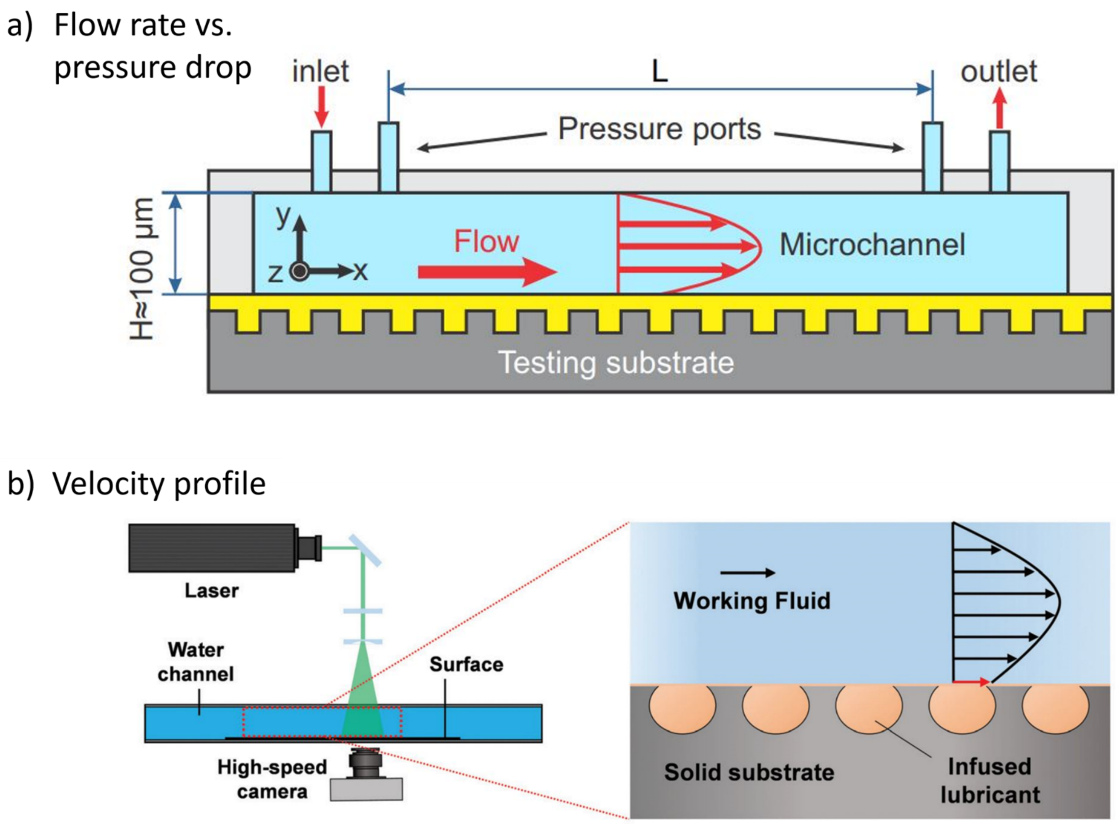

FIGURE 1.8: Drag reduction methods used on liquid infused surface. Indirect method[21], direct method[22]

1.4.2 Velocity profile

Measurement of the velocity profile provides a direct measurement of viscous shear and evidence of possible non-zero wall velocity at the wall. Experiments involve the flow of a particle laden liquid and tracking the particles in the flow channel[23]. The method is called particle image velocimetry (PIV) or particle tracking velocimetry (PTV). The particles are fluorescent beads excited using a laser of suitable wavelength. The emitted wavelength from the particles provide the signal for local velocity detection. A time sequence of images is recorded using a CCD camera, through an optical setup with bandpass filter and objective. The image sequences are analyzed by cross correlation of consecutive images for PIV, or single particle trajectory tracking in PTV. Fig.1.7 b) shows measurement setup for imaging velocity profiles over a structured surface[20]. Fig.1.8 b) shows the same setup with a liquid infused surface and a velocity profiles with non-zero velocity at the liquid-liquid interface[22]. This non-zero velocity is called the slip velocity along with another important measurement quantity called slip length (b), shown in Fig.1.9, defined as the distance between the wall bounding the flow and the point where the extended velocity profile intercepts zero. It can be observed that due to liquid-liquid interface (red line in Fig.1.9), the velocity is non-zero at the flow wall (zero for Poiseuille flow). This reduces the velocity gradient and hence the shear stress. In the small slip length regime the slip length is modelled as a linear extrapolation of the flow profile (Fig.1.9) given by

$$b = u_s \frac{\partial u}{\partial y} \tag{1.8}$$

where u_s is the velocity at the wall.

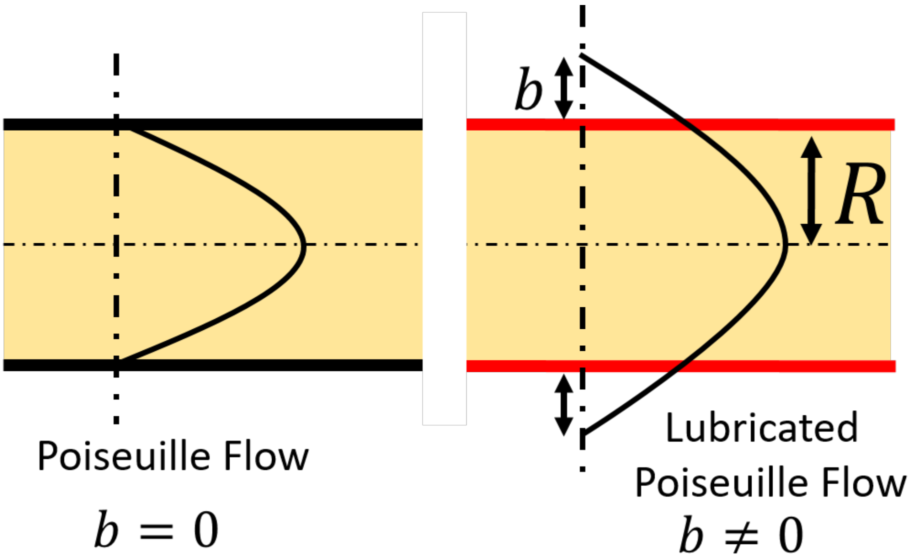

FIGURE 1.9: Slip length (b). Poiseuille flow with parabolic profile and zero velocity at the solid wall. Lubricated flow with non-zero velocity at bounding wall (red line).

Though direct methods are required to measure a slip length, this value can also be defined for indirect method by casting the pressure drop or force in terms of slip length. In this case the slip length is called as effective slip length. Fig.1.10 shows a compilation[20] of slip length values ($b = \delta$) over structured surfaces

Fig.1.10 a) shows the slip length $\delta = b$ as a function of pitch length (L). The surface is shown in Fig.1.5 b). The pitch L is similar to the parameter P in Fig.1.5 b). It can be seen that most of the data in literature show values in the range $100\mu m < \delta < 10nm$. The broken line plotted as $\delta = L$ illustrates how most experiments find $\delta < L$. Fig.1.10 b) shows the parameter $\frac{\delta}{L}$ for increasing gas fraction ϕ_g, where the fraction is the ratio of surface area

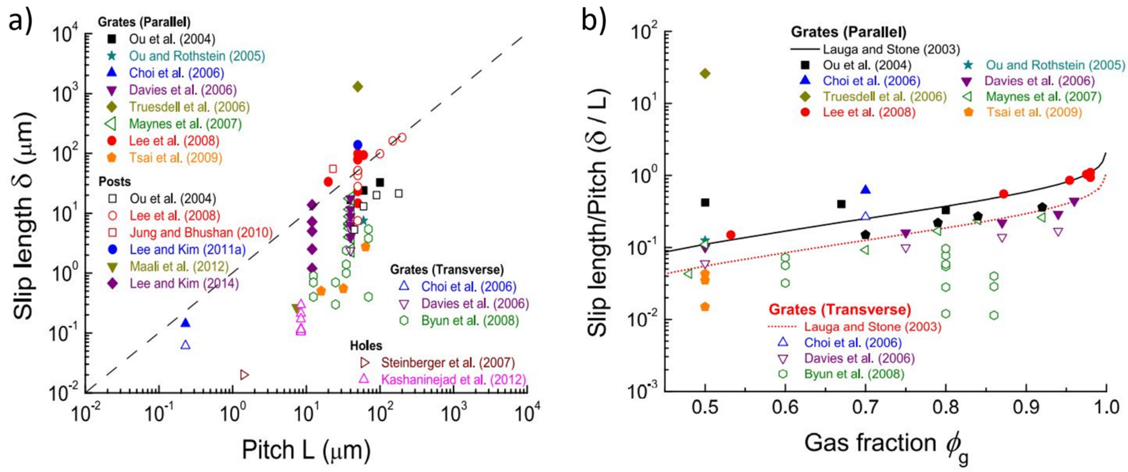

FIGURE 1.10: Experimental Slip length ($b = \delta$) on structured surfaces[20]. a) Slip length δ as a function of pitch L, b) δ/L as a function of gas fraction (ϕ)

Study	Typical size of structures (μm)	Viscosity ratio	Slip length (μm)
Solomon et al. (2014)[19]	50	0.031	2.7
		0.3	2.1
		20	4.1
		261	18
Kim (2016)[25]	$10.9 < R_{rms} < 15.4$	0.2	6 ± 7
		5.2	7 ± 7
		9.2	8 ± 7
Lee et al. (2019)[22]	100	0.006	47
Vega-Sánchez et. al (2022)[21]	random rough surface	0.1	5.2
		0.1	6.7
		5.5	12.8
		9.7	17.9

TABLE 1.1: Slip length in a liquid infused surface.

of the gas-liquid interface area to the total flow area. It can be seen that $\frac{\delta}{L}$ increases with ϕ_g. This behavior is also predicted by an analytical model proposed for flows on structured surfaces with parallel and transverse gratings shown by the continuous and broken lines respectively. This suggest that a continuously lubricated flow channel will have a larger slip length. The lubricant is gas (air) in the presented data. Air lubricated surfaces could also increase the hydrodynamic resistance to flow beyond a certain interface curvature[24]. If the lubricant is a liquid, the slip length is presented in Tab. 1.1 for different viscosity ratio η_r, where η_r is the ratio of viscosity of flowing liquid to the viscosity of lubricant. It is a general trend that the slip length increases with increase in viscosity ratio. The slip length remains however smaller than the typical size of the structures.

It should be noted that due to the complex measurement procedure required for direct measurement of the velocity profile, the literature on direct measurement method is less documented than the one using indirect methods. The number of studies decreases further when measuring velocity profile with liquid infused surfaces. The fundamental reason is the stability of liquid infused surfaces[26, 27].

1.5 Interface instability issues in lubricated flow

The instability of liquid interfaces is one of the most interesting and challenging topic of fluid mechanics. It is worth to dedicate some efforts here to focus on Plateau-Rayleigh instability (PRI) relevant in our research. PRI occurs in the flow of a liquid cylinder originally studied for a falling liquid jet[28]. Here we apply it for a cylindrical liquid-in-liquid flow

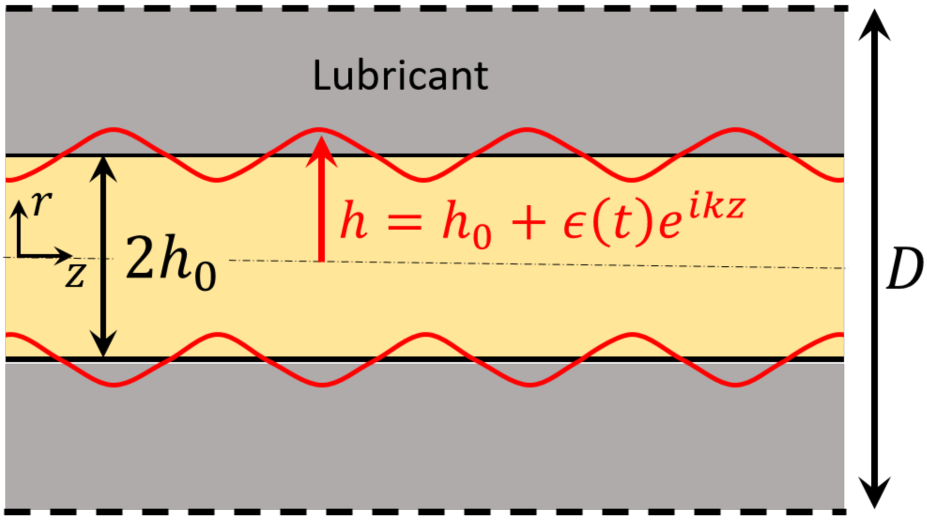

FIGURE 1.11: Schematic for PRI instability. Bright central part is flowing liquid of diameter $2h_0$ and darker surrounding lubricant. Black line in between the liquids is the liquid-liquid interface and black broken line is the solid wall. The red curve shows the perturbation of the liquid-liquid interface

Consider a cylindrical lubricated flow as shown in Fig.1.11 a). The brighter central part is the liquid of interest(flowing liquid) and the grey part show the encapsulation by the lubricant. The momentum equation governing the flow is Eq.1.2. The velocity profile for the flowing liquid is then given by

$$u(r) = \frac{r^2}{4\eta}\frac{\partial P}{\partial z} + a_1 \tag{1.9}$$

The flow in the lubricating layer is considered as a shear driven flow with a general velocity profile as

$$u_f(r) = a_2 r + a_3 \tag{1.10}$$

Using the boundary conditions as

$$u_f = 0, \;\; at \;\; r = D/2 \tag{1.11}$$

$$u_f = u, \;\; at \;\; r = h \tag{1.12}$$

$$\tau = \tau_f, \;\; at \;\; r = h \tag{1.13}$$

where a_1, a_2 and a_3 are constants of integration. Eq.1.11 , Eq.1.12 and Eq.1.13 defines no-slip at the solid wall, continuity of velocity at the liquid-liquid interface and continuity of shear stress at the liquid-liquid interface. The velocity profile in the flowing liquid ($u(r)$)

$$u(r) = \frac{1}{4\eta}\frac{\partial P}{\partial z}\left[r^2 - h^2\right] + \frac{1}{4\eta}\frac{\partial P}{\partial z}\left[2h\eta_r\left(h - \frac{D}{2}\right)\right] \tag{1.14}$$

The flow rate Q is given by integrating the flow velocity over the cross section

$$Q = 2\pi\left[\frac{\gamma}{16\eta}\left(h^2h' + h'''h^4\right) - \frac{\gamma\eta_r}{4\eta}\left(h'h^2 - \frac{h'Dh}{2} + h^4h''' - \frac{Dh^3h'''}{2}\right)\right] \tag{1.15}$$

With the pressure (P) given by the Laplace pressure

$$P = \gamma\kappa \tag{1.16}$$

where $\kappa = \left[\frac{1}{h} - h''\right]$ is the curvature giving $\frac{\partial P}{\partial z} = -\left[\frac{h'}{h^2} + h'''\right]$ The volume conservation of the flowing liquid dictates

$$\frac{\partial h}{\partial t} + \frac{1}{2\pi h}Q' = 0 \tag{1.17}$$

$$Q' = \left[2\pi\left[\frac{\gamma}{16\eta}\left(h^2h'' + 2hh'^2 + h^4h'''' + 4h^3h'h'''\right)\right.\right.$$
$$\left.\left.-\frac{\gamma\eta_r}{4\eta}\left(h^2h'' + 2hh'^2 + \frac{D}{2}(hh'' + h'^2) + h^4h'''' + 4h'''h'h^3 - \frac{D}{2}(h^3h'''' + 3h^2h'h'''')\right)\right]\right] \tag{1.18}$$

In the linear stability analysis we assume a perturbation to the initially flat liquid-liquid interface (black line between the two liquids) given by $h = h_0 + \epsilon(t)e^{ikz}$ (red oscillations at the interface) where $\epsilon(t)$ is the amplitude of disturbance with $\epsilon << h_0$ and we only keep the first order terms in ϵ. Following these conditions and using Eq.1.17 and Eq.1.18 gives

$$\frac{\partial\epsilon(t)}{\partial t} = \epsilon(t)\left(1 - h_0^2k^2\right)k^2\left[\frac{\gamma h_0}{16\eta} + \frac{\gamma\eta_r}{4\eta}\left(\frac{D}{2} - h_0\right)\right] \tag{1.19}$$

Eq.1.19 shows the growth rate of the amplitude of the perturbation to the liquid-liquid interface. It shows that for volume conservation of the flowing liquid, the growth rate of the perturbations is positive $\frac{\partial\epsilon(t)}{\partial t} > 0$ for at least one (some) wave number (k) and hence the system is unstable.

The amplitude of perturbation is

$$\epsilon(t) \propto \exp(t/\omega) \tag{1.20}$$

where

$$\omega(k) = \frac{1}{\left(1 - h_0^2k^2\right)k^2\left[\frac{\gamma h_0}{16\eta} + \frac{\gamma\eta_r}{4\eta}\left(\frac{D}{2} - h_0\right)\right]} \tag{1.21}$$

The fastest growing mode is the experimentally observed mode of disturbance which corresponds to the minimum ω given by

$$\frac{\partial\omega(k)}{\partial k} = 0 \tag{1.22}$$

k=$\sqrt{2}h_o$, which is the conventional PRI mode of instability[29].

In context of stability of the liquid infused interfaces (LIS), two failure modes are of interest, the shear induced failure[26] and the PRI instability[30]. Fig.1.12 a)-i) shows a typical experiment design used in literature to understand the shear driven failure of LIS. A flow of aqueous solution (blue) is set over the LIS with lubricant (green) and shearing process imaged. Fig.1.12 a)-ii) shows the top view of the measurement cell. The central horizontal green patch is made of 50 longitudinal grooves. Fig.1.12 a)-iii) shows the time evolution of the shearing process. The shearing of the lubricant oil increases with time with a steady lubricated surface left as l_{inf} for a given flow rate (shear stress). Fig.1.12 a)-iv) shows the structure of the surface. Though the study provides an excellent understanding on the drainage of the LIS, it is limited to flow over a flat surface. When it comes to stability of coflowing liquid streams with cylindrical lubrication, we fall back to PRI. Fig.1.12 b)-i) shows a

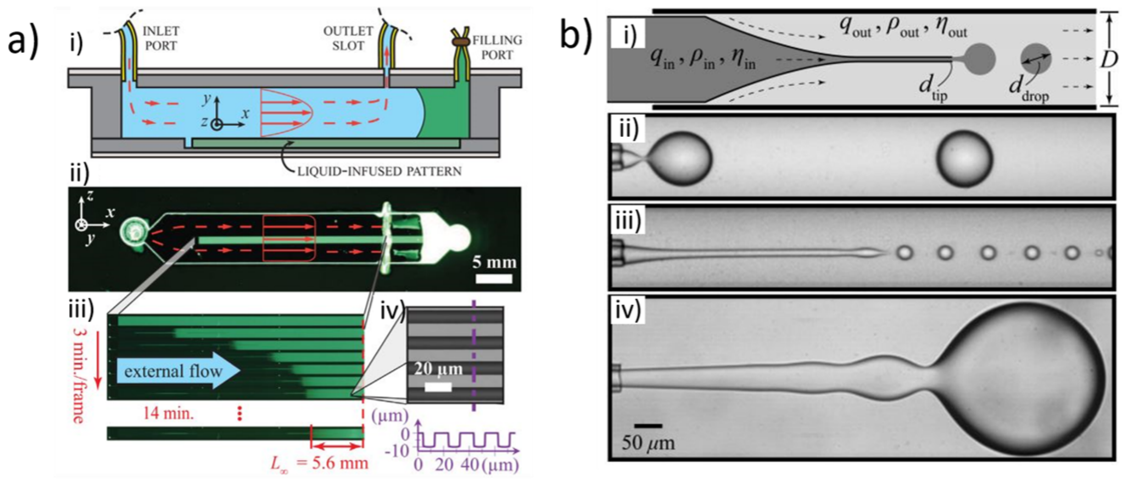

FIGURE 1.12: Stability issues in lubricated flows. a) Shearing of liquid infused surface[26], i) Schematics for shear measurement setup, blue is the flowing liquid and green is the lubricant, ii) Top view of the flow channel, iii) time lapse of the lubricant depletion, iv) micrographs showing the surface structure. b) Instability in co-flowing liquid streams[30], i) schematic of a two liquids flow setup, ii) dripping of inner liquid, iii) jetting or stable liquid-liquid interface for finite distance, iv) widening of jet with increasing flow rate of inner liquid.

schematic design of a two phase system, where the inner liquid is the liquid of interest (to be transported) and the outer encapsulating liquid is the lubricating liquid. The flowing liquid experiences 3D lubrication. q , ρ and η are flow rate, density and viscosity of liquids, in and out are subscripts for inner and outer liquids respectively. The inner liquid is injected with a tapered capillary with in a flowing outer liquid. Two regimes are observed under in this flow condition, dripping shown in Fig.1.12 b)-ii) where the inner liquid as it comes out of the capillary breaks up into droplets, or jetting shown in Fig.1.12 b)-iii) where the inner liquid forms a jet like structure over a limited distance. The transition from dripping to jetting happens on increasing q_{out} while keeping q_{in} constant. It shows that the shear stress (increasing with increasing flow rate Q_{out}) stabilizes the system. Further increasing Q_{out} results in widening of the jet (Fig.1.12 b)-iii)) and unstable interface. The experiments suggest that it is possible to stabilize a liquid-in-antitube of limited length if we control the flow rate ratio of the involved liquids. The transition from dripping to jetting depends on the density, viscosity, velocity of the involved liquids as well as the interfacial tension at the liquid-liquid interface. Two non-dimensional numbers, namely the Weber number of the inner liquid ($W_{in} = \frac{\rho_{in} d_{tip} u_{in}^2}{\gamma}$) and the capillary number of the outer liquid ($C_{out} = \frac{\eta_{out} u_{out}}{\gamma}$) contribute to the aforementioned physical properties. When W_{in} and C_{out} are small the interfacial tension dominates and the system is forced to drip whereas when C_{out} is large (> 1), the shear stress overcomes the interfacial tension and jetting results[30].

1.6 Stable liquid-in-liquid flow: Flow focusing

The phenomena of stable flowing liquid of interest lubricated concentrically by another flowing liquid is called *"flow focusing"*. It is widely used for a large range of applications like drug delivery[31], drug discovery[32], cell counting and beyond[33] or simply to reduce drag[6]. Fig.1.13 a) shows a schematic design of flow focusing[34] where the liquid of interest (red) is lubricated concentrically (grey). Fig.1.13 b) shows a top view under a microscope. The flow rates of the two liquids are chosen such that the system remains in jetting regime. Fig.1.13 c) show schematics with the velocity profiles (white arrows) expected in unlubricated and lubricated flows. A lower viscosity liquid (compared to the inner liquid one) is used for lubrication (viscosity ratio $\eta_r > 1$). The lubricated flow shows that a flatter velocity profile suggesting a lower shear stress[6]. Fig.1.13 d) shows the arrangement for making a micro-needle using flow focusing for flowing biological fluids with concentrated drugs.

Though flow focusing provides a possibility of lubricated flow, they suffer from some disadvantages

- Static cylindrical liquid structures are unstable.
- Co-flowing liquids are required, where the handling of the lubricating liquid requires extra adjustments and control.
- Flow rates are needed to avoid the formation of droplets.
- Rayleigh-Plateau instability restrict the geometry to a cylindrical one

A solution could be the use of magnetic liquid as lubricating liquid (Fig.1.6 c)) and magnets to hold the magnetic liquid in place. This bring us to the discussion on magnetic liquid: ferrofluids[35].

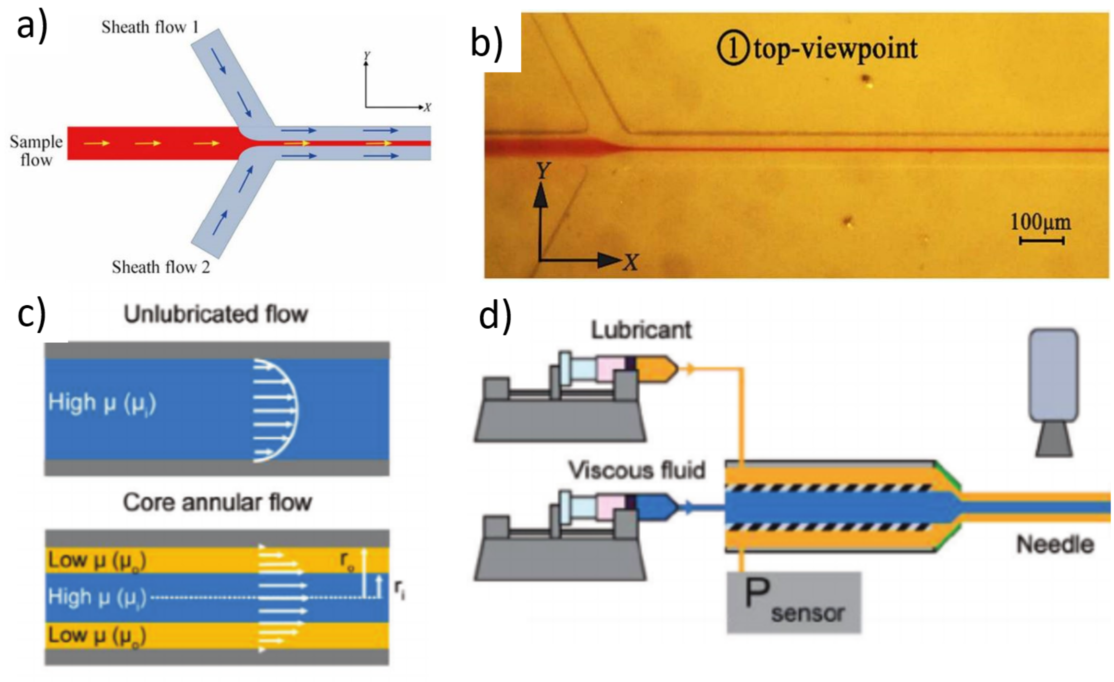

FIGURE 1.13: Flow focussing. a) and b) Microchannel[34], c) and d) Medical microneedle[6]

1.7 Ferrofluids

Ferrofluids are colloidal suspensions of ferromagnetic particles typically of nanometer size stabilized in a carrier liquid. In colloidal suspensions, the stability of the material is essential for it to act as a fluid. This allows the use of Eulerian approach to be applied for describing a ferrofluid without going into statistical approach (Lagrangian description of fluid). Apart from chemical stability of ferrofluid, there are four main competing energies for a ferromagnetic particle in a carrier liquid:

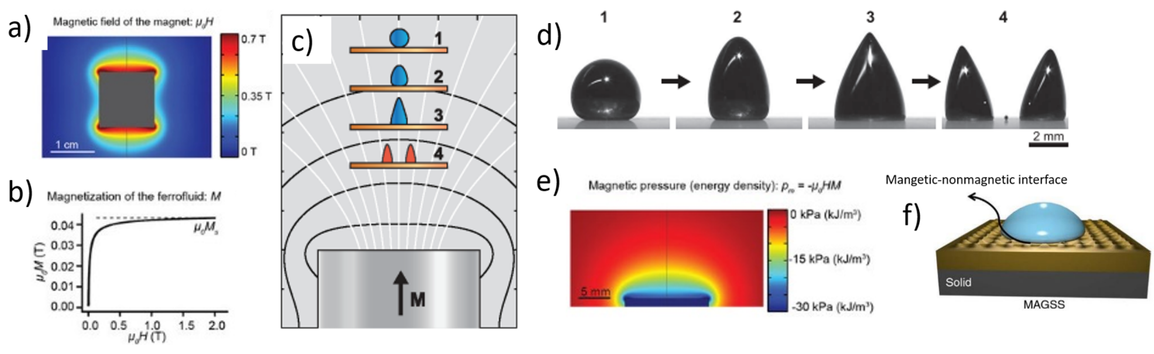

FIGURE 1.14: Ferrofluid as magnetic liquid. a) Magnetic field generated by a permanent magnet[36], b) Typical magnetisation curve for ferrofluid in magnetic field[36], c) Schematic of response of ferrofluid with increasing magnetic field[37], d) experiments showing change of shape of ferrofluid with increasing field[37], e) Contour of Magnetic pressure[36], f) Schematic of a drop on magnetic liquid (Ferrofluid) infused surface[38]

the magnetic energy ($\mu_0 M_p HV$), the gravitational potential energy ($\Delta\rho ghV$), the thermal energy (kT) and the dipole-dipole interaction energy ($\frac{\mu_0 M_p^2 V}{12}$)[35]. Here μ_0 is magnetic permeability , M_p is the magnetisation of the particle in applied magnetic field H. $\Delta\rho$ is the density difference between the particle and the carrier liquid, g is the gravitational acceleration and h is the height , k and T are Boltzmann constant and absolute temperature respectively. V is the volume of the particle $\frac{\pi d_p^3}{6}$ with d_p as the diameter of a spherical particle.
Fig.1.14 a) shows a typical magnetic field generated by a permanent magnet above a magnet[36]. The field gradient thus created would apply a magnetic force on the ferromagnetic particle.

$$\frac{kT}{\mu_0 M_p HV} > 1 \tag{1.23}$$

Hence in a magnetic field gradient, to avoid the movement of particles towards high field region, the thermal energy must be larger than the magnetic energy. Eq.1.23 provide one criterion for ferrofluid stability.

$$\frac{\Delta\rho gh}{\mu_0 M_p H} < 1 \tag{1.24}$$

To ensure the stability against gravity, or settling of ferromagnetic particle in gravitational field, the magnetic energy should be larger than the gravitational potential energy, condition given by Eq.1.24. Finally since every particle of ferrofluid in the presence of a magnetic field act as a magnet, the condition for avoiding agglomeration of the particle in magnetic field dictates that the thermal energy should be greater than the dipole-dipole interaction energy, condition given by Eq.1.25

$$\frac{12kT}{\mu_0 M_p^2 V} > 1 \tag{1.25}$$

Note that the particle-particle interactions are also tuned by coating the ferromagnetic particles by surfactants. Thus a stable ferrofluid is obtained with the design principles governed by the Eq.1.23 to Eq.1.25. This allows us to treat the ferrofluid using the conventional continuum approach of fluid mechanics with a possible extra term of magnetic body force (for one dimension, just like gravity) in the Navier-Stokes equation. The ferrofluid properties are thus is an average of all particles. Fig.1.14 b) shows the magnetisation of a ferrofluid with increasing magnetic field[36]. Similarly to other fluid properties like viscosity, density and interfacial tension can be ascribed to the ferrofluid. Fig.1.14 c) illustrates ferrofluid behavior in magnetic field. Ferrofluids act as a smart material and change their shape in response to the strength of applied magnetic field[37]. As the field strength increases the ferrofluid drop becomes more pyramidal (Fig.1.14 d)) and finally breakes up into two drops to minimize the potential energy (magnetostatic energy + surface energy+ gravitational potential energy). Further increase of the magnetic field could result in division of drops into multiple smaller drops. The shape and curvature of the drop depends on the balance of the pressures acting on the ferrofluid. There are three pressures namely the magnetic pressure (P_m) which is also the magnetostatic energy per unit volume, the magnetic normal traction (P_n) due to the field continuity requirement at the magnetic-nonmagnetic interface, and the Laplace pressure (P_{La})[39].

$$P_m = \int_0^H \mu_0 M dH \tag{1.26}$$

$$P_n = \frac{1}{2}\mu_0 M_I^2 \tag{1.27}$$

$$P_{La} = \kappa\gamma \tag{1.28}$$

Fig.1.14 e) shows the evolution of magnetic pressure[36] with the magnetic field shown in Fig.1.14 a). With appropriate pressure magnitude, a magnetic fluid infused surface[38] could be made as shown in Fig.1.14 f). This help to increase the stability of liquid infused surfaces and studies have used a magnetic liquid as the lubricating liquid for movements of drops[40].

These magnetically lubricated surfaces could be used for myriad of applications. Fig.1.15 depicts some of them. Fig.1.15 a) shows the formation of Rosenweig spikes[35] on application of a magnetic field and back to flat topology on removal of the field[36]. By infusing the ferrofluid in a structured surface, we can create and control the wetting dynamics. Fig.1.15 b) shows the wetting of a water drop on ferrofluid infused structured surface, schematic design (top) and experiments (bottom)[36]. If the surrounding medium is air then the ferrofluid covers the water drop, however if the surrounding medium is replaced with hydrocarbon liquid the ferrofluid only wets the foot print of the drop. Hence we can tune the wetting of a liquid drop. The drop can be manipulated using a magnetic field of a permanent magnet[40] (Fig.1.15 c)) as well as an electromagnet[41] (Fig.1.15 d)). Similarly a non-magnetic colloid can be transported on a surface of a ferrofluid by moving the infused ferrofluid using a magnet or other sources, schematically shown in (Fig.1.15 e)). The colloid position with time is plotted (Fig.1.15 e)) right, showing that when the magnet is on, the colloid moves and on stopping the magnet (unshaded region) the bead has a steady position[36]. Another very important application of ferrofluid infused surfaces is their antifouling property, resulting from the moving liquid-liquid interface that impedes the biofilms growth[36], with schematics of experiments shown in Fig.1.15 f).

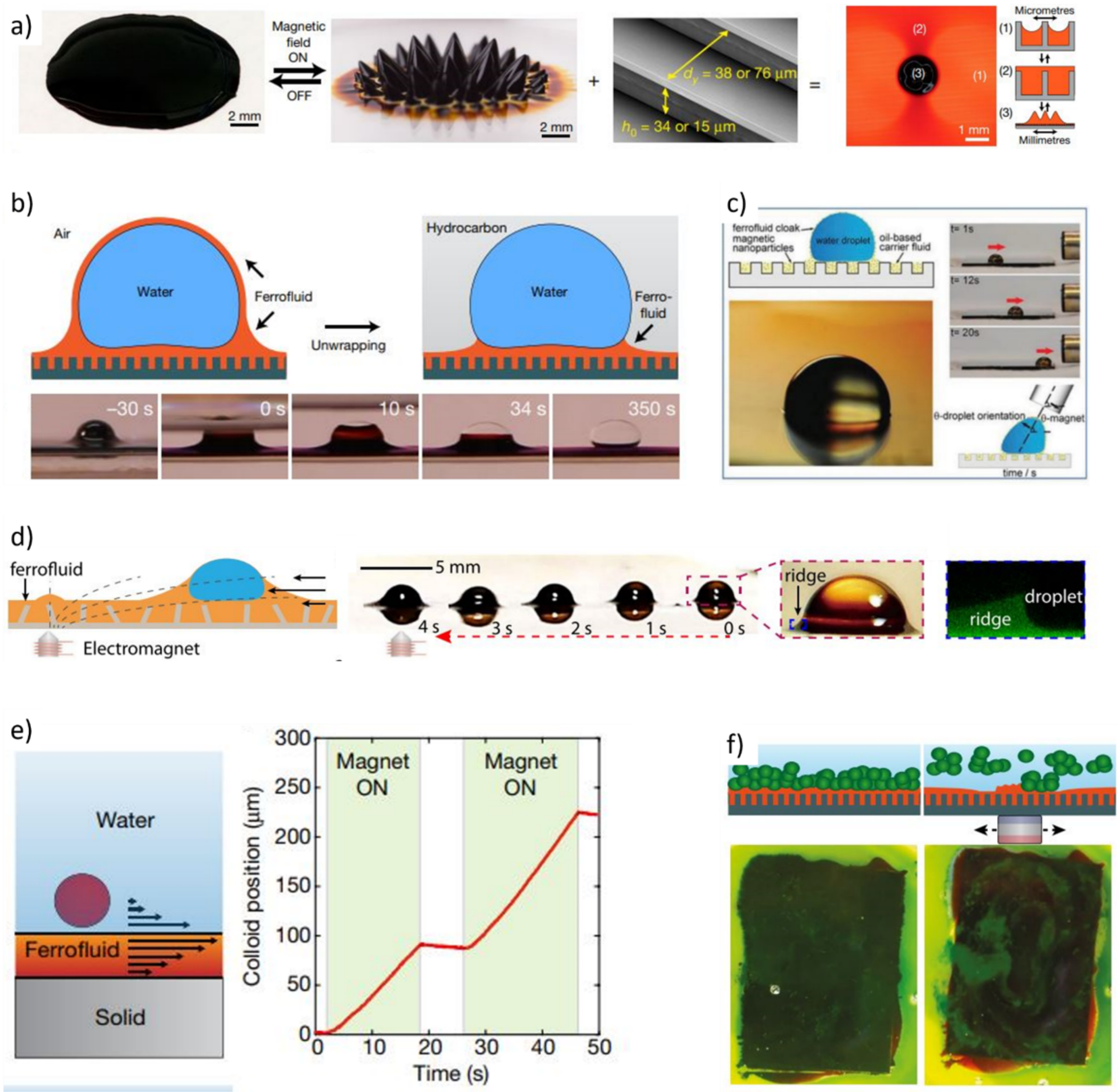

FIGURE 1.15: Ferrofluid and applications. a) Reversible topology of ferrofluid with magnetic field, infused in structured surface form Ferrofluid infused surface (FIS)[36], b) Wetting of water drop on FIS in air(left) and hydrocarbon(right) environment[36], c) and d) manipulation of drops on FIS using a permanent magnet[40] and an electromagnet[41] respectively, e) motion control of a nonmagnetic colloidal particle on a FIS[36], f) Antifouling surface due to moving liquid interface[36].

Even though ferrofluid-infused surfaces provide various advantage over liquid infused surface, the concept of magnetic lubrication is limited to open surfaces and the creation of flow focusing kind of systems seems challenging. Even though early pioneers in ferrofluid lubrication[42] in a hydrocarbon oil transport pipelines were published in the 90's, where simple permanent magnets where used to hold ferrofluid lubricant in place, there broader relevance and essential physics still remains to be understood. Magnetic encapsulation of cylindrical antitube has been suggested.

1.8 Magnetic encapsulation of a antitube

By designing an appropriate magnetic field arrangement, it is possible to avoid the solid wall altogether and form a cylindrical liquid-in-liquid flow channel[43] shown in Fig.1.16 . This is the base idea at the source of the manuscript presented here.

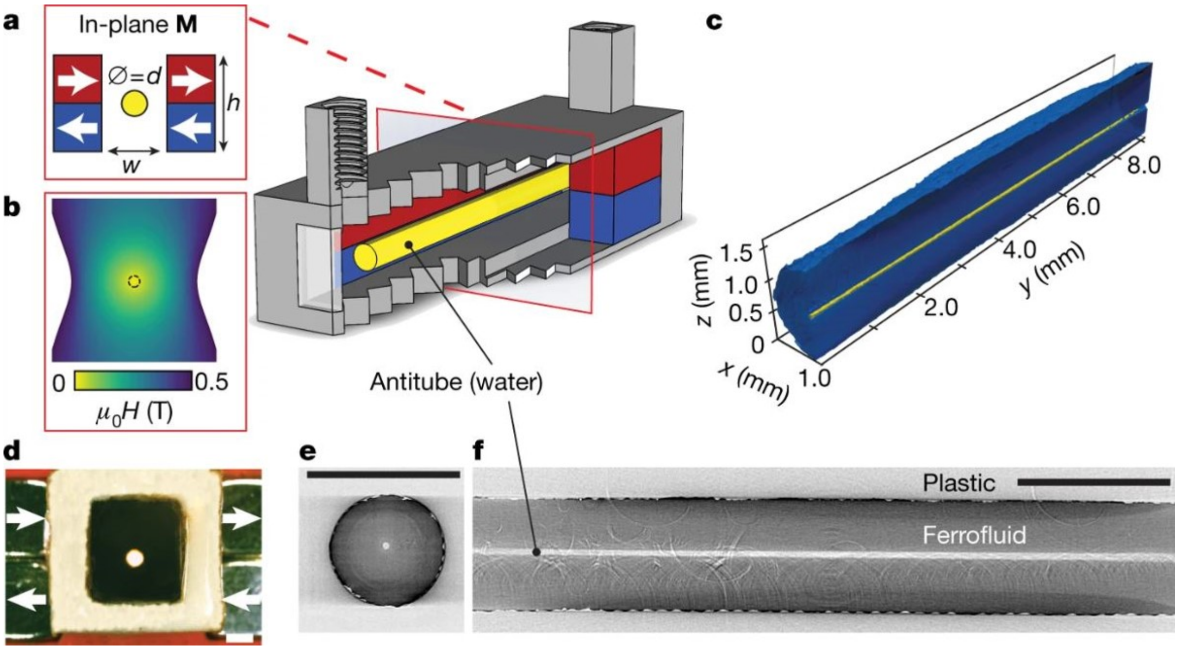

FIGURE 1.16: a, Permanent magnets (red, blue) in an in-plane quadrupolar configuration create a low-field zone at the centre, where an antitube of water (yellow) is stabilized inside an immiscible magnetic liquid (white). b, Contour plot of the magnetic field. c, Synchrotron X-ray tomographic reconstruction of a water antitube (yellow) with diameter 81 μm, surrounded by ferrofluid (blue), see AppendixC for imaging setup. d, Optical end view of a water antitube in ferrofluid. e, X-ray end-view cross-section from tomographic data at y = 4 mm. f, X-ray side-view cross-section from tomographic data at x = 1 mm. Scale bars (black/white), 2 mm.

It starts with specific magnet arrangements of four magnets shown in Fig.1.16 a) housed in a 3D printed circuit, where white arrows show the direction of magnetization of the permanent magnets generating a magnetic field in between the magnets (inset) zero at the center and increasing radially (Fig.1.16 b). On inserting a limited amount of ferrofluid, the magnetic forces attract the ferrofluid towards the magnet while keeping the center encapsulation for a diamagnetic liquid (or much less paramagnetic than the ferrofluid) named antitube. 3D X-ray tomography shown in Fig.1.16 c) and optical image shown in Fig.1.16 d) shows a bright central part as the antitube (water) and a darker encapsulation as a ferrofluid. Fig.1.16 e) and Fig.1.16 f) shows the X-ray radiography images. Note that the fluids are static in Fig.1.16.

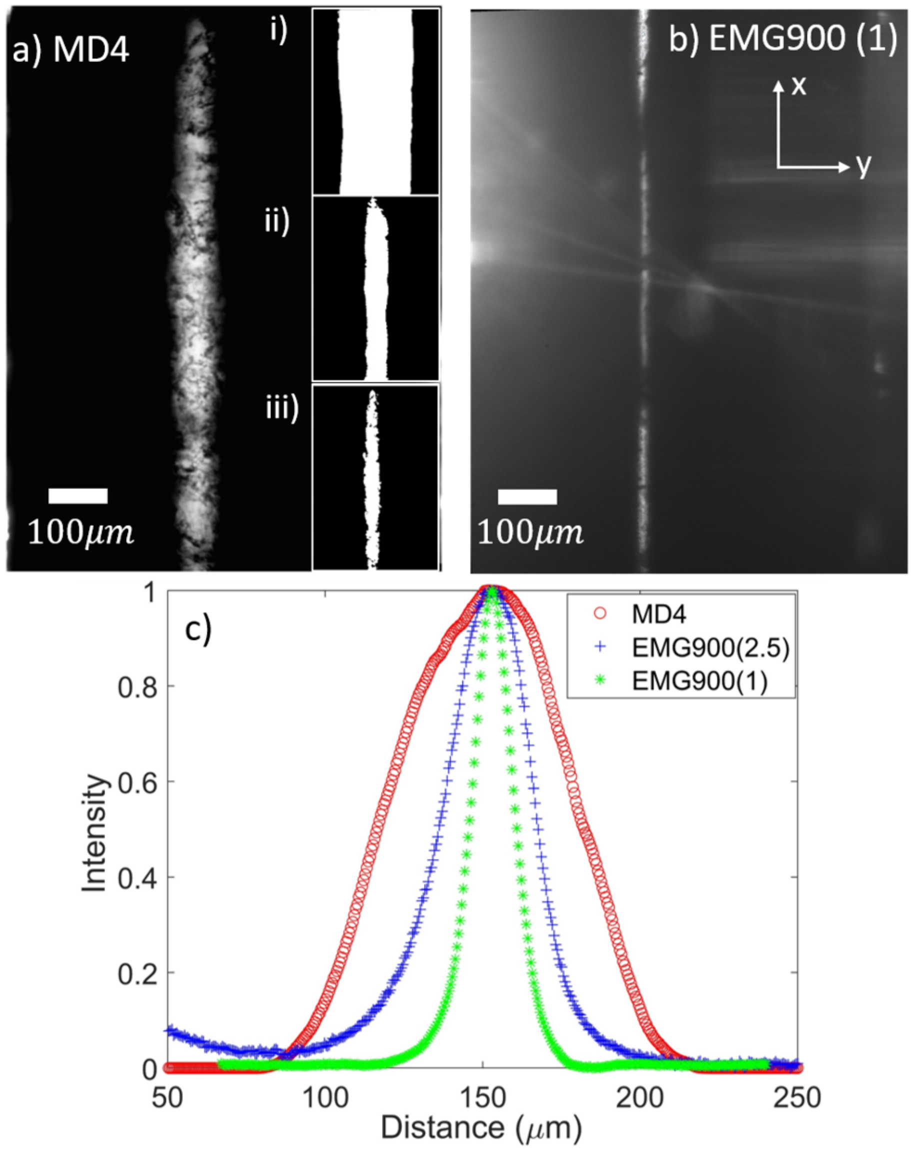

FIGURE 1.17: a) Optical image of a sub-100-μm water antitube in an MD4 ferrofluid and b) EMG900 ferrofluid (double surfactant), c) Intensity profile across the microfluidic channel in the vicinity of the water antitube. The profile is column-averaged along the length of microfluidic channel. EMG900(1) reads ferrofluid EMG900 and the magnet seperation 1 mm. double surfactant is case where the flowing liquid and the ferrofluid both are mixed with surface trension. See AppendixC for microscopy details

The equilibrium diameter d_{eq} of the diamagnetic liquid is given by the balance of magnetic pressure , magnetic normal traction and Laplace pressure

$$d_{eq} = \frac{4\gamma}{2\mu_0 \overline{M} H_I + \mu_0 M_I^2} \tag{1.29}$$

where γ, H_I and M_I are interfacial tension, magnetic field and ferrofluid magnetisation at the magnetic-nonmagnetic interface respectively. $\overline{M}$ is the field averaged magnetisation of the ferrofluid. The d_{eq} can be reduced by tuning the magnetisation and the interfacial tension. Fig.1.17 a) and Fig.1.17 b) show brighfield microscopy images with two different ferrofluid MD4 and EMG900 respectively. The two ferrofluids (darker encapsulation) provide two different combinations of magnetisation and interfacial tension with water as flowing liquid (brighter). Ferrofluids MD4 shows d_{eq} of about $50\mu m$, Inset show stages of ferrofluid filling to reach d_{eq}. Ferrofluid EMG900 (Fig.1.17 b)) shows d_{eq} of 14 μm $\pm$ 0.5 μm. Fig.1.17 c) shows the intensity profile plotted across y and averaged over x, with half maximum width giving d_{eq}.

1.9 Research objectives of the thesis

The available literature suggest a need of scientific research in the domain of lubricated interfaces. These interfaces are ubiquitous in nature and are used for applications ranging in technological to biological flows. Though structured surfaces as well as liquid infused surfaces have been studied intensively, there are several fundamental issues which need to be addressed. We focus on primarily on the physics behind the magnetically confined flow, which can address the shortcomings of the current state of research and also reveal novel scientific knowledge. In our study, we use the combination of magnetic field with ferrofluids to create a microfluidic channel for diamagnetic liquids with unique properties like tunable drag reduction, plug flow and soft interface suitable for frictionless pumping, handling complex flow like oscillating flows, mimicking compliant conduits in nature like blood vessels in human body, transport of delicate biological cells, bio-printing of non-Newtonian liquids. We use experimental techniques like X-ray absorption contrast imaging, brightfield microscopy, fluorescence microscopy, particle tracking velocimetry supported by numerical solutions and theory to demonstrate the science behind our research of magnetically confined liquid channel. Specifically we address:

- **Drag reduction**

  Drag reduction is one of the most important application of lubricated surfaces. Reducing this drag by more than a few tens of percent remain elusive and research claiming drag reduction of more than 50% are scarce[44]. It is essential to develop experimental drag reduction methods and setup for continuous stable liquid-liquid interface. The understanding of physics and a full analytical model may propel our quantitative as well as qualitative understanding of the involved physical parameters. This can help in developing microfluidic channels with tunable viscous drag. **In chapter 2**, we study in detail the viscous drag reduction properties of the magnetically confined flow channel using experiments , numerical simulation and theory. The experiments involve flow rate vs pressure drop studies called as indirect method for quantifying drag reduction or slip length. Here, we show how cylindrical liquid–in–liquid flow leads to drag reduction of 60–99% for sub-mm and mm-sized channels[45]. The pressure drop reduces by more that one order of magnitude and suggests a large effective slip length at the liquid-liquid interface. This illustrates how it is beneficial to have a cylindrical flowing liquid confined by a liquid interface rather than by solid walls. Analytically, in a laminar flow model with appropriate boundary conditions, we introduce a modified Reynolds number with a scaling that depends on geometrical factors and viscosity ratio of the two liquids. It explains our whole range of data and reveal the key design parameters for optimizing the drag reduction values.

- **Direct measurement of large slip length: Near plug flow for biomaterial transport**

  The slip length (b) reported in the literature is always smaller than the typical length scale in the system, which is usually the flow radius (R), $b < R$. Methods to increase slip length beyond the radius of flow $b >> R$, are needed to realize near plug flow. A magnetically confined stable continuously lubricated flow channel can serve this purpose with tunable slip length for low shear biomaterial transport. Furthermore, experimental measurements of slip length with liquid-liquid interface is challenging. Hence the understanding of magnetic design and flow mechanics is crucial for experimental measurements in a microfluidic channel. **In Chapter 3**, we explore the magnetic design, flow profile symmetry and study the possibility of realizing near plug flow. We focus on measuring the velocity profile using particle tracking velocimetry to quantify the slip length (b) and show a direct evidence of approaching plug flow. Here we show evidence of shearless flow at room temperature and direct measurement of slip length (b) with continious liquid lubricated microchannel, which can be used for flow of biomaterials. We also observe and explain the asymmetric velocity profile for asymmetric lubrication thickness. The wall velocity for the flowing liquid depends on the viscosity ratio and more than 98% of the maximum velocity (98% plug flow) could be achieved. The measured slip length is found to be larger than the radius of the flow channel ($b >> R$) which has never been observed in microchannels. These findings are explained by an analytical model agreeing with the experiments.

- **Stability of complex liquid-liquid interface: Effect of magnetic stress**

  A static liquid-liquid interface in a cylindrical liquid-in-liquid arrangement is unconditionally unstable, due to the Plateau-Rayleigh Instability (PRI). It has been shown that two co-flowing liquids can be stable over limited length under the action of shear stress. However, there is a need to stabilize the flowing liquid for an arbitrary length without the requirement of flowing the lubricating liquid. Moreover the physics of liquid cylinder stability under the action of magnetic stress remains to be understood. **In chapter 4**, we study experimentally and theoretically the possibility of avoiding PRI using magnetic pressure/energy and explore the stability regime of magnetically stabilized liquid cylinder.

- **Soft deformable flow channels**

  Soft wall flow channels are also very important to generate fluid instabilities required for fluid mixing in microchannels at low Reynolds number[46]. It is therefore required to come up with novel strategies to create soft walled channels. Nozzles are required for targeted delivery and for bio-printing, but they might result in jamming or offer large shear stress. After understanding the dynamics of flow, the physics of the response of a magnetic-nonmagnetic flow interface, more specifically its apparent elastic behavior in response to a pressure driven flow, remains to be understood. **In chapter 4**, we focus our attention on discussing the behavior of the liquid-liquid interface, specifically their deformation under variable flow. The coupling between magnetic pressure and viscous stress results in a deformation length scale (l_d) governing the shape of deformed interfaces. Different combinations of magnetic pressure and viscous stress can be represented by a single parameter.

$$l_d = \left[\frac{\eta_f QWL}{\mu_0 M_s M_r \beta_0}\right]^{\frac{1}{5}} \tag{1.30}$$

where η_f is the ferrofluid viscosity, M_s and M_r are saturation magnetization of ferrofluid and remenant magnetization of permanent magnets, μ_0 is magnetic permeability, W and L are distance between pair of magnet and length of the flow channel, Q is the flow rate of antitube liquid and β_0 is the drag reduction factor for undeformed antitube ($Q = 0$). Beyond cylindrical tubes, complex soft shapes could be created. The Plateau-Rayleigh instability (PRI) shape[30] at the liquid-liquid interface can be mimicked and stabilized under flow. The shape is stable because the magnetic stresses are significantly larger than the Laplace pressure and gravity.

- **Mimicking complex flow and complex flow structures**

  The approach could possibly be used to mimic complex shapes in nature, for example small veins which are not of circular cross section. Understanding this, the concept can be extended for soft stable microfluidics. Since the advent of polymers like PDMS, the microfluidic technology have shifted to polymers for its preparation and used it to mimic the biological soft materials. Flow through blood veins and flow over soft tissues involve complex deformation of the interface. However, there are systems in nature and technological applications where the flow is not constant but oscillating or pulsating, for example flow through veins. Furthermore in flow focusing only the cylindrical flow structure can be stabilized. However there are cases where the flow channel is of complex shape, like the human intestine which is a flexible channel, disease like arterial thrombosis are a couple of examples. Hence it is essential to develop stable lubricated channel with an arbitrary shape. **In chapter 5,** we study experimentally the possibility of using a magnetically stabilized antitube for these mimicking complex flow and complex flow structure (arteries). Moreover most of the biological fluids are non Newtonian. Blood is shear thinning whereas concentrated biological drugs can be shear thickening. We therefore extend our models to show the viscosity behavior of non-Newtonian liquids in magnetically stabilized antitube.

In chapter 6, we conclude the thesis with some proof of concept experiments showing the application range of the magnetically confined antitubes in fluid physics and bio-applications. We also highlight the improvements to be made for engineering such novel devices.

1.10 Contributions

The concept of magnetically encapsulated liquid channel is developed by Peter Dunne (PD), Bernard Doudin (BD) and Thomas Hermans (TH). Arvind Arun Dev learned the concept of magnetic encapsulation from PD, BD and TH. AAD performed the brightfield microscopy experiments and assisted in the X-ray synchrotron measurement. The research article with the details of magnetic encapsulation is published[43].

Bibliography

[1]B. Gibson, D. Furbish, I. Rahman, M. Schmeeckle, M. Laflamme, and S. Darroch, "Ancient life and moving fluids", Biological reviews of the Cambridge Philosophical Society **96**, 10.1111/brv.12649 (2020).

[2]L. Bourouiba, "The fluid dynamics of disease transmission", Annual Review of Fluid Mechanics **53**, 473–508 (2021).

[3]D. Qin, Y. Xia, and G. Whitesides, "Soft lithography for micro- and nanoscale patterning", Nature protocols **5**, 491–502 (2010).

[4]Yole-Development, "The microfluidics industry is boosted by the covid-19 outbreak", Press Release, Lyon France (2020).

[5]M. Barocio, E. Hidalgo-Vázquez, Y. Kim, L. Rodas-Zuluaga, W.-N. Chen, D. Barcel, H. Iqbal, R. Parra, and C. Castillo-Zacarias, "Portable microfluidic devices for in-field detection of pharmaceutical residues in water: recent outcomes and current technological situation -a short review", Case Studies in Chemical and Environmental Engineering **3**, 10.1016/j.cscee.2020.100069 (2020).

[6]V. Jayaprakash, M. Costalonga, S. Dhulipala, and K. K. Varanasi, "Enhancing the injectability of high concentration drug formulations using core annular flows", Advanced Healthcare Materials **9**, 2001022 (2020).

[7]E. Dressaire and A. Sauret, "Clogging of microfluidic systems", Soft Matter **13**, 37–48 (2017).

[8]R. Rusconi, J. Guasto, and R. Stocker, "Bacterial transport suppressed by fluid shear", Nature Physics **10**, 212–217 (2014).

[9]L. LANOTTE, J. Mauer, S. Mendez, D. a. Fedosov, J.-m. FROMENTAL, V. Claveria, F. Nicoud, G. Gompper, and M. ABKARIAN, "Red cells' dynamic morphologies govern blood shear thinning under microcirculatory flow conditions", Proceedings of the National Academy of Sciences of the United States of America **113**, 13289–13294 (2016).

[10]A. Blaeser, D. Duarte Campos, U. Puster, W. Richtering, M. Stevens, and H. Fischer, "Controlling shear stress in 3d bioprinting is a key factor to balance printing resolution and stem cell integrity", Advanced healthcare materials **5**, `10.1002/adhm.201500677` (2015).

[11]S. Arora, A. Srinivasan, A. Leung, and Y.-C. Toh, "Bio-mimicking shear stress environments for enhancing mesenchymal stem cell differentiation", Current Stem Cell Research Therapy **15**, `10.2174/1574888X15666200408113630` (2020).

[12]Z. Lian, J. Xu, Z. Wang, and H. Yu, "Biomimetic superlyophobic metallic surfaces: focusing on their fabrication and applications", Journal of Bionic Engineering **17**, 1–33 (2020).

[13]A. A. Dev, R. Dey, and F. Mugele, "Behaviour of flexible superhydrophobic striped surfaces during (electro-)wetting of a sessile drop", Soft Matter **15**, 9840–9848 (2019).

[14]C. Zhang, D. A. Mcadams II, and J. C. Grunlan, "Nano/micro-manufacturing of bioinspired materials: a review of methods to mimic natural structures", Advanced Materials **28**, 6292–6321 (2016).

[15]Y. Zhu, F. Yang, and Z. Guo, "Bioinspired surfaces with special micro-structure and wettability for drag reduction: which surface design will be a better choice?", Nanoscale **13**, `10.1039/D0NR07664C` (2021).

[16]B. Bhushan, "Biomimetics inspired surfaces for drag reduction and oleophobicity/philicity", Beilstein journal of nanotechnology **2**, 66–84 (2011).

[17]H. C. VON BAEYER, "The lotus effect", The Sciences **40**, 12–15 (2000).

[18]P. Irajizad, M. Hasnain, N. Farokhnia, S. M. Sajadi, and H. Ghasemi, "Magnetic slippery extreme icephobic surfaces", Nature Communications **7**, `10.1038/ncomms13395` (2016).

[19]B. Solomon, K. Khalil, and K. Varanasi, "Drag reduction using lubricant-impregnated surfaces in viscous laminar flow", Langmuir : the ACS journal of surfaces and colloids **30**, 10970–10976 (2014).

[20]C. Lee, C.-H. Choi, and C.-J. Kim, "Superhydrophobic drag reduction in laminar flows: a critical review", Experiments in Fluids **57**, 176 (2016).

[21]C. Vega-Sánchez, S. Peppou-Chapman, L. Zhu, and C. Neto, "Nanobubbles explain the large slip observed on lubricant-infused surfaces", Nature Communications **13**, `10.1038/s41467-022-28016-1` (2022).

[22]S. J. Lee, H. N. Kim, W. Choi, G. Y. Yoon, and E. Seo, "A nature-inspired lubricant-infused surface for sustainable drag reduction", Soft Matter **15**, 8459–8467 (2019).

[23]E. Karatay, A. S. Haase, C. W. Visser, C. Sun, D. Lohse, P. A. Tsai, and R. G. H. Lammertink, "Control of slippage with tunable bubble mattresses", Proceedings of the National Academy of Sciences **110**, 8422–8426 (2013).

[24]A. Steinberger, C. Cottin-Bizonne, P. Kleimann, and E. Charlaix, "High friction on a bubble mattress", Nature materials **6**, 665–8 (2007).

[25]J.-H. Kim and J. P. Rothstein, "Delayed lubricant depletion on liquid-infused randomly rough surfaces", Experiments in Fluids **57**, 1–9 (2016).

[26]J. S. Wexler, I. Jacobi, and H. A. Stone, "Shear-driven failure of liquid-infused surfaces", Phys. Rev. Lett. **114**, 168301 (2015).

[27]S. Peppou-Chapman and C. Neto, "Depletion of the lubricant from lubricant-infused surfaces due to an air/water interface", Langmuir **37**, 3025–3037 (2021).

[28]L. Rayleigh, "On the stability, or instability, of certain fluid motions", Proceedings of the London Mathematical Society **s1-11**, 57–72 (1879).

[29]S. Haefner, M. Benzaquen, O. Bäumchen, T. Salez, R. Peters, J. Mcgraw, K. Jacobs, E. Raphael, and K. Dalnoki-Veress, "Influence of slip on the plateau-rayleigh instability on a fibre", Nature communications **6**, `10.1038/ncomms8409` (2015).

[30]A. S. Utada, A. Fernandez-Nieves, H. A. Stone, and D. A. Weitz, "Dripping to jetting transitions in coflowing liquid streams", Phys. Rev. Lett. **99**, 094502 (2007).

[31]S. Damiati, U. B. Kompella, S. A. Damiati, and R. Kodzius, "Microfluidic devices for drug delivery systems and drug screening", Genes **9**, `10.3390/genes9020103` (2018).

[32]P. Neuži, S. Giselbrecht, K. Länge, T. Huang, and A. Manz, "Revisiting lab-on-a-chip technology for drug discovery", Nature reviews. Drug discovery **11**, 620–32 (2012).

[33]A. Rajawat and S. Tripathi, "Disease diagnostics using hydrodynamic flow focusing in microfluidic devices: beyond flow cytometry", Biomedical Engineering Letters **10**, 241–257 (2020).

[34]Y.-J. Chiu, S. Cho, Z. Mei, V. Lien, T.-F. Wu, and Y.-H. Lo, "Universally applicable three-dimensional hydrodynamic microfluidic flow focusing", Lab on a chip **13**, `10.1039/c3lc41202d` (2013).

[35]R. Rosensweig, *Ferrohydrodynamics*, Dover Books on Physics (Dover Publications, 1997).

[36]W. Wang, J. Timonen, A. Carlson, D.-M. Drotlef, C. Zhang, S. Kolle, A. Grinthal, T. S. Wong, B. Hatton, S. Kang, S. Kennedy, J. Chi, R. Blough, M. Sitti, L. Mahadevan, and J. Aizenberg, "Multifunctional ferrofluid-infused surfaces with reconfigurable multiscale topography", Nature **559**, `10.1038/s41586-018-0250-8` (2018).

[37]J. V. I. Timonen, M. Latikka, L. Leibler, R. H. A. Ras, and O. Ikkala, "Switchable static and dynamic self-assembly of magnetic droplets on superhydrophobic surfaces", Science **341**, 253–257 (2013).

[38]P. Irajizad, M. Hasnain, N. Farokhnia, S. M. Sajadi, and H. Ghasemi, "Magnetic slippery extreme icephobic surfaces", Nature Communications **7**, `10.1038/ncomms13395` (2016).

[39]M. Latikka, M. Backholm, J. V. Timonen, and R. H. Ras, "Wetting of ferrofluids: phenomena and control", Current Opinion in Colloid Interface Science **36**, Wetting and Spreading, 118–129 (2018).

[40]K. S. Khalil, S. R. Mahmoudi, N. Abu-dheir, and K. K. Varanasi, "Active surfaces: ferrofluid-impregnated surfaces for active manipulation of droplets", Applied Physics Letters **105**, 041604 (2014).

[41]Z. J., W. X., W. Z., P. S., Y. B., A. L., G. J., M. F., and Y. X., "Wetting ridge assisted programmed magnetic actuation of droplets on ferrofluid-infused surface", Nat Commun **12**, Wetting and Spreading, 1–8 (2021).

[42]M. S. Krakov, E. S. Maskalik, and V. F. Medvedev, "Hydrodynamic resistance of pipelines with a magnetic fluid coating", Fluid Dynamics **24**, 715–720 (1989).

[43]P. Dunne, T. Adachi, A. A. Dev, A. Sorrenti, L. Giacchetti, A. Bonnin, C. Bourdon, P. H. Mangin, J. M. D. Coey, B. Doudin, and T. M. Hermans, "Liquid flow and control without solid walls", Nature **581**, 58–62 (2020).

[44]D. Saranadhi, D. Chen, J. A. Kleingartner, S. Srinivasan, R. E. Cohen, and G. H. McKinley, "Sustained drag reduction in a turbulent flow using a low-temperature leidenfrost surface", Science Advances **2, e1600686**, `10.1126/sciadv.1600686` (2016).

[45]A. A. Dev, P. Dunne, T. M. Hermans, and B. Doudin, "Fluid drag reduction by magnetic confinement.", Langmuir : the ACS journal of surfaces and colloids (2022).

[46]M. K. S. Verma and V. Kumaran, "A dynamical instability due to fluid–wall coupling lowers the transition Reynolds number in the flow through a flexible tube", en, Journal of Fluid Mechanics **705**, Publisher: Cambridge University Press, 322–347 (2012).

Chapter 2

Drag Reduction by Magnetic Confinement

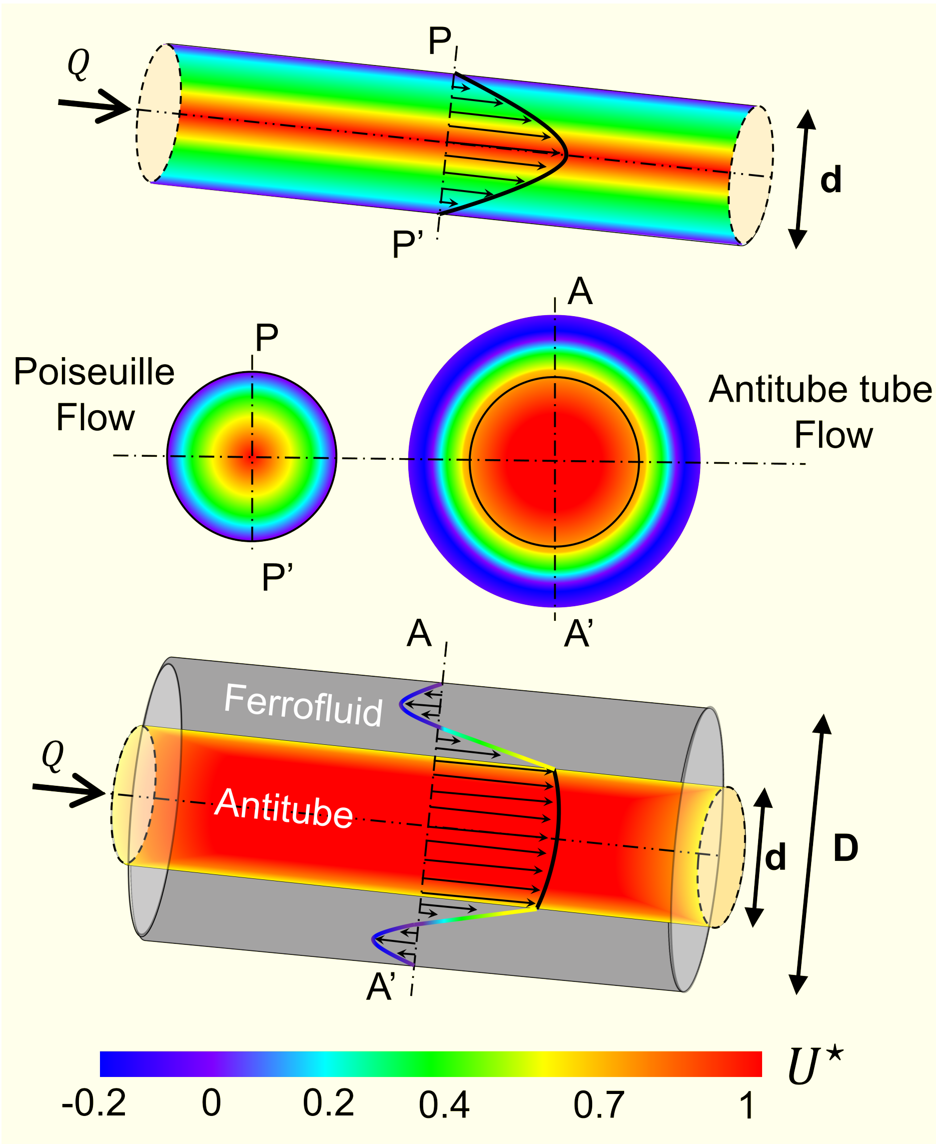

FIGURE 2.1: Flow profiles in solid wall channel (Poiseuille flow) and ferrofluid lubricated flow channel (Antitube)

2.1 Introduction

Friction is a multifaceted problem existing in most physical processes and accounts for almost 25% of energy loss in the world[1, 2]. Fluid friction or hydrodynamic viscous drag is decisive when designing energy efficient large scale flow systems[3, 4]. At smaller, microfluidic sizes, the frictional forces of a viscous liquid flow severely limits the device practical use. Microfluidic channels provide unique advantages for handling small volumes with reduced waste and manufacturing costs, ideal for drug delivery and discovery[5, 6]. Flow-focusing using microfluidic channels for drug delivery and chaotic mixing of reactants forms an essential part of pharmaceutical research[7]. However, delivery of highly concentrated drugs through sub-mm diameter medical needles is difficult because of large drag due to the nonlinear increase in viscosity with increasing concentration[8]. This results in pumping forces beyond the range of manual injection[9]. Furthermore, to limit shear damage, aggregation, and sedimentation in medically significant flows, like blood through tubes and arteries[10], reducing viscous drag is essential. Enabling drag control is also key in studying the response of cancer cells[11] and viruses[12]. Reducing the hydrodynamic viscous drag and shear are therefore key design issues and have led to many solutions, like mixing with additives[13], surface chemical treatment[14], or thermal creation of two-phase systems[15]; while Nature's way, the Lotus effect[16][17], has steered research towards engineered (super)hydrophobic surfaces[18–20] with stabilized[21, 22] liquid/gas interfaces[23–25]. To overcome the drawback of the limited time stability of interstitial gas, oil/liquid infused surfaces have been proposed[26, 27]. Establishing liquid walls by means of an interstitial liquid lubricant is of particular interest for microfluidic applications, with several strategies documented in the literature[28–33]. Nanostructured surfaces are shown to enhance lubricant retention thereby extending the lifetime of planar lubricated surfaces[34]. Hydrodynamic fluid focusing and microdroplets microfluidics are designed for surrounding the transported liquid material with an immiscible liquid envelope[35, 36]. Core annular flows, where the transported liquid is lubricated coaxially using a liquid of lower viscosity is proposed to handle highly viscous flows in microfluidics[9]. However, forming a stable annular flow is difficult, and the risk of draining the lubricating liquid[37, 38] limits the maximum achievable drag reduction. The use of ferrofluids as confining liquid can improve the stability and draining issues, taking advantage of magnets to generate a force field that hold the confining ferrofluid in place. Recent results using ferrofluid-infused surfaces showed superhydrophobic behaviour[39], and early pioneers[40] showed how pressure gradients

can be reduced by an intermediate ferrofluid layer in large pipes[41, 42].
Here we show how drag reduction, defined as the percentage change in friction factor[14, 25, 43–46], is remarkably enhanced in milli- and micro-fluidic circuits using magnetic confinement of ferrofluid lubricants with appropriate magnet assemblies. Its key element is the implementation of our design of quadrupolar confining magnetic field[47], capable of stabilizing the cylindrical flow of a diamagnetic liquid 'antitube[48]' inside a ferrofluid envelope attracted towards the magnets (details of the design provided in chapter 1.8). Our experimental system forms an ideal liquid–in–antitube system where the lubricating liquid forms a perfect concentric confinement for the flowing liquid, using a magnetic force design best suited to preserve the cylindrical geometry and providing optimum robustness of the system. This allows us to compare and verify a simple, axially-symmetric theory with experiments for a significant range of hydrodynamic parameters. The study goes beyond the assumption of unidirectional flow of the involved liquids, ideal for maximum drag reduction[9, 27, 31]. We previously discussed the expected and measured equilibrium diameter d_{eq} of the antitube under static conditions (no flow), stabilized by the equilibrium between magnetic pressure and interfacial tension between the liquids[47] (see chapter 1.8). Here we investigate the dynamic case, where the fluid viscosities are key properties, and show how antitube circuits can exhibit drastically reduced pressure drop for significant ranges of viscosity and flow conditions. Our approach promises a new route for microfluidics designs with pressure gradient reduced by orders of magnitudes. Fig.2.1 shows the schematic of the hypothesis of drag reduction. A Poiseuille flow is characterized by zero velocity at the walls whereas ferrofluid lubricated flow channel is expected to have a plug-like velocity profile resulting in minimal viscous drag. Essentially our research focuses on

- Lubricated or sheath flow, without continuous flow of the confining lubricant.
- Large tunable drag reduction exceeding 99% in a flow channel and extendable to microfluidics applications.
- Flow mechanics in concentrically lubricated flow channel.
- Introduction of a modified Reynolds number with a scaling that depends on geometrical factors and viscosity ratios of the two liquids.

2.2 Experiments

The fluidic cell design follows the discussion of chapter 1 and is sketched in Fig.2.2 a) and Fig.2.2 b). The white arrows show the magnetization direction of the permanent magnets. To perform flow experiments, the four-magnet assembly were housed in a 3D-printed support with built-in fluidic connectors for pressure measurements (Fig.2.2 a)) . For larger diameter antitubes (> 1 mm) we used a support with a magnet spacing$w$ = 6 mm, internal cavity with diameter D = 4.4 mm and inlet-outlet separation L = 52 mm. The magnetic field in the

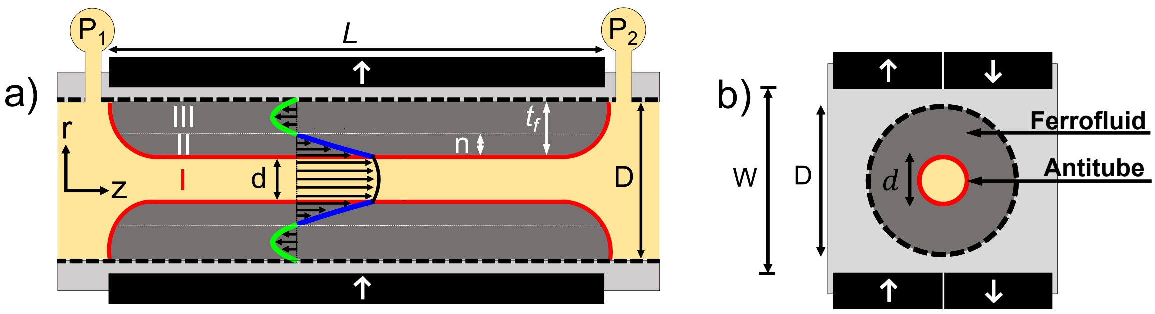

FIGURE 2.2: a) Experimental setup for differential pressure measurement (P1, P2). An antitube of diameter d inside a rigid cavity of diameter D is shown with a velocity profile following the hypothesis of a 2-fluid, 3-region model. The red line between the ferrofluid and antitube depicts the liquid-liquid interface. See AppendixD for the details of experimental cell.

3D cavity varies[47] from 0 T at the center to a maximum of 0.5 T at the wall for magnet separation W = 6 mm and 0 T to 0.48 T for magnet separation W = 0.9 mm. The 3D printed cavity (D, Fig.1a) is first filled with the non-magnetic liquid, then slowly replaced by injecting the ferrofluid with resulting formation of the antitube. We control the diameter d, which is always $> d_{eq}$, by varying the injected trapped volume of ferrofluid. We determined the antitube diameter from X-ray absorption contrast images with our 20 μm resolution setup[47]. Fig.2.3 shows an X-ray absorption contrast image of an antitube near the end of the magnet (near outlet) for $d > 1$ mm.

2.2.1 Antitubes measurements

To characterize the antitube diameter, we analyse the absorption contrast obtained. Since the liquids at the center (Honey or Glycerol) absorbs X-ray lesser than the surrounding ferrofluid, we obtain a brighter band (antitube) inside a darker surrounding. At the left and right of the image (Fig.2.4 (a)) are the magnets which are opaque to X-rays at this thickness, and appear as two black regions, separated from the ferrofluid by the nearly-transparent 3D printed support. Near the ends of the magnets, the antitubes widen due to the fringe

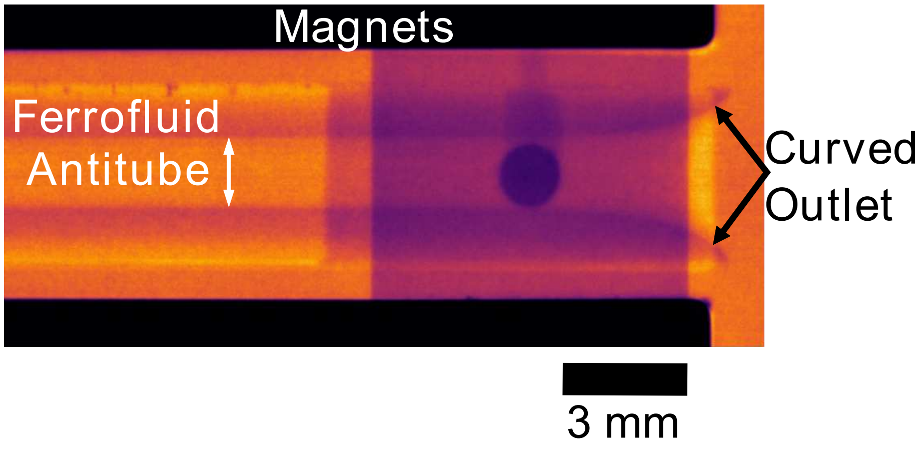

FIGURE 2.3: X-ray absorption contrast image of the fluidic circuit, inside a cavity surrounded by magnets. The brighter central flowing liquid (antitube) is surrounded by a darker immiscible ferrofluid. See AppendixC for the imaging setup.

lower magnetic fields; fortuitously, these curved inlets and outlets improve the trapping of the ferrofluid.

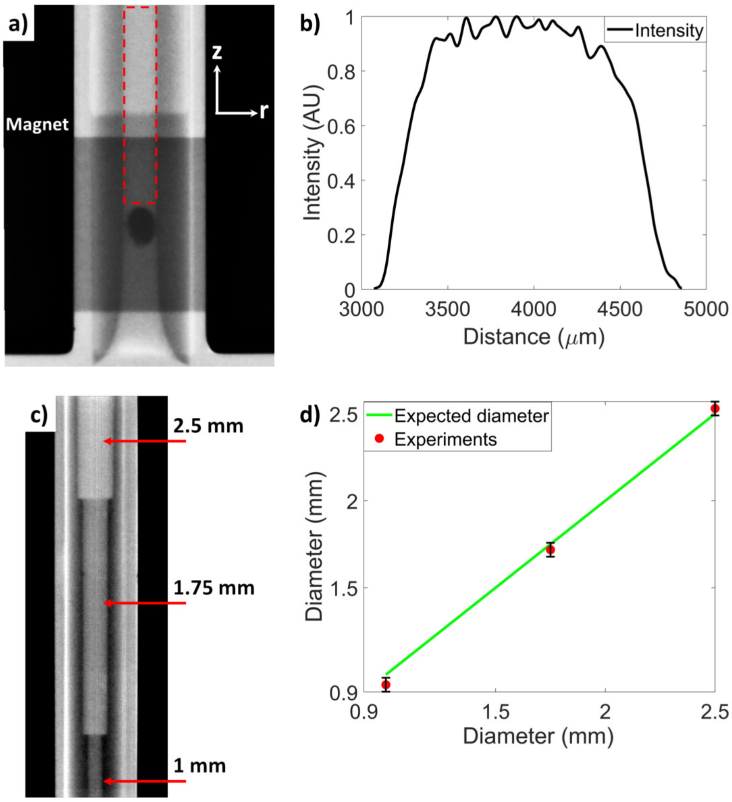

FIGURE 2.4: Measurement of antitube diameter. a) Absorption contrast image of liquid-in-antitube. Horizontal (along r) distance between magnets is 6 mm. b) Intensity profile across r, averaged over z in red box in Fig.2.4(a). c) Absorption contrast image of a test sample with three different known diameters; 2.50 ± 0.025 mm , 1.75 ± 0.025 mm, 1.0 ± 0.025 mm. d) Measurement using the intensity profiles. Markers show width of the intensity profile at 30% of maximum intensity.

The antitube diameter increases at the end of the magnets (bottom part in Fig.2.4 (a)), is due to the stray field of the magnets. The distance along z for which the diameter is measured 3 mm. The width of the intensity profile gives the diameter of the antitube, Fig.2.4 b). However, since the width varies with intensity, we need calibration. To calibrate the intensity profile and thereby to extract diameter, we used known 3D printed cavities of given diameter in place of honey and glycerol (shown in Fig.2.4 c)) and measured their profiles with X-rays. Fig.2.4 d) shows the comparison of known diameters with the experimentally measured values (markers) using intensity profiles. It follows that the antitube diameter is given by the width of the profile at 30% of the maximum intensity. The error bars corresponds to the resolution limit of $\pm 20 \mu$m.

2.2.2 Viscosity measurements

On the cross section, along the radius of the antitube, the magnetic field variation is shown in Fig.4a)[47]. The variation of magnetic field also effects the ferrofluid viscosity. Fig.2.5 a)

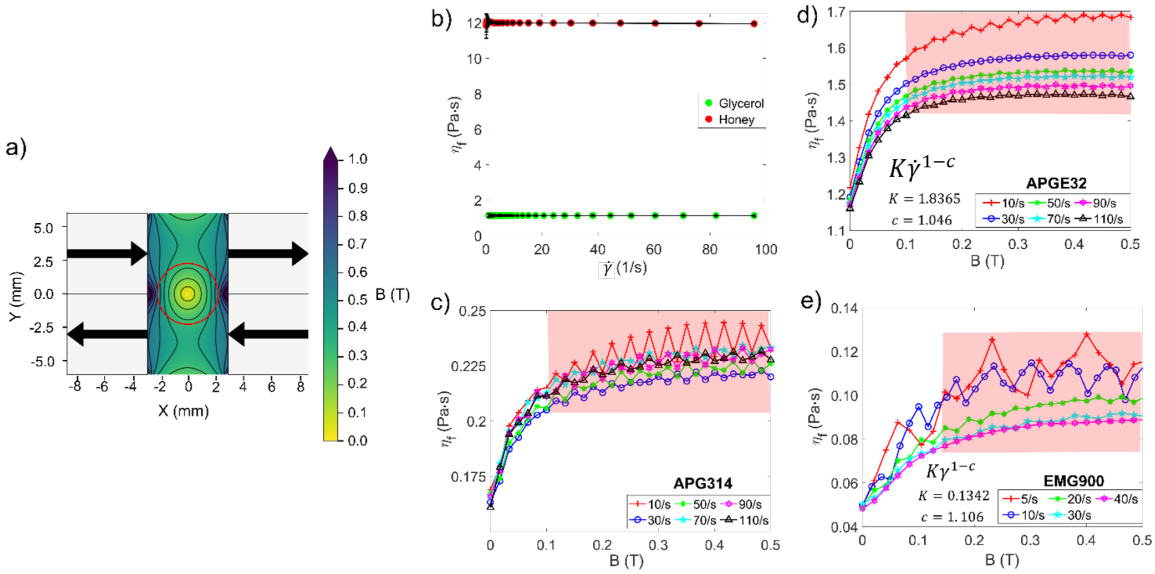

FIGURE 2.5: Magnetic field and viscosity measurements. a) Magnetic field variation from the center of 3D cavity to the magnets located at $X = \pm$ 3 mm, W = 6 mm. The red circle shows the cavity diameter D = 4.4 mm, b) Viscosity of antitube liquids, honey and glycerol as a function of shear rate. c) Increasing viscosity with applied magnetic field (B) for ferrofluid APG314 (F1) for shear rate 10/s to 110/s. d) Increasing viscosity with applied magnetic field for ferrofluid APGE32 (F2) for shear rate 10/s to 110/s. e) Increasing viscosity with applied magnetic field (B) for ferrofluid EMG900 for shear rate 5/s to 40/s. Lines are guide to eyes. Expressions show the dependence of saturated viscosity η on shear rate $\dot{\gamma}$. The shaded region on the viscosity curves (Fig.2.5 c) , 2.5 d) and 2.5 e)) shows the zone of magnetic fields experienced by the ferrofluid and their corresponding viscosity. See AppendixE for the details and protocol followed for the viscosity measurement.

shows the magnetic field calculated map with magnets located at $X = \pm$ 3 mm, with the red circle delineating the cavity of diameter D = 4.4 mm, corresponding to our experimental conditions. Fig.2.5 b) shows the viscosity of glycerol and honey with increasing shear rate. We measured the viscosity of the involved fluids using a viscometer from Anton Paar. The measurements were done using a plate type viscometer with 1 mm gap between plates for honey, glycerol, APGE32 and APG314. Gap for EMG900 is 0.1 mm. All the measurements were performed at 23$\pm$0.5 $^\circ$c. The viscosity of glycerol and honey remains constant at 11.99$\pm$0.03 Pa.s and 1.130$\pm$0.004 Pa.s. The density of glycerol and honey is 1260 $\pm$ 2 kg/m^3 and 1420 $\pm$ 2 kg/m^3. We measured the viscosity of ferrofluids in perpendicular magnetic fields. The increase in viscosity with increasing field is shown in Fig.2.5. The viscosity of ferrofluid APG314 (F1) (Fig.2.5 c)) increases with increase in magnetic field and reaches a plateau. Most of the increase in viscosity happens below 0.2 T. It is also important to note here that with the increase in shear rate, viscosity curves remains invariant (compare different profiles in Fig.2.5 c)). Viscosity curves of APGE32 (F2) (Fig.2.5 d)) and EMG900 (Fig.2.5 e)) on the other hand shows clear dependence on applied shear rate (compare different profiles in Fig.2.5 d) and Fig.2.5 e)). The viscosity decreases with increasing applied shear rate. The magnetic field saturated viscosity (at the flat region) decreases with increasing shear. Considering saturated viscosity, the variation of viscosity with applied shear rate ($\dot{\gamma}$) is given by $\eta = K\dot{\gamma}^{1-c}$. Shaded region in Fig.2.5 c) , 2.5 d) and 2.3 e) corresponds to the magnetic field experienced by the ferrofluid for the several diameters of antitube used in the experiments. The ferrofluid viscosity is almost saturated, hence we assume a single value of viscosity for ferrofluid at the plateau in the viscosity curve, 0.23 $\pm$ 0.01 Pa.s for APG 314, 1.65 $\pm$ 0.05 Pa.s for APGE32 and 0.10 $\pm$ 0.01 Pa.s for EMG 900.

2.2.3 Pressure drop measurements

After characterization of the antitube, magnetic fields and involved liquids, we measured the pressure drop, ΔP, between inlet and outlet, with Honeywell pressure transducers (HSCDLND001PG2A3, HSCDLNN400MGSA5) under a constant flow set by a syringe pump (Harvard apparatus PHD 2000). Note that experiments are carried out at 23 °C in a temperature and humidity controlled environment. Any variation in the physical properties of fluids due to temperature affects is included in the pressure measurement errors (standard deviation on multiple measurements), taken into account in our indicated error bars. The reduction in viscous drag is better described by the dimensionless friction factor, f. For a fluid with density ρ, the measured pressure drop ΔP resulting from a flow rate Q through a tube of diameter d and length L is related to the experimental friction factor by[25]

$$f_{exp} = \frac{\pi^2 \Delta P d^5}{8 \rho Q^2 L} \tag{2.1}$$

The drag reduction factor DR is then defined as[14]

$$DR = \frac{f_P - f_{exp}}{f_P} \times 100 \tag{2.2}$$

which is the percentage change of the measured friction factor f_{exp} compared to the factor f_p under the same flow rate that follows Poiseuille's law. At a solid wall boundary, f_p = 64/Re , where the Reynolds number Re = ρUd/η is defined for diameter d, density ρ , viscosity η and average velocity U corresponding to the flow rate Q. Friction factors of a Poiseuille flow were shown to correspond to those measured on solid wall tubes (Fig.2.6) on the circuit in Fig.2.2

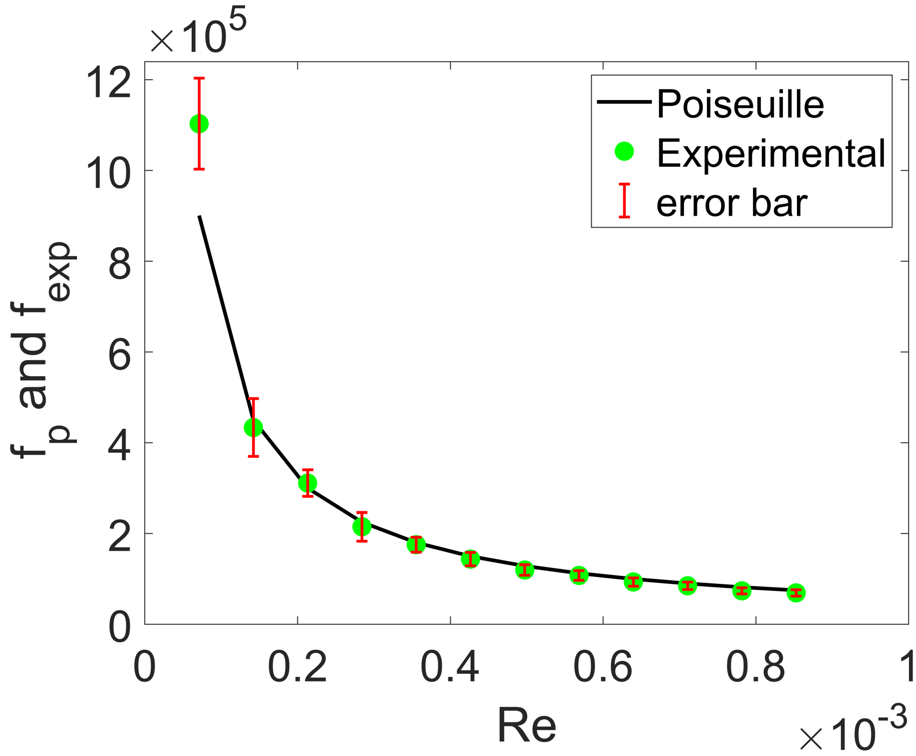

FIGURE 2.6: Test measurements performed on the fluidic circuit shown in Fig.2.2, with all cylindrical channel of 4.4 mm. The friction factor of a Poiseuille flow f_p is compared to experimental data f_{exp}. Fluid is honey with viscosity η = 11.99 ± 0.023 Pa.s , ρ = 1420 ± 2 kg/m^3.

Fig.2.6 shows that the cavity follows the Poiseuille law, and deviations at smallest Reynolds number most likely relate to the inaccuracy of pressure sensors at small pressures. In the antitube however, due to the liquid-liquid interface, the zero-velocity boundary condition at the transported liquid wall (antitube–ferrofluid interface) does not apply, and the deviation from Poiseuille's law results in hydrodynamic drag reduction. An insight into drag reduction possible values is gained by testing how it evolves under flow when varying the viscosity of both transported and confining liquids as well as the antitube diameter. We limit ourselves to viscous liquids (for appropriate measurable pressure differences) and investigate near mm-sized channels for straightforward X-ray imaging. The transported viscous liquids were glycerol (Sigma Aldrich) and honey (Famille Michaud), and the confining ferrofluids used were APG314 (F1) and APGE32 (F2) (FerroTech), resulting in experiments on four combinations of magnetic and non–magnetic liquids. The viscosities of these liquids for glycerol is constant at 1.1 Pa.s and for honey 11.99 Pa.s under strain rate of 100 s^{-1} (maximum strain rate in our experiments with honey in antitube is below 10 s^{-1}). Our measurements span a viscosity ratio η_r between transported and confining liquids both larger ($\leq$52) and smaller ($\geq$0.65) than one, with data for three different antitube diameters and four different viscosity ratios summarized in Fig.2.7 and Fig.2.8.

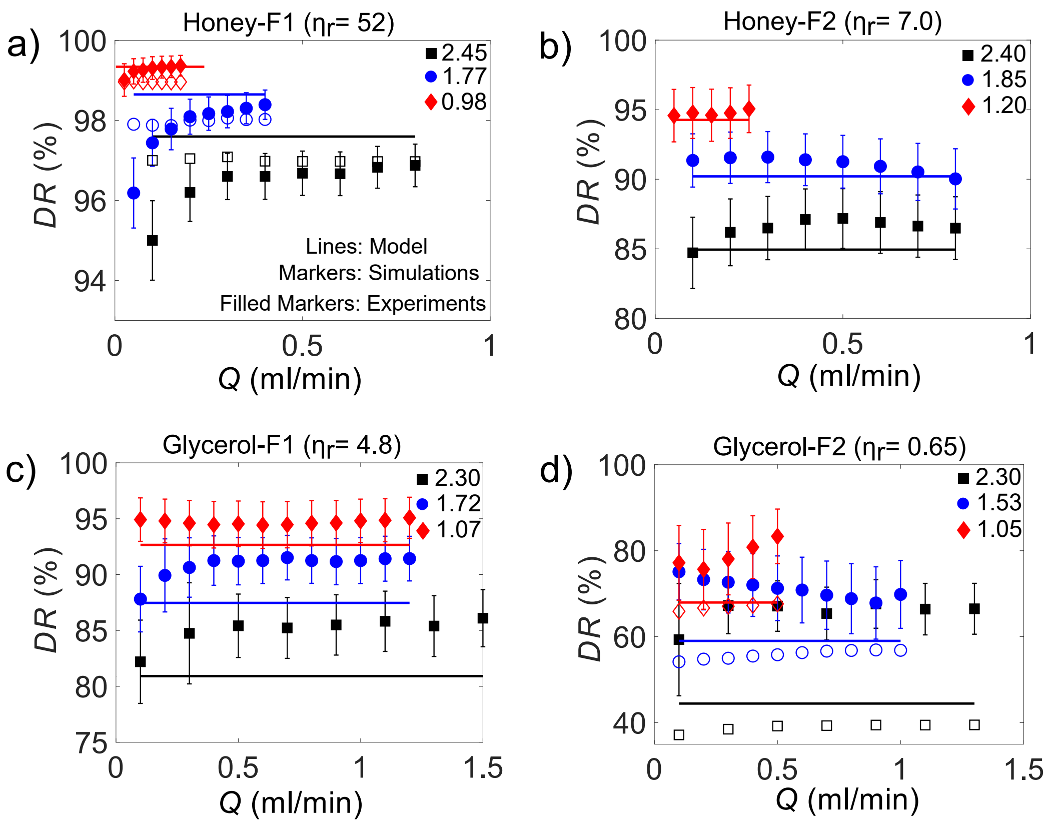

FIGURE 2.7: Drag reduction, *DR*, for three antitube diameters as a function of flow rate for a) honey as the transported liquid with APG314 ferrofluid (F1) as the confining liquid, b) honey with APGE32 ferrofluid (F2), c) glycerol with F1 and d) glycerol with F2. η_r is the ratio between the antitube and ferrofluid viscosities. Legend shows the antitube diameter in mm. Lines, markers and filled markers compare model, simulations, and experiments, respectively.

All four combinations of transported and confined liquids show remarkably high drag reduction values ranging from 60 % to 99.3 % (Fig.2.7). The errors correspond to errors in diameter translated into friction factor and DR. Drag reduction increases with increasing viscosity ratio, with a maximum for Honey-F1 with η_r = 52 (Fig.2.7 a)). On the contrary, no drag reduction is expected when the ratio goes to zero, describing an infinitely viscous envelope, or a solid wall. However, in contrast to prior expectations[27], large drag reduction can still be achieved, even if the confining ferrofluid has a larger viscosity than the transported one, such as for Glycerol-F2, where a drag reduction of up to 80% is observed (Fig.2.7 d). Additionally, the drag reduction increases with decreasing antitube diameter (Fig.2.7 a,b,c,d), which is beneficial when miniaturizing the fluidic circuit.

Alternatively, the large drag reduction can be expressed as an improvement ratio $\alpha_p = \Delta P_p$ / ΔP_{exp}, which compares the measured pressure drop in a liquid-walled interface, ΔP_{exp}, to a solid-wall interface, ΔP_p, of equivalent diameter, d. Fig.2.8 shows more than two orders of magnitude of improvement (α_p) can be achieved. For η_r = 52, the antitube system results in

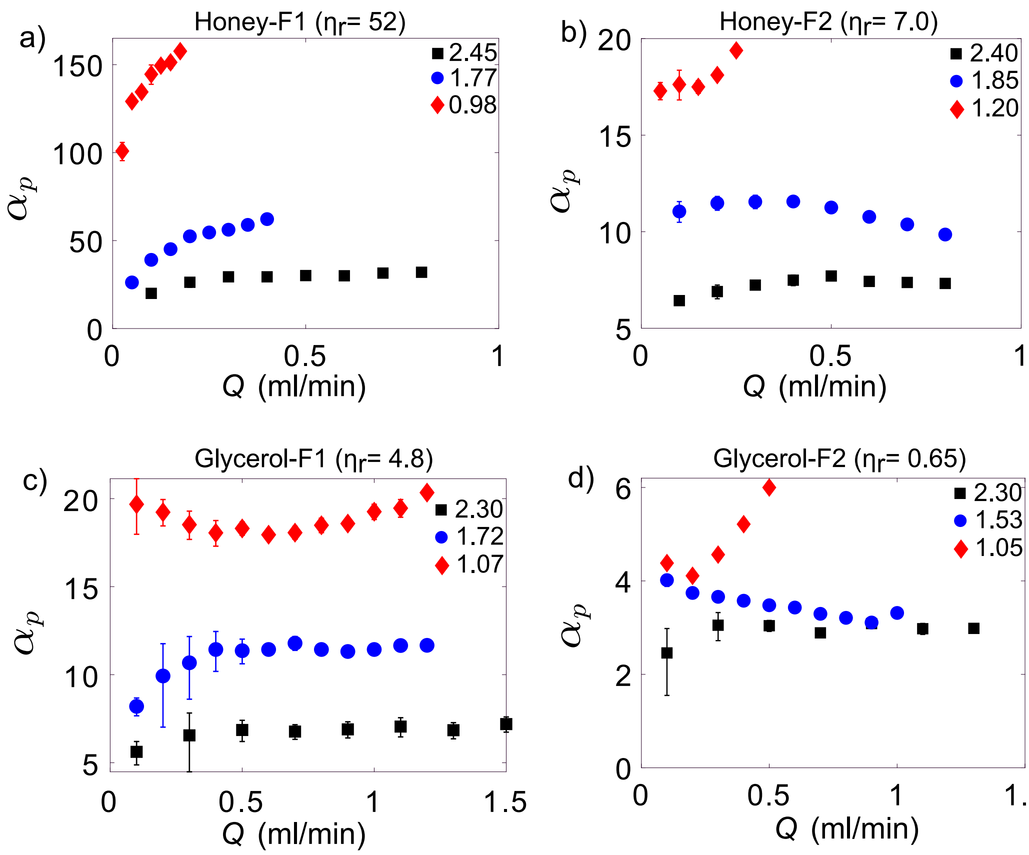

FIGURE 2.8: Pressure drop reduction. a) Honey-APG314 (η_r=52), b) Honey-APGE32 (η_r=7.0), c) Glycerol-APG314 (η_r=4.8), d) Glycerol-APGE32 (η_r=0.65). $\alpha_p = \Delta P_p$ / ΔP_{exp} is the ratio of pressure drop for solid wall tube to the antitube with identical diameter. Legends corresponds to antitube diameter in mm. The error bars are smaller than the size of markers where not visible.

157 times less pressure drop than the solid wall tube (Fig.2.8 a), red markers). Interestingly a viscosity ratio η_r = 0.65 still results in an almost 6 times smaller pressure drop (Fig.2.8 d), and the improvement ratio α_p increases with decreasing antitube diameter (Fig.2.8 a),b),c),d)).

2.2.4 Drag reduction in sub-mm flow channels

The concept can be also extended to microfluuidics sizes. For sub-mm antitube we have w = 0.9 mm, D = 600 μm, and L = 12 mm. The antitube is imaged using a micro computed tomography system (RX-Solutions EasyTom 150/160) with 6 μm resolution. Inset in Fig.2.9 a) shows the antitube near the outlet with curved edges. Fig.2.9 a) shows the measured pressure drop as a function of flow rate of glycerol (Sigma Aldrich) flowing through EMG900 (FerroTech) ferrofluid (markers). This pressure drop is more than one order of magnitude lower than a Poiseuille flow in a solid channel with equivalent diameter (200 $\pm$ 6 μm). This illustrates how it is beneficial to have a cylindrical flowing liquid confined by a liquid interface rather than by solid walls. Fig.2.9 b) shows the experimental drag reduction (markers) based on Eq.2.1 and Eq.2.2 and from data in Fig.2.9 a), with values reaching 95.5 %.

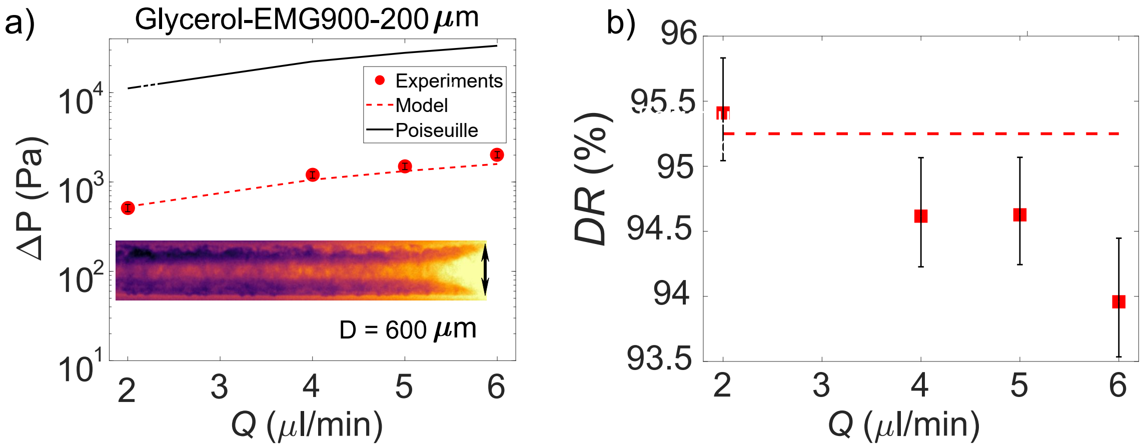

FIGURE 2.9: a) Pressure-drop versus flow rate for an antitube of diameter 200 μm, with inset showing the X-ray image near the outlet (bright central part is antitube). Markers are experiments, the continuous line is the expectation from a Poiseuille flow of diameter d, and the dashed line is the prediction of the model detailed in the text below. b) Corresponding drag reduction with respect to Poiseuille flow. The viscosity ratio between the transported liquid and the ferrofluid is η_r=11
. See AppendixC and AppendixD for the details of imaging and experimental cell respectively.

2.3 Numerical simulations

Details on the flow profile in the antitube and ferrofluid computational fluid dynamics (CFD) simulations. The numerical solution of the liquid-in-liquid system includes solving the full 3 dimensional steady state Navier-Stokes equation while taking into account the curved edges of the antitube and the non-Newtonian behavior of ferrofluid APGE32 through a user defined shear rate dependent viscosity. We use ANSYS 18 computational fluid dynamics package with ANSYS-CFX finite volume based solver. We model the interface as common non deforming wall between two fluids with equal shear stress (initial guess $\tau_{an} = \tau_f$) and check in the solution for the equal velocity at the interface $u_{an} = u_f$. If the interface does not have equal axial velocity, we modify the value of shear stress and iterate untill the velocities at the interface becomes equal with in 2%. Fig.2.10 shows the numerical process using a flow chart.

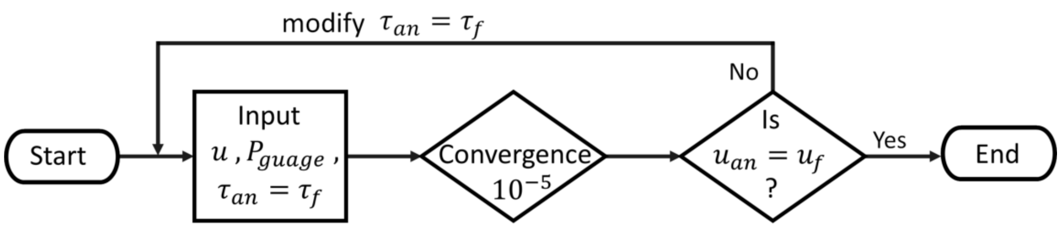

FIGURE 2.10: Flow chart of numerical algorithm. u_{an} and u_f are velocities at interface for antitube fluid and ferrofluid respectively.

The numerical simulations also consider the shear dependent viscosity of ferrofluids. As illustrated in Fig.2.11, a counter flow occurs in the ferrofluid close to the outer wall for Honey-F1 with d = 1.73 mm (Fig.2.11 a)) and Glycerol-F2 with d = 1.54 mm (Fig.2.11 b)), flow rate fixed at Q = 300 μl min^{-1}. Good agreement between numerical and analytical velocity profiles (described in the next section) using the full model for both Honey-F1, η_r = 52 (Fig.2.11 c)), and Glycerol-F2,η_r = 0.65, (Fig.2.11 d)) validates our numerical algorithm.

To more accurately model the experimental system shown in Fig.2.2 , we extended the simulations to consider the finite length of a device, and the effect of fringe fields on the shape of interface at the inlet and outlet (curved inlet and outlet, Fig.2.3, beyond the hypothesis of the infinite tube of the analytical model). Numerical simulations in Fig.2.12 were found to reproduce well the drag reduction data in Fig.2.7 a), while systematically underestimating observed drag reduction for η_r = 0.65 (Fig.2.7 d). This might result from the deformation of the magnetic-nonmagnetic interface, expected to be more important for low viscosity ratio values and increasing flow rates. Note that the numerical drag reduction is

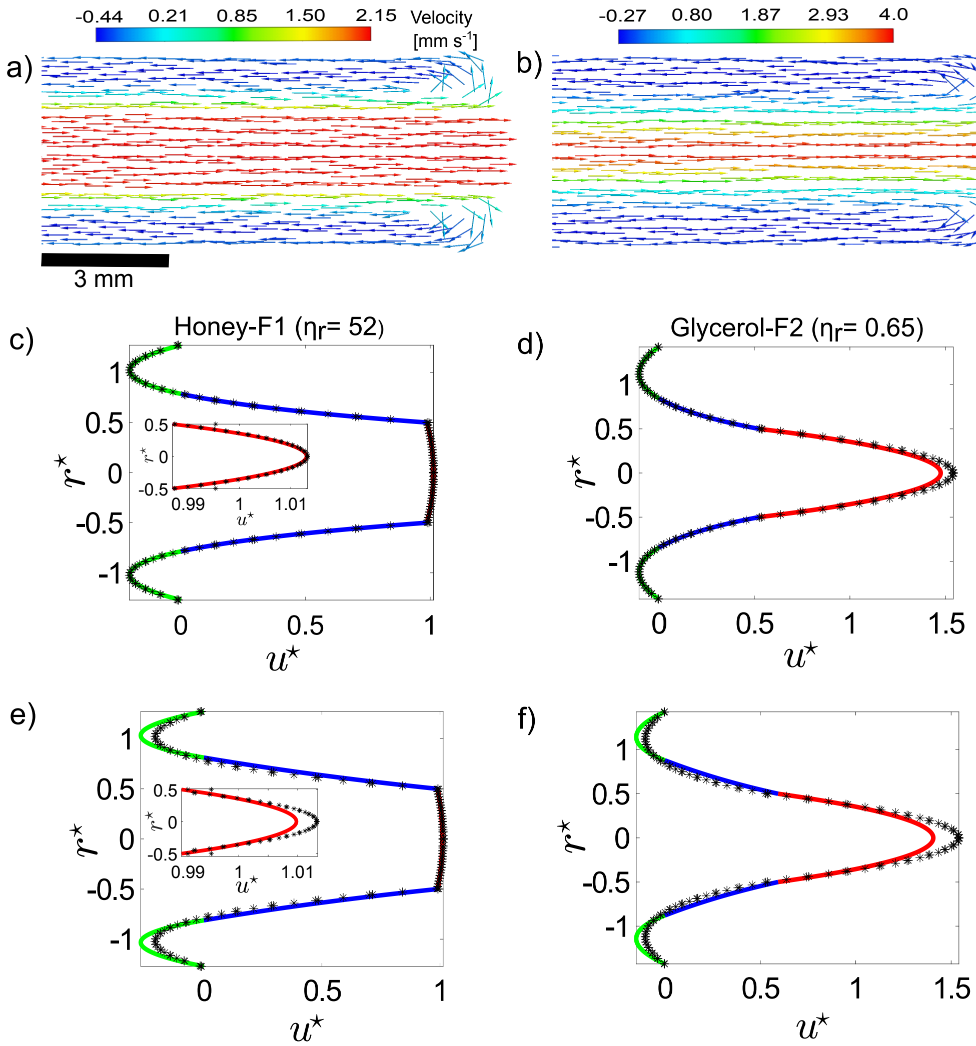

FIGURE 2.11: Simulated visualization of counter flow. a) and b) Velocity vectors near the outlet showing counter flow for Honey-F1 and Glycerol-F2 respectively. c) and d) comparison of the non-dimensional velocity profile of the full analytical model and simulations in Fig.2.11 (a) and Fig.2.11 (b). e) and f) comparison using simplified analytical model neglecting pressure gradient term. Lines are model predictions and markers are simulations calculations. Inset shows the magnified view of velocity profile in an antitube. The antitube diameter for left and right column is 1.73 mm and 1.54 mm respectively. η_r is viscosity ratio. $r^\star = r/d$ is the non-dimensionalised radial coordinate with d as the diameter of antitube.

calculated using Eq.2.1 and Eq.2.2 with ΔP obtained from numerical simulations. To further understand the characterize the flow dynamics in the antitube, we model the flow using Navier-Stokes (NS) equation.

2.4 Two fluids 1D model

We explain our results using a two-fluid model, following previous pioneering work[42], based on the steady-state one dimensional Navier-Stokes equation with velocity as a function of radius in a cylindrical geometry, $u = u(r)$, under modified boundary conditions. Note

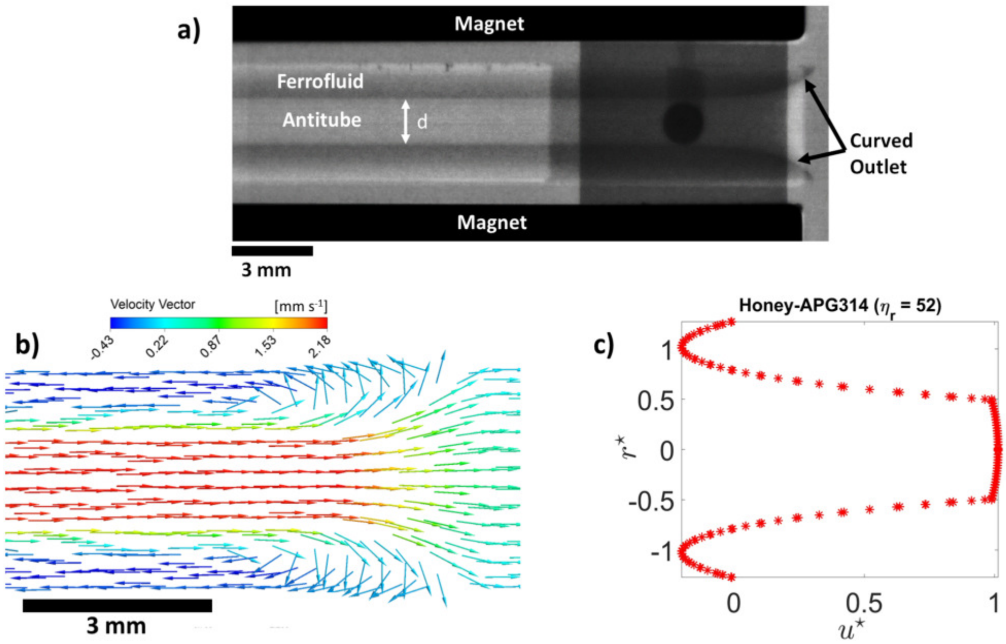

FIGURE 2.12: Numerical results. a) Experimental image of antitube with surrounding ferrofluid, curved part at the edge of the magnet can be seen. b) Velocity vectors corresponding to Fig.2.12 a) with curved edges. APG314 as ferrofluid and Honey antitube showing reverse flow of ferrofluid. c) Non dimensional velocity profile. d=1.73 mm is diameter of antitube.

that we present below equations that differ from those presented in literature[42], motivated by the need to compare the analytical expressions to numerical simulations. We checked that the outcomes of both analytical approaches are identical, under the hypothesis of non-deformable interfaces detailed below. A key ingredient of the model is the occurrence of a counter flow within the confining ferrofluid (Fig.2.2 a)) resulting from avoiding drainage of the ferrofluid by means of the magnetic sources. This suppression is due to the non-uniform magnetic fields at the inlet and outlet opposing any egress of ferrofluid. As the ferrofluid cannot escape but noting that a) flux must be conserved and b) that the drag reduction should result from a non-zero velocity at the ferrofluid-antitube interface, a return path for the ferrofluid flow must exist. The simplest hypothesis is illustrated by the velocity profile in Fig.1a, where we define three regions: I inside the antitube, II the part of the ferrofluid that travels alongside the antitube flow, and III where counter-flow occurs. The non-dimensional governing equations for the three regions (i = I, II, II) are given by

$$\frac{1}{Re_i\, r^\star} \frac{\partial}{\partial r^\star} \left(r^\star \frac{\partial u_i^\star}{\partial r^\star} \right) = \frac{\partial P_i^\star}{\partial z^\star} \tag{2.3}$$

where $u_i^\star$,$r^\star$ are dimensionless velocity and coordinates scaled by the average velocity u_m and the diameter d of the region I (antitube), respectively. The dimensionless pressure is defined as $P_i^{\star}$=P_i/$\rho_i u_m^2$ with the corresponding Reynolds numbers for each region being Re_i=$\rho_i u_m d$/η_i . Note that the pressure gradients along the main flow in both ferrofluid regions are equal, under the hypothesis that these two regions do not mix, resulting in the absence of pressure gradient along r, and therefore $\frac{\partial P_{II}^{\star}}{\partial z^{\star}} = \frac{\partial P_{III}^{\star}}{\partial z^{\star}}$. The magnetic-nonmagnetic interface is modelled as a non-deforming fixed liquid wall. This hypothesis limits us to experiments under low-enough flow values. The case of diameter depending on flow and position along z is discussed in Chapter 4, where we need to introduce explicitly magnetic stress forces in the model. A deformable interface flow model wil be detailed in Chapter 4. We assume here that the pressure gradients in regions I and II are different, to ensure a non-deformable interface. Note that earlier research[42] presented the analytical model as a 2 fluid model with equal pressure gradient, $\frac{\partial P_{I}^{\star}}{\partial z^{\star}} = \frac{\partial P_{II}^{\star}}{\partial z^{\star}}$., but since the numerical simulations do not take into account the magnetic forces field, it is essential to define the magnetic-nonmagnetic interface as non-deformable wall resulting in $\frac{\partial P_{I}^{\star}}{\partial z^{\star}} \neq \frac{\partial P_{II}^{\star}}{\partial z^{\star}}$. We insist, that as long as the shear stress and velocity boundary conditions at the magnetic-nonmagnetic interface are satisfied, the assumption of pressure gradients do not affect the drag reduction calculations.

Our hypothesis allows us to consider a diameter d, set experimentally by the amount of ferrofluid trapped in the cavity, independent of the flow rate and treat the problem numerically to match our experimental conditions. These governing equations are solved for all velocities ($u_I^{\star}$,$u_{II}^{\star}$,$u_{III}^{\star}$), pressure gradient $\frac{\partial P_{III}^{\star}}{\partial z^{\star}}$ and thickness n of region II, using boundary conditions depicted in Fig.1a: finite velocity at the antitube centre, zero velocity at the solid wall and at interface of II and III, continuity of velocity and shear stress at interfaces I-II and II-III. Along with these boundary conditions, the volume conservation of ferrofluid dictates that the flow rate in region II and III must be equal, $Q_{II}^{\star} = Q_{III}^{\star}$. We present two models, one with no assumption (full model) and another with assumption $\frac{\partial P_{II}^{\star}}{\partial z^{\star}} = 0$, which explicitly shows the contribution of geometric and fluid parameters for drag reduction. In the full model Eq.2.3 expands to

$$\frac{1}{Re_{III}\, r^{\star}} \frac{\partial}{\partial r^{\star}} \left(r^{\star} \frac{\partial u_{III}^{\star}}{\partial r^{\star}} \right) = \frac{\partial P_{III}^{\star}}{\partial z^{\star}} \tag{2.4}$$

$$\frac{1}{Re_{II}\, r^{\star}} \frac{\partial}{\partial r^{\star}} \left(r^{\star} \frac{\partial u_{II}^{\star}}{\partial r^{\star}} \right) = \frac{\partial P_{II}^{\star}}{\partial z^{\star}} \tag{2.5}$$

$$\frac{1}{Re_{I}\, r^{\star}} \frac{\partial}{\partial r^{\star}} \left(r^{\star} \frac{\partial u_{I}^{\star}}{\partial r^{\star}} \right) = \frac{\partial P_{I}^{\star}}{\partial z^{\star}} \tag{2.6}$$

Solving which with the boundary conditions mentioned above in text gives the analytical expressions of the velocity profiles as:

$$u^{\star}_{III} = \frac{Re_{III}}{4}\frac{\partial P^{\star}_{III}}{\partial z^{\star}}\left[r^{\star^2} - a_1 \ln(r^{\star}) - a_2\right] \tag{2.7}$$

$$u^{\star}_{II} = \frac{Re_{II}}{4}\left[\frac{\partial P^{\star}_{III}}{\partial z^{\star}}\left(r^{\star^2} - \left(\frac{d+2n}{2d}\right)^2\right) + \frac{1}{2}\left(\frac{\rho_I}{\rho_{II}}\frac{\partial P^{\star}_{I}}{\partial z^{\star}} - \frac{\partial P^{\star}_{III}}{\partial z^{\star}}\right)\ln\left(\frac{2dr^{\star}}{d+2n}\right)\right] \tag{2.8}$$

$$u^{\star}_{I} = \frac{Re_{I}}{4}\frac{\partial P^{\star}_{I}}{\partial z^{\star}}\left[r^{\star^2} + 4(a_3 - a_4 - a_5)\right] \tag{2.9}$$

where, a_1,a_2, a_3,a_4,a_5 are scalar constants that can be expressed as explicit functions of d, and the thicknesses n of the region II and t_f of the ferrofluid. These constants required in velocity profiles are

$$a_1 = \left[\frac{(d+2t_f)^2 - (d+2n)^2}{4d^2}\right]\frac{1}{\ln\left(\frac{d+2t_f}{d+2n}\right)} \tag{2.10}$$

$$a_2 = \left[\frac{(d+2t_f)^2}{4d^2} + \frac{\ln\left(\frac{d+2t_f}{2d}\right)}{\ln\left(\frac{d+2t_f}{d+2n}\right)}\left(\frac{(d+2n)^2 - (d+2t_f)^2}{4d^2}\right)\right] \tag{2.11}$$

$$a_3 = \frac{1}{32a_6}\eta_r\left[\left(\frac{d+2n}{2d}\right)^2 - \frac{1}{4}\right], a_4 = \frac{1}{4}\ln\left(\frac{d+2n}{d}\right)\eta_r\left(\frac{1}{2} + \frac{1}{16a_6}\right), a_5 = \frac{1}{16} \tag{2.12}$$

Since the diameter of antitube (d) increases near the edge of magnet, we use the weighted average of the diameter along the length and get an average constant diameter as

$$\frac{L^{\frac{1}{4}}}{d} = \left(\sum_{i=1}^{i=L/l}\frac{l}{d_i^4}\right)^{\frac{1}{4}} \tag{2.13}$$

where, l is the small length over which the diameter is considered constant. We consider l equals 0.1 mm and L= 51 mm. In order to determine the unknown n value, we use the experimental diameter of antitube d, thickness of ferrofluid t_f in the condition of volume conservation of ferrofluid $Q^{\star}_{II} = -Q^{\star}_{III}$ and the continuity of the shear stresses at the interface II and III, given by

$$\frac{\partial P^{\star}_{III}}{\partial z^{\star}} = -\frac{1}{8a_6}\frac{\rho_I}{\rho_{II}}\frac{\partial P^{\star}_{I}}{\partial z^{\star}} \tag{2.14}$$

$$\frac{\partial P^{\star}_{III}}{\partial z^{\star}} = -\frac{2a_8}{a_7 - 2a_8 + a_9}\frac{\rho_I}{\rho_{II}}\frac{\partial P^{\star}_{I}}{\partial z^{\star}} \tag{2.15}$$

The artefact of different pressure gradients in Eq. 2.14 and Eq. 2.15 results from our simplified hypothesis considering liquid-liquid interface as a non-deformable fixed liquid wall. This avoids solving a pressure equation that must take into account the magnetic stress with a resulting non-linear governing equation.

Using Eq. 2.14 and Eq. 2.15, we can write

$$\frac{1}{8a_6} = \frac{2a_8}{a_7 - 2a_8 + a_9} \tag{2.16}$$

n can be analytically calculated using Eq. 2.16 because the parameters a_6,a_7,a_8,a_9 are functions of n,d and t_f where d and t_f are fixed by experimental conditions. a_6 to a_9 are given by

$$a_6 = \left[\frac{1}{2}\left(\frac{d+2n}{2d}\right)^2 - \frac{1}{8} - \frac{1}{4}\left(\frac{d+2n}{2d}\right)^2 \left(2 - \frac{a_1}{\left(\frac{d+2n}{2d}\right)^2}\right)\right] \tag{2.17}$$

$$a_7 = \left[-\frac{(d+2n)^4}{64d^4} - \frac{1}{64} + \frac{(d+2n)^2}{32d^2}\right] \tag{2.18}$$

$$a_8 = \left(\frac{1}{4}\right)\left[-\frac{(d+2n)^2}{16d^2} - \frac{1}{8}\ln\left(\frac{1}{2}\right) + \frac{1}{16} + \frac{1}{8}\ln\left(\frac{d+2n}{2d}\right)\right] \tag{2.19}$$

$$\begin{aligned} a_9 = \Bigg[& \frac{(d+2t_f)^4}{64d^4} - \frac{(d+2n)^4}{64d^4} - a_1\left(\ln\left(\frac{d+2t_f}{2d}\right)\frac{(d+2t_f)^2}{8d^2} - \frac{(d+2t_f)^2}{16d^2}\right. \\ & \left. - \ln\left(\frac{d+2n}{2d}\right)\frac{(d+2n)^2}{8d^2} - \frac{(d+2n)^2}{16d^2}\right) - a_2\left(\frac{(d+2t_f)^2}{8d^2} - \frac{(d+2n)^2}{8d^2}\right)\Bigg] \end{aligned} \tag{2.20}$$

The antitube flow rate through is obtained by integrating Eq.2.9 over its cross section and is given by

$$Q_I^\star = \frac{\pi Re_I}{4}\frac{\partial P_I^\star}{\partial z^\star}\left[\frac{1}{32} + a_3 - a_4 - a_5\right] \tag{2.21}$$

resulting friction factor written as

$$f_A = 64/Re_I\,\beta \tag{2.22}$$

where

$$\beta = 32(a_5 + a_4 - a_3) - 1 \tag{2.23}$$

and a_3, a_4, a_5 are scalar constants that can be expressed as explicit functions of d, the thicknesses n of the region II and t_f of the ferrofluid.

This 'full model' is therefore fully analytically solvable; however, Eq.2.22 and Eq.2.23 together presents a complex expression where the contribution of fluid and geometric properties are hidden. Simplified expressions illustrating better the key contributions to drag reduction are obtained by neglecting the pressure gradient in region II. We show below that this artificial hypothesis has limited impact on the accuracy of the results. This approximation $\frac{\partial P^{\star}_{II}}{\partial z^{\star}} = 0$ results in a simplified expression for β:

$$\beta_0 = 1 + 4\ln\left(1 + \frac{2n_0}{d}\right)\eta_r \tag{2.24}$$

where n_0 is the thickness of the ferrofluid in region II under this approximation. $\eta_r = \eta_a/\eta_f$ is the ratio of viscosity of antitube (η_a) and ferrofluid (η_f) liquids. Note that we take the viscosity of the ferrofluid at saturation in a magnetic field.

The analytical model with a minimum set of hypotheses presented here captures reasonably well the experimental measurements for all measurements presented in Fig.2.7 and Fig.2.9 for mm and sub-mm channels. The modified Reynolds number is the non-dimensional governing parameter and spans four orders of magnitude in our experiments. For a cylindrical tube flow f = 64/Re , the liquid-in-liquid system results in f_A=64/Reβ for

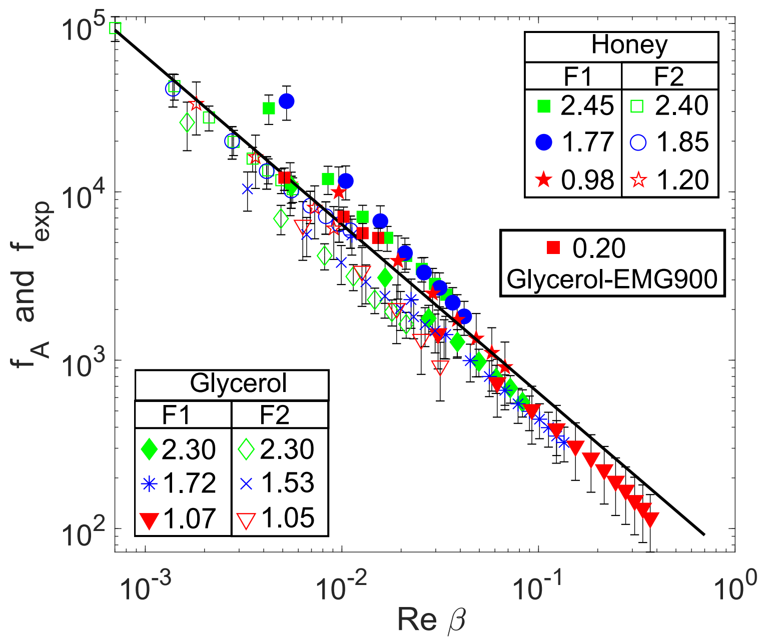

FIGURE 2.13: Comparison of experimental fexp (markers) and analytical f_A (line) friction factors. Inset gives the diameter of antitubes (mm) for each case. Re denotes the Reynolds number and β is the scaling factor (= 1 for solid-walled tube).

the same flow rate Q, revealing explicitly how the friction factor is reduced by a scaling factor β. Fig.2.13 illustrates how the calculated friction factor f_A which is a function of the modified Reynolds number ($Re_I\ \beta$, from Eq.2.22) compares with the experimental one f_{exp} computed using Eq.2.1 The errors in the friction factor for mm scale diameters are calculated by error propagation including errors in pressure drop measurement and uncertainity in distance measurements using X-ray imaging (40 μm). The friction factor f_A is similar to the fit parameter presented in the literature[42]. We provide here full analytical expressions for f_A, necessary for the equation of the drag reduction defined as percentage change in friction factor f_A with respect to friction factor for Poiseuille flow f_p. Similar rescaling of the friction factor was also discussed for a highly water-repellent wall system[14]. Furthermore, the large drag reduction results into a large effective slip length (b) given by

$$b = \frac{d}{2}\left[\sqrt{\frac{\beta+1}{2}} - 1\right] \tag{2.25}$$

with data reported in Table 1. Note that the effective slip length (b), of the order of the antitube diameter, can even exceed the ferrofluid thickness for large enough viscosity ratios. Although the model cannot completely account for minor offsets observed at low viscosity ratio values, where deformations of the antitube start to take place, Fig.2.13 nevertheless illustrates the broad range of fluidic conditions that the model can apply to. Note that a significant variation of drag reduction with flow rate is found for the largest viscosity ratio (η_r = 52). In such cases, the pressure drop becomes very small at small flow rates, and the difficulties in neglecting the pressure loss related to the interconnects and pressure indicators limit the reliability of the data, systematically underestimating the drag reduction values. We also expect that more complicated fluid velocity profiles along z can develop, especially for high viscosity confining liquids where the magnetic/non-magnetic interface might deform significantly due to the high pressure drop. The simplified expression β_0 in Eq.2.24, illustrates the deviation from the asymptotic β_0 = 1 value for solid walls, and is a simple and explicit way to quantify the reduction in the friction resulting from liquid-in-liquid flow. Compared to β, this approximation underestimates the frictional drag (visible in Fig.2.11) , especially when the thickness of the ferrofluid decreases (see Tab. 2.1). However, β_0, explicitly reveals the contributions of the antitube geometry and fluid properties: the drag reduction can be tuned by the choice of viscosities (η_r) and the amount of ferrofluid trapped in the device cavity, i.e. antitube diameter d, and ferrofluid thickness t_f.

Case	d (mm)	t_f (mm)	n (mm)	β	b (mm)	n_0 (mm)	β_0
	2.45	0.98	0.34	41.6	4.42	0.38	58.6
Honey-APG314	1.77	1.32	0.49	74.1	4.53	0.53	98.3
	0.98	1.71	0.67	151.7	3.79	0.73	183.3
	2.40	1.00	0.36	6.7	1.16	0.39	9.1
Honey-APGE32	1.85	1.28	0.47	10.2	1.26	0.51	13.3
	1.20	1.60	0.61	17.4	1.22	0.67	21.4
	2.30	1.05	0.38	5.2	0.88	0.41	6.9
Glycerol-APG314	1.72	1.34	0.50	7.9	0.96	0.54	10.2
	1.07	1.67	0.65	13.6	0.91	0.70	16.4
	2.3	1.05	0.38	1.57	0.15	0.41	1.8
Glycerol-APGE32	1.53	1.44	0.54	2.1	0.18	0.58	2.4
	1.05	1.68	0.65	2.7	0.19	0.71	3.1

TABLE 2.1: Comparison of the full and simplified models

2.5 Conclusion and perspectives

We have studied the flow of viscous liquids through cylindrical liquid-in-antitubes where the confining liquid is held in place by a quadrupolar magnetic field. Our results show that drag reductions exceeding 99% can be achieved by exploiting the non-zero velocity of a viscous liquid at its interface with the encapsulating liquid. The friction reduction is quantified by rescaling of the Reynolds number with a factor β in Eq.2.22. The drag reduction improves when decreasing the diameter of an antitube relative to its surrounding ferrofluid, or when increasing the ratio of the antitube to ferrofluid viscosities. The former is relevant for the needs and length-scales of microfluidics, while the latter indicates that large drag reduction is expected when flowing highly viscous liquids. The low friction micro channels could be beneficial for existing microfluidic applications. Immiscibility and chemical reactivity of the transported liquid and encapsulated ferrofluid could be key in deciding the suitability of this method for transport of oils, emulsions, slurry and droplets. In biological transport, where the reduced shear transport could be of great importance, bio compatibility of the ferrofluid is a key factor. Given the large bank of ferrofluids being developed based on different base liquids like kerosene, krytox, mineral oil and even water, ad-hoc required conditions for fluid transport are within reach. Moreover, with antitube diameters as small as 10 μm already achievable[47], antitube diameter to ferrofluid thickness ratios of order 100 are within reach. Therefore, very large drag reduction in microfluidic channels is possible for a broad range of confining liquid viscosities. Downsizing or designing magnetic force gradients along the flow direction can also further enhance the stability of the ferrofluid against shearing, paving the way to both high velocity and low viscosity fluidic applications in domains ranging from nanofluidics to marine or hydrocarbon cargo transport.

2.6 Contributions

Arvind Arun Dev (AAD) and Bernard Doudin (BD) conceptualised the project. AAD did the experiments in Hermans lab with supervision of Thomas Hermans (TH). AAD did the X-Ray imaging experiments at the Institut Charles Sadron, Strasbourg, France with Antonie Egele and Damien Favier. AAD developed the analytical model and numerical simulations. AAD and BD further developed the simplified model. AAD, BD and Peter dunne (PD) discussed the technical part during the course of the project. The magnetoviscosity measurement and numerical simulation using ANSYS CFX were done by AAD in MMML lab Latvia with Prof. Cebers. AAD, PD, TH and BD wrote the research article published[49].

Bibliography

[1]K. Sayfidinov, S. D. Cezan, B. Baytekin, and H. T. Baytekin, "Minimizing friction, wear, and energy losses by eliminating contact charging", Science Advances **4, eaau3808**, 10.1126/sciadv.aau3808 (2018).

[2]K. Holmberg and A. Erdemir, "Influence of tribology on global energy consumption, costs and emissions", Friction **05**, 263, 263–284 (2017).

[3]W. Brostow, "Drag reduction in flow: review of applications, mechanism and prediction", Journal of Industrial and Engineering Chemistry **14**, 409–416 (2008).

[4]W. Brostow and H. E. Hagg Lobland, *Materials: introduction and applications*, 1st ed. (Wiley, Hoboken, NJ, USA, 2017).

[5]P. Dittrich and A. Manz, "Lab-on-a-chip: microfluidics in drug discovery", Nature reviews. Drug discovery **5**, 210–8 (2006).

[6]P. Neuži, S. Giselbrecht, K. Länge, T. Huang, and A. Manz, "Revisiting lab-on-a-chip technology for drug discovery", Nature reviews. Drug discovery **11**, 620–32 (2012).

[7]S. Damiati, U. B. Kompella, S. A. Damiati, and R. Kodzius, "Microfluidic devices for drug delivery systems and drug screening", Genes **9**, 10.3390/genes9020103 (2018).

[8]V. K. Sharma, T. W. Patapoff, B. Kabakoff, S. Pai, E. Hilario, B. Zhang, C. Li, O. Borisov, R. F. Kelley, I. Chorny, J. Z. Zhou, K. A. Dill, and T. E. Swartz, "In silico selection of therapeutic antibodies for development: viscosity, clearance, and chemical stability", Proceedings of the National Academy of Sciences **111**, 18601–18606 (2014).

[9]V. Jayaprakash, M. Costalonga, S. Dhulipala, and K. K. Varanasi, "Enhancing the injectability of high concentration drug formulations using core annular flows", Advanced Healthcare Materials **9**, 2001022 (2020).

[10]W. Reinke, P. Gaehtgens, and P. C. Johnson, "Blood viscosity in small tubes: effect of shear rate, aggregation, and sedimentation", American Journal of Physiology-Heart and Circulatory Physiology **253**, H540–H547 (1987).

[11]M. J. Mitchell and M. R. King, "Computational and experimental models of cancer cell response to fluid shear stress", Frontiers in Oncology **3**, 44 (2013).

[12]T. A. Grein, D. Loewe, H. Dieken, T. Weidner, D. Salzig, and P. Czermak, "Aeration and shear stress are critical process parameters for the production of oncolytic measles virus", Frontiers in Bioengineering and Biotechnology **7**, 78 (2019).

[13]S. Lee and N. D. Spencer, "Sweet, hairy, soft, and slippery", Science **319**, 575–576 (2008).

[14]K. Watanabe, Y. Udagawa, and H. Udagawa, "Drag reduction of newtonian fluid in a circular pipe with a highly water-repellent wall", Journal of Fluid Mechanics **381**, 225–238 (1999).

[15]D. Saranadhi, D. Chen, J. A. Kleingartner, S. Srinivasan, R. E. Cohen, and G. H. McKinley, "Sustained drag reduction in a turbulent flow using a low-temperature leidenfrost surface", Science Advances **2, e1600686**, `10.1126/sciadv.1600686` (2016).

[16]H. C. VON BAEYER, "The lotus effect", The Sciences **40**, 12–15 (2000).

[17]H. Ensikat, P. Ditsche-Kuru, C. Neinhuis, and W. Barthlott, "Superhydrophobicity in perfection: the outstanding properties of the lotus leaf", Beilstein Journal of Nanotechnology **2**, 152–161 (2011).

[18]Y. Tuo, H. Zhang, W. Rong, S. Jiang, W. Chen, and X. Liu, "Drag reduction of anisotropic superhydrophobic surfaces prepared by laser etching", Langmuir **35**, 11016–11022 (2019).

[19]Y. S. Ko, H. J. Kim, C. W. Ha, and C. Lee, "Quantifying frictional drag reduction properties of superhydrophobic metal oxide nanostructures", Langmuir **36**, 11809–11816 (2020).

[20]N. J. Shirtcliffe, G. McHale, M. I. Newton, and Y. Zhang, "Superhydrophobic copper tubes with possible flow enhancement and drag reduction", ACS Applied Materials & Interfaces **1**, 1316–1323 (2009).

[21]C. F. Carlborg and W. van der Wijngaart, "Sustained superhydrophobic friction reduction at high liquid pressures and large flows", Langmuir **27**, 487–493 (2011).

[22]B.-E. Pinchasik, H. Wang, H. Möhwald, and H. Asanuma, "Fully reversible transition between cassie and wenzel states via acoustic waves", Advanced Materials Interfaces **3**, 1600722 (2016).

[23]H. Hu, J. Wen, L. Bao, L. Jia, D. Song, B. Song, G. Pan, M. Scaraggi, D. Dini, Q. Xue, and F. Zhou, "Significant and stable drag reduction with air rings confined by alternated superhydrophobic and hydrophilic strips", Science Advances **3, e1603288**, `10.1126/sciadv.1603288` (2017).

[24]C.-H. Choi and C.-J. Kim, "Large slip of aqueous liquid flow over a nanoengineered superhydrophobic surface", Phys. Rev. Lett. **96**, 066001 (2006).

[25]E. Karatay, A. S. Haase, C. W. Visser, C. Sun, D. Lohse, P. A. Tsai, and R. G. H. Lammertink, “Control of slippage with tunable bubble mattresses”, Proceedings of the National Academy of Sciences **110**, 8422–8426 (2013).

[26]T.-S. Wong, S. H. Kang, K. Y. S. Tang, E. J. Smythe, B. D. Hatton, A. Grinthal, and J. Aizenberg, “Bioinspired self-repairing slippery surfaces with pressure-stable omniphobicity”, Nature **477**, 443–447 (2011).

[27]B. Solomon, K. Khalil, and K. Varanasi, “Drag reduction using lubricant-impregnated surfaces in viscous laminar flow”, Langmuir : the ACS journal of surfaces and colloids **30**, 10970–10976 (2014).

[28]H. Sharma, A. Gaddam, A. Agrawal, and S. Joshi, “Slip flow through microchannels with lubricant-infused bi-dimensional textured surfaces”, Microfluidics and Nanofluidics **23**, 1–13 (2019).

[29]X. Hou, J. Li, A. Tesler, Y. Yao, M. Wang, L. Min, Z. Sheng, and J. Aizenberg, “Dynamic air/liquid pockets for guiding microscale flow”, Nature Communications **9**, 733 (2018).

[30]S. Darvishi and T. Cubaud, “Lubrication of Highly Viscous Core-Annular Flows in Microfluidic Chambers”, Journal of Fluids Engineering **133**, 031203, `10.1115/1.4003733` (2011).

[31]E. Walsh, A. Feuerborn, J. Wheeler, A. Tan, W. Durham, K. Foster, and P. Cook, “Microfluidics with fluid walls”, Nature Communications **8**, `10.1038/s41467-017-00846-4` (2017).

[32]L. R. J. Scarratt, L. Zhu, and C. Neto, “How slippery are slips? measuring effective slip on lubricated surfaces with colloidal probe atmoc force microscopy”, Langmuir **35**, 2976–2982 (2019).

[33]L. Scarratt, L. Zhu, and C. Neto, “Large effective slip on lubricated surfaces measured with colloidal probe afm”, Langmuir **36**, 6033–6040 (2020).

[34]S. K. Laney, M. Michalska, T. Li, F. V. Ramirez, M. Portnoi, J. Oh, I. G. Thayne, I. P. Parkin, M. K. Tiwari, and I. Papakonstantinou, “Delayed lubricant depletion of slippery liquid infused porous surfaces using precision nanostructures”, Langmuir **37**, 10071–10078 (2021).

[35]A. Rajawat and S. Tripathi, “Disease diagnostics using hydrodynamic flow focusing in microfluidic devices: beyond flow cytometry”, Biomedical Engineering Letters **10**, 241–257 (2020).

[36]C. Baroud, F. Gallaire, and R. Dangla, “Dynamics of microfluidic droplets”, Lab on a chip **10**, 2032–45 (2010).

[37]J. S. Wexler, I. Jacobi, and H. A. Stone, "Shear-driven failure of liquid-infused surfaces", Phys. Rev. Lett. **114**, 168301 (2015).

[38]S. Peppou-Chapman and C. Neto, "Depletion of the lubricant from lubricant-infused surfaces due to an air/water interface", Langmuir **37**, 3025–3037 (2021).

[39]W. Wang, J. Timonen, A. Carlson, D.-M. Drotlef, C. Zhang, S. Kolle, A. Grinthal, T. S. Wong, B. Hatton, S. Kang, S. Kennedy, J. Chi, R. Blough, M. Sitti, L. Mahadevan, and J. Aizenberg, "Multifunctional ferrofluid-infused surfaces with reconfigurable multiscale topography", Nature **559**, 77–82 (2018).

[40]V. Medvedev and M. Krakov, "Flow separation control by means of magnetic fluid", Journal of Magnetism and Magnetic Materials **39**, 119–122 (1983).

[41]V. Medvedev, M. Krakov, E. Mascalik, and I. Nikiforov, "Reducing resistance by means of magnetic fluid", Journal of Magnetism and Magnetic Materials **65**, 339–342 (1987).

[42]M. S. Krakov, E. S. Maskalik, and V. F. Medvedev, "Hydrodynamic resistance of pipelines with a magnetic fluid coating", Fluid Dynamics **24**, 715–720 (1989).

[43]K. Fukuda, J. Tokunaga, T. Nobunaga, T. Nakatani, T. Iwasaki, and Y. Kunitake, "Frictional drag reduction with air lubricant over a super-water repellent surface", Journal of Marine Science and Technology **5**, 123–130 (2000).

[44]P. Mirbod, Z. Wu, and G. Ahmadi, "Laminar flow drag reduction on soft porous media", Scientific Reports **7**, 17263 (2017).

[45]W. Liu, H. Ni, P. Wang, and Y. Zhou, "An investigation on the drag reduction performance of bioinspired pipeline surfaces with transverse microgrooves", Beilstein Journal of Nanotechnology **11**, 24–40 (2020).

[46]P. O. Ayegba, L. C. Edomwonyi-Otu, N. Yusuf, and A. Abubakar, "A review of drag reduction by additives in curved pipes for single-phase liquid and two-phase flows", Engineering Reports **3**, e12294 (2020).

[47]P. Dunne, T. Adachi, A. A. Dev, A. Sorrenti, L. Giacchetti, A. Bonnin, C. Bourdon, P. H. Mangin, J. M. D. Coey, B. Doudin, and T. M. Hermans, "Liquid flow and control without solid walls", Nature **581**, 58–62 (2020).

[48]J. M. D. Coey, R. Aogaki, F. Byrne, and P. Stamenov, "Magnetic stabilization and vorticity in submillimeter paramagnetic liquid tubes", Proceedings of the National Academy of Sciences **106**, 8811–8817 (2009).

[49] A. A. Dev, P. Dunne, T. M. Hermans, and B. Doudin, "Fluid drag reduction by magnetic confinement.", Langmuir : the ACS journal of surfaces and colloids (2022).

Chapter 3

Direct measurement of large slip length in microfluidic channel with ferrofluid lubrication

3.1 Introduction

Friction-less flow requires exotic physical working conditions like super fluidity at low temperature[1], flow through nanofluidic channel (nanopores) made up of atomically flat crystals [2] or, superfluid like behavior of bacterial suspensions[3]. These specific physical conditions providing plug flow behavior, however limit the possibilities of biological transport. The large drag reduction discussed in previous chapter resulting form a liquid-in-liquid flow is expected to result in large slip length , as detailed in Tab.2.1. In this chapter, we focus on experimental insight into the flow profile, that shows an ideal plug-flow like behavior.
The parameter of interest is the slip length (b) defined as the distance from the bounding wall at which flow velocity is zero (see Fig.3.1). For Poiseuille flow, the flow velocity is zero at the bounding walls (Fig.3.1 a)). If a lubricant is placed at the wall, the wall velocity is non-zero (Fig.3.1 b)) with a slip length, b. The slip length (b) is the distance from the wall of the flowing liquid where the extended velocity profile (white line in Fig.3.1) approaches zero. The flow profile is parabolic for confined flow and since the slip length is usually much smaller than the effective radius (R) of flow (Fig.3.1 b)), it is calculated as a linear extrapolation of the flow profile given by

$$b = u_s \frac{\partial u}{\partial y} \tag{3.1}$$

In cases where $b > R$ (Fig.3.1 c)), Eq.3.1 can not predict the slip length accurately and is calculated by considering the full velocity profile given by the solution of Stokes equation.

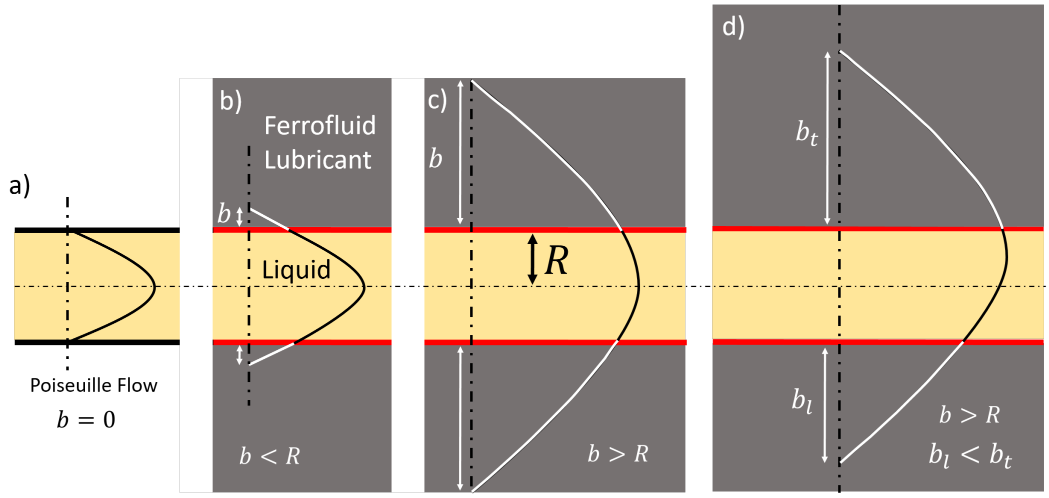

FIGURE 3.1: Slip length definition in lubricated flow channels. a) Poiseuille flow in solid wall channel, black line show the parabolic velocity profile with zero velocity at the walls. b) Ferrofluid lubricated flow channel with non zero velocity at flow wall (red line), slip length $b < R$, where R is half of the flow width, white line shows the extrapolated velocity profile to intercept zero velocity c) Slip length $b > R$ d) Asymmetric lubrication with asymmetric slip length, $b_l < b_t$.

Furthermore with asymmetric lubrication thickness (Fig.3.1 d)), the velocity profile is asymmetric and the location of maximum velocity shifts from the center of the channel to one of the wall. This also results in asymmetric slip length, $b_l < b_t$ (Fig.3.1 d)) .

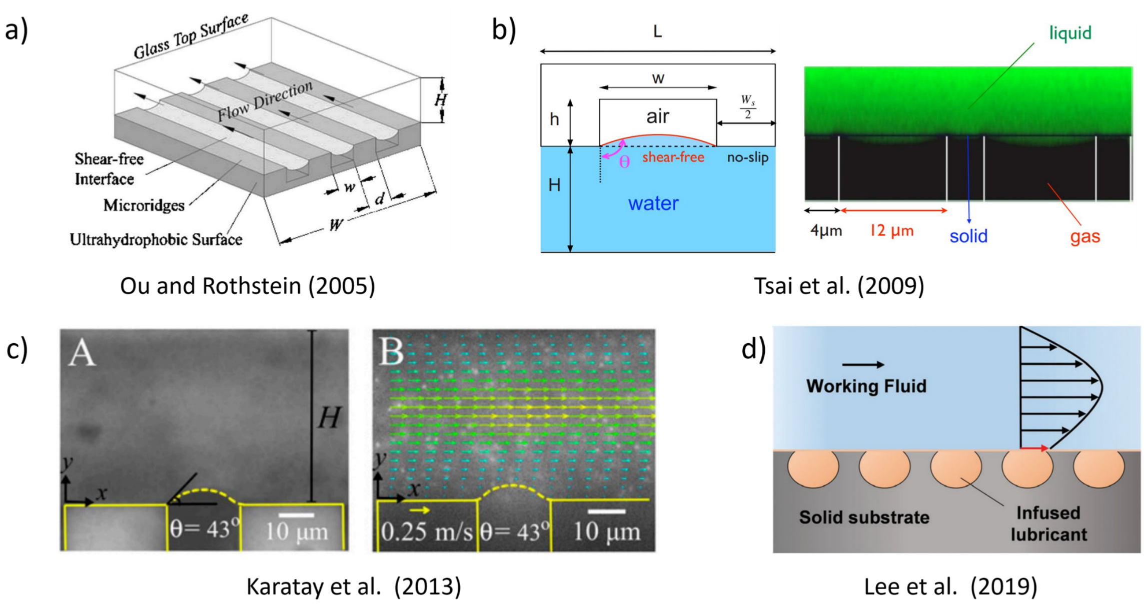

FIGURE 3.2: Experimental direct measurement of slip length in literature. a) Flow over superhydrophobic surface with grooves filled with air[4], b) Slip length dependence on geometry of the surface by varying the width of the microgrroves[5], c) Flow of water over bubble mattress showing effect of the curvaturre of the gas-liquid interface on slip length[6], d) slip length measurement on liquid infused surface with surface design for lubricated liquid retention[7].

The slip length b is predicted using many experimental techniques that are mainly categorised as indirect and direct methods. Indirect methods include flow rate vs pressure drop experiments, force measurements and atomic force microscopy[8]. In flow rate-pressure drop method, a known flow rate is applied and the deviation of the measured pressure drop from the Poiseuille flow quantifies an apparent slip length (see Chapter 2, Tab.2.1). In force measurements, the shear force is measured and its deviation from the expected solid wall value quantifies the slip length. Colloidal probe atomic force microscopy (AFM) is also used to measure small slip length at the surface. In this method, a probe approaches a surface coated with the lubricated liquid and the fluid over it is squeezed in order to record the hydrodynamic drainage force. This force is compared with the analytical solution of the Navier-Stokes equation for a sphere approaching a wall, or Brenner's solution, given by $F_d = \left[\frac{6\pi\eta r^2 v}{h}\right] f_c$, where η, r, and h, are viscosity of fluid, radius of the probe, separation between the probe and liquid interface respectively. v and f_c are velocity of the approaching probe and correction factor respectively. Though the indirect methods are well established, they provide an estimate of the slip length often termed as an apparent slip length.
Direct measurement of the slip length relies on the measurement of the flow velocity profile using particle tracking velocimetry (PTV), particle image velocimetry (PIV) or micro PIV (μPIV) that commonly involves using florescence beads. The beads are mixed in the flowing liquid and the flow is imaged under a microscope using a high speed camera. The beads are assumed to follow the flow profile of the flowing liquid. The beads are tracked (PTV) by means of comparing consecutive recorded images. For PIV, group of beads are tracked from one frame to the other in an image window. This gives the direct measurement of the flow profile. To calculate the slip length, the flow profile is fitted with a second order polynomial following the solution of Navier Stokes equation for velocity (u) of second order in flow channel radial/transversal coordinate r, $u \propto r^2$, see Fig.3.1 c) and Eq.3.3. Ou and Rothstein[4] studied the flow of water over structured superhydrophobic surface using μPIV technique (Fig.3.2 a)). The solid microridges were 30 μm wide separated by 30 μm of entrapped air acting as a shear-free air-water interface. A slip velocity of more than 60% of the average flow velocity was found. Direct measurement of the slip length (b) was 7.5 μm, which was smaller than the structure width. Tsai et al.[5], studied the effect of geometry on slip length characteristics for air entrapped micro-stuructured surface (Fig.3.2 b)) . It was shown that the slip length increases with increasing width of the microgrooves. This suggest that a continuous lubrication could have a larger slip length compared to no slip or partial slip surfaces. Another important observation was the possible dependence of

the slip length on the curvature of the air-water interface. A more detailed understanding of the effect of air water curvature on the slip length was established by Karatay et al.[6] (Fig.3.2 c)). They studied water flow over a bubble mattress in a microfluidic channel. The gas bubbles were formed at regular interval on the wall of the microfluidic channel under application of gas pressure. This provides additional advantage of varying the curvature of the air-water interface. Using μPIV, it was shown that the slip length depends on the protrusion angles of the bubbles controlled by gas pressure. The slip length varies from 2μm to 4μm with maximum drag reduction of 23%. Most slip length measurements in the literature have been performed with superhydrophobic structured surface with air entrapment in the grooves. The air water interface ruptures as the interface cannot resist large pressures. To overcome this, liquid infused surfaces (LIS) were proposed. Lee et al.[7] studied LIS with special attention on the geometry of the grooves to retain the lubricant shown in Fig.3.2 d). They used re-entrant shaped cavities inspired by the biological world. The lubricant and the flowing liquid used were with viscosity 80 cSt and 20 cSt respectively. The largest slip length recorded was 68 μm. Though studies of Lee et al.[7] shows large slip lengths with LIS, the studies on direct measurement of slip length with LIS are scarce. Moreover the LIS are mostly limited to planar surfaces and stabilizing a LIS for a microchannel with lubrication on the microchannel wall is experimentally challenging[9]. The main limiting factor is the unstable continuous liquid-liquid interface making microgrooves design extremely important. The deduced slip lengths are always significantly than the radius of the flow channel, as it is impossible to fully cover the walls with the lubricant. Magnetic forces to stabilise continuous liquid lubricant at a microchannel wall makes possible the stabilization of a liquid flow through a magneto-fluidic channel of sub mm size with large tunable slip length, near frictionless flow, and capable of forming a lubricated microchannel for transporting biological cells. Our research focuses on the physics of lubricated flow with resulting

- Direct measurement of the slip length with a continuous liquid lubricated microchannel.
- Large slip lengths $b >> R$, where $R = d/2$ is half of the flow channel width d.
- Asymmetric velocity profile for asymmetric lubrication thickness.

3.2 Magnetic design

A major hindrance in imaging velocity profile with a cylindrically lubricated flow channel is non-transparency of the ferrofluid. To over come this, we design a magnetic sources arrangement such that the ferrofluid inserted forms a two side boundary lubrication, keeping the normal direction (incident light direction) free from ferrofluid. To get such 2D lubrication, the magnetic field needs to be stronger in one direction (y) and weaker in the other direction (x). The four magnet assembly is arranged in the geometry shown in Fig.3.3 a). White arrows indicate the directions of magnetisation of the magnets. The distance between

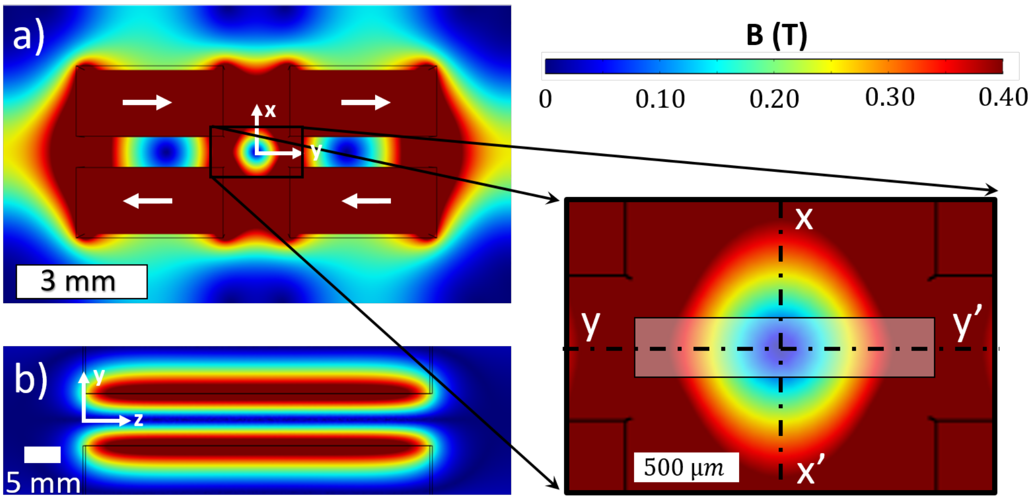

FIGURE 3.3: Magnetic field design for 2D ferrofluid lubrication. a) Magnet (four in number) arrangement with white arrows showing direction of magnetisation, highlighted part magnified image shows the location of microchannel of width 1500 μm and height 280 μm, b) Magnetic field along the flow channel showing stray magnetic field at the edges.

pair of magnets in the y direction is 1500 μm and is 700 μm in the x direction. The magnetic field generated by this arrangement of magnets is calculated using COMSOL Multiphysics. The size of the magnets are taken as the permanent magnet used in experiments (10 mm in length, 1.58 mm in thickness and 3.3 mm in width). The surface remanent magnetisation of these magnets is 0.5 T. The field distribution with-in the space between magnets is shown in Fig.3.3. Fig.3.3 a) shows the cross section of the magnet arrangement. The highlighted section in the magnified part shows the microchannel location. Its boundaries are highlighted with two directions yy' and xx'. Fig.3.3 b) shows the magnetic field along the length of the microchannel. It can be seen that the field along yy' direction is stronger than the one along xx' in the highlighted part. Fig.3.4 quantifies this difference in terms of magnetic field (B) and product of field and field gradient ($B\nabla B$) which is proportional to magnetic force on the ferrofluid . Fig.3.4 a) and Fig.3.4 b) shows the magnetic field variation in x and y direction

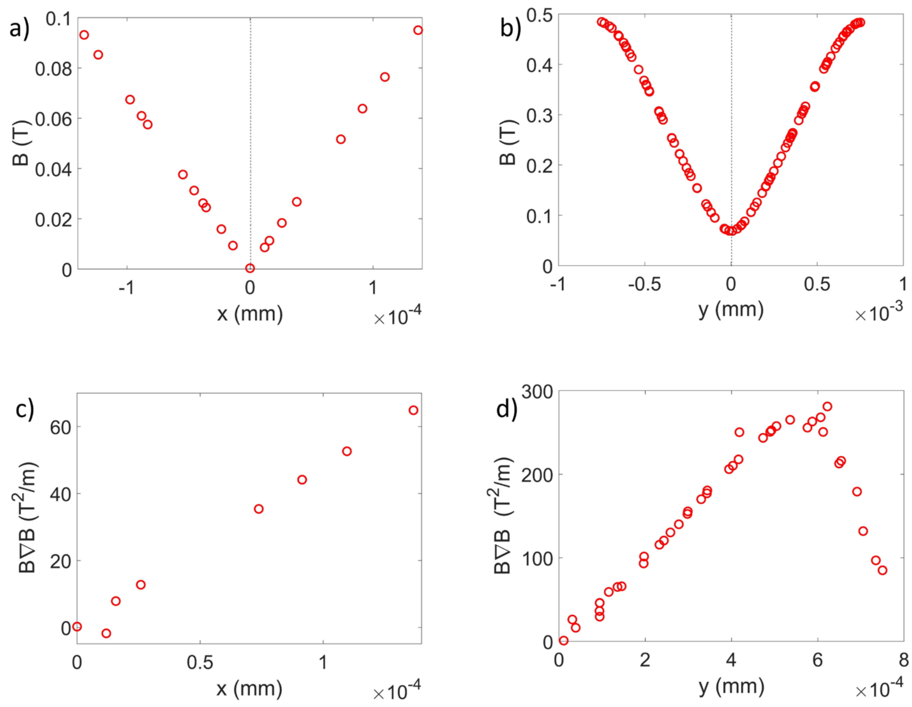

FIGURE 3.4: Magnetic field data in the microchannel (in the highlighted part of 3.3 a)). a) and b) Magnetic field B along xx' and yy' , c) and d) product of field and field gradient ($B\nabla B$) along xx' and yy'.

respectively in the microchannel (highlighted part in magnified region of Fig.3.3 a)). The magnetic field along xx' is almost 5 times weaker than along yy'. Fig.3.4 c) and Fig.3.4 d) shows the product of magnetic field and magnetic field gradient along xx' and yy' respectively. The quantity $B\nabla B$ is smaller along xx' than along yy'. Note that since the magnetic field is symmetric around the origin, ($B\nabla B$) is plotted only for positive coordinates. This makes the inserted ferrofluid to first lubricate the region in yy' direction close to the magnets. Controlling the amount of ferrofluid therefore results in a 2-dimensionally lubricated microchannel required for particle tracking velocimetry (PTV) with no obstruction for the imaging light source.

3.3 Fluidic cell/microchannel

Following the magnetic design, the microfluidic channel is 3D printed (Form Labs, Form 3 printer) with a clear transparent resin, incorporating connectors for flow inlet and outlet. Fig.3.5 a) to Fig.3.5 c) shows the design of the cell and microchannel. In the top view (Fig.3.5 a)), two slots are created for inserting permanent magnets of length L = 10 mm, width 3.3 mm and thickness 1.58 mm. The printing precision is 25 μm. The microfluidic channel is

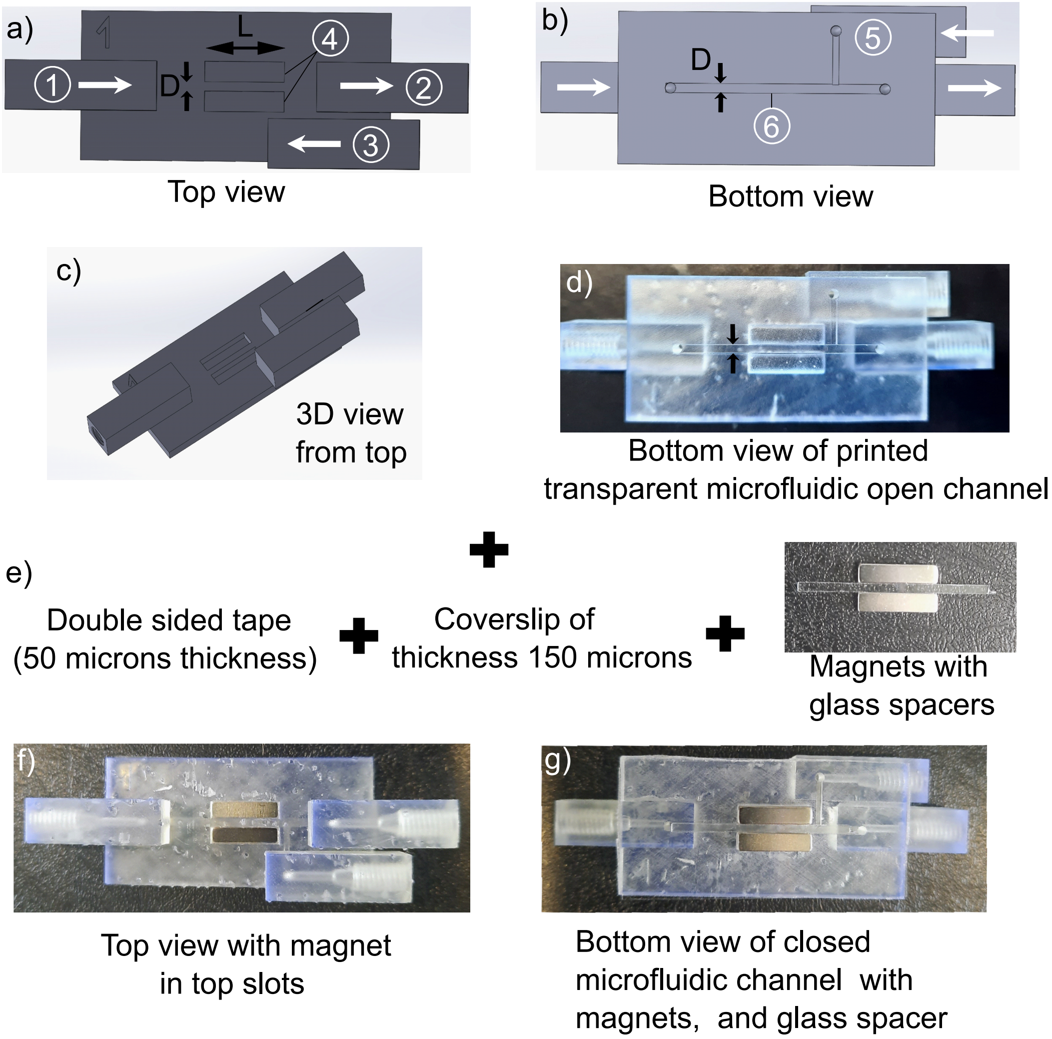

FIGURE 3.5: Fabrication of microfluidic channel. a) Design of 3D printed microchannel from top view, 1 and 2 depicts the inlet and outlet for flowing liquid (glycerol), 3 depicts the entry of ferrofluid, 4 shows two slots for magnets of length L , b) open microchannel bottom view , 5 and 6 show the flow channel for glycerol and entry channel for ferrofluid, D = 1500 μm is the size of micrichannel cavity without ferrofluid, c) 3D view of the microchannel design from top, d) 3D printed microchannel with transparent resin, e) steps after 3D printing to close the open microchannel from bottom and forming quadrupole , starting by applying a double sided tape followed by coverslip and then two magnets with spacers to complete the quadrupolar magnetic design[10], f) and g) Microfluidic channel for PTV measurement from top and bottom.

printed open from bottom, as seen in Fig.3.5 b). Fig.3.5 c) shows a 3D view of the printed setup from top. The printed micro-channel channel cavity is transparent with width and depth D = 1500 μm and 250 μm respectively (Fig.3.5 d)). To seal the microfluidic channel from below, we use a double side tape of thickness 50 μm followed by a cover glass of thickness 150 μm. Finally, to complete the quadrupolar magnetic design[10], we use a pair of magnets separated by glass spacers (Fig.3.5 e)). This ensures a 1500 μm separation between the pair of magnets in the plane and 700 μm separation to the magnets plane, as required for magnetic field distribution. Fig.3.5 f) and Fig.3.5 g) shows the top view and bottom of the final microfluidic cell for PTV measurements.

3.4 Flow dynamics

Flow dynamics in a planar lubricated flow is more complicated than a simple cylindrical lubricated flow channel geometry[11]. This is due to the solid wall effects and asymmetric lubrication. In the analytical model, we neglect the solid wall effect and limit ourself to the central plane of flow away from the solid walls. We solve the Stokes equation in the cartesian coordinate with appropriate boundary condition to include the case of asymmetric velocity profile.

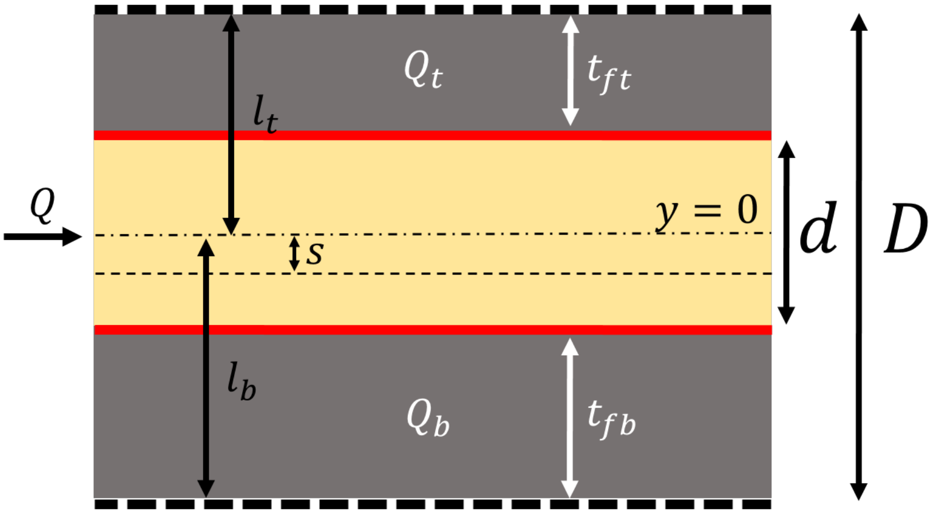

FIGURE 3.6: Schematic of the hypothesis and geometry used for solving the Stokes equation. Brighter cerntal part is the flowing liquid (glycerol) surrounded by darker ferrofluid. d is the flow channel width and D is the microchannel cavity size, $y = 0$ is the center of the flow channel and y = s is the location of maximum velocity due to asymetric ferrofluid coverage $t_{ft} > t_{fb}$, Q is the applied flow rate resulting in the flow rate Q_t and Q_b in the ferrofluid region, l_t and l_b are the distance between the solid walls and the the center of the flow channel.

Fig.3.6 shows the schematic design used in the analytical approach. Red line depicts the liquid-liquid interface between non-magnetic flowing liquid (bright central part) and ferrofluid (darker encapsulation). The broken black line shows the solid boundary of the cavity. A flow rate, Q through a channel of width d is imposed for the flowing liquid with the ferrofluid lubrication thickness being t_{ft} and t_{fb} with corresponding induced flow rates Q_t and Q_b respectively. Note that the lubrication is asymmetric $t_{ft} > t_{fb}$. This is supposed to shift the location of maximum velocity from $y = 0$ to $y = s$. D is the width of the microchannel cavity. Since the Reynolds number is small (<1), we neglect the inertial terms in the Navier-Stokes equation and the flow is viscous dominated, modelled by the Stokes equation in one dimension given by

$$-Re\frac{\partial P^{\star}}{\partial z^{\star}}+\frac{\partial^{2}u^{\star}}{\partial y^{\star 2}}=0 \tag{3.2}$$

The physical variables are non-dimensionalised as, pressure ($P^{\star}=\frac{P}{\rho u_m^2}$), velocity ($u^{\star}=\frac{u}{u_m}$) and length scales ($z^{\star},y^{\star},s^{\star}=\frac{z}{d},\frac{y}{d},\frac{s}{d}$) where d, ρ and u_m are diameter of the flow, density of the flowing liquid and average flow velocity of flow respectively. For the flow in antitube, integrating Eq.3.2 gives

$$u^{\star}=Re\frac{\partial P^{\star}}{\partial z^{\star}}\frac{y^{\star 2}}{2}+C_a y^{\star}+D_a \tag{3.3}$$

Eq.3.3 indicates a parabolic velocity profile. By analogy, we suppose a similar parabolic velocity profile in the ferrofluid given by

$$u_t^{\star}=A_t y^{\star 2}+C_t y^{\star}+D_t \tag{3.4}$$

$$u_b^{\star}=A_b y^{\star 2}+C_b y^{\star}+D_b \tag{3.5}$$

The constants in Eq.3.3 to Eq.3.5 resulting from the following boundary conditions at

$$y^{\star}=s^{\star},\quad \frac{\partial u^{\star}}{\partial y^{\star}}=0 \tag{3.6}$$

$$y^{\star}=l_t^{\star},\quad u_t^{\star}=0 \tag{3.7}$$

$$y^{\star}=\frac{1}{2},\quad u_t^{\star}=u^{\star} \tag{3.8}$$

$$y^{\star}=\frac{1}{2},\quad \eta_a\frac{\partial u^{\star}}{\partial y^{\star}}=\eta_f\frac{\partial u_t^{\star}}{\partial y^{\star}} \tag{3.9}$$

$$y^{\star}=-\frac{1}{2},\quad u_b^{\star}=u^{\star} \tag{3.10}$$

$$y^{\star}=-\frac{1}{2},\quad \eta_a\frac{\partial u^{\star}}{\partial y^{\star}}=\eta_f\frac{\partial u_b^{\star}}{\partial y^{\star}} \tag{3.11}$$

$$y^{\star}=l_b^{\star},\quad u_b^{\star}=0 \tag{3.12}$$

$$Q_t=0,\quad \int_{\frac{1}{2}}^{l_t^{\star}}u_t^{\star}\ dy^{\star}=0 \tag{3.13}$$

$$Q_b=0,\quad \int_{-\frac{1}{2}}^{l_b^{\star}}u_b^{\star}\ dy^{\star}=0 \tag{3.14}$$

Using Eq.3.6 to Eq.3.9 we have

$$s^{\star} = \frac{-C_a}{Re\frac{\partial P}{\partial z}} \tag{3.15}$$

$$D_t = -\left[A_t l_t^{\star 2} + C_t l_t\right] \tag{3.16}$$

$$\frac{A_t}{4} + \frac{C_t}{2} + D_t = \frac{Re}{8}\frac{\partial P^{\star}}{\partial z^{\star}} + \frac{Ca}{2} + D_a \tag{3.17}$$

$$\frac{\eta_a}{\eta_f}\left(\frac{Re}{2}\frac{\partial P^{\star}}{\partial z^{\star}} + C_a\right) = A_t + C_t \tag{3.18}$$

Using Eq.3.10 to Eq.3.12, we have

$$\frac{A_b}{4} - \frac{C_b}{2} + D_b = \frac{Re}{8}\frac{\partial P^{\star}}{\partial z^{\star}} - \frac{Ca}{2} + D_a \tag{3.19}$$

$$\frac{\eta_a}{\eta_f}\left(-\frac{Re}{2}\frac{\partial P^{\star}}{\partial z^{\star}} + C_a\right) = -A_b + C_b \tag{3.20}$$

$$D_b = -\left[A_b l_b^{\star 2} + C_b l_b\right] \tag{3.21}$$

Using Eq.3.13 to Eq.3.14 we get

$$A_t\left(\frac{l_t^{\star 3}}{3} - \frac{1}{24}\right) + C_t\left(\frac{l_t^{\star 2}}{2} - \frac{1}{8}\right) + D_t\left(l_t^{\star} - \frac{1}{2}\right) = 0 \tag{3.22}$$

$$A_b\left(\frac{l_b^{\star 3}}{3} + \frac{1}{24}\right) + C_b\left(\frac{l_b^{\star 2}}{2} - \frac{1}{8}\right) + D_b\left(l_b^{\star} - \frac{1}{2}\right) = 0 \tag{3.23}$$

Using Eq.3.16 to Eq.3.23, we have

$$C_t = \frac{\eta_r}{1-a_1}\left[\frac{Re}{2}\frac{\partial P^{\star}}{\partial z^{\star}} + C_a\right] \tag{3.24}$$

$$A_t = -C_t a_1 \tag{3.25}$$

$$C_b = \frac{\eta_r}{1-a_3}\left[-\frac{Re}{2}\frac{\partial P^{\star}}{\partial z^{\star}} + C_a\right] \tag{3.26}$$

$$A_b = C_b a_3 \tag{3.27}$$

$$D_a = \frac{C_a}{4}\left[2 + \frac{4a_4\eta_r}{1-a_3}\right] - \frac{Re}{8}\frac{\partial P^{\star}}{\partial z^{\star}}\left[1 + \frac{4\eta_r a_4}{1-a_3}\right] \tag{3.28}$$

$$-D_a = \frac{C_a}{4}\left[2 + \frac{4a_2\eta_r}{1-a_2}\right] + \frac{Re}{8}\frac{\partial P^{\star}}{\partial z^{\star}}\left[1 + \frac{4\eta_r a_2}{1-a_1}\right] \tag{3.29}$$

Using Eq.3.28 and Eq.3.29 we get,

$$C_a = \frac{Re\,\eta_r}{2}\frac{\partial P^\star}{\partial z^\star}a_5 \tag{3.30}$$

$$D_a = \frac{Re\,\eta_r}{2}\frac{\partial P^\star}{\partial z^\star}a_6 \tag{3.31}$$

with

$$a_1 = \frac{-\frac{l_t^{\star 2}}{2} - \frac{1}{8} + \frac{l_t^\star}{2}}{-\frac{2l_t^{\star 3}}{3} - \frac{1}{24} + \frac{l_t^{\star 2}}{2}} \tag{3.32}$$

$$a_2 = a_1\left(\frac{1}{4} - l_t^{\star 2}\right) - \frac{1}{2} + l_t^\star \tag{3.33}$$

$$a_3 = \frac{\frac{l_b^{\star 2}}{2} + \frac{1}{8} + \frac{l_b^\star}{2}}{-\frac{2l_b^{\star 3}}{3} + \frac{1}{24} - \frac{l_b^{\star 2}}{2}} \tag{3.34}$$

$$a_4 = a_3\left(\frac{1}{4} - l_b^{\star 2}\right) - \frac{1}{2} - l_b^\star \tag{3.35}$$

$$a_5 = \frac{\left[\frac{a_4}{1-a_3} - \frac{a_2}{1-a_1}\right]}{1 + \eta_r\left(\frac{a_4}{1-a_3} - \frac{a_2}{1-a_1}\right)} \tag{3.36}$$

$$a_6 = \frac{1}{4}\left[a_5\left(2 + \frac{4a_4\eta_r}{1-a_3}\right) - \frac{1}{\eta_r}\left(1 + \frac{4a_4\eta_r}{1-a_3}\right)\right] \tag{3.37}$$

Using Eq.3.3

$$u^\star = \frac{Re}{2}\frac{\partial P^\star}{\partial z^\star}\left[y^{\star 2} + \eta_r\left(a_5 y^\star + a_6\right)\right] \tag{3.38}$$

with the non-dimensional flow rate given by

$$Q^\star = -\frac{Re}{12}\frac{\partial P^\star}{\partial z^\star}\beta_{2D} \tag{3.39}$$

$$\beta_{2D} = -\left[\frac{1}{2} + 6a_6\eta_r\right] \tag{3.40}$$

β_{2D} is the drag reduction factor[11] for a two dimensional lubricated microchannel. For comparison with experiments, the velocity profile is renormalized by the maximum velocity as u/u_{max}

$$\frac{u}{u_{max}} = \frac{y^{\star 2} + \eta_r\left(a_5 y^\star + a_6\right)}{s^{\star 2} + \eta_r\left(a_5 s^\star + a_6\right)} \tag{3.41}$$

Fig.3.7 shows the velocity profile in antitube (red line) and in ferrofluid (green and blue line). The ferrofluid is APGE32 (η = 1.7 Pa.s) and the flowing liquid glycerol (η = 1.1 Pa.s).

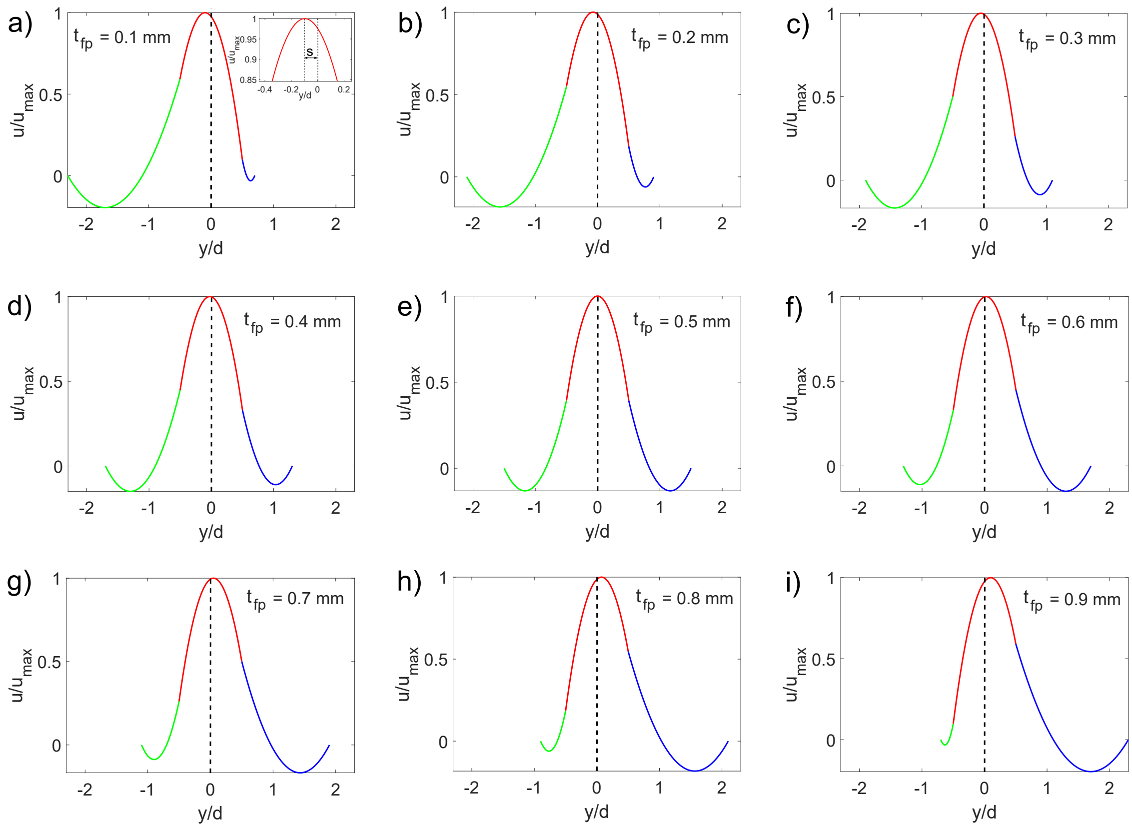

FIGURE 3.7: Velocity profile in antitube and ferrofluid for different ferrofluid coverage, APGE32 ferrofluid with resulting viscosity ratio η_r = 0.65. a) to i), ferrofluid thickness t_{ft} changes from 0.1 mm to 0.9 mm. The corresponding change in t_{fb} also takes as the channel size d = 500 μm and d = 1500 μm is fixed. s denotes the shift in maximum velocity location in the microchannel.

The viscosity ratio is hence η_r = 0.65. The antitube diameter d = 500 μm and the cavity width is D = 1500 μm are fixed. Fig.3.7 a) to Fig.3.7 i) show the velocity profile with increasing t_{ft} from 100 μm to 900 μm. Due to this asymmetric coverage of ferrofluid, the antitube velocity profile (red line) is asymmetric and the maximum velocity is not located at the center of the antitube (y/d = 0) but shifted by an amount s. Fig.3.7 a) shows the velocity profile shifted to the left of the center (y/d=0). Inset in Fig.3.7 a) shows the shift by an amount s. From Fig.3.7 a) to Fig.3.7 i) the maximum velocity in the antitube shifts from the negative half of y/d (left) to positive half (right). Fig.3.7 e) shows case with symmetric coverage of ferrofluid ($t_{ft} = t_{fb}$ = 0.5 mm), and hence symmetric velocity profile (s = 0). The asymmetricity in the velocity profile increases with increase in the viscosity ratio for the same set of geometric parameters, d = 500 μm, D = 1500 μm and t_{ft} varying from 100 μm to 900 μm. Fig.3.8 shows the asymmetric velocity profiles for a bio compatible ferrofluid of viscosity 0.144 Pa.s and hence viscosity ratio η_r=7.64. Fig.3.8 indeed illustrates how the shift of velocity profile for asymmetric cases is more pronounced than the case of η_r = 0.65 in Fig.3.8. Fig.3.9 shows the

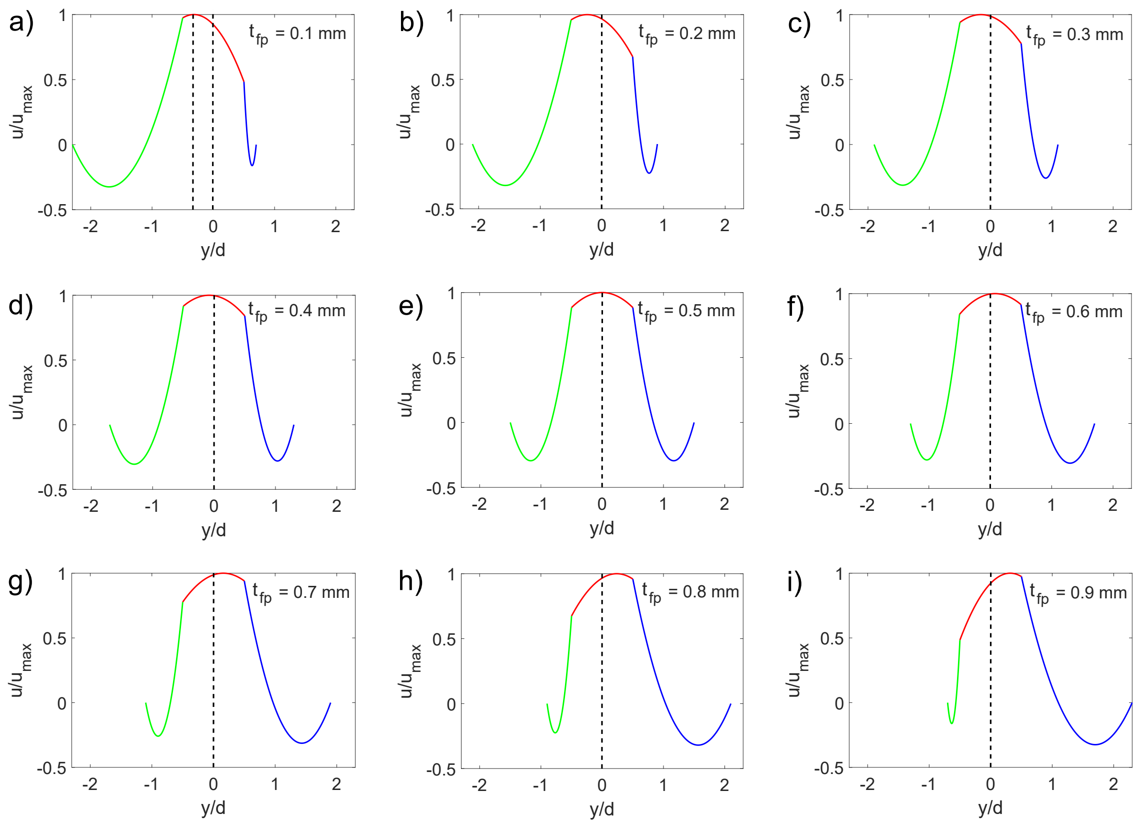

FIGURE 3.8: Velocity profile in antitube and ferrofluid for different ferrofluid coverage Biocompatible ferrofluid with resulting viscosity ratio η_r = 7.64. a) to i), ferrofluid thickness t_{ft} changes from 0.1 mm to 0.9 mm.

magnitude of the shift ($s^\star$) for asymmetric coverage of ferrofluid. The asymmetric coverage is quantified by ζ given by

$$\zeta = \frac{t_{ft} - t_{fb}}{d} \tag{3.42}$$

The shift increases with increasing asymmetricity and increasing viscosity ratio (Fig.3.9). Another major effect of increasing viscosity ratio is to increase the wall velocity at the magnetic non-magnetic interface for a symmetric lubrication (s = 0),

$$\frac{u_{wall}}{u_{max}} = \frac{R^{\star 2} + \eta_r\left(a_5 R^\star + a_6\right)}{a_6 \eta_r} \tag{3.43}$$

If q is the distance from the center of channel where the extended velocity appproaches zero, equating Eq.3.43 to zero with $R^\star = q^\star$

$$0 = q^{\star 2} + \eta_r\left(a_5 q^\star + a_6\right) \tag{3.44}$$

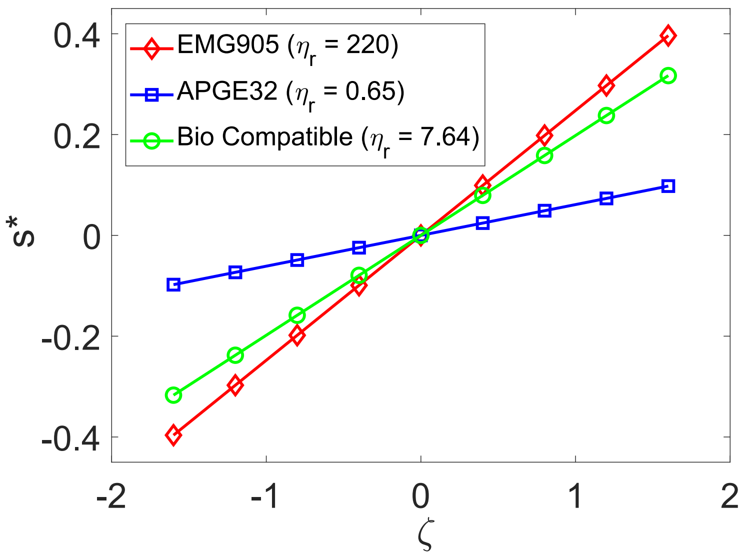

FIGURE 3.9: Shift of maximum velocity location $s^{\star}$ with asymmetry in ferrofluid coverage $\zeta^{\star}$

and solving the quadratic equation we get q and the slip length is given by

$$b = q - R \tag{3.45}$$

3.5 Experimental results

We used glycerol (η = 1.1 Pa.s) as flowing liquid and various ferrofluids APGE32 (η = 1.7 Pa.s), EMG905 (η = 0.005 Pa.s) from ferrotech and a biocompatible ferrofluid (η = 0.144 Pa.s) from Qfluidics, such that viscosity ratios η_r spanning three orders of magnitude can be studied. To begin with the experiments, we mix the flowing liquid Glycerol (Sigma Aldrich) with fluorescence particle of size 4μm (FluoSpheres ™).

The excitation and emission maxima for the particles are 580 nm and 605 nm respectively. We use a source of light with a bandpass filter, 572/25 for excitation and 629/62 for emission. Fig.3.10 a) shows the schematic of the imaging setup. Fig.3.10 b) and Fig.3.10 c) show the microfluidic channel before and after inserting the ferrofluid. Fig.3.10 d) shows a magnified brightfield image of the region of interest for PTV measurements. The depth of field at this magnification is 3 μm which is less than the diameter (4 μm) of the particles. This makes possible recording images with minimum contribution from the off focus particles (below or above the imaging plane). The time elapsed images frames are recorded with Zeiss Axio zoom V16 microscope and a Phantom v2511 camera. The exposure time is 400 μs. The experiments were performed at Laboratory for Fluid Physics, Pattern Formation and

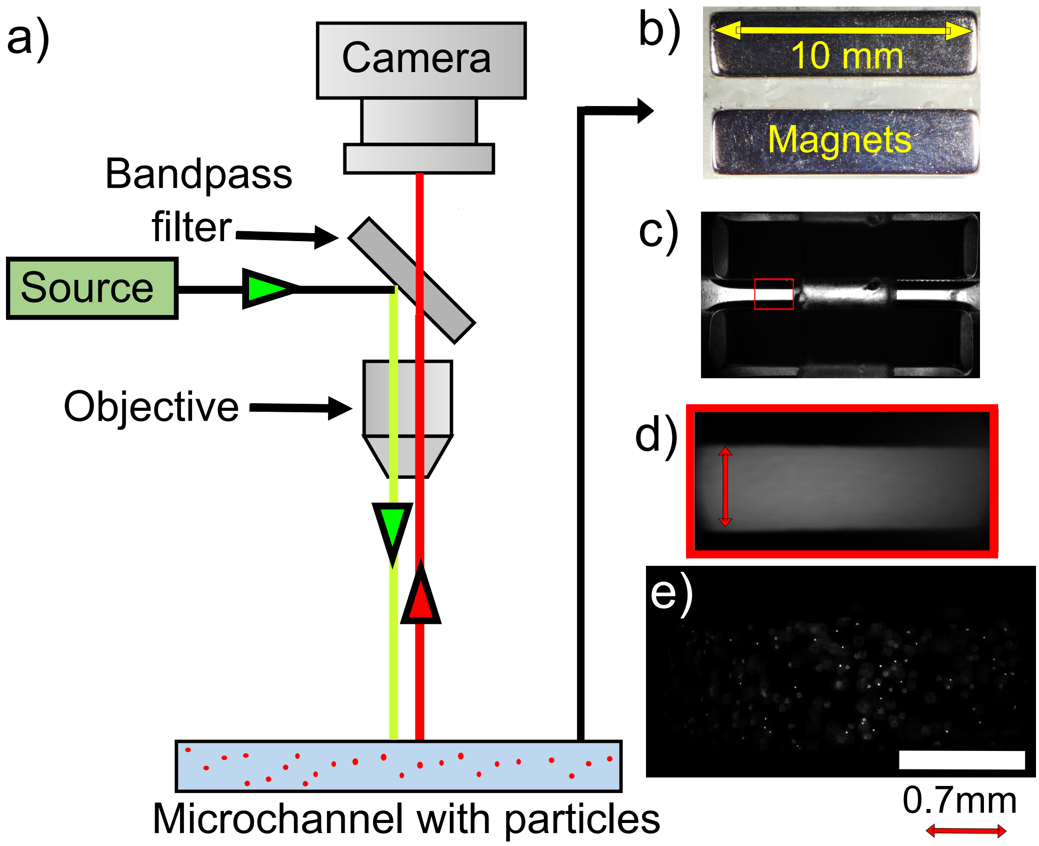

FIGURE 3.10: Experimental set up. a) Optical system for PTV measurements, b) Microfluidic channel without ferrofluid, c) Microfluidic channel with ferrofluid, d) Brightfield image of region of interest under microscope, e) Fluorescence particles in flow.

Biocomplexity (LFPB), Max Planck institute for dynamics and self organisation, Gottingen, Germany. The images were analysed with their homemade code tracking differences in positions of particles in consecutive frames. Fig.3.10 e) particles under fluorescence in the micro channel.

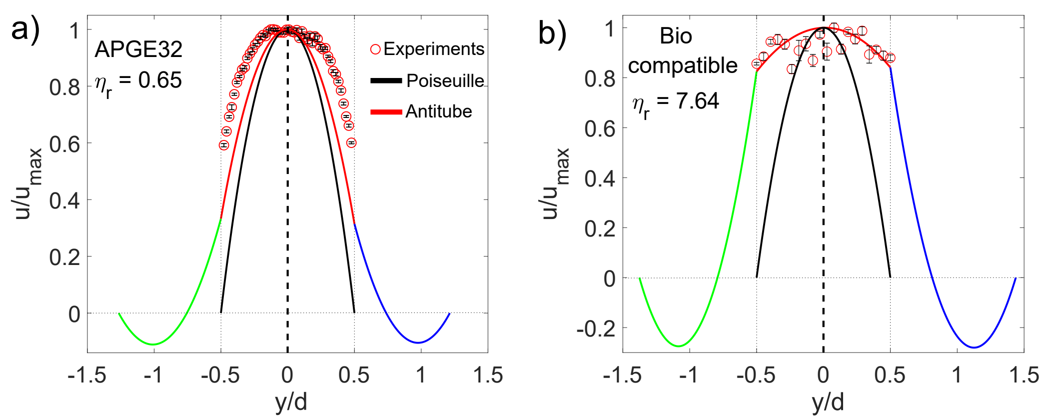

FIGURE 3.11: Comparison of velocity profiles. Lines are analytical and markers are experimental. Black line is Poiseuille flow, red line for solution of Stokes equation in the antitube, green and blue line in ferrofluid. a) For APGE32 ferrofluid with viscosity ratio $\eta_r = 0.65$ and b) For Bio compatible ferrofluid with $\eta_r = 7.64$

Fig.3.11 shows the analytical and experimental velocity profile using μPTV measurements. Markers are experimental and lines are predicted analytical velocity profiles. Black lines denote the Poiseuille flow, red lines denote the calculated flow profile (Eq.3.38) green and blue lines are calculated flow profiles in the ferrofluid using Eq.3.4, Eq.3.5 as integration constants. The errors corresponds to the standard deviation of velocities measured over 10000 images sequences. The antitube lies between $y/d = \left[-0.5 \quad 0.5\right]$. The Poiseuille flow shows the zero velocity at the two walls coordinates $y/d = 0.5$ and $y/d = -0.5$. Experimental markers in Fig.3.11 a) shows that for η_r = 0.65 with APGE32 as ferrofluid, the wall velocity at the liquids interface is large, up to 60% of the maximum velocity and is well predicted by the analytical model. This wall velocity reaches almost 85% of the maximum velocity for $\eta_r = 7.64$ as seen in Fig.3.11 b) for a bio-compatible ferrofluid. The ferrofluid coverage is slightly asymmetric for η_r = 0.65 with t_{ft} = 0.43 mm. For η_r= 7.64, the ferrofluid coverage is symmetric. Further increasing the viscosity ratio by one order of magnitude to η_r = 220 (Fig.3.12) with EMG905 as ferrofluid, we observe even larger wall velocity and asymmetric velocity profile for t_{ft} = 0.36. Fig.3.12 a) shows that the wall velocity is different at the two walls. At y/d = -0.5 , the wall velocity reaches 95% of the maximum velocity and at y/d=0.5 around 75%.

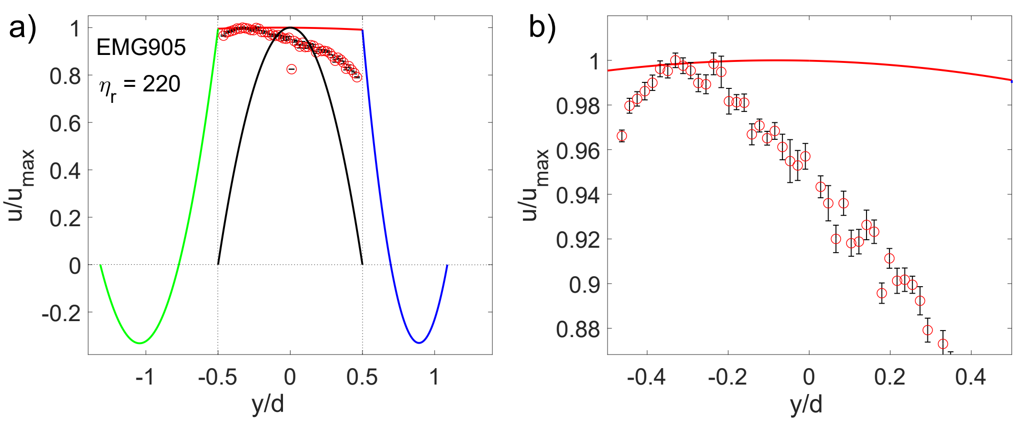

FIGURE 3.12: Velocity profile for EMG905 ferrofluid with η_r = 220. a) Comparison of analytical and experimental results, b) Magnified data near maximum velocity showing shift in the maximum velocity location and asymmetric velocity profile.

The experimentally measured slip length is significantly larger than the radius of the flow channel (R). We are not aware of such large values of the slip length in the literature, where direct measurement of slip is limited to the cases of small slip values, where $b < R$, with Eq.3.1 sufficient to estimate the slip length. Fig.3.14 clearly shows that the slip length at a continuous liquid-liquid interface, cannot be simply approximated by the linear assumption of small slip length values and requires the analytical expressions given by Eq.3.43 and

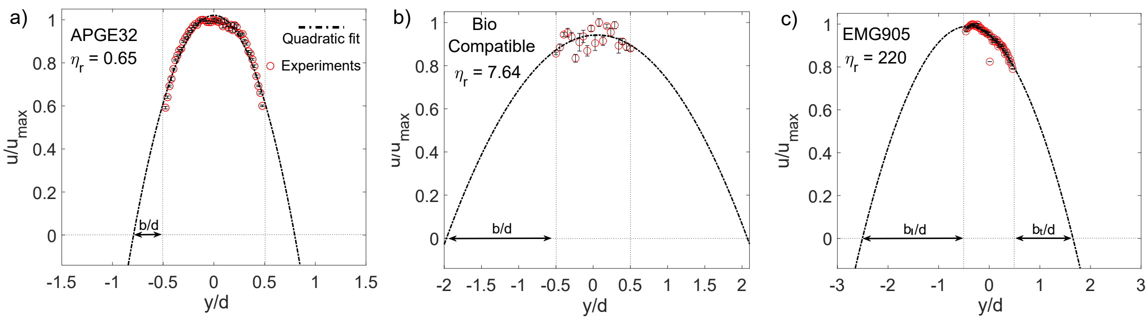

FIGURE 3.13: Velocity profile fit for slip length b/d. a) for APGE32, b) For Bio compatible ferrofluid, c) For EMG905, showing asymmetric slip length

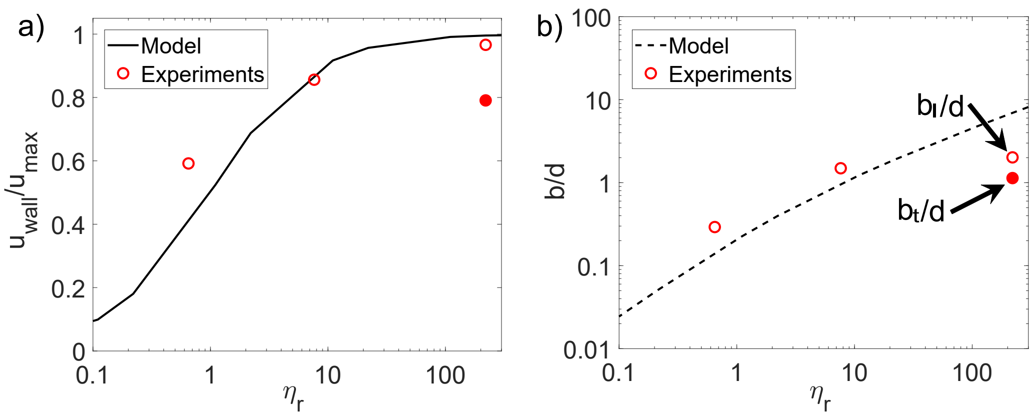

FIGURE 3.14: Comparison of wall Velocity and slip length for three order of magnitide of viscosity ratio. Line is analytical and markers are experiment. a) Wall velocity, b) Slip length

Eq.3.45 through Eq.3.44. Fig.3.14 shows the comparison of model and experimental data for wall velocity with respect to viscosity ratio (Fig.3.14 a)) and slip length versus viscosity ratio (Fig.3.14 b)). Note that the model used is for symmetric coverage of ferrofluid (s=0).

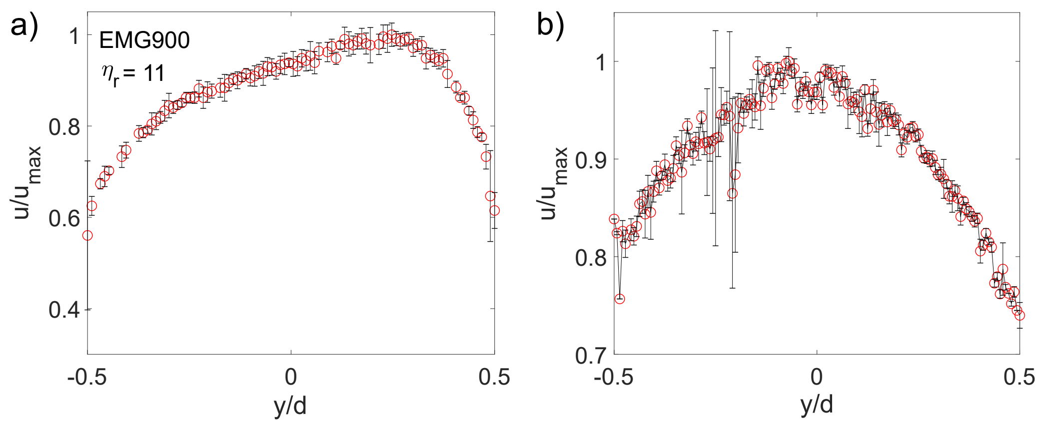

FIGURE 3.15: Velocity profile in the antitube for EMG900 ferrofluid with η_r = 11. a) Maximum velocity shifted to right from y/d = 0, b) Shifted to left

The data is extracted from the velocity profile in Fig.3.13. Fig.3.14 a) shows that with the increase in viscosity ratio beyond 10, the rate of change of wall velocity with respect to viscosity ratio reduces and the curve flattens, as measured in experiments. The slip length on the other hand increases with viscosity ratio. The measurement of differences in wall velocity beyond $\eta_r = 100$ is experimentally challenging and thus limits the calculations of the slip length evolution with increasing viscosity ratio beyond $\eta_r = 100$. Measurements at $\eta_r = 11$ have also shown large wall velocity and asymmetric velocity profile (Fig.3.15). Fig.3.15 a) and Fig.3.15 b) shows the shift of maximum velocity in the positive and negative half of y/d respectively. The ferrofluid used was EMG900 with a saturation magnetisation of 100 mT. The microchannel was not of uniform width (d) along the length of flow. The data was recorded at a very small section of flow where the flow channel had uniform width. Hence, the analytical data is not compared with the experiments.

3.6 Conclusion and perspectives

Magnetic fluid lubrication stabilized by a magnetic force field has therefore been shown as a viable strategy to create a continuously lubricated flow channel with 2D lubrication and potential for developing complex lubricated channel beyond liquid infused open surfaces. Continuously lubricated flow channels result in record high values of large slip length and our work shows direct measurement of such slip lengths using μPTV techniques. The slip length can be tuned by the choice of viscosities of the involved liquids. We predict the flow profile using Stokes equation and necessary boundary conditions, with predictions of slip length values beyond a simple linear assumption. The analytical model also predicts asymmetric velocity profile for asymmetric lubrication , as found in experiments. Experiments and model suggest that asymmetric velocity profiles are better revealed for large slip length values.

We envisage that, these magnetically confined microchannels could be also used as a model system to study the flow of biomaterials used to prepare pharmaceutical products. Biological cells suffer from solid walls and delicate cells gets damage in the location of large shear stress[12], especially in microchannels. Sudden changes in shear stress may lead to serious medical conditions for disease atherosclerosis where inflammatory regions are formed in medium and large arteries[13]. To mimic and study the phenomena by means of microfluidics chips[14], a tunable shear stress microfluidic channel presented in our research could act as a model system to study the biological phenomena. Magnetically confined microchannels show large tunable slip length and hence tunable shear in the microchannel. This could be exploited to transport delicate biological cells as well as for studying cells in low shear environment. The shear rate (dimensional form) in the flow is given by

$$\frac{\partial u}{\partial y} = \frac{1}{\eta}\frac{\partial P}{\partial z}\left[y + \frac{a_5 \eta_r d}{2}\right] \tag{3.46}$$

The shear rate can be tuned by the choice of viscosity ratio η_r and geometric parameters (a_5). Note that $\frac{\partial P}{\partial z}$ equals to $\frac{\partial P}{\partial z}_p / \beta_{2D}$ where $\frac{\partial P}{\partial z}_p$ is the pressure drop for flow through solid wall tube. Since β_{2D} (Eq.3.40) is greater than 1 and can be tuned (we show tuning from 1 to ≈ 200) using viscosity ratio and geometric parameter, the shear rate can be reduced by $\approx \beta$ times. It is also important to tune the shear as it dictates the distribution of population of bacteria in a microchannel. It has been shown that bacterias are trapped in high shear region when exposed to flow[15]. Asymmetric lubrication resulting in asymmetric velocity profile (asymmetric shear) could be used to selectively control the density of microbes along a microchannel. This might provide control on the bacterial population and their location. Bacterial motility also depends on the presence of solid walls. Tumbling of bacteria is an important phenomena in bacterial dynamics and is suppressed near a solid wall by almost 50%[16]. Presence of continuous liquid wall could effect the motion of bacteria and the formation of biofilm since the wall itself is moving.

A whole new perspective is required while replacing solid confining walls by liquid walls, especially in the context of biomaterial transport/swimming microorganisms[17] because microbial process of chemotaxis is also effected by the presence of shear in flow[18]. Stabilizing a continuously liquid lubricated microchannel and tunable shear flow makes possible studies of phenomena involving the interaction of bounding surfaces with moving boundaries (liquid walls). Our understanding of flow profile and flow mechanics could then impact and enhance fundamental understanding on bacterial motility and cell health, possibly providing a new approach for low shear transport of delicate cells as well as mimicking the shear environment in biological world.

3.7 Contributions

Arvind Arun Dev (AAD), Bernard Doudin (BD) and Thomas Hermans (TH) conceptualised the project. AAD did the particle tracking velocimetry(PTV) experiments in Max Planck institute for dynamics and self organisation (MPIDS) with supervision of Prof. Bodenschatz. After the experiments the PTV data is analyzed by Dr. Bagheri of MPIDS using a homemade code. AAD developed the analytical model. The research article is under preperation.

Bibliography

[1]J. Keeling and N. G. Berloff, "Condensed-matter physics: Going with the flow", **457**, 273–274 (2009).

[2]A. Keerthi, S. Goutham, Y. You, P. Iamprasertkun, R. Dryfe, A. Geim, and R. Boya, "Water friction in nanofluidic channels made from two-dimensional crystals", Nature Communications **12**, 3092 (2021).

[3]H. M. Lopez, J. Gachelin, C. Douarche, H. Auradou, and E. Clément, "Turning bacteria suspensions into superfluids", Physical Review Letters, `10.1103/PhysRevLett.115.028301` (2015).

[4]J. Ou and J. P. Rothstein, "Direct velocity measurements of the flow past drag-reducing ultrahydrophobic surfaces", Physics of Fluids **17**, 103606 (2005).

[5]P. Tsai, A. M. Peters, C. Pirat, M. Wessling, R. G. H. Lammertink, and D. Lohse, "Quantifying effective slip length over micropatterned hydrophobic surfaces", Physics of Fluids **21**, 112002 (2009).

[6]E. Karatay, A. S. Haase, C. W. Visser, C. Sun, D. Lohse, P. A. Tsai, and R. G. H. Lammertink, "Control of slippage with tunable bubble mattresses", Proceedings of the National Academy of Sciences **110**, 8422–8426 (2013).

[7]S. J. Lee, H. N. Kim, W. Choi, G. Y. Yoon, and E. Seo, "A nature-inspired lubricant-infused surface for sustainable drag reduction", Soft Matter **15**, 8459–8467 (2019).

[8]A. Maali and B. Bhushan, "Measurement of slip length on superhydrophobic surfaces", Philosophical Transactions of the Royal Society A: Mathematical, Physical and Engineering Sciences **370**, 2304–2320 (2012).

[9]S. Peppou-Chapman, J. K. Hong, A. Waterhouse, and C. Neto, "Life and death of liquid-infused surfaces: a review on the choice, analysis and fate of the infused liquid layer", Chem. Soc. Rev. **49**, 3688–3715 (2020).

[10]P. Dunne, T. Adachi, A. A. Dev, A. Sorrenti, L. Giacchetti, A. Bonnin, C. Bourdon, P. H. Mangin, J. M. D. Coey, B. Doudin, and T. M. Hermans, "Liquid flow and control without solid walls", Nature **581**, 58–62 (2020).

[11]A. A. Dev, P. Dunne, T. M. Hermans, and B. Doudin, "Fluid drag reduction by magnetic confinement.", Langmuir : the ACS journal of surfaces and colloids (2022).

[12]A. Blaeser, D. Duarte Campos, U. Puster, W. Richtering, M. Stevens, and H. Fischer, "Controlling shear stress in 3d bioprinting is a key factor to balance printing resolution and stem cell integrity", Advanced healthcare materials **5**, `10.1002/adhm.201500677` (2015).

[13]S. Birol, R. Fuçucuoğlu, S. Cadirci, A. Sayi-Yazgan, and L. Trabzon, "Studying dynamic stress effects on the behaviour of thp-1 cells by microfluidic channels", Scientific Reports **11**, 14379 (2021).

[14]Y. B. Bae, H. K. Jang, T. H. Shin, G. Phukan, T. T. Tran, G. Lee, W. R. Hwang, and J. M. Kim, "Microfluidic assessment of mechanical cell damage by extensional stress", Lab Chip **16**, 96–103 (2016).

[15]R. Rusconi, J. Guasto, and R. Stocker, "Bacterial transport suppressed by fluid shear", Nature Physics **10**, 212–217 (2014).

[16]M. Molaei, M. J. Barry, R. Stocker, and J. Sheng, "Failed escape: solid surfaces prevent tumbling of escherichia coli.", Physical review letters **113 6**, 068103 (2014).

[17]A. P. Berke, L. Turner, H. C. Berg, and E. Lauga, "Hydrodynamic attraction of swimming microorganisms by surfaces", Phys. Rev. Lett. **101**, 038102 (2008).

[18]J. S. Guasto, R. Rusconi, and R. Stocker, "Fluid mechanics of planktonic microorganisms", Annual Review of Fluid Mechanics **44**, 373–400 (2012).

Chapter 4

Deformation of antitubes under flow: competing magnetic pressure and shear stress

4.1 Introduction

Deformable or elastic interfaces are ubiquitous in nature, ranging from simple bubbles[1] to biofluidics through compliant ducts in a human body[2]. For example, the deformation of blood vessels under flow makes them of high compliance and flow stability is more complex in the soft flow channels[3]. Inspired by the natural world, the coupling of fluid flow and elasticity has been studied in the form of soft lubrication[4], elastocapillarity[5] and viscous peeling[6], to name a few. Deformable interfaces also impact hydrodynamic fundamentals, for example by suppressing the flow fingering instability[7] as well as decreasing the Reynolds number where laminar flow becomes turbulent[3]. Promising technological applications in soft robotics[8], adaptive optics[9], reconfigurable microfluidics, valves and soft actuators[10, 11] also take advantage of controlled soft wall confinement. Flow-induced reversible deformations are required for making analog of electronic circuits[12] namely fluidic resistors, capacitors, diodes and transistors[13, 14]. In nature, a simple liquid-air interface acts as a soft deformable interface which provides insects and other creatures with the abilities to walk on water[15], as shown in Fig.4.1 a)-i)-viii). This is due to the finite interfacial tension at the air-water interface and the phenomena has been mimicked[16, 17] forming various small robots[18]. Fig.4.1 a)-vii) shows a sketch by Leonardo da Vinci of a man walking on water with a floating device. Though walking on water is not yet common using devices, tuning shear thickening liquids have however made it possible to walk[19] or sink[20] in a liquid bath under the action of an applied stimulus. Such materials which

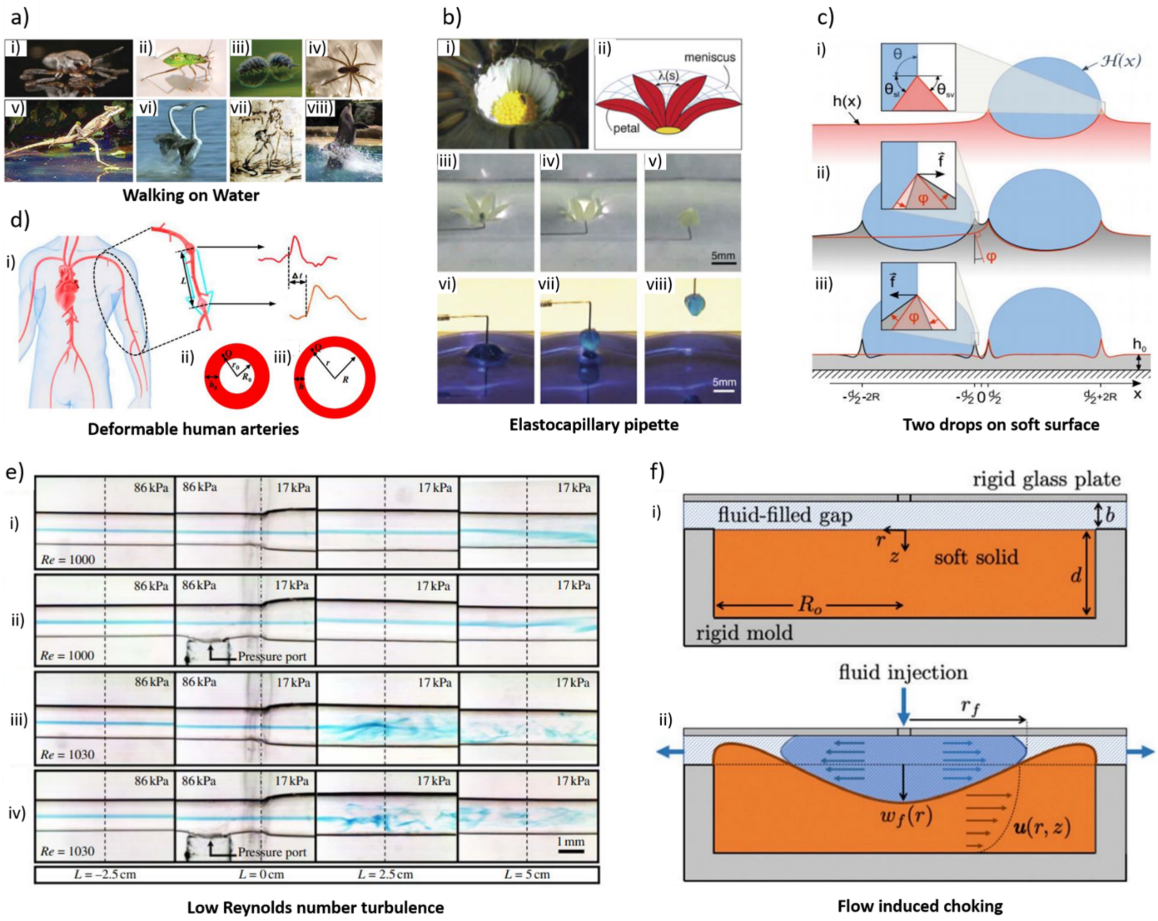

FIGURE 4.1: Deformable interfaces. a) Walking insects and creature on water[15] , b) Mimicking flower petal behavior with engineered soft structure[21] , c) Interaction of drops on soft substrates[22] , d) Deformable blood carrying arteries in humans [23] , e) early transition from laminar to turbulent flow in soft channel flow[3] , f) Flow induced choking of fluid channel[12]

respond to an external stimulus[19, 24, 25] are required to provide technical solutions ranging from electronics[26] to medical[27] applications. Especially, flexible materials capable of reversible deformations have been extensively used in wearable electronics[28–30]. The interaction of soft structures with liquid can also be seen in nature in the form of flower petals wetting in water, shown in Fig.4.1 b)-i) ii). The flower petals close when they move inside the water. The phenomena has been mimicked with soft engineered flat structures having the shape of the flower petal and tuning the interfacial tension between water and the soft structure. This results in mimicking fluid structure interaction in nature is illustrated in Fig.4.1 b)-iii)-v). Furthermore this system can be used to make an elastocapillarity pipette shown in Fig.4.1 b)-vi)-viii). A more fundamental understanding of the interaction of the drops with soft deformable substrates is depicted in Fig.4.1 c). A drop on a soft substrate Fig.4.1 c)-i) deforms the substrate with profile $h(x)$, the profile depends on the balance of capillary force and elasticity of the substrate. A Neumann triangle in the inset shows the force balance. On placing another drop in the vicinity of the first drop Fig.4.1 c)-ii), the Neumann force balance is disturbed and the drops attract each other. Similarly for a thin substrate the force balance causes the two drops to repel each other shown in Fig.4.1 c)-iii). Essentially, the phenomena is governed by the balance of elasticity and capillarity. The flow of blood in veins and arteries is also classified as flow through compliant ducts. Fig.4.1 d)-i) shows a schematics of the human blood system, where the inset shows the pressure pulse in the arteries. Fig.4.1 d)-ii) and Fig.4.1 d)-iii) shows a schematics of the expansion of blood carrying artery. The artery expands with the pressure pulse and return to its original shape with the reduction of pressure. Technological applications could also get effected at fundamental level with the flow of liquid in soft tubes shown in Fig.4.1 e). The transition from laminar to turbulent flow in a cylindrical tube normally happens for $Re > 2000$. However for a soft tube this transition may happen at lower Re. Fig.4.1 e)-i)-ii) show the flow in a channel with $Re = 1000$ and the shear modulus of 86 kPa, entry of the channel and 17 kPa further down the channel (right). The flow is laminar in the 86 kPa region shown by the dye(blue) whereas a transition in the 17 kPa region can be seen (far right of the flow channel). Further increasing the Re = 1030 in Fig.4.1 e)-iii)-iv), the transition length decreases but essentially happens in the softer section (17 kPa). Soft materials have also been used to study the possibility of flow induced choking of a microchannel[12]. Fig.4.1 f)-i) shows the schematics used in the study, where a fluid fills in the gap above the soft solid, with the top closed by a rigid glass plate with a hole for fluid entry. Fig.4.1 f)-ii) shows the deformation of a soft material (brown) with the entry of the liquid (blue). $w_f(r)$ and $u(r,z)$ are stress and displacement vector respectively. The deformation profile depends on a fluid structure interaction parameter which is the ratio of fluid pressure and shear modulus of the soft material. Apart from mechanical applications, in cell mechanics, a deformable or soft surface could be also used as a stimulus for promoting stem cell differentiation[31].

There is therefore a strong need of appropriate soft materials, presently pioneered by the use of highly flexible elastomers[32] for building microfluidic circuits[33]. It is notably used to mimic flow through veins [23] and understand the mechanical response of blood vessels[14]. Their limited elastic properties, in particulars for pressures below 100 kPa, however limit their deformation under flow as well as their low-pressure adequacy for bio-mimicking. Lubrication becomes therefore a limiting factor, as the viscous drag increases when the circuits dimensions decrease. Hence the miniaturization capability of these pressure-driven

solid wall soft tubes is under question, because the resulting large viscous drag requires micro compressor disproportionate in size due to low energy density and high weight[34]. A liquid-in-liquid flow is ideally suited to reduce the drag, especially in microfluidics, but such liquid cylinder flows are highly unstable and form a classical hydrodynamics issue known as Plateau Rayleigh instability (PRI)[35] (see also Chapter 1), which is a fundamental issue that require a short length scale for keeping stability under the action of shear stress[36] or very specific conditions, like high external electric field[37], nanostructured interfaces[38]. A stable magnetic liquid lubrication[39] could mitigate the PRI instability. Ferrofluids form a class of smart magnetic liquid adaptive[40], flexible[41] and capable of responding to applied magnetic field [42] for the purpose of forming a reconfigurable surface [43].
Here we report a novel reversibly deformable smart material interface in the form of a cylindrical flow tube, made up of a magnetic-nonmagnetic liquid-liquid interface in the presence of a magnetic field. We show experimentally that the creation of deformable low shear antitube provides a solution to the classical problem of instabilities by stabilizing liquid-liquid interface against PRI at mm as well as at microfluidic length scales, with length scales only limited by the extension of the magnetic source. We show that by tuning the magnetic and liquid properties, the softness of the interface can be controlled and the soft interface can withstand large shear stress. Our research can be applied in fabricating hybrid microfluidic channels with flexible liquid walls of low shear with potential applications in bio-mimicking, biomaterial transport, cell dynamics, drug-delivery. The theoretical framework presented could be used to engineer devices with flow structure (liquid structure) interaction, leading to wider applications of soft microfluidics.

4.2 Materials and methods

4.2.1 Magnetic field design

We explore two types of magnetic circuits: i) a design to mimic sinusoidal variation of magnetic field in the axial direction (flow direction, z) shown in the top row of Fig.4.2 , ii) the continuous magnetic encapsulation design used earlier in our study[39, 44] shown in the bottom row of Fig.4.2. For the sinusoidal design, the magnet arrangement along the length is shown in Fig.4.2 a). The magnets (black) are inserted inside a 3D printed setup with entry points for ferrofluid in between the magnets. White arrows show the direction of magnetisation of the permanent magnets. The gap between two magnets along z is 2 mm. Fig.4.2 b) shows the magnetic field generated by the field arrangement shown in Fig.4.2 a), illustrating how the magnitude of magnetic field between the magnets varies along their length, creating a wavy structure. Fig.4.2 c) and Fig.4.2 d) shows the cross section of the arrangement with the magnetic field at planes AA′ and BB′ respectively. The magnetic field is lower at BB′

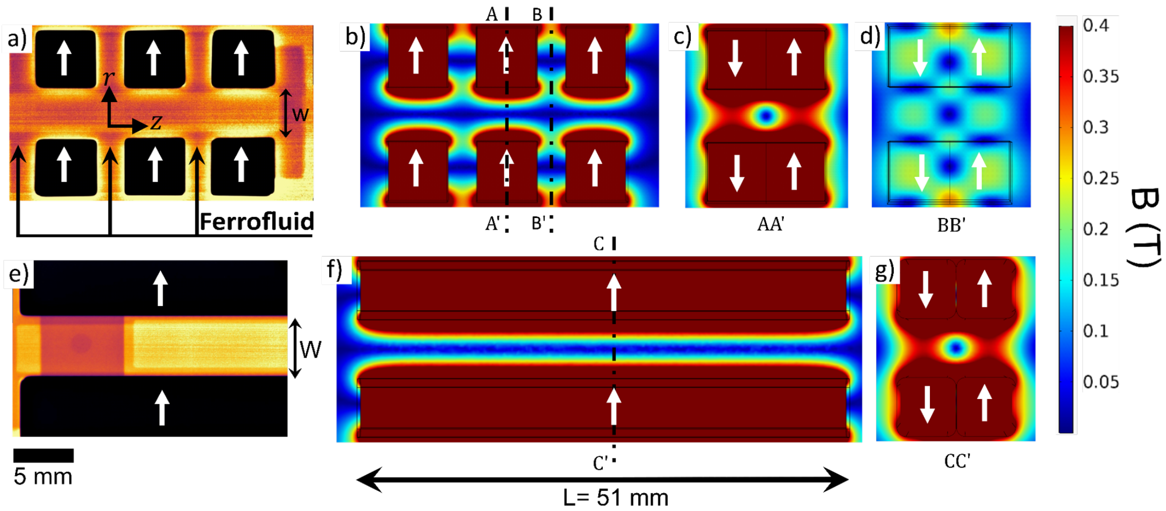

FIGURE 4.2: Magnetic field design. a) Magnets arrangement for wavy flow channel or mimicking PRI instability shape b) Magnetic field generated by the magnets arrangement. c), d) cross section magnet arrangement and magnetic field generated at AA′ and BB′ in Fig.1b). e) Magnet arrangement (Half channel length) for avoiding end effects. f) Magnetic field generated with the continuous magnet arrangement. g) Magnetic field cross section at CC′. w and W are width between the pair of magnets. White arrows show the direction of magnetisation.

compared to AA′ and essentially retains the magnetic encapsulation field arrangement[44]. For the other design, Fig.4.2 e) shows half the length of the circuit, made of four magnets[44] with magnetic field generated shown in Fig.4.2 f) for the full length. The non-uniform magnetic field is now limited to the ends of the magnets or flow channel and the axial direction has a constant magnetic field along z direction. The cross section at CC′ in Fig.4.2 g) shows the quadrupolar arrangement[44].

4.2.2 Ferrofluid Magnetisation

We use three magnetic liquids, ferrofluids APG314, APGE32 and APG1141 from Ferrotech. The $M - H$ curve of ferrofluid is important to estimate the saturation magnetisation (M_s), where M is magnetisation and H is the applied magnetic field. Fig.4.3 a) , b) , c) show the $M - H$ curve (markers) obtained from Ferrotech for ferrofluid APG314 , APGE32 and APG1141 respectively. The black line is a polynomial fit to be used later in analytical model. P_1 to P_{11} are constants in the polynomial equation.

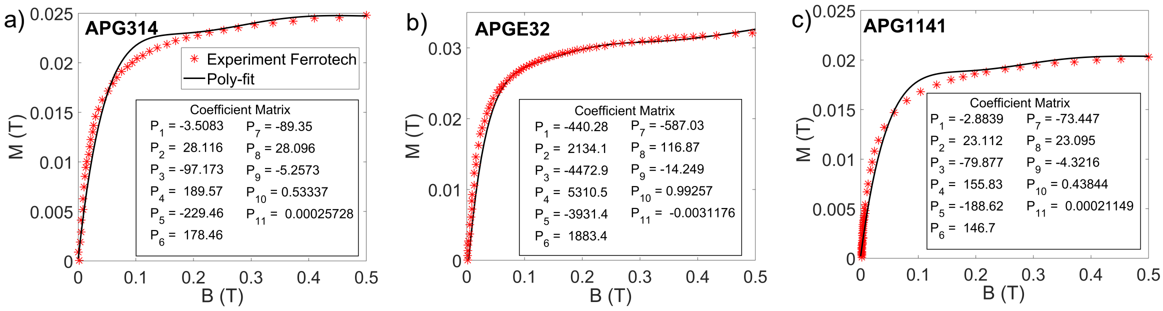

FIGURE 4.3: Fitting of magnetisation curve. a) For APG314 b) APGE32 c) APG1141. P_1 to P_{11} are the coefficient required in a 10th order polynomial for fitting (line) to the experiment (markers). Note the experimental data is from Ferrotech.

4.3 Experiments

We use glycerol as the non-magnetic fluid and various ferrofluids as encapsulating liquids to tune the viscosity ratio η_r, interfacial tension γ and saturation magnetisation M_s of ferrofluids. See AppendixE for the ferrofluid properties including protocol for measurement of interfacial tension. We image the system using a homemade X-ray setup (for radiography, 2D image) and a micro computed tomography system (RX-Solutions EasyTom 150/160) system for 3D tomography. The images are analysed using ImageJ and the interface is tracked using MATLAB[45].

To understand the physics of the interaction of magnetic pressures and viscous stress, we consider a system where the magnetic field (H) is only a function of radial coordinate (r), this is achieved by using a continuous permanent magnet[39, 44] as shown in Fig.4.4 a). The stray magnetic field is now limited only at the edges of the flow channel. Fig.4.4 b) shows the reversible deformation of the antitube before, during and after flow. For a $Q = 150\ \mu$L/min flow from left to right, the antitube is deformed (widened at the inlet and contracted at the outlet) and some ferrofluid tries to escape the system (black circled zone). This suggests that there is a cutoff flow rate Q_c above which the ferrofluid leaks.

Hence, in our research we investigate: i) the interaction of fluid mechanics and magnetism governing the final stable deformed cylindrical flow state shown in tomography image in Fig.4.4 c) with inset showing cross sections, ii) the cutoff flow rate (Q_c) at which the ferrofluid begins to escape. Note that the tompgraphy image show that the cross section is not exactly circular. This could be attributed to the magnetic field not being perfectly axisymmetric at the center, see Fig. 4.2c) and g). We begin by recording reversible deformations of the glycerol antitube with three different ferrofluid encapsulations (APG1141, APGE32 and APG314 from Ferrotech) such that we have viscosity ratio (η_r=η_g/η_f) between glycerol and

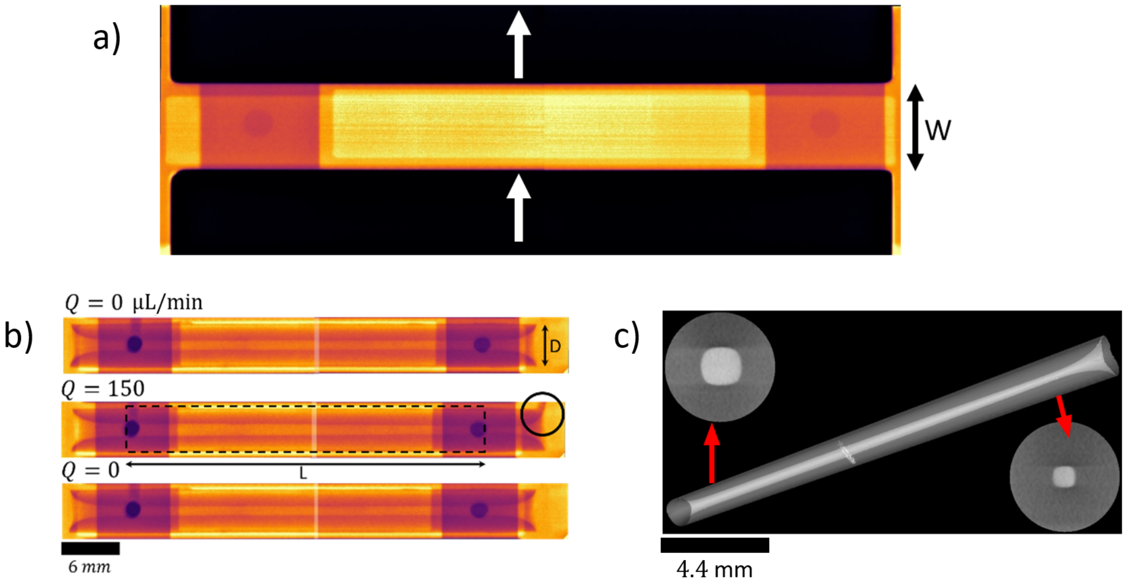

FIGURE 4.4: Reversibly deformable soft antitubes with Glycerol and APGE32 feroofluid, viscosity ratio η_r = 0.65. a) Magnet design with continuous magnets[44]), W = 6 mm, b) Flow induced reversible deformation of antitubes, before flow (Q = 0 μL/min), during flow (Q = 150 μL/min) and after flow (Q = 0 μL/min), rectangle of length L = 40 mm in Q = 150 μL/min shows the volume used for analytical studies comparisons avoiding stray magnetic field. The black circle shows the location where the ferrofluid tries to escape. c) 3D X-ray tomography showing deformed conical antitube at Q = 75 μL/min. Insets show the cross section of the antitube at inlet and outlet, the scale bar is related to the cross sections. A tomography video of the deformed stable liquid nozzle shape is presented in AppendixA-V1. See AppendixC for the RX-Solution EasyTOM 150/160 X-Ray setup details and mounting of experimental cell.

ferrofluids less than and greater than 1. For each η_r, three different initial diameters (d_0) are used for each of which three different flow rate are applied using a syringe pump (Harvard apparatus PHD 2000). This gives us 27 combinations of magnetic pressure, Laplace pressure and viscous stress.

Fig.4.5 a) and Fig.4.5 b) show the tracked antitube diameter along the length (using edge detector algorithm[45]) before flow and during flow for APGE32 as ferrofluid respectively. The curvature near inlet (left) and outlet (right) is due to the non-uniform magnetic fields. Fig.4.5 c) and Fig.4.5 d) show the tracked antitube diameter during flow for APG314 and APG1141 as ferrofluid respectively. Comparing Fig.4.5 a) and Fig.4.5 b) where η_r = 0.65, the deformations increases with increasing Q and decreasing d_0 , due to increased shear stress and lower magnetic pressure, with a similar trend is also seen for glycerol-APG314 (η_r = 4.8) and glycerol-APG1141 (η_r = 0.1) . Furthermore, when the flow rate is increased beyond a critical value Q_c, there is an egress of ferrofluid as observed in Fig.4.4 e) (see black circle), Q = 150 μL/min and also shown in inset of Fig.4.6 (a) corresponding to Fig.4.5 c), blue

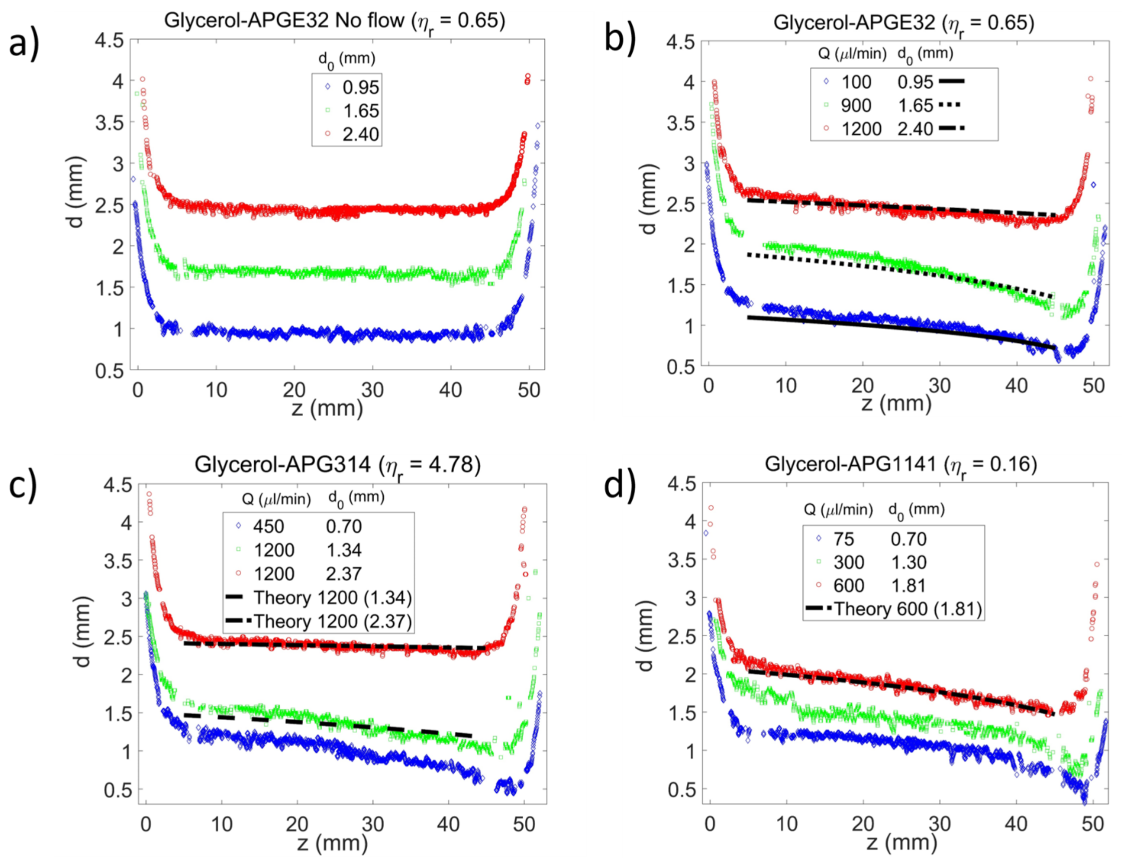

FIGURE 4.5: Deformation of antitube over length. a) Diameter profile without flow for Glycerol-APGE32 system, three different d_0 avoiding near inlet and outlet, b) deformed diameter profile for flow rate Q, c) deformed diameter profile for Glycerol-APG314. η_r is viscosity ratio, d) deformed diameter profile for Glycerol-APG1141. η_r is viscosity ratio. Lines are analytical predictions.

markers. Fig.4.6 shows the experimental ferrofluid egress states (open markers) and stable

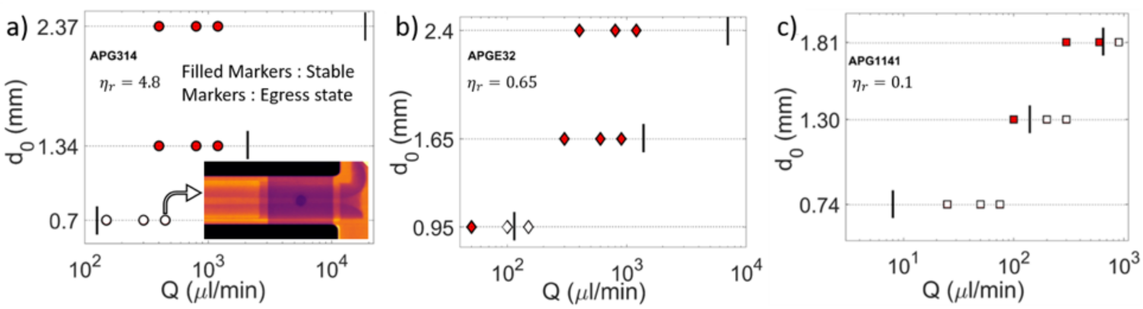

FIGURE 4.6: Cutoff flow rate (Q_c) for escape of ferrofluid. a) Glycerol-APG314 with η_r = 4.8, inset shows a case where ferrofluid tries to escape. Filled markers and open markers denote experimentally stable and egress states, vertical line corresponds to Q_c calculated analytically for respective d_0, b) Glycerol-APGE32, η_r = 0.65 , c) Glycerol-APG1141, η_r = 0.1. . d_0 is the diameter of antitube before flow.

states (filled markers). The egress state is defined as the state where the ferrofluid starts to escape through a hole provided next to the magnet (inset Fig.4.6 a)). The maximum permissible flow rate (Q_c) to avoid egress of ferrofluid decreases with decrease in η_r and d_0 and moreover with change in ferrofluid (Fig.4.6 a), Fig.4.6 b) and Fig.4.6 c)), the magnetisation of ferrofluid changes.

To understand the extent of deformations and scaling of Q_c, we need to consider the balance of different pressures involved in the system and their variations with increasing flow rate.

4.4 Model: Deformation along the length

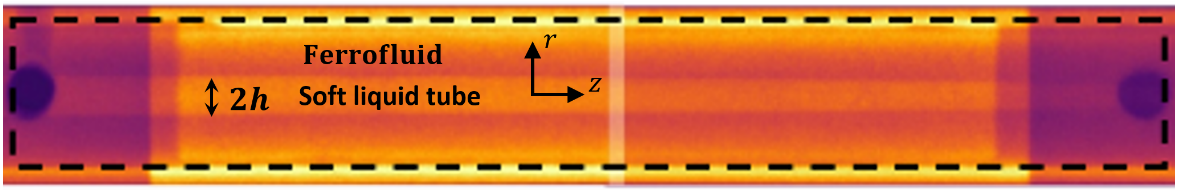

FIGURE 4.7: Deformed antitube length considered in the model avoiding stray magnetic field region, h is the radius of the flow channel (bright central part)

Fig.4.7 shows the magnified image from Fig.4.4 e) where we apply the analytical model. We avoid the ends where the effect of stray magnetic field can not be neglected. The excess pressure inside the antitube during flow is given by

$$P = \int_0^H \mu_0 M dH + \frac{1}{2}\mu_0 M_I^2 + \kappa\gamma \tag{4.1}$$

where M is the magnetisation of the ferrofluid, γ is the interfacial tension between magnetic non magnetic interface and κ is the curvature of the antitube. Note that in the absence of magnetic stress/pressure, the excess pressure inside a liquid cylinder is given by only the last term with interfacial tension, which is known to be an unstable shape[46]. The curvature of a deformed cylinder under the assumption of small slope of deformation

$$\kappa = \left(\frac{1}{h} - h''\right) \tag{4.2}$$

where $h(z)$ is the height of the magnetic-nonmagnetic interface from the center of antitube and h'' is second derivative of h with respect to axial coordinate, z. The gradient of the excess pressure P along z is responsible for the flow rate Q, given by

$$\frac{\partial P}{\partial z} = \frac{\partial}{\partial z}\left(\int_0^H \mu_0 M dH\right) + \frac{\partial}{\partial z}\left(\frac{1}{2}\mu_0 M_I^2\right) + \frac{\partial}{\partial z}(\kappa\gamma) \tag{4.3}$$

M_I is the magnetisation of the ferrofluid at the magnetic-non magnetic interface and is a function of applied field H, which can be written as[44]

$$H = \frac{4M_r h}{\pi W} \tag{4.4}$$

where M_r is the remnant magnetisation of the magnets and W is the distance between magnets.

$$\frac{\partial P}{\partial z} = \frac{\partial}{\partial z}\left(\int_0^H \mu_0 M dH\right) + \frac{\partial}{\partial z}\left(\frac{1}{2}\mu_0 M_I^2\right) + \gamma \frac{\partial}{\partial z}\left(\frac{1}{h} - h''\right) \tag{4.5}$$

The experimental magnetisation curve ($M(H)$) can be fitted using a 10^{th} order polynomial for mathematical simplicity (see Fig.4.3), given by

$$M(H) = \frac{1}{\mu_0}\sum_{m=1}^{m=11} P_m(\mu_0 H)^{11-m} \tag{4.6}$$

which gives,

$$\frac{\partial}{\partial z}\left(\int_0^H \mu_0 M dH\right) = \frac{4Mrh'}{\pi W}A \tag{4.7}$$

$$\frac{\partial}{\partial z}\left(\frac{1}{2}\mu_0 M_I^2\right) = \frac{4Mrh'}{\pi W}AB \tag{4.8}$$

$$\frac{\partial}{\partial z}\left(\frac{1}{h} - h''\right) = -\gamma\left(\frac{h'}{h^2} + h'''\right) \tag{4.9}$$

with

$$A = \left[\sum_{m=1}^{m=11} P_m \left(\frac{4\mu_0 M_r h}{\pi W}\right)^{11-m}\right] \tag{4.10}$$

$$B = \left[\sum_{m=1}^{m=11} P_m (11-m) \left(\frac{4\mu_0 M_r h}{\pi W}\right)^{10-m}\right] \tag{4.11}$$

Pressure gradient $\frac{\partial P}{\partial z}$ for flow rate Q is given by[39]

$$\frac{\partial P}{\partial z} = \frac{-8\eta_I Q}{\pi h^4 \beta} \tag{4.12}$$

where η_1 is the viscosity of the non-magnetic liquid (here glycerol), h is the flow radius. β is the drag reduction parameter due to lubricated flow[39] respectively. Using Eq.4.3 to Eq.4.12 we get

$$\frac{-8\eta_I Q}{\pi h^4 \beta} = A\frac{4\mu_0 M_r h'}{\pi W}\left[1 + B\right] - \gamma\frac{h'}{h^2} - \gamma h''' \tag{4.13}$$

Since $h''' \approx d_0/L^3$, it can be neglected compared to other terms, giving

$$h' = \frac{-8\eta_I Q}{\pi h^4 \beta \left[\frac{4\mu_0 M_r}{\pi W} A \left[1 + B\right] - \frac{\gamma}{h^2} \right]} \tag{4.14}$$

Solving Eq.4.14 with the condition that the volume of ferrofluid should be conserved before and after the deformation gives the profile $h(z)$. The condition is

$$\int_0^L h^2 dz = h_0{}^2 L \tag{4.15}$$

where $h_0 = d_0/2$ is the initial undeformed radius of the antitube.
The deformation profile given by Eq.4.14 is compared with experiments in Fig.4.5. The equations are solved using MATLAB, a sample code is provided in Appendix B. It can be seen that the model captures the phenomena satisfactorily for three different ferrofluid (magnetic pressure) with different viscosity ratio and flow rate (shear stress) , and interfacial tension (Laplace pressure). The experimental cases not compared with model are states where volume of ferrofluid is not conserved and the ferrofluid starts to escape, which indicates the occurence of instability.

4.5 Instability

To simplify the mathematical complexities, we assume that the ferrofluid is magnetically saturated, $M = M_I = M_s$. The excess pressure is given by

$$P = (\mu_0 M_s H) + \left(\frac{1}{2}\mu_0 M_s^2\right) + \gamma\left(\frac{1}{h} - h''\right) \tag{4.16}$$

For the initial undeformed state, $\kappa = \frac{1}{h}$, the magnitude of three pressures, Magnetic pressure , Maxwell pressure jump and Laplace pressure (three terms on right in Eq.4.16 respectively) is shown Fig.4.8. In case of magnetically saturated ferrofluid, the Maxwell pressure jump is constant and does not depends on the size of the flow channel of radius h. The magnetic pressure is directly proportional to h whereas Laplace pressure is inversely proportional to h. The crossover between the two is shown in the inset. It can be seen that the interfacial tension becomes increasingly important at smaller h. The crossover depends on the ferrofluid, a ferrofluid with higher saturation magnetisation exhibits a crossover at lower value of h.

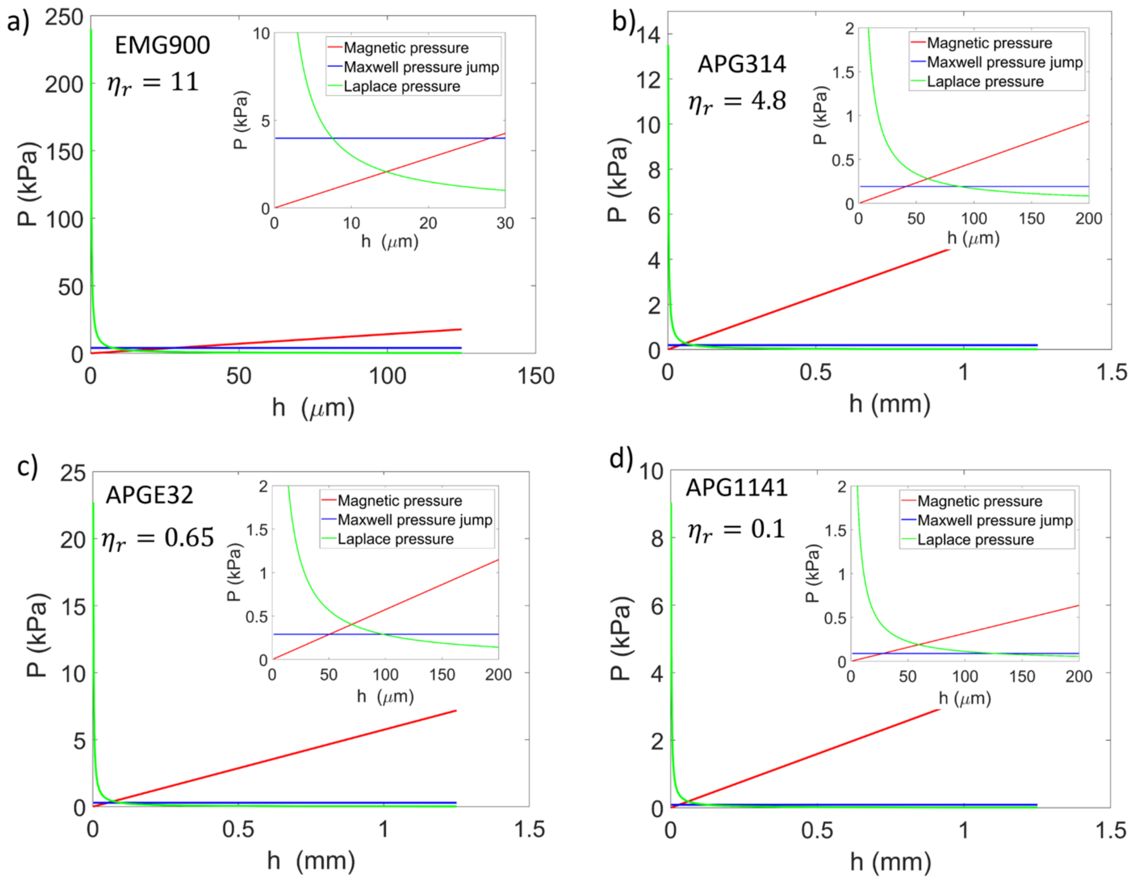

FIGURE 4.8: Pressures inside antitube varying with the size of antitube for glycerol as soft antitube and ferrofluid a) EMG900, b) APG314 c) APGE32 and d) APG1141. Red line, blue line and green line shows the magnetic pressure, Maxwell pressure jump and Laplace pressure respectively. Inset shows the cross-over of magnetic pressure and Laplace pressure respectively

The excess pressure gradient is given by

$$\frac{\partial P}{\partial z} = \frac{\partial}{\partial z}(\mu_0 M_s H) + \frac{\partial}{\partial z}\left(\frac{1}{2}\mu_0 M_s^2\right) + \gamma\frac{\partial}{\partial z}\left(\frac{1}{h} - h''\right) \tag{4.17}$$

Combining Eq.4.17, Eq.4.12 and Eq.4.4

$$\frac{-8\eta_I Q}{\pi h^4 \beta} = \frac{4\mu_0 M_s M_r h'}{\pi W} - \gamma\left(\frac{h'}{h^2} + h'''\right) \tag{4.18}$$

Eq.4.18 is the governing equation for $h(z)$. Non-dimensionalizing Eq.4.13 with $h^* = (h - h_0)/l_d$, $z^* = z/L$, we get

$$-\frac{\beta_0\eta_r}{\beta C^4} = \frac{1}{2}\left(\frac{h_0}{l_d}\right)^4 h^{*\prime} - 2\left(\frac{h_0}{l_d}\right)^2 \frac{l_d}{l_s}\left(\frac{h^{*\prime}}{C^2} + h^{*\prime\prime\prime}\left(\frac{h_0}{l_d}\right)^2\right) \tag{4.19}$$

Effect 1	Effect 2	Length scale
Stretching rigidity	Surface energy	γ/E
Surface energy	Bending rigidity	$\sqrt{Eh^3/\gamma}$ or $\sqrt{Er^3/\gamma}$
Gravity	interfacial tension	$\sqrt{\gamma/\rho_1 g}$
Gravity	Bending rigidity surface	$(Eh^2/\rho_s g)^{\frac{1}{3}}$ or $(Er^2/\rho_s g)^{\frac{1}{3}}$
Fluid inertial drag	Bending rigidity	$(Eh^3/\rho_l U^2)^{\frac{1}{3}}$
Fluid viscous drag	Bending rigidity	$(Er^3/\eta\omega)^{\frac{1}{4}}$
Bending rigidity	Thermal fluctuation	$(Er^4/k_B T)$

TABLE 4.1: Deformation length scales with different competing effects[47]

Effect	symbol
Surface energy	γ
Elastic Young's modulus	E
Poisson ratio	ν
Length of the structure	L
Thickness, for planar structures	h
Radius for rod structures	r
Bending stiffness, for planar structures	$B = Eh^3/12(1-\nu^2)$
Bending stiffness, for rod structures	$B_{rod} = \pi E r^4/4$
Gravity constant	g
Liquid density	ρ_l
Solid density	ρ_s
Oscillation frequency (for flagella)	ω
Thermal energy	$k_B T$

TABLE 4.2: Quantities used in effects listed in Tab. 4.1[47].

with l_s and l_d given as

$$l_s = \left(\frac{16\eta_f\eta_r QL}{\gamma\pi\beta_0}\right)^{\frac{1}{3}} \tag{4.20}$$

$$l_d = \left(\frac{\eta_f\eta_r QWL}{\mu_0 M_s M_r \beta_0}\right)^{\frac{1}{5}} \tag{4.21}$$

with $C = \frac{l_d}{h_0}h^* + 1$ and l_d is the deformation length scale which shows the competing effect between fluid viscous drag and magnetic pressure. Here L is the channel length with η_f and η_r the viscosity of ferrofluid and viscosity ratio respectively. Q is the flow rate, γ is the interfacial tension at the liquid-liquid interface. Other deformation length scales are listed in Tab. 4.1 from literature with different competing effects. The definition of the symbols is strictly limited to the effects listed in Tab. 4.1 are shown in Tab. 4.2

The length scale of deformations shown with different competing effects govern the extent of deformations in the respective system. Beyond providing a physical understanding of the system, the length scales also work as a measure of softness(hardness) of the system. Though list of length scales have been reoprted in the literature, a length scale with competing magnetic pressure and viscous shear is not presented, which is the contribution of the present work.

4.5.1 Instability (Viscous energy dissipation rate)

The hypothesis of viscous energy dissipation rate states that, *"if a fluid flow system is perturbed, the system changes to new state if the new state guarantees lower viscous energy dissipation."* The velocity gradient of flow in the antitube is given by

$$\frac{\partial V_1}{\partial r} = \frac{r}{2\eta_1}\frac{\partial P}{\partial z} \tag{4.22}$$

The rate of viscous energy dissipation per unit volume is given by[48]

$$\frac{\partial e}{\partial t} = \eta_1\left(\frac{\partial V_1}{\partial r}\right)^2 \tag{4.23}$$

$$\frac{\partial e}{\partial t} = \eta_1\left(\frac{r}{2\eta_1}\frac{\partial P}{\partial z}\right)^2 \tag{4.24}$$

Integrating over cross section gives the viscous energy dissipation rate per unit length

$$\frac{\partial E}{\partial t} = \int_0^h 2\pi r\eta_1\left(\frac{r}{2\eta_1}\frac{\partial P}{\partial z}\right)^2 dr \tag{4.25}$$

$$\frac{\partial E}{\partial t} = \frac{\pi h^4}{8\eta_1}\left(\frac{\partial P}{\partial z}\right)^2 \tag{4.26}$$

From Eq.4.17, we get $\frac{\partial P}{\partial z}$ as

$$\frac{\partial P}{\partial z} = \frac{4\mu_0 M_s M_r h'}{\pi W} - \gamma\left[\frac{h'}{h^2} + h'''\right] \tag{4.27}$$

$$\left(\frac{\partial P}{\partial z}\right)^2 = \left(\frac{4\mu_0 M_s M_r h'}{\pi W}\right)^2 + \gamma^2\left[\frac{h'}{h^2} + h'''\right]^2 - \frac{8\mu_0 M_s M_r h'}{\pi W}\gamma\left[\frac{h'}{h^2} + h'''\right] \tag{4.28}$$

Since we assumed $h' << 1$, $h'^2 \approx 0$

$$\left(\frac{\partial P}{\partial z}\right)^2 = \gamma^2\left[h'''^2 + \frac{2h'h'''}{h^2}\right] - \frac{8\gamma\mu_0 M_s M_r h' h'''}{\pi W} \tag{4.29}$$

Using Eq.4.26 and Eq.4.29 with non-dimentionalized variables gives

$$\frac{\partial E}{\partial t} = \frac{\pi\gamma^2}{8\eta_1}\Big[(h^* l_d + h_0)^4 h^{*'''2}\Big(\frac{l_d}{L^3}\Big)^2 + 2\frac{l_d}{L}\frac{l_d}{L^3}h^{*'}h^{*'''}(h^* l_d + h_0)^2 - \frac{8\mu_0 M_s M_r}{\pi W\gamma}\frac{l_d}{L}\frac{l_d}{L^3}(h^* l_d + h_0)^4\Big] \tag{4.30}$$

We apply perturbation to this viscous energy dissipation (Eq.4.30). We use the perturbation of the form $h^* = h^*_{min0} + \partial h_{min} cosKZ$ with assumption $\frac{\partial h^*_{min}}{h^*_{min}} << 1$. Hence the perturbed viscous energy dissipation rate per unit length scales as

$$\frac{\partial E}{\partial t} = -\frac{\pi\gamma^2}{8\eta_1}\Big(\frac{l_d}{L^3}\Big)(h^* l_d + h_0)^4 K^4 \partial h^2_{min} sin^2 KZ\Big[-K^2 + \frac{2}{h^2_{min}}\frac{l_d}{L} - \frac{8\mu_0 M_s M_r}{\gamma}\frac{l_d}{L}\Big] \tag{4.31}$$

Integrating over one wave length Λ

$$\frac{\partial E_\Lambda}{\partial t} = -\frac{\pi\gamma^2}{8\eta_1}\Big(\frac{l_d}{L^3}\Big)(h^* l_d + h_0)^4 K^4 \partial h^2_{min}\Big[-K^2 + \frac{2}{h^2_{min}}\frac{l_d}{L} - \frac{8\mu_0 M_s M_r}{\gamma}\frac{l_d}{L}\Big] \tag{4.32}$$

If $\frac{\partial E_\Lambda}{\partial t} < 0$, the system favours the perturbation and the growth of perturbation reduces the viscous dissipation, meaning it would lead to non stable interface. Hence for stability $\frac{\partial E_\Lambda}{\partial t} > 0$. For all the wave numbers, the system is stable if and only if

$$\frac{2}{h^2_{min}}\frac{l_d}{L} - \frac{8\mu_0 M_s M_r}{\gamma}\frac{l_d}{L} < 0 \tag{4.33}$$

which leads to

$$h_{min} > 2\Big(\frac{l_d^5}{l_s^3}\Big)^{\frac{1}{2}} \tag{4.34}$$

Eq.4.34 and Eq.4.14 together can predict the egress of ferrofluid shown in Fig.4.6 a) inset. The vertical lines at each diameter in Fig.4.6 a) , b) , c) show the analytical cutofff flow rate Q_c (predicted using Eq.4.34 and Eq.4.14) above which the ferrofluid leaves the system and the antitube is no longer stable. Q_c decreases with decrease in d_0 and η_r as observed in experiments. The model captures the experimental observations satisfactorily and provides a prediction for different combination of magnetic and non-magnetic liquids flow.

In the ferrofluid encapsulated soft antitubes, the resistance against deformation is the magnetic pressure which changes with the the radius h of the antitube (shown in Fig.4.8. Hence a deformable tube with variable stiffness is realised, which is hard to get in a elastomer based soft flow channel.

4.6 Stabilizing the oscillating liquid-in-liquid flow structure

An oscillating liquid-in-liquid flow structure under flow can be stabilized which is similar to the Plateau-Rayleigh instability (PRI) mode shape [36, 46]. Fig.4.2 a) shows the cell with permanent magnets for stabilizing a PRI failure mode shape. The magnetic field in between the magnets is shown in Fig.4.2 b). The space between the magnets is filled with Glycerol (η_g = 1.1 Pa.s , Sigma Aldrich) and on introducing the ferrofluid (Ferrotech) in between the magnets, a antitube is formed with brighter central part (glycerol) and darker encapsulation (ferrofluid) mimicking the PRI mode shape for glycerol (Fig.4.9 a), $Q = 0$ μL/min). With flow (Q = 75 μL/min) from left to right, the shape deforms and on stopping the flow regains the shape before flow (Q = 0 μL/min), compare three figures in Fig.4.9 a). Fig.4.9 b) show a 3D

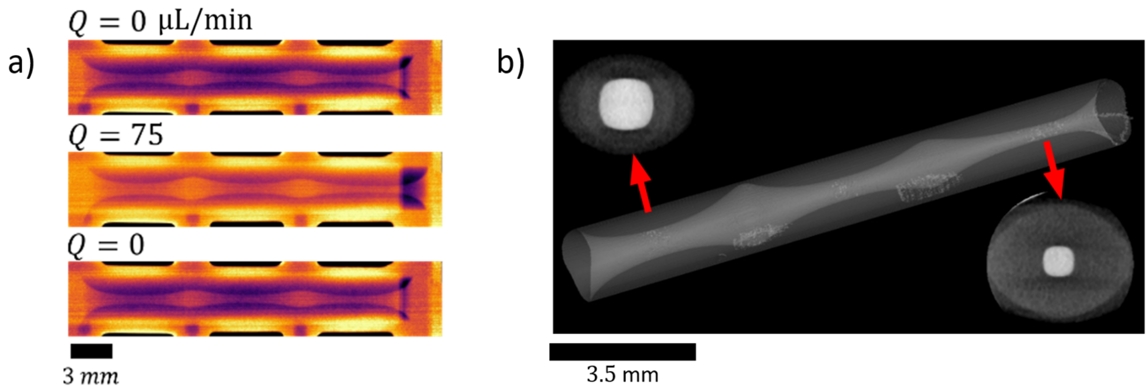

FIGURE 4.9: Stable oscillating liquid-in-liquid flow structure with Glycerol and APGE32 ferrofluid, viscosity ratio η_r = 0.65. a) Stable PRI mode shape before flow (Q = 0 μL/min) , during flow (Q = 75 μL/min) and after flow (Q = 0 μL/min), c) 3D X-ray tomography of PRI mode shape under flow, the scale bar is for the cross section images. Inset show the cross section of the antitube at inlet and outlet, the scale bar is related to the cross sections. A tomography video of the deformed stable liquid structure is presented in AppendixA-V2

tomography of the stable PRI mode shape under flow Q = 75 μL/min, with bright central part glycerol in darker encapsulation of ferrofluid APGE32, $\eta_r = 0.65$. The insets show the cross sections of the deformed antitube near inlet and outlet. Note that for a system with liquid-liquid interface (flow focusing), the PRI mode shape is unstable at Q = 0 μL/min and it is not possible to sustain the variable diameter flow channel along its length for $Q > 0$ μL/min. The shape is stable here at Q = 0 μL/min because the magnetic pressure is significantly larger than the Laplace pressure and gravity. The stable deformations at $Q > 0$ μL/min then stems from the balance of viscous stress and magnetic pressure.

4.7 Conclusion

In conclusion, we studied the interaction of magnetic stresses, viscous stress and Laplace pressure in a cylindrical liquid-in-liquid flow arrangement. The system stabilises a liquid cylinder in a liquid environment, mitigating the failure mode of hydrodynamic flow focusing and completely avoiding the dripping mode of failure in co-flowing liquid streams, as there is no lower limit on flow rate[36]. The balance of magnetic pressure and viscous stress further allowed us to form a soft liquid-in-liquid nozzle of mm and sub-mm ($d_{min} = 96 \pm 6\ \mu$m) sizes which can find applications in bio-printing. We identified two length scales l_d (ratio of viscous and magnetic parameters) and l_s (ratio of viscous and interfacial tension parameters) such that l_d governs the softness/deformations of the flow channel under a critical flow rate Q_c governed by $(l_d^5/l_s^3)^{\frac{1}{2}}$. The stable continuous liquid-liquid interface also reduces the shear stress compared to Poiseuille flow, which is required in medical applications and pharmaceutical research with potential applications in transport of biological cells, drug delivery and mimicking bio-interfaces. Moreover, beyond straight antitubes, complex flow structures can be stabilised at mm as well as at microfluidic length scales for mimicking soft bio-interfaces. Our understanding could pave the way for soft microfluidics with stable liquid walls for technological and biological applications.

4.8 Contributions

Arvind Arun Dev (AAD), Bernard Doudin (BD) conceptualised the project. AAD did the experiments in Hermans Lab with supervision of Thomas Hermans (TH) and BD. AAD did the tomography experiments at the Institut Charles Sadron, Strasbourg, France with Antonie Egele and Damien Favier. AAD and BD developed the analytical model. The research article is under preperation.

Bibliography

[1]O. Vincent and P. Marmottant, "On the statics and dynamics of fully confined bubbles", en, Journal of Fluid Mechanics **827**, Publisher: Cambridge University Press, 194–224 (2017).

[2]J. B. Grotberg and O. E. Jensen, "Biofluid Mechanics in Flexible Tubes", Annual Review of Fluid Mechanics **36**, _eprint: https://doi.org/10.1146/annurev.fluid.36.050802.121918, 121–147 (2004).

[3]M. K. S. Verma and V. Kumaran, "A dynamical instability due to fluid–wall coupling lowers the transition Reynolds number in the flow through a flexible tube", en, Journal of Fluid Mechanics **705**, Publisher: Cambridge University Press, 322–347 (2012).

[4]J. M. Skotheim and L. Mahadevan, "Soft Lubrication", Physical Review Letters **92**, Publisher: American Physical Society, 245509 (2004).

[5]J. Bico, B. Roman, L. Moulin, and A. Boudaoud, "Elastocapillary coalescence in wet hair", en, Nature **432**, Number: 7018 Publisher: Nature Publishing Group, 690–690 (2004).

[6]A. E. Hosoi and L. Mahadevan, "Peeling, Healing, and Bursting in a Lubricated Elastic Sheet", Physical Review Letters **93**, Publisher: American Physical Society, 137802 (2004).

[7]D. Pihler-Puzović, P. Illien, M. Heil, and A. Juel, "Suppression of Complex Fingerlike Patterns at the Interface between Air and a Viscous Fluid by Elastic Membranes", Physical Review Letters **108**, Publisher: American Physical Society, 074502 (2012).

[8]P. Polygerinos, N. Correll, S. Morin, B. Mosadegh, C. Onal, K. Petersen, M. Cianchetti, M. Tolley, and R. Shepherd, "Soft robotics: review of fluid-driven intrinsically soft devices; manufacturing, sensing, control, and applications in human-robot interaction: review of fluid-driven intrinsically soft robots", Advanced Engineering Materials **19**, e201700016 (2017).

[9]N. Chronis, G. L. Liu, K.-H. Jeong, and L. P. Lee, "Tunable liquid-filled microlens array integrated with microfluidic network", EN, Optics Express **11**, Publisher: Optica Publishing Group, 2370–2378 (2003).

[10]T. Thorsen, S. J. Maerkl, and S. R. Quake, "Microfluidic Large-Scale Integration", Science **298**, Publisher: American Association for the Advancement of Science, 580–584 (2002).

[11]M. A. Unger, H.-P. Chou, T. Thorsen, A. Scherer, and S. R. Quake, "Monolithic Microfabricated Valves and Pumps by Multilayer Soft Lithography", Science **288**, Publisher: American Association for the Advancement of Science, 113–116 (2000).

[12]F. Box, G. G. Peng, D. Pihler-Puzović, and A. Juel, "Flow-induced choking of a compliant Hele-Shaw cell", en, Proceedings of the National Academy of Sciences **117**, Publisher: National Academy of Sciences Section: Physical Sciences, 30228–30233 (2020).

[13]D. C. Leslie, C. J. Easley, E. Seker, J. M. Karlinsey, M. Utz, M. R. Begley, and J. P. Landers, "Frequency-specific flow control in microfluidic circuits with passive elastomeric features", en, Nature Physics **5**, Bandiera_abtest: a Cg_type: Nature Research Journals Number: 3 Primary_atype: Research Publisher: Nature Publishing Group, 231–235 (2009).

[14]E. W. Lam, G. A. Cooksey, B. A. Finlayson, and A. Folch, "Microfluidic circuits with tunable flow resistances", Applied Physics Letters **89**, Publisher: American Institute of Physics, 164105 (2006).

[15]J. W. Bush and D. L. Hu, "Walking on water: biolocomotion at the interface", Annual Review of Fluid Mechanics **38**, 339–369 (2006).

[16]X. Zhang, J. Zhao, Q. Zhu, N. Chen, M. Zhang, and Q. Pan, "Bioinspired aquatic microrobot capable of walking on water surface like a water strider", ACS Applied Materials & Interfaces **3**, PMID: 21650460, 2630–2636 (2011).

[17]F. Xia and L. Jiang, "Bio-inspired, smart, multiscale interfacial materials", Advanced Materials **20**, 2842–2858 (2008).

[18]D. Feldmann, R. Das, and B.-E. Pinchasik, "How can interfacial phenomena in nature inspire smaller robots", Advanced Materials Interfaces **8**, 2001300 (2021).

[19]S. R. Waitukaitis and H. M. Jaeger, "Impact-activated solidification of dense suspensions via dynamic jamming fronts", Nature **487**, 205–209 (2012).

[20]R. Niu, M. Ramaswamy, C. Ness, A. Shetty, and I. Cohen, "Tunable solidification of cornstarch under impact: how to make someone walking on cornstarch sink", Science Advances **6**, eaay6661 (2020).

[21]P. Reis, J. Hure, S. Jung, J. Bush, and C. Clanet, "Grabbing water", Soft Matter **6**, `10.1039/C0SM00895H` (2012).

[22]S. Karpitschka, A. Pandey, L. A. Lubbers, J. H. Weijs, L. Botto, S. Das, B. Andreotti, and J. H. Snoeijer, "Liquid drops attract or repel by the inverted cheerios effect", Proceedings of the National Academy of Sciences **113**, 7403–7407 (2016).

[23]Y. Ma, J. Choi, A. Hourlier-Fargette, Y. Xue, H. U. Chung, J. Y. Lee, X. Wang, Z. Xie, D. Kang, H. Wang, S. Han, S.-K. Kang, Y. Kang, X. Yu, M. J. Slepian, M. S. Raj, J. B. Model, X. Feng, R. Ghaffari, J. A. Rogers, and Y. Huang, "Relation between blood pressure and pulse wave velocity for human arteries", en, Proceedings of the National Academy of Sciences **115**, Publisher: National Academy of Sciences Section: Physical Sciences, 11144–11149 (2018).

[24]R. Vaia and J. Baur, "Adaptive composites", Science **319**, 420–421 (2008).

[25]P. Sehgal, M. Ramaswamy, I. Cohen, and B. J. Kirby, "Using acoustic perturbations to dynamically tune shear thickening in colloidal suspensions", Phys. Rev. Lett. **123**, 128001 (2019).

[26]W. Weng, P. Chen, S. He, X. Sun, and H. Peng, "Smart electronic textiles", Angewandte Chemie International Edition **55**, 6140–6169 (2016).

[27]H. Kuroki, I. Tokarev, and S. Minko, "Responsive surfaces for life science applications", Annual Review of Materials Research **42**, 343–372 (2012).

[28]M. D. Bartlett, "Liquid assets for soft electronics", Nature Materials **20**, 714–715 (2021).

[29]C. Shi, Z. Zou, Z. Lei, P. Zhu, W. Zhang, and J. Xiao, "Heterogeneous integration of rigid, soft, and liquid materials for self-healable, recyclable, and reconfigurable wearable electronics", Science Advances **6**, eabd0202 (2020).

[30]J. H. Koo, D. C. Kim, H. J. Shim, T.-H. Kim, and D.-H. Kim, "Flexible and stretchable smart display: materials, fabrication, device design, and system integration", Advanced Functional Materials **28**, 1801834 (2018).

[31]S. Arora, A. Srinivasan, A. Leung, and Y.-C. Toh, "Bio-mimicking shear stress environments for enhancing mesenchymal stem cell differentiation", Current Stem Cell Research Therapy **15**, `10.2174/1574888X15666200408113630` (2020).

[32]A. A. Dev, R. Dey, and F. Mugele, "Behaviour of flexible superhydrophobic striped surfaces during (electro-)wetting of a sessile drop", en, Soft Matter **15**, Publisher: The Royal Society of Chemistry, 9840–9848 (2019).

[33]P. Karan, S. S. Das, R. Mukherjee, J. Chakraborty, and S. Chakraborty, "Flow and deformation characteristics of a flexible microfluidic channel with axial gradients in wall elasticity", en, Soft Matter **16**, Publisher: The Royal Society of Chemistry, 5777–5786 (2020).

[34]S. Li, H. Bai, R. Shepherd, and H. Zhao, "Bio-inspired design and additive manufacturing of soft materials, machines, robots, and haptic interfaces", Angewandte Chemie International Edition **58**, `10.1002/anie.201813402` (2019).

[35]L. Rayleigh, "On the stability, or instability, of certain fluid motions", Proceedings of the London Mathematical Society **s1-11**, 57–72 (1879).

[36]A. S. Utada, A. Fernandez-Nieves, H. A. Stone, and D. A. Weitz, "Dripping to jetting transitions in coflowing liquid streams", Phys. Rev. Lett. **99**, 094502 (2007).

[37]M. Song, K. Kartawira, K. D. Hillaire, C. Li, C. B. Eaker, A. Kiani, K. E. Daniels, and M. D. Dickey, "Overcoming rayleigh–plateau instabilities: stabilizing and destabilizing liquid-metal streams via electrochemical oxidation", Proceedings of the National Academy of Sciences **117**, 19026–19032 (2020).

[38]Z. Niroobakhsh, J. A. LaNasa, A. Belmonte, and R. J. Hickey, "Rapid stabilization of immiscible fluids using nanostructured interfaces via surfactant association.", Physical review letters **122 17**, 178003 (2019).

[39]A. A. Dev, P. Dunne, T. M. Hermans, and B. Doudin, "Fluid drag reduction by magnetic confinement.", Langmuir : the ACS journal of surfaces and colloids (2022).

[40]A. Ahmed, I. Hassan, I. M. Mosa, E. Elsanadidy, M. Sharafeldin, J. F. Rusling, and S. Ren, "An ultra-shapeable, smart sensing platform based on a multimodal ferrofluid-infused surface", Advanced Materials **31**, 1807201 (2019).

[41]X. Zhang, L. Sun, Y. Yu, and Y. Zhao, "Flexible ferrofluids: design and applications", Advanced Materials **31**, 1903497 (2019).

[42]J. V. I. Timonen, M. Latikka, L. Leibler, R. H. A. Ras, and O. Ikkala, "Switchable static and dynamic self-assembly of magnetic droplets on superhydrophobic surfaces", Science **341**, 253–257 (2013).

[43]W. Wang, J. Timonen, A. Carlson, D.-M. Drotlef, C. Zhang, S. Kolle, A. Grinthal, T. S. Wong, B. Hatton, S. Kang, S. Kennedy, J. Chi, R. Blough, M. Sitti, L. Mahadevan, and J. Aizenberg, "Multifunctional ferrofluid-infused surfaces with reconfigurable multiscale topography", Nature **559**, `10.1038/s41586-018-0250-8` (2018).

[44]P. Dunne, T. Adachi, A. A. Dev, A. Sorrenti, L. Giacchetti, A. Bonnin, C. Bourdon, P. H. Mangin, J. M. D. Coey, B. Doudin, and T. M. Hermans, "Liquid flow and control without solid walls", Nature **581**, 58–62 (2020).

[45]A. A. Dev, R. Dey, and F. Mugele, "Behaviour of flexible superhydrophobic striped surfaces during (electro-)wetting of a sessile drop", Soft Matter **15**, 9840–9848 (2019).

[46]S. Haefner, M. Benzaquen, O. Bäumchen, T. Salez, R. Peters, J. Mcgraw, K. Jacobs, E. Raphael, and K. Dalnoki-Veress, "Influence of slip on the plateau-rayleigh instability on a fibre", Nature communications **6**, `10.1038/ncomms8409` (2015).

[47]B. Roman and J. Bico, "Elasto-capillarity: deforming an elastic structure with a liquid droplet", Journal of physics. Condensed matter : an Institute of Physics journal **22**, 493101 (2010).

[48]S. Chandrasekhar, *Hydrodynamic and hydromagnetic stability* (Dover Publications, 1961).

Chapter 5

Towards Bio-Applications and Bio-mimicking

5.1 Introduction

Microfluidics is extensively used in medical research because they can handle small volume of liquids, usually required in disease diagnostic[1] and drug delivery[2]. Beyond a transfer line used for flow of liquids, microfluidics plays a crucial role in mimicking organs on chip[3], bio-devices, biological interfaces, biological flow environment[4]. The bio-liquids in the bio-flow environment are complex as they are made up of contents which can change shape (like red blood cells (RBC)[5]) to impart non-Newtonian characteristics, here specifically blood. The non-Newtonian behavior means deviation from the Newton's law of viscosity, which assumes a linear relationship between applied stress and shear rate. Fig.5.1 a) show viscosity curves of blood from different species. Blood is a shear thinning liquid and at higher shear rate[6], the non-newtonian behavior comes form deformations of RBCs[5]. Microfluidic channels following Poiseuille's law are used to mimic the shear stress/shear rate found in blood carrying arteries. The flow of blood in arteries is time dependent and pulsatile and the blood carrying conduits are soft and they deform. The combination of soft flow channel and pulsatile flow results in pressure pulses shown in Fig.5.1 b). Pressure pulses in three different arteries show different pressure relaxation: femoral arteries have smaller peak pressure and flatter curve compared to dorsalis pedis and radial artery. To mimic this pressure relaxation behavior, microfluidic channels with different elasticity are required and made up of soft polymers used to capture the deformable environment.

However, with decreasing size of the flow channel, larger power (or pressure) required to deform the channel is unavoidable. Furthermore, complex flow channel shapes beyond simple cylindrical geometry are needed to mimic blood flow geometries, for example to investigate arterial thrombosis (Fig.5.1 c)) related to a formation of blood clot in an artery.

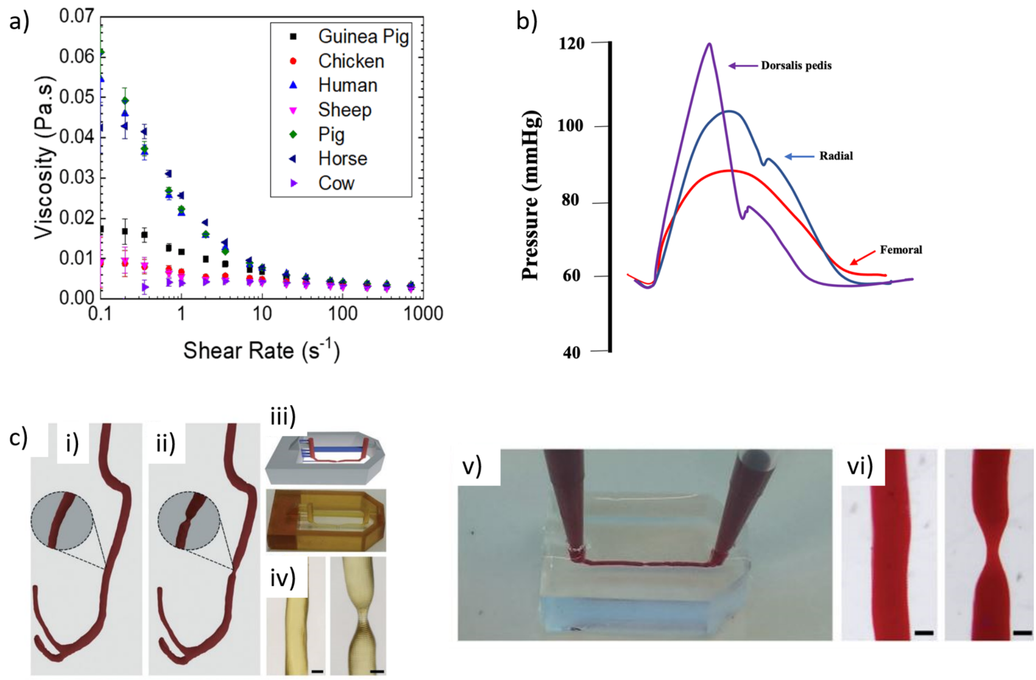

FIGURE 5.1: Biological environment and flow behavior of blood. a) Non-Newtonian (shear thinning) viscosity of blood (different species) with increasing shear rate $\dot{\gamma}$[6], b) Pressure pulse in different arteries due to pulsating flow of blood, c) Mimicking arterial thrombosis using microfluidics[7], i)-ii) show healthy and stenotic blood vessel with magnified region in inset, iii)-iv) show the 3D printed mold, printed flow channel respectively , v)-vi) show microfluidic channel with red food dye.

The clot effects the deformation of the arteries as well as hamper proper flow of blood, with resulting diseases like heart attack, transient ischaemic attack (TIA) and critical limb ischaemia to name a few. Fig.5.1 c)-i)-ii) show the schematic of a healthy and stenotic blood vessel. The shape is reproduced by means of a 3D printed mould (Fig.5.1 c)-iii) top) followed by soft lithography using PDMS to define the flow channel (Fig.5.1 c)-iii) bottom). Fig.5.1 c)-iv) show the healthy and stenotic flow channel. Fig.5.1 c)-v)-vi) show the microfluidic channel with coloured food dye. Owing to the vast potential medical applications, there is a need for a new design of microfluidic channel with ease of deformablity with small pressure and mimicking complex (arbitrary) shape flow channel.

The formost important requirement is bio compatibility environment. We show here preliminary experiments with biological cells to ensure the suitability of magnetic lubrication for bio-applications.

The bio-compatibility of the biological cells with the ferrofluid used is a limiting factor, however there are various bio-compatible ferrofluid available commercially based on various carrier liquid like mineral oil (from Qfluidics) We performed a proof of concept experiment for cardiomyocyte (primary cells) . We flow the primary cells through the liquid tube with

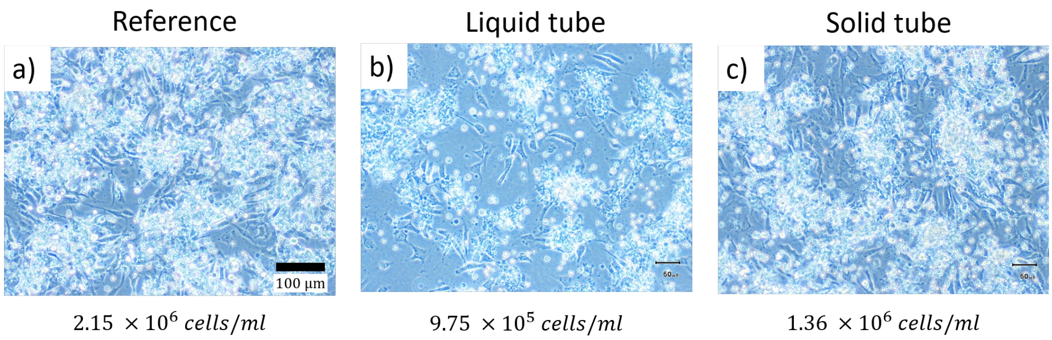

FIGURE 5.2: Primary cells cardiomyocyte in a) Reference, b) Liquid tube, and c) Solid tube.

design of the flow channel as shown in Chapter 2. The ferrofluid used is from Qfluidics with viscosity 144 mPa.s. The flow rate is 100 μl/min through a diameter of 1 mm. The cardiomyoctyte were developed in a petri dish, taken in the syringe, pumped through the liquid tube, collected in petri dish, developed under 37 °c and counted. Fig.5.2 a) shows cardiomyocytes grown in a petri dish as reference, passed through a liquid tube (Fig.5.2 b)) and passed through a solid tube (Fig.5.2 c)). The elongated cells sticking at the bottom of the petri dish depicts the live cells. We can see that the ferrofluid does not deteriorate the health of the primary cells, though we see reduction in the number of cells. A detailed study on biocompatibility is required depending on the many biological factors, however that is beyond the scope of this thesis. However, with the initial bio compatibility experiments and the bank of commercial ferrofluid available, the magnetically confined liquid tubes can be considered of high potential for mimicking biological scenarios.

Here we present the bio-mimicking capability and features of the magnetically confined microchannels, to the characteristics of blood vessels, where non-Newtonian liquids , tunable pressure relaxation and deformable microchannels with complex shapes are key.

5.2 Non-Newtonian liquid

Non-Newtonian liquids are defined as liquids with non-linear stress-strain rate relationship. One of the non-linear function is the power law. The power law relation between stress (τ) and strain rate ($\dot{\gamma}$) is given by

$$\tau = K\dot{\gamma}^n \tag{5.1}$$

and the viscosity η is given by

$$\eta = K\dot{\gamma}^{n-1} \tag{5.2}$$

Here we extend the analytical model of fluid flow in a liquid tube (Chapter 2) by considering the non-Newtonian behavior of magnetic as well as non-magnetic liquids. The Stokes equation governing the flow of the non-Newtonian liquid reads as

$$\frac{-\partial P^\star}{\partial z^\star} = \frac{1}{Re r^\star}\frac{\partial}{\partial r^\star}\left[r^\star\left(\frac{-\partial u^\star}{\partial r^\star}\right)^n\right] \tag{5.3}$$

where $u^\star = u/u_m$, $r^\star = r/d_0$ are dimensionless velocity and coordinates scaled by the average velocity u_m and the diameter of flow d_0, respectively. The dimensionless pressure is defined as $P^\star$=$P/\rho u_m^2$ and the Reynolds numbers, $Re = \frac{\rho u_m d_0}{K\left(\frac{u_m}{d_0}\right)^{n-1}}$. Note that if $n = 1$, we have the case of Newtonian liquid and then $K = \eta$. For liquid tube and ferrofluid, $n = c_h$ and $n = c_f$ respectively. With these nondimensional quantities, the friction factor for a non-Newtonian liquid flow through a solid wall tube is given by

$$f_{pNN} = \frac{4}{Re\left[\frac{8}{1+c_h}\left(\left(\frac{1}{2}\right)^{\frac{1}{c_h}+4} - \frac{\left(\frac{1}{2}\right)^{\frac{1}{c_h}+3}}{\frac{1}{c_h}+3}\right)\right]^{c_h}} \tag{5.4}$$

For a flow through a liquid tube of diameter d, Eq.5.3 is solved with the boundary conditions

$$r^\star = 0 \quad , \quad \frac{\partial u^\star}{\partial r^\star} = 0 \tag{5.5}$$

$$r^\star = \frac{D}{2d} \quad , \quad u_f^\star = 0 \tag{5.6}$$

$$r^\star = \frac{1}{2} \quad , \quad u_f^\star = u^\star \tag{5.7}$$

$$r^\star = \frac{1}{2} \quad , \quad K_h\left(\frac{u_m}{d_0}\right)^{c_h}\left(\frac{-\partial u^\star}{\partial r^\star}\right)^{c_h} = K_f\left(\frac{u_m}{d_0}\right)^{c_f}\left(\frac{-\partial u^\star}{\partial r^\star}\right)^{c_f} K_f\left(\frac{-\partial u}{\partial r}\right)^{c_f} \tag{5.8}$$

$$Q = 0 \quad , \quad \int_{\frac{1}{2}}^{\frac{D}{2d}} u_f^\star \; 2\pi r^\star = 0 \tag{5.9}$$

The velocity profile of the non-Newtonian liquid tube is given by

$$u^\star(r^\star) = \left(\frac{Ref}{4}\right)^{\frac{1}{4}} \frac{1}{\frac{1}{c_h}+1}\left[\left(\frac{1}{2}\right)^{\frac{1}{c_h}+1} - r^{\star\frac{1}{c_h}+1}\right] \tag{5.10}$$

from which the friction factor f_{ANN} can be calculated from

$$\left[8\left(\frac{Ref_{ANN}}{4}\right)^{\frac{1}{c_h}}\frac{1}{\frac{1}{c_h}+1}\left((\frac{1}{2})^{\frac{1}{c_h}+4}-\frac{\left(\frac{1}{2}\right)^{\frac{1}{c_h}+3}}{\frac{1}{c_h}+3}\right)+\left(\frac{Ref_{ANN}}{8}\frac{K_h}{K_f}\right)^{\frac{1}{c_f}}\frac{a_4}{\left(\frac{u_m}{d_0}\right)^{\frac{c_f-c_h}{c_f}}}\right]=1 \tag{5.11}$$

with

$$a_4=\frac{-1}{2(a_2/a_3+1)}\left[\frac{a_2}{2a_3}\left(1-\left(\frac{D}{d}\right)^2\right)+\ln\left(\frac{1}{2}\right)-\ln\left(\frac{D}{2d}\right)\right] \tag{5.12}$$

$$a_3=\left(\frac{D}{2d}\right)^4-\frac{1}{16}-2\left(\frac{D}{2d}\right)^2\left(\left(\frac{D}{2d}\right)^2-\frac{1}{4}\right) \tag{5.13}$$

$$a_2=\left(\left(\frac{D}{2d}\right)^2-\frac{1}{4}\right)\ln\left(\frac{D}{2d}\right)-a_1 \tag{5.14}$$

$$a_1=\left(\left(\frac{D}{2d}\right)^2-\frac{1}{4}\right)\ln\left(\frac{D}{2d}\right)-a_1 \tag{5.15}$$

The drag reduction is given by

$$DR=\frac{f_{pNN}-f_{ANN}}{f_{pNN}} \tag{5.16}$$

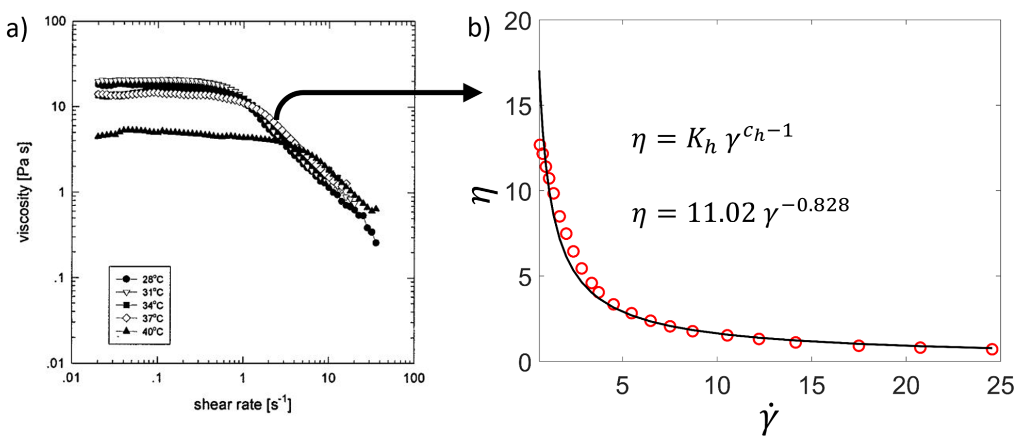

FIGURE 5.3: Non-Newtonian liquid with mixture of cetyltrimethylammonium bromide (CTAB) and Sodium salicylate (NaSal) forming miscelle structures[8], a) Decreasing viscosity with increasing shear rate , b) Fitted power law function to the viscosity data in Fig.5.3 a)

To demonstrate the features of a non-Newtonian, shear thinning magnetically confined liquid tube, we choose a mixture of cetyltrimethylammonium bromide (CTAB) and Sodium salicylate (NaSal) at temperature 37 °C as working fluid[8]. The viscosity of CTAB+NaSal viscosity decreases with increasing shear rate as shown in Fig.5.3 a). Fig.5.3 b) shows a fit to one of the data set (37 °C) in Fig.5.3 a). The fit is used to define the non-Newtonian liquid in the model and the resulting friction factors are shown in Fig.5.4 a). f_{pNN} , f_{AN} and f_{ANN} are friction factors (f). The subscript denote, solid wall Poiseuille flow of a non-Newtonian liquid (pNN) , Newtonian liquid under magnetic confinement (AN) and non-Newtonian liquid magnetic confinement (ANN). At small flow rate (small shear rate), the difference between friction factors of the Newtonian and the non-Newtonian liquid is minuscule (blue and black markers). However with increasing flow rate, the shear rate increases and the dif-

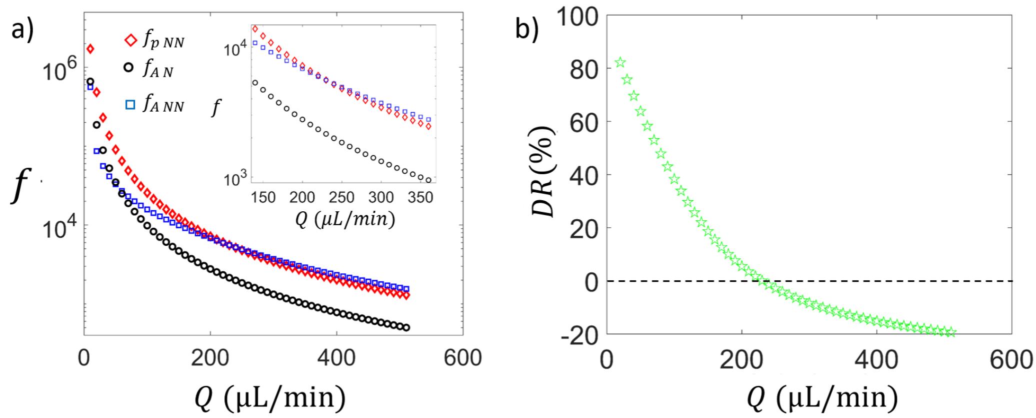

FIGURE 5.4: Friction factors. a) Friction factor for non-Newtonian liquid in solid wall tube (f_{pNN}), non-Newtonian liquid in magnetically confined liquid tube (f_{ANN}) and Newtonian liquid in liquid tube (f_{AN}), b) Drag reduction for non-Newtonian liquid following Eq.5.16

ference in the friction factor increases. This is due to the decrease of viscosity and therefore viscosity ratio η_r of non-Newtonian shear thinning liquid with increasing flow (or shear) rate. Comparing the two non-Newtonian cases, f_{pNN} and f_{ANN} (red and blue markers) shows that for a flow rate $Q < 250$ μL/min, $f_{pNN} > f_{ANN}$ however for $Q > 250$ μL/min, the $f_{pNN} < f_{ANN}$. Inset shows the crossover with flow rate. If we consider only the viscous drag, then flowing of a non-Newtonian liquid is only beneficial below a threshold flow rate above which the decrease in viscosity due to increase shear stress is helpful in pumping. Fig.5.4 b) shows that the drag reduction following Eq.5.16 is negative (drag penalty) for $Q > 250$ μL/min.

It is very intuitive that for the non-Newtonian liquid, for a flow rate Q, the change of viscosity (from the initial viscosity) will be higher in a solid wall tube than in the liquid tube. This is due to the lower shear in the liquid tube. Hence apparently the liquid tube suppresses/tunes the non-Newtonian behavior. Moreover since the choice of ferrofluids can tailor the shear stress, hence the non-Newtonian behavior can therefore be tuned. The velocity profile and shear rate of a non-Newtonian liquid in a solid tube and liquid tube are

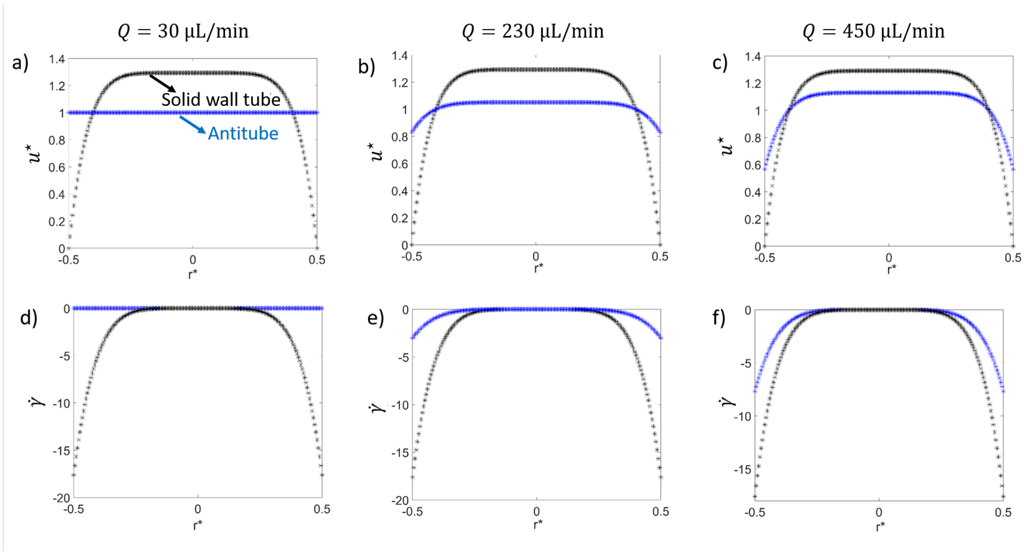

FIGURE 5.5: Velocity profile and shear rate in magnetically confined liquid tube and solid tube. a) , b) and c) show the velocity profile with increasing flow rate, d), e), f) show shear rate with increasing flow rate.

shown in Fig.5.5. At low flow rate, 30 μL/min the velocity $u^{\star}$ is plug like (Fig.5.5 a)) for a liquid tube and a higher order polynomial shape for a solid tube. This is because of very small shear in the liquid tube (Fig.5.5 d)). On increasing the flow rate, the velocity profile turns more like the solid tube (Fig.5.5 b), c)). This is because with increasing flow rate Q, the shear rate increases in liquid tube (Fig.5.5 e), f)) which decreases the viscosity ratio η_r and hence in contrast to Newtonian liquids, the shear rate and drag reduction depends on flow rate (Fig.5.4).

5.3 Pressure damping

To highlight the possibility of mimicking the pressure relaxation in arteries, we record the pressure of the glycerol liquid tube at the inlet of the flow channel during the relaxation, when the flow is stopped. The schematics of the experimental setup are described in chapter 2. Fig.5.6 shows the pressure (at inlet) profile for glycerol-APG314 ferrofluid system. The flow rate is increased in steps, resulting in increasing pressures and then the flow is stopped to record the decrease of pressure with time. To better characterize the pressure relaxation in liquid tube, we used three different ferrofluids namely APG314, APGE32 and APG1141 to have different magnetic and fluid properties. Since the maximum experimental pressure is different in different ferrofluid system, the pressure is nondimensionalised as

$$P^{\star} = \frac{P - P_{min}}{P_{max} - P_{min}} \tag{5.17}$$

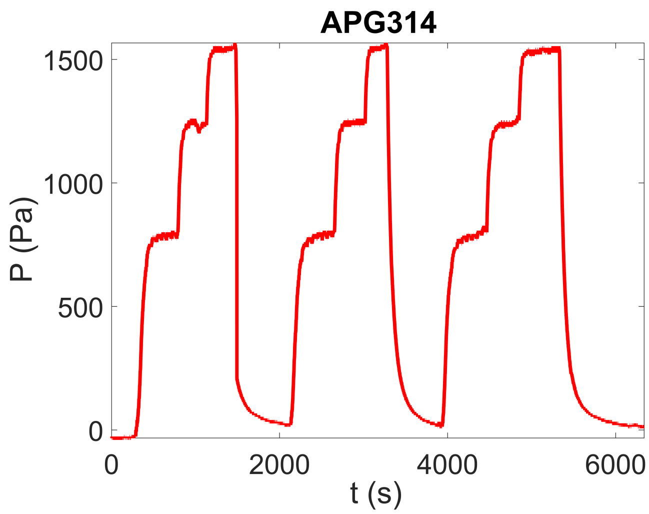

FIGURE 5.6: Pressure vs time at inlet of the flow channel (Glycerol-APG314), increased in steps, three cycles.

Fig.5.7 shows the decrease of pressure with time for different ferrofluids and initial diameters d_0 of the liquid tube. The relaxation time is shortest for ferrofluid APG314 with the smallest viscosity η_f = 0.23 Pa.s (Fig.5.7 a)). The relaxation time increases with the increase in η_f for ferrofluids APGE32 and APG1141 respectively (Fig.5.7 b) , c)). The pressure relaxation time is also observed to be dependent on initial flow diameter (d_0), as illustrated in Fig.5.7 a) , b) , c). Fig.5.8 show the pressure profiles for similar flow diameters and different ferrofluids marked in legend by their viscosity η_f. The relaxation time is larger for small d_0. Note that similar behavior is also observed in deformation of the liquid tube: the deformation of the liquid tube increases with decresing d_0 and decreasing viscosity ratio η_r (larger η_f). Intuitively, the pressure relaxation should follow the deformation dynamics, the volume of ferrofluid should return to the initial shape for pressure to relax completely.

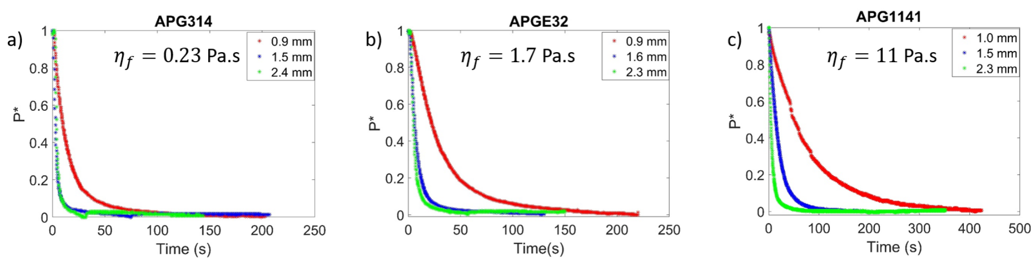

FIGURE 5.7: Pressure relaxation for different no flow diameter d_0 and viscosity of ferrofluid η_f, a) APG314 , b) APGE32, c) APG1141.

In order to get a quantitative estimate of the pressure relaxation time, we must consider the unsteady Navier-Stokes equation under limit of low Re. We limit our self to a qualitative understanding. For doing so, we assume that the pressure relaxation will follow the

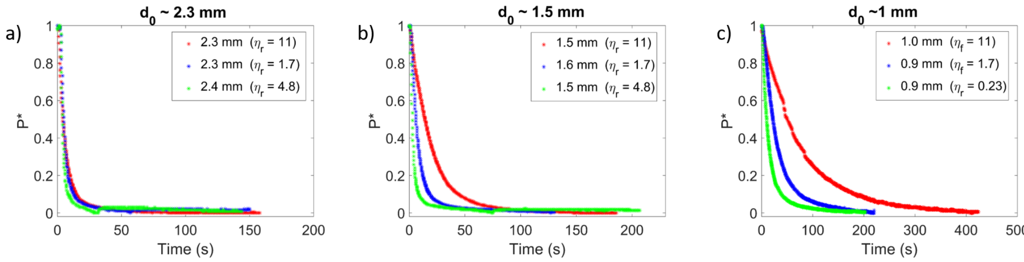

FIGURE 5.8: Pressure relaxation for similar no flow diameter d_0 and different viscosity of ferrofluid η_f, a)d_0 = 2.3 mm , b) d_0 = 1.5 mm, c) d_0 = 1.0 mm.

deformation dynamics of the liquid tube. The temporal evolution of the deformation of liquid tube shape under pressure can be modelled by the volume conservation equation along with the momentum equation. In order to get a scaling of the relaxation time, considering the volume conservation of the liquid tube

$$\frac{\partial h}{\partial t} + \frac{1}{2\pi h} Q' = 0 \tag{5.18}$$

Non-dimensionalizing Eq.5.18 with $h^* = (h - h_0)/l_d$, $z^* = z/L$, and $t^* = t/\tau_d$ where τ_d is the time scale for relaxation of the liquid tube from the deformed state and Q′ is $\frac{\partial Q}{\partial z}$ with z being the direction of relaxation (or flow) obtained from Eq.4.18. From the non-dimensional form of Eq.5.18, the relaxation time scale τ_d is given by

$$\tau_d = \frac{8\pi\eta_f}{\mu_0 M_s M_r} \frac{W}{d_0} \frac{L}{D} \tag{5.19}$$

Note that we have neglected the surface tension parameters, as the contribution of the Laplace pressure is much less than the magnetic pressure (Fig.4.8). The relaxation time is inversely proportional to d_0 and directly proportional to $\eta_f/\mu_0 M_s M_r$ which captures the change of relaxation time with different d_0 and different ferrofluid respectively.

5.4 Towards mimicking deformable arteries of complex shapes

Blood carrying compliant conduits in human body ranges from large arteries with diameter 2.4 cm to smallest capillaries of diameter 4 μm[9]. The Reynolds number (Re) in these ducts also varies from 0.001 to greater than 2000. Table 1 shows the blood carrying arteries key properties[9] and possible ferrofluid system to study the flow phenomena based on presented experiments and model. The density and viscosity of blood is considered as 0.994 kg/m^3 and 0.005 Pa.s respectively.

The ferrofluid system of APG314, APGE32, APG1141 and EMG900 with glycerol as the liquid tube under limit $Re < 1$ could possibly be used to mimick the flow behavior of/in pial, cartoid and arterioles arteries. Fig.5.9 a) shows the non-dimensionalised quantity of liquid

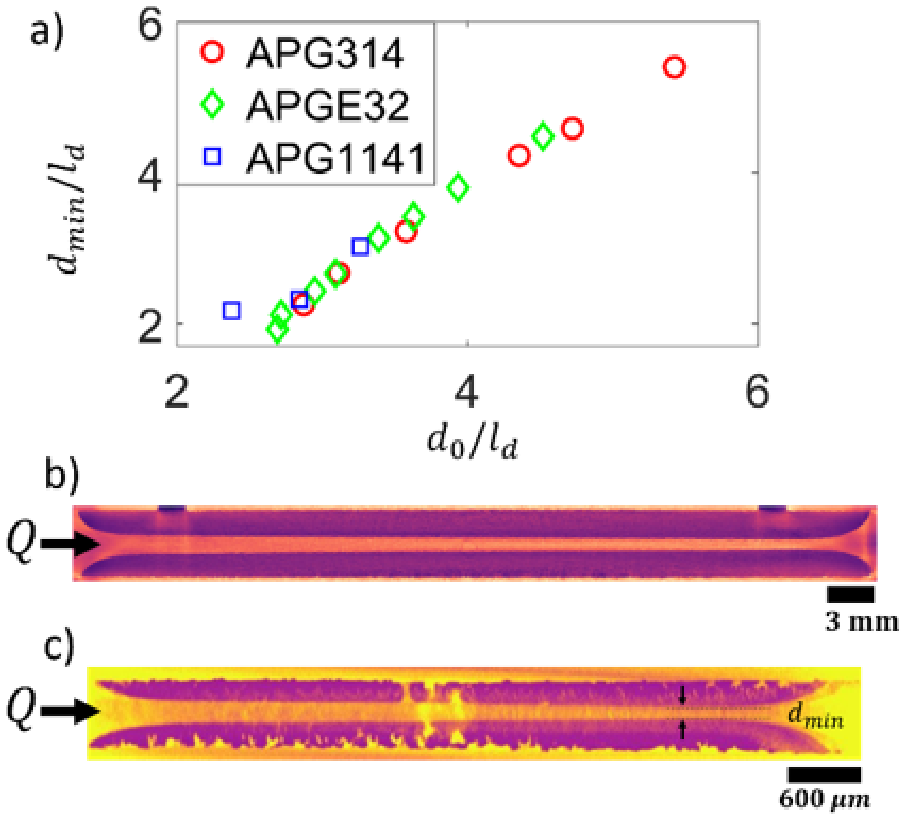

FIGURE 5.9: Towards deformable microfluidics. a) Experimental non-dimensionalised undeformed diameter d_0/l_d and minimum diameter after deformation, d_{min}/l_d for all the cases below Q_c. l_d is the deformation length scale. The line is a linear fit. b) Liquid nozzle with Glycerol-APGE32, d_{min} = 0.5 mm, W = 6 mm, c) Liquid nozzle with Glycerol-EMG900 (η_r = 10), d_{min} = 96 ± 6 μm, W = 0.9 mm.

tube deformation with l_d as the deformation length scale for flowrate below Q_c. d_{min} and d_0 denotes the minimum diameter after deformation and initial no flow constant diameter respectively. Different combinations of magnetic and viscous stresses can be represented by a single parameter l_d. Understanding this, the concept can be extended for soft stable microfluidics, Fig.5.9 b) (Glycerol-APGE32, η_r = 0.65, Q = 100 μL/min, d_{min}=0.5 mm), Fig.5.9 b) c) (Glycerol-EMG900, η_r = 10 , Q = 10 μL/min, d_{min} = 96 ± 6 μm). Furthermore the deformed liquid tube can also act as act as a fluid nozzle with small shear stress required in bio-printing applications. We highlighted here quantitative data and understanding for the arteries with $Re < 1$ as our experiments are limited to the cases where $Re < 1$.

5.5 Beyond low Reynolds number (Re) DC flow: Oscillating flows at high Re

One of the major limitation of flow focusing (liquid in liquid flow) is that it can only stabilize time invariant flow rate, DC flow analogous to DC current. However, the need of time variant flow is increasing, specially in the context of lab on a chip and organ-on-chip studies. We have shown that the magnetic confinement of liquid tube stabilizes the PRI by deforming the liquid tube. The stability depends on the ratio of two length scales l_d and l_s such that the minimum radius of flow $h_{min} > 2\left(\frac{l_d^5}{l_s^2}\right)^{\frac{1}{2}}$ (Eq.4.34) for DC flow. Following this stability condition, beyond DC flow, oscillating flow at high Reynolds number could also be stabilized. For large Reynolds number flow $Re > 1000$ in arteries and aorta, we present qualitative data and based on our understanding some appropriate combination of magnetic and non-magnetic liquid (Water with EMG905). Fig.5.10 show the details of oscillating

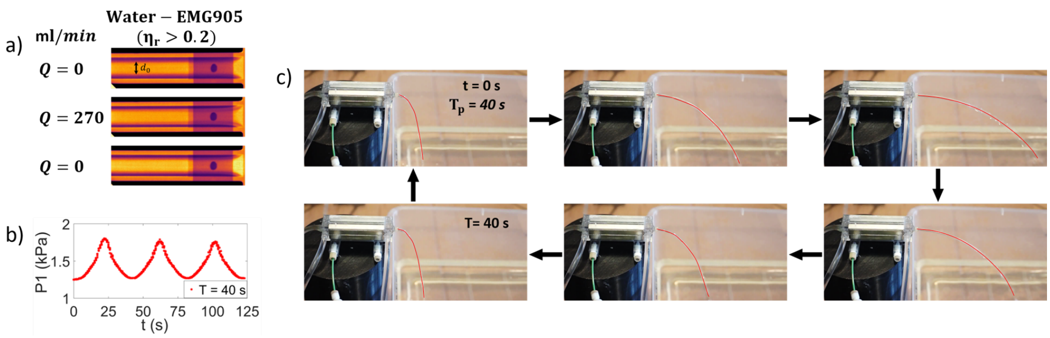

FIGURE 5.10: Oscillating flows in liquid tube. a) X-ray image of the stable system with and without flow, b) Pressure at inlet of the liquid tube during oscillating flow (Q_{max} at the peak of the curve is 250 ml/min), the liquid tube diameter is 2.4 mm, c) Snapshots at different time interval of the oscillating flow. The time period of sinosoidal oscillation is 40 s. A video showing stable flow through the liquid tube for all time period of oscillations (T = 10 s, 20s, 40s) is presented in AppendixA-V3

flow in the liquid tube. The oscillating pressure is imposed using an OB1 pressure pump from Elveflow with a time period of 10 s, 20 s and 40 s. Fig.5.10 b) shows the pressure profile with T = 40 s measured at the inlet of the flow channel (design same as used Chapter 4, Fig.4.2). The cyclic images (Fig.5.10 b)) show the stages of oscillating flow due to oscillating pressure, shown by the water jet at outlet (red line highlight the jet profile at outlet). No ferrofluid is sheared with these flow parameters, with largest flow rate during the cycle was Q = 250 mL/min. Fig.5.10 c) show the X-ray images of the liquid tube of diameter d = 2.4 mm with water and EMG905 ferrofluid. The liquid tube slightly deforms at Q = 270 mL/min and regains the shape with Q = 0 mL/min. The Reynolds number for the flow is Re > 2000. Hence it is possible to stabilize high Reynolds number oscillating flow, paving way towards

Arteries	U_{max} (mm/s)	d_{max} (m)	Re_{max}	P_m (MPa)	E (MPa)
Cartoid[11]	1.5	0.002	0.60	0.0130	4
Femoral[9]	70	0.0066	92.12	0.0128	0.8
Large arteries and Aorta[9]			> 1000		

TABLE 5.1: Examples of compliant blood vessels for humans.

mimicking flow of blood in large arteries. Apart for bio-applications, the oscillating flows are also important to make fluid analog of electronic circuits like alternating current and take advantage of their frequency dependent impedance.

5.6 Perspectives

We have shown that the behavior of the flow through magnetically confined non-Newtonian liquid tubes can be tuned, mimicking different blood flow environment. We envisage that the liquid tube microfluidic channel could be used as model system to study the shear responsive biomaterials.

a)

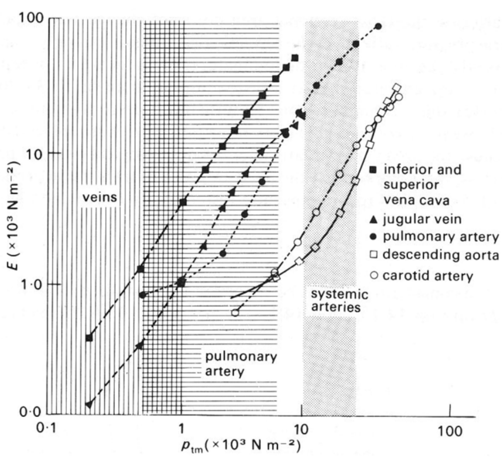

b)

Vessel	Shear stress dyn/cm^2
Arteries	10–60
Veins	1–10
Stenosis in arteries	>100
High Stenosis in arteries	>1,000
Ascending Aorta	12
Descending Aorta	5–8
Pulmonary Artery	5
Small vein	11
Large vein	5

FIGURE 5.11: Behavior of arteries under flow. a) The incremental Young's modulus (E) with transmural pressure (p_{tm}) for a dog[9], b) Shear stress in different human blood vessel[10].

The compliant response and incremental Young's modulus of a flow conduits can also be studied with small pressure requirements, not attainable by current lab-on-chip microfluidic designs. The Young's modulus of blood vessels is not constant and increases with the transmural pressure (p_{tm}) (Fig.5.11 a)[9] for blood vessel of a dog). The shaded portions are the normal operating range. For the liquid tubes, the resistance against deformation is the magnetic pressure, which increases with the the radius h of the liquid tube and the magnitude of transmural pressure shown in Fig.5.11 is attainable using liquid tube (see in

Fig.4.8). The variable Young's modulus is also an essential feature in human blood vessel[12] which exhibits variable shear stress[10] (Fig.5.11 b)). A liquid tube can mimic the shear stress environment as well (See chapter 2 and Chapter 3). Hence a deformable tube with variable stiffness and shear stress is realised, which is hard to get in a elastomer based soft flow channel besides the elastomer based soft flow channels required large pressure to deform the flow channel[13] and their miniaturization is a limiting issue. The liquid tube can be used to mimic complex flow structures and flow hydrodynamic environment. Tab. 5.1 show examples of human blood vessel and their properties which can be mimicked using liquid tube. The cartoid and femoral artery show two different Young's Modulus and two order of Reynolds number (Re). Though we have focused on the flow physics and quantitative details of compliance of liquid tubes with $Re < 1$ and channels sizes of order 1 mm , since the limit for liquid tube systems are only on the smallest sizes[14], larger diameter compliant conduits with high Reynolds number can be realized. The large Re flows can be mimicked using water liquid tube with EMG905 ferrofluid and the low Re flows can use glycerol and APG314 or APG1141 or APGE32 or EMG900 as ferrofluids.

5.7 Contributions

Bernard Doudin (BD) , Thomas Hermans (TH) and Arvind Arun Dev (AAD) conceptualised the project. AAD did the experiments and analytical modelling. AAD did the biocompatibility experiments at MPIDS Germany with the help of biologists. The research article is under preperation.

Bibliography

[1]L. Bourouiba, “The fluid dynamics of disease transmission”, Annual Review of Fluid Mechanics **53**, 473–508 (2021).

[2]S. Damiati, U. B. Kompella, S. A. Damiati, and R. Kodzius, “Microfluidic devices for drug delivery systems and drug screening”, Genes **9**, `10.3390/genes9020103` (2018).

[3]S. Bhatia and D. Ingber, “Microfluidic organs-on-chips.”, Nature Biotechnology **32(8)**, 760–72 (2014).

[4]R. Dong, Y. Liu, L. Mou, J. Deng, and X. Jiang, “Microfluidics-based biomaterials and biodevices”, Advanced Materials **31**, 1805033 (2019).

[5]L. LANOTTE, J. Mauer, S. Mendez, D. a. Fedosov, J.-m. FROMENTAL, V. Claveria, F. Nicoud, G. Gompper, and M. ABKARIAN, “Red cells’ dynamic morphologies govern blood shear thinning under microcirculatory flow conditions”, Proceedings of the National Academy of Sciences of the United States of America **113**, 13289–13294 (2016).

[6]J. S. Horner, N. J. Wagner, and A. N. Beris, “A comparative study of blood rheology across species”, Soft Matter **17**, 4766–4774 (2021).

[7]P. Costa, H. Albers, J. Linssen, H. Middelkamp, L. Hout, R. Passier, A. Van den Berg, J. Malda, and A. van der Meer, “Mimicking arterial thrombosis in a 3d-printed microfluidic: in vitro vascular model based on computed tomography angiography data”, Lab Chip **17**, `10.1039/C7LC00202E` (2017).

[8]Kim and Yang, “Effects of sodium salicylate on the microstructure of an aqueous micellar solution and its rheological responses.”, Journal of colloid and interface science **232 2**, 225–234 (2000).

[9]C. G. Caro, T. J. Pedley, R. C. Schroter, W. A. Seed, and K. H. Parker, *The mechanics of the circulation*, 2nd ed. (Cambridge University Press, 2011).

[10]A. J. A. Leloup, C. E. Van Hove, A. Heykers, D. M. Schrijvers, G. R. Y. De Meyer, and P. Fransen, “Elastic and muscular arteries differ in structure, basal no production and voltage-gated ca2+-channels”, Frontiers in Physiology **6**, `10.3389/fphys.2015.00375` (2015).

[11]M. E. Safar, J. Blacher, J. J. Mourad, and G. M. London, "Stiffness of carotid artery wall material and blood pressure in humans", Stroke **31**, 782–790 (2000).

[12]C. Bussy, P. Boutouyrie, P. Lacolley, P. Challande, and S. Laurent, "Intrinsic stiffness of the carotid arterial wall material in essential hypertensives", **35**, 1049–1054 (2000).

[13]P. Karan, S. S. Das, R. Mukherjee, J. Chakraborty, and S. Chakraborty, "Flow and deformation characteristics of a flexible microfluidic channel with axial gradients in wall elasticity", en, Soft Matter **16**, Publisher: The Royal Society of Chemistry, 5777–5786 (2020).

[14]P. Dunne, T. Adachi, A. A. Dev, A. Sorrenti, L. Giacchetti, A. Bonnin, C. Bourdon, P. H. Mangin, J. M. D. Coey, B. Doudin, and T. M. Hermans, "Liquid flow and control without solid walls", Nature **581**, 58–62 (2020).

Chapter 6

Conclusion and perspectives

6.1 Overview

Fluid mechanics is ubiquitous in nature, and researchers have paid enormous efforts towards understanding the fundamental behavior of fluid flow. This has impacted technological as well as biological applications. With continuous growth in manufacturing techniques, flow through channel of small sizes has resulted in the field of bio-microfluidics which contributed immensely towards drug delivery, drug discovery, disease diagnostics, bio-mimicking to name a few. But, it is well known that the flow through microchannels suffers from large shear stress and viscous drag which stems from the condition of zero velocity at the flow walls. Hence, there are still various issues which needs considerable attention to realize stable and low shear flow in microchannels.

This thesis was focused on understanding a cylindrically lubricated flow channel (liquid tube or antitube) tailored to maximize its stability and velocity profile. The novelty lies in the use of ferrofluids as lubricant and magnets to hold them in place. There is an ongoing effort in the scientific community to propose ways of tailoring the wall velocity to control the shear stress. The efforts are mainly focused on avoiding the solid walls as much as possible by means of a lubricant layer. We rely on a novel design with high potential, capable of confining a flowing liquid in a ferrofluid envelope making a liquid-in-liquid cylindrical geometry stable. Chapter 1 presents an overview of key fundamentals of fluid flow governing equations and state-of-the-art ways of reducing drag and maximizing the slip length. Literature shows that it is not possible to avoid the solid wall completely for a cylindrical flow channel due to interface instability issues leading to limited control on the viscous shear stress. We show how our strategy to stabilize a static liquid cylinder inside a encapsulating magnetic medium can be extended to the dynamic case. The method of magnetic encapsulation is detailed in Chapter 1.8 (also briefly presented here in center image of Fig.6.1) showing the permanent magnet arrangements (blue and red) in a 3D printed setup with white arrows showing the direction of magnetisation of the magnets and stable static liquid cylinder as a result of balance of magnetic and Laplace pressure (white cylinder of water inside blue surrounding of ferrofluid). Chapter 2 to 5 focuses on different aspects and groundbreaking properties of such liquid tube (Fig.6.1)

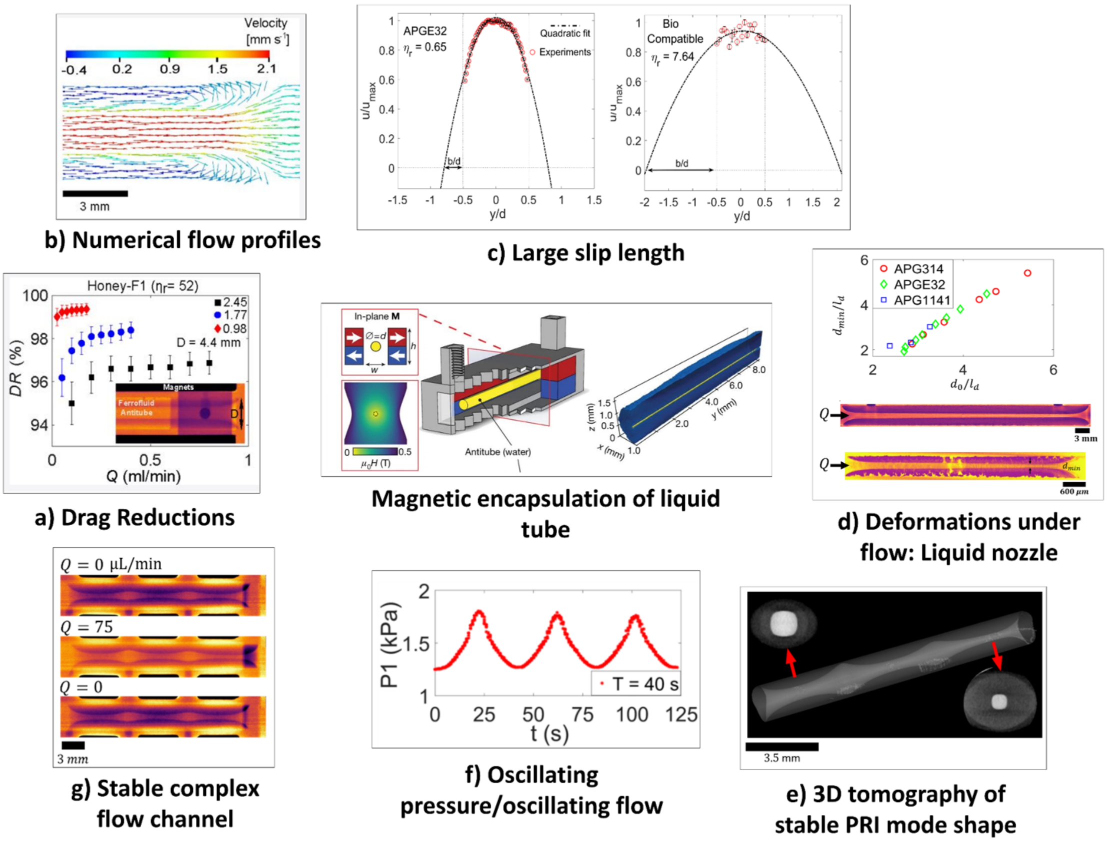

FIGURE 6.1: Summary of the thesis. Magnetic encapsulation and formation of a liquid tube (center image), a) drag reduction of record values (greater than 99%) in liquid tube, b) numerical simulations showing the counter flow in the ferrofluid, c) direct measurements of slip length (b) for a flow diameter d; small, large and asymmetric slip length b/d shown in left center and right panel respectively, d) flow induced reversible deformation of a liquid tube, wider inlet and contracted outlet, l_d is the deformation length scale, e) 3D X-ray tomography of stable PRI mode shape under flow, f) oscillating pressure at the inlet of a flow channel with high Reynolds number (>2000), g) stable complex flow channel with wavy structure before flow $Q = 0$, deformed during flow $Q = 75$ μL/min and reversible after flow $Q = 0$

Drag Reduction. Chapter 2 details how the ferrofluid held by the magnetic forces forms a liquid wall for the flowing liquid by means of experimental, numerical and theoretical tools to elucidate the flow mechanics inside the liquid tube. The resulting non-zero wall velocity boundary findings translated into very resulted large reduction of the viscous drag. We used glycerol and honey with two ferrofluids APG314 and APGE32 to get four combinations of viscosity ratio, $\eta_r < 1$ as well as $\eta_r > 1$. The achieved drag reduction larger than 99% (Fig.6.1

a)) did correspond to a very large slip length (Chapter 2, Tab. 2.1), of magnitudes never observed or reported in literature to the best of our knowledge. Corresponding pressure drop gains by more than 50 times were found, with design rules making even larger values possible. Our experimental observations were fully supported by means of numerical simulations and analytical modelling. We presented numerical flow profiles in the system showing the counter flow in ferrofluids (Fig.6.1 b)) essential for retaining ferrofluids in the system. We also computed pressure drop values using ANSYS computational fluid dynamics package that agreed with the experimental data. Finally we presented a theoretical framework, showing that the flow was governed by a modified Reynolds number $Re\beta$ for a liquid tube instead of Re for solid wall flow, where β is the drag reduction parameter which depends on the viscosity ratio η_r between the two liquids and geometric parameters. A simplified drag reduction parameter (β_0) was also presented which explicitly shows the contribution of viscosity ratio and geometric parameters, and of practical use to get a close estimate of drag reduction for engineering applications.

Large slip length. In chapter 3, we show direct evidence of slip length (b) of record value at the magnetic-non magnetic interface. We measured the velocity profile $u(y)$, in the liquid tube using μ-particle tracking velocimetry (μPTV) method confirming the scaling of slip length with viscosity ratio, as predicted in Chapter 2. The slip length values reported in the literature were limited to cases with $b < R$, where R is the flow channel radius. We showed slip lengths that can be tuned by the viscosity ratio with different η_r case; $b < R$, small slip length for $\eta_r = 0.65$ (Fig.6.1 c) left). We reported remarkable large slip lengths reaching the mm scale with $b >> R$ for $\eta_r = 7.64$ (Fig.6.1 c) right). This is due to the continuous liquid-liquid interface, which opens a new regime for lubricated flows. Large wall velocity u_{wall}, up to 99% of the maximum velocity is recorded and the shear rate $\frac{\partial u(y)}{\partial y}$ can be tuned, with related control over the viscous shear stress ($\eta \frac{\partial u(y)}{\partial y}$). Due to the large slip length and wall velocity, an asymmetric velocity profile for asymmetric lubrication thickness at the two bounding flow wall was revealed experimentally. The experimental observations are explained by a 2D flow model including the predictions of asymmetric velocity profile.

Chapter 2 and Chapter 3 provided conclusive evidence of a large slip length and related low shear flow channel due to moving liquid wall, which can find applications in flow circuits requiring control over viscous drag. The moving wall will effects biofilm formation[1], particle laden flows and flow with adhesives, resulting in a cleaner self cleaning cylindrical flow channel. The flow of highly viscous materials is very challenging in microfluidic circuits, for example when flowing drugs through medical micro needle[2], essential for drug delivery[3]. The use of liquid tubes can greatly reduce the viscous drag facilitating flow of concentrated drugs. The shear rate also dictates the density of bacteria in the microchannel[4] which can be tuned using the asymmetric velocity profile (asymmetric shear). Differentiation of Mesenchymal stem cells (MSC) into various lineages requires different magnitude of shear stimulation[5], the control over viscous shear using different ferrofluid encapsulation could provide a new approach for invitro cell differentiation. The healthy transport of delicate cells also require a low shear biocompatible environment[6], provided by the liquid tube. Furthermore, the ease of fabrication of the magnetically confined microchannel makes it very attractive for preparing microfluidic circuits.

Reversible deformations and stability criterion. After understanding the physics of low shear flow, we focus on the understanding of the stability and deformation dynamics of the liquid tube in **Chapter 4**. Liquid tubes can form forming a soft liquid nozzle, with wider inlet, and contracted outlet for large enough flows (Fig.6.1 d)). A liquid in liquid flow with a static lubricating liquid is unconditionally unstable, due to the well known Plateau-Rayleigh instability (PRI) (See Chapter 1, section 1.5) . We have shown that it is not true for magnetically confined liquid tubes, as the magnetic pressure has a stabilizing effect and can be made much larger than the Laplace pressure. In fact, we show that beyond the straight flow channels, the PRI mode shape (wavy flow channel) itself can be stabilized by adequate design of the confining magnetic field (Fig.6.1 e)), which is not possible even with moving lubricating liquid used in literature (flow focusing). The liquid tube stabilizes by deforming the magnetic-nonmagnetic interface and the deformation depends on the balance of viscous shear stress and magnetic pressure. We presented a theoretical framework to study the flow induced reversible deformations of liquid tube and identify two length scales: l_d which shows the competing effects of fluid viscous drag and magnetic pressure, and l_s showing the competition between fluid viscous drag and surface tension. For small Reynolds number, $Re << 1$, the extent of deformations is governed by l_d where as the stability/shearing of ferrofluid is governed by the combination of l_d and l_s, more specifically $\left(\frac{l_d^5}{l_s^2}\right)^{\frac{1}{2}}$. It is possible to tune the response of the liquid tube by the physical properties of the involved liquids for a fixed flow rate and given magnetic field design. The liquid tube has small deformations if the saturation magnetisation is large, the viscosity of ferrofluid is small compared to the liquid tube, and the surface tension is small, with vice versa requirements for large deformations. Understanding the underlying physics opens new possibilities for making complex lubricated flow channels and realizing ultra soft microfluidics. Current methods to make compliant tubes depend on polymers[7], but in miniaturized polymeric flow channel with fixed elasticity and large pressure/work limit their deformation capabilities[8]. In the liquid tube, the liquid-liquid interface is softer and the deformability of the liquid tube depends on the distance between magnets, hence tunable. Since the magnets are not in contact with the ferrofluid, this gives an additional tuning parameter without disturbing the system (non-destructive tuning) unlike the polymeric soft channels where a change in softness, requires a change in confining polymer.

Bio-mimicking and bio-applications. In **Chapter 5**, we pinpoint some of the properties of the liquid tube for mimicking biological environment and flows. We showed some preliminary bio compatibility experiments performed at Max-Planck institute for dynamics and self organisation, Gottingen Germany. We showed that using a bio-compatible ferrofluid, we can create a healthy environment for flowing delicate cells. Since we lacked the expertise in biophysics, we limited our self to these preliminary experiments. However, motivated with the experiments we highlighted the physical aspects of liquid tube necessary for a biological environment. Flow of a non-Newtonian liquid in liquid tube was studied theoretically by including the shear dependent viscosity in the flow model. It revealed that a shear thinning liquid like blood can have negative drag reduction (drag penalty) above a threshold flow rate. This is because with increasing flow rate the viscosity decreases in a solid tube (due to large shear stress) but, in a liquid tube the viscosity does not decrease comparatively (due to low shear stress). Another interesting feature is the pressure damping which appears in the blood carrying arteries and can be observed in the liquid tube. We showed that the relaxation of inlet pressure follows the deformation dynamics and depends on magnetic properties and the initial no-flow diameter. This could be used to mimic the behavior of soft biological interfaces, arteries or veins. Since arteries have large Reynolds number pulsating flow, we extended the flow regime in the liquid tube to large Reynolds number oscillating flow, Fig.6.1 f) shows the oscillating pressure at the inlet of a flow channel with, a Reynolds number Re obtained for a 2.4 mm diameter liquid tube that can exceed 2000. None of the lubricated flows in literature shows the possibility of stable oscillating flow channel. The stability illustrates the robustness of the liquid tube in complex flow environments. Unhealthy blood flowing arteries show pinched shape (Arterial thrombosis[9]) and the liquid tube could be used to mimic the flow through such deformed flow channels (Fig.6.1 g)).

Beyond the planned research presented in the chapters of thesis, we envision some interesting extensions of the liquid tube applications. In the next section, we highlight some examples of the work with future perspectives using proof of concept experiments.

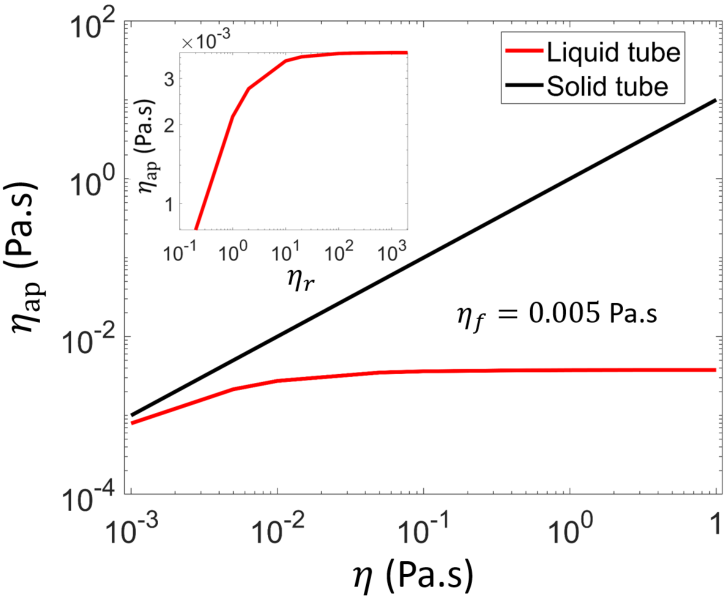

FIGURE 6.2: Apparent viscosity η_{ap} in a liquid tube,inset shows variation of η_{ap} with increasing viscosity of liquid tube η. The ferrofluid viscosity is 0.005 Pa.s. The liquid tube diameter 1 mm, the magnetic arrangement is shown in Chapter 2.

6.2 Effective viscosity

The friction factor that quantifies drag for a liquid tube (f_A), it is given by Eq.6.1

$$f_A = \frac{64}{Re\,\beta} \tag{6.1}$$

$$f_A = \frac{64\eta}{\rho U d\,\beta} \tag{6.2}$$

where η and ρ are the viscosity and the density of the liquid tube. U and d are average velocity and diameter of flow. β shows the drag reduction parameter. The friction factor in the liquid tube (Eq.6.2) can be seen as $f_A = \frac{64\eta_{ap}}{\rho U d}$, where $\eta_{ap} = \eta/\beta$ is the apparent viscosity of the flowing liquid in magnetic encapsulation. Fig.6.2 shows the variation of η_{ap} with increasing viscosity of the flowing liquid η. The viscosity of ferrofluid used in this calculation is taken as η_f = 0.005 Pa.s. The black line depicts the flow through a solid wall tube (Poiseuille flow) where $\eta_{ap} = \eta$. However for liquid tube, $\eta_{ap} < \eta$ results in the fluid that behaves as if it has lower viscosity. With increasing η, their viscosity ratio $\eta_r = \frac{\eta}{\eta_f}$ increases (shown in inset), increasing the drag reduction and η_{ap} increases and flattens. It shows that beyond $\eta_r = 100$, the drag reduction curve will also flattens with minimal further increase in drag reduction.

6.3 Soft Magneto-fluidics

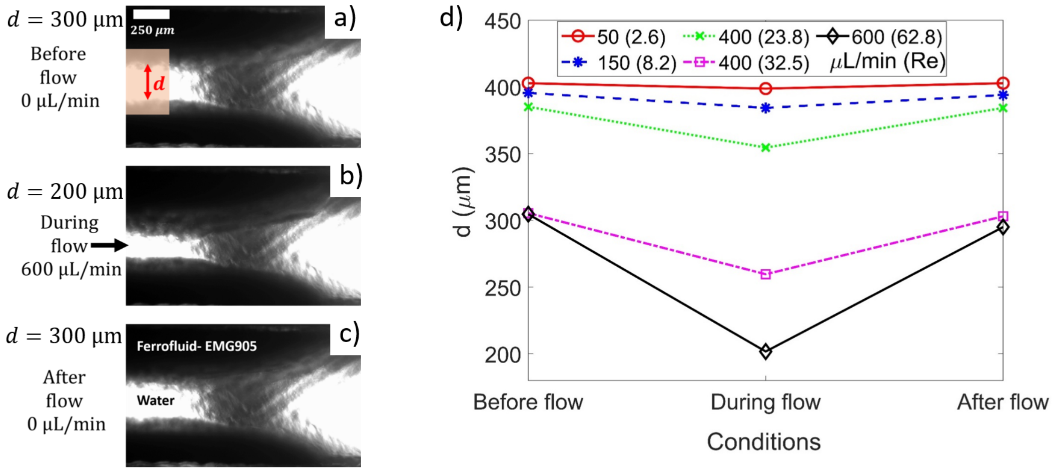

FIGURE 6.3: Soft Magneto-microfluidics. Microfluidics channel near outlet with Water-EMG905. The a) Zero flow diameter is 300 μm , b) the flow rate during flow is Q = 600 μl/min with Reynolds number Re = 62.8, c) Microchannel after stopping the flow. d) Change in the diameter of microchannel at outlet for various flow rate and initial diameter.

Due to stabilized liquid-liquid interfaces, we could realize a reversibly deformable liquid tube with tunable softness for $Re < 1$, modified by the flow rate. It is then possible to create a high throughput, soft microfluidic circuit with $Re >> 1$. Fig.6.3. Fig.6.3 a), b), c) show the outlet of a liquid tube system with water and EMG905 ferrofluid. Initially at no flow (Fig.6.3 a)), the diameter of the water channel (averaged over the highlighted part) is 300 μm. At Q = 600 μl/min flow rate, the diameter reduces down to 200 μm at the outlet with the liquid tube regaining the initial flow diameter when stopping the flow. Fig.6.3 d) show the reversible deformations of a microchannel near outlet for various flow rates and initial diameters showing how high Reynolds numbers flows are possible. Reducing further the initial diameter before flow leads to instability at microchannels apparent by the oscillations in the ferrofluid. Two videos, V4 and V5 showing stable and unstable microfluidic channels are presented in AppendixA-V4-V5.

6.4 Stability of liquid interfaces with temperature

The deformable liquid-liquid interface is stable under the balance of viscous shear, magnetic pressure and Laplace pressure. However a stable liquid tube can show instability with increasing local temperature. We observed the phenomena under microscope with focused fluorescence source. The setup is the μPTV arrangement used for velocity profile measurements (Fig.3.10). We used Glycerol in the liquid tube and EMG905 as ferrofluid. Fig.6.4 a)

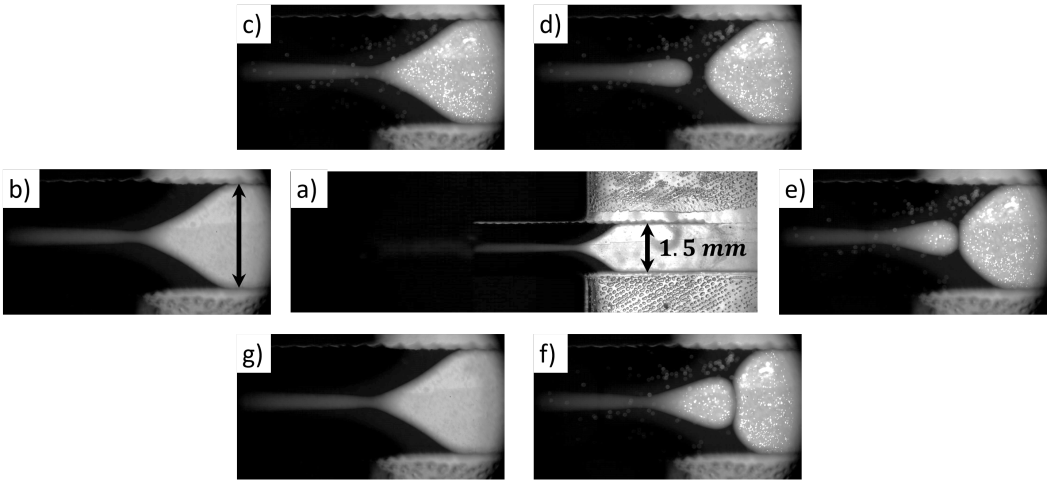

FIGURE 6.4: Stability of liquid tube with temperature a) Brightfield image near outlet of microfluidic channel of glycerol (bright) with EMG905 ferrofluid encapsulation (dark), b) magnified view near outlet, c) brightfield + fluorescence image with shining micro at time t = 0 s, d) broken microchannel t = 10 s, showing instability, e) and f) growing microchanel due to continious flow (unstable state with brocken microchannel), g) stable continious microchannel on stopping the fluorescence source.

shows the deformed liquid tube under flow (bright central channel) near the outlet and Fig.6.4 b) show the magnified view of the liquid tube. Under illumination, we can see the flowing fluorescence beads (Fig.6.4 c)) evolve over time (10 s): necking starts, the minimum diameter reduces further, which eventually leads to the breaking of the continuous flow channel (Fig.6.4 d)). With the flow rate still on, the interrupted part is pushed forward (Fig.6.4 e) , f)). If the fluorescence source is kept on the system behaves in a cyclic manner between Fig.6.4 e)-f)-d)-e)-f)-d). If the light source is switched off after Fig.6.4 f), the system stabilizes again in a continuous liquid tube form (Fig.6.4 f)).

The liquid tube instability relates to the focused illumination source that increase the local temperature, which in turn decreases the saturation magnetisation M_s of the ferrofluid[10, 11]. The decrease in M_s leads to a decrease in magnetic pressure and the liquid tube deforms more (Eq.4.21) and finally becomes unstable (Eq.4.34). During the sequence of Fig.6.4 d)-e)-f), circulations in liquid tube can be observed with the beads motions (AppendixA-V6), suggesting emergence of an unstable flow.

6.5 Towards nanofluidic channel

The magnetic encapsulation of liquid tube can be extended towards nano-fluidics. The magnetic pressure required to reduce the liquid tube diameter can be achieved by reducing the distance between magnets. Fig.6.5 a) show the schematics of the experimental cell design. The distance between the magnets is reduced down to 150 μm, with white arrows showing the direction of magnetisation. On inserting the ferrofluid in the system, the liquid tube is formed. Fig.6.5 b) to Fig.6.5 g) show the liquid tube cross-section of reducing size with increasing ferrofluid amount. The diameter is calculated from the intensity profile plotted along y, with full width half max.

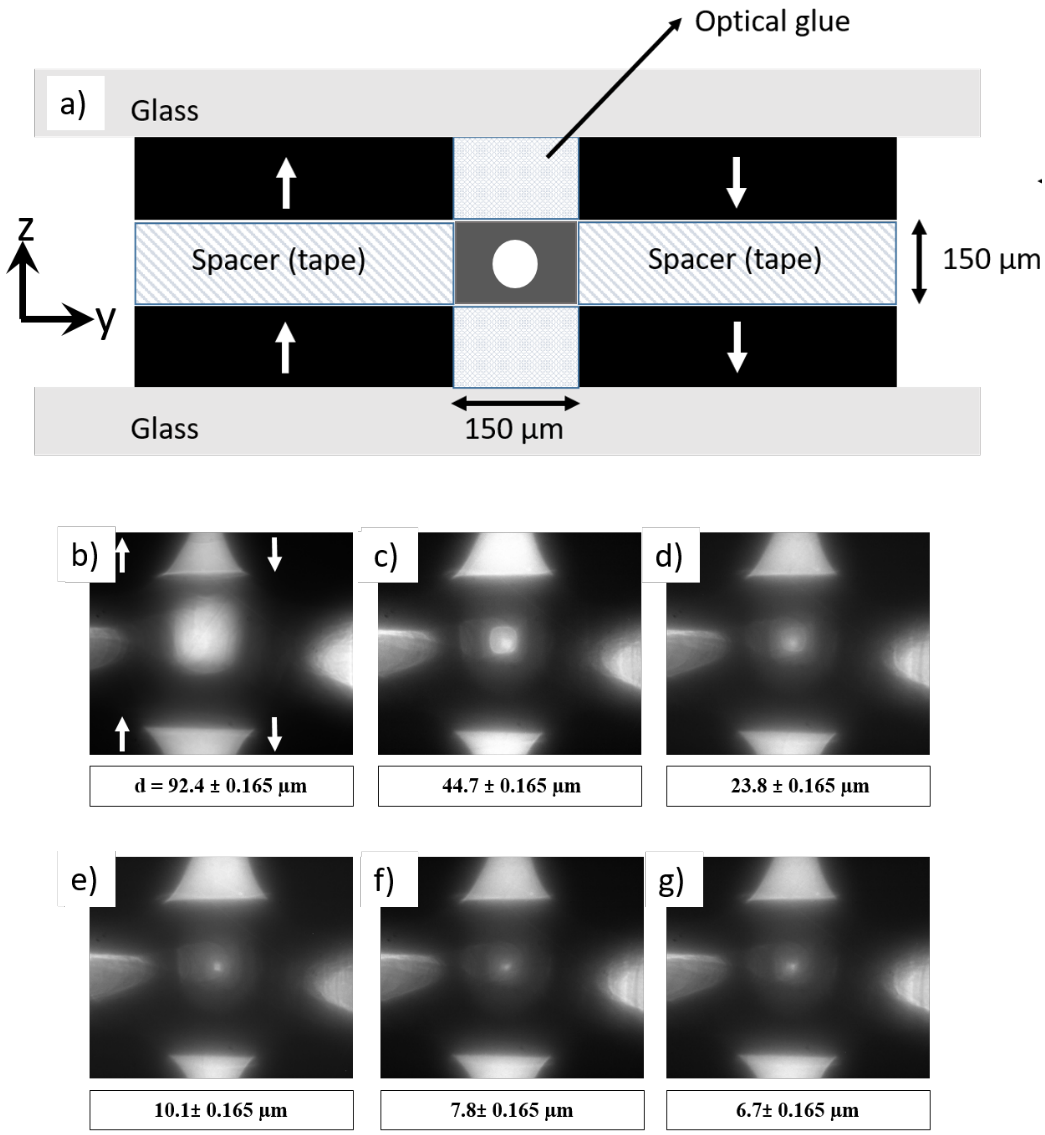

FIGURE 6.5: Towards 1 micrometer frictionless microfluidic channel. a) Cell design for the microchannel (central white circle), b)-g) decreasing size of microchannel with increasing ferrofluid.

Smallest cross section of 6.7 $\pm 0.165\mu$m was observed with X-ray setup on a synchrotron beamline. It was not possible to get an image of the liquid tube along the length, possibly due to too much scattering of X-ray by the ferrofluid. The balance of magnetic and Laplace pressure suggests that further decrease in diameter of liquid tube is possible by reducing the spacing between the magnets (See[12] for explicit calculations and equations in Chapter 1, 1.8). But, it is experimentally challenging to achieve decreasing spacing between magnets and overcoming imaging resolution and conditions. Electrostatic pressure (electrowetting) could be one of the solution to achieve smaller liquid diameter. This is because the net effect of electrostatic energy/ pressure at a liquid-liquid interface is to reduce the surface tension[13]. Hence the Laplace pressure would reduce. A thorough study on the effect of electric field on the liquid tube therefore might pay way towards nano-fluidic liquid tube.
It has been shown that, though viscosity is a material property and it can not be changed for a Newtonian liquid at a fixed temperature. However, the liquid wall reducing the drag, apparently has an effect of reducing viscosity of flow. For non-Newtonian liquids, especially shear thinning liquid, the effect could be even more dramatic. Hence the liquid tube provide an additional wall effect to mimic complex flow environment, for example the non-Newtonian viscosity of blood. Apart from the apparent tuning of viscosity, the tunable shear environment could be used to study the response of bio materials. Furthermore, the liquid tube can be used as a model system to understand the dynamics of shear dependent micro-swimmers. Controlling l_d will result in controlling the stable deformed liquid tube which can create microfluidic liquid nozzle.

In conclusion, novel groundbreaking properties can be achieved by liquid-in-liquid flow, stabilized by a magnetized fluid. Large drag reduction and slip length unattainable by other designs will provide a new model system to study the response of bio-materials in tunable shear environment. The reversibly deformable microfluidics could possibly guide in the realization of hybrid microfluidic channels with low shear and deformable interfaces. The unique bio-compatibility and bio-mimicking capabilities make this approach highly attractive for extending the possibilities for organ on chip studies. The non-linear elasticity of the liquid tube makes it more suitable to mimic complex biological interfaces, not attainable using polymers. Our theoretical framework and rigorous experimental investigations provide a novel perspectives to overcome the current limitations of microfluidics and open new possibilities.

Bibliography

[1]W. Wang, J. Timonen, A. Carlson, D.-M. Drotlef, C. Zhang, S. Kolle, A. Grinthal, T. S. Wong, B. Hatton, S. Kang, S. Kennedy, J. Chi, R. Blough, M. Sitti, L. Mahadevan, and J. Aizenberg, "Multifunctional ferrofluid-infused surfaces with reconfigurable multiscale topography", Nature **559**, 10.1038/s41586-018-0250-8 (2018).

[2]V. Jayaprakash, M. Costalonga, S. Dhulipala, and K. K. Varanasi, "Enhancing the injectability of high concentration drug formulations using core annular flows", Advanced Healthcare Materials **9**, 2001022 (2020).

[3]S. Damiati, U. B. Kompella, S. A. Damiati, and R. Kodzius, "Microfluidic devices for drug delivery systems and drug screening", Genes **9**, 10.3390/genes9020103 (2018).

[4]R. Rusconi, J. Guasto, and R. Stocker, "Bacterial transport suppressed by fluid shear", Nature Physics **10**, 212–217 (2014).

[5]S. Arora, A. Srinivasan, A. Leung, and Y.-C. Toh, "Bio-mimicking shear stress environments for enhancing mesenchymal stem cell differentiation", Current Stem Cell Research Therapy **15**, 10.2174/1574888X15666200408113630 (2020).

[6]A. Blaeser, D. Duarte Campos, U. Puster, W. Richtering, M. Stevens, and H. Fischer, "Controlling shear stress in 3d bioprinting is a key factor to balance printing resolution and stem cell integrity", Advanced healthcare materials **5**, 10.1002/adhm.201500677 (2015).

[7]P. Karan, S. S. Das, R. Mukherjee, J. Chakraborty, and S. Chakraborty, "Flow and deformation characteristics of a flexible microfluidic channel with axial gradients in wall elasticity", en, Soft Matter **16**, Publisher: The Royal Society of Chemistry, 5777–5786 (2020).

[8]S. Li, H. Bai, R. Shepherd, and H. Zhao, "Bio-inspired design and additive manufacturing of soft materials, machines, robots, and haptic interfaces", Angewandte Chemie International Edition **58**, 10.1002/anie.201813402 (2019).

[9]P. Costa, H. Albers, J. Linssen, H. Middelkamp, L. Hout, R. Passier, A. Van den Berg, J. Malda, and A. van der Meer, "Mimicking arterial thrombosis in a 3d-printed microfluidic: in vitro vascular model based on computed tomography angiography data", Lab Chip **17**, 10.1039/C7LC00202E (2017).

[10]T. Upadhyay, R. V. Upadhyay, R. V. Mehta, V. K. Aswal, and P. S. Goyal, "Characterization of a temperature-sensitive magnetic fluid", Phys. Rev. B **55**, 5585–5588 (1997).

[11]Y. Chen, D. Li, Y. Zhang, Z. Li, and H. Zhou, "The influence of the temperature rise on the sealing performance of the rotating magnetic fluid seal", IEEE Transactions on Magnetics **56**, 1–10 (2020).

[12]P. Dunne, T. Adachi, A. A. Dev, A. Sorrenti, L. Giacchetti, A. Bonnin, C. Bourdon, P. H. Mangin, J. M. D. Coey, B. Doudin, and T. M. Hermans, "Liquid flow and control without solid walls", Nature **581**, 58–62 (2020).

[13]F. Mugele and J.-C. Baret, "Electrowetting: from basics to applications", Journal of Physics: Condensed Matter **17**, R705–R774 (2005).

Appendix A

Videos

V1. 3D Tomography of a deformed liquid tube.

V2. 3D tomography of stabilized PRI mode shape.

V3. Oscillating Flow.

V4. Stable deformations for soft microfluidics.

V5. Unstable microchannel flow with oscillations.

V6. Stability with temperature.

Link for videos

https://ipcms-cloud.u-strasbg.fr/owncloud/s/EFIzNbqj7KZhfkS

Appendix B

MATLAB Code

Example of MATLAB Code for Deformation and Stability of liquid tube

```
clear all
close all
clc
%%%%%%%%%%%% This file has various sections %%%%%%%%%%%%

% Section 1. Physical properties required
%Define the properties of system magnetic and fluidic

% Section 2. Saturation magnetisation curve M(H)--Experimental
%Locate the file with experimental data
%Save the experimental data "milli tesla"
% Section 3. Fitting function to saturation magnetisation curve M(H)
% fit the experimental data with polynomial equation
% take the polynomial value and put in place of p(1,1) p(2,1), ...
% Section 4. Magnetic Field calculation in the antitube

% Section 5. Numerical model for calculating deformation of antitube and stability

%%
%%%%% Section 1. Physicsl properties-- All in SI units %%%%%

% 1.1    %%%For magnetic saturation curve%%%

Mb=480000; %Bulk magnetisation of ferromagnetic particles
dp=12*10^-9; % diameter of ferromagnetic particles
mu=1.25*10^-6; % magnetic permeability
Mr=1.26/mu;     %Remanant magnetisation of magnets
Kb=1.385*10^-23; %Boltzmann constant
T=(273+23.00); % Temperature in Kelvin
W=0.006;          % Distance between magnets
alpha_p=(mu*Mb*pi*(dp^3))/(6*Kb*T); % Magnetic parameter
phi=(0.21); % Volume fraction of particle


% 1.2    %%%For deformation curve and stability%%%

d0=0.00095; % diameter of antitube at Flow rate == 0
```

```
Dc=0.0044;  % diameter of cavity without ferrofluid
muh=1.1;    % dynamic viscocity of antitube fluid
muf=1.7;    % dynamic viscocity of ferrofluid
rhoh=1260;  % density of antitube liquid
rhof=1091;  % density of ferrofluid
QQ=100*(1.66*10^-11); % Flow rate in m^3/s, multiplicative factor converts from ul/min to m^3/s i.e. (QQ=ul/min*(1.66*10^-11))
bb=muh/muf; % Viscosity ratio
LL=0.040;   % length of anitube channel
mu_0=4*pi*10^-7; %Magnetic Permeability
sigma=0.0283783;    %Surface Tension
Mr=1.26/(mu_0);   %Remenant Magnetisation of magnets
Ms=(27*10^-3)/mu_0;% saturation magnetisation of ferrofluid
chi=0.6;    % Initial susceptibility of ferrofluid


ld_linear=(((pi*muh*QQ*W^2)/(2*mu_0*chi*(1+chi)*Mr^2))^(0.20)); % Magnetic deformation length scale Linear model
ld_sat=(((2*muh*QQ*W)/(mu_0*Ms*Mr))^(0.25));                        % Magnetic deformation length scale Saturation model
ls=((8*muh*QQ)/(sigma*pi))^(0.5);  %  length scale with surface tension and shear

%%
%%%%%% Section 2. Saturation magnetisation curve M(H) %%%%%%

SquidFerrotech=xlsread('C:\PhD Personal\Publications\DeformationAntitube\Experimental And Theory.xlsx',4);
figure (1)
plot((SquidFerrotech(1:10,1))*0.001,(SquidFerrotech(1:10,2))*0.001,'*r')
hold on
%Coefficients:
%%
%%%%%% Section 3. Fitting function to saturation magnetisation curve M(H) %%%%%%

%%Polynomials for fitting is found by fitting a 10th order polynomial to data in Fig. 1%%


```

```
p=zeros(11,1); % Array for polynomial storage
p(1,1) = -440.28
p(2,1) = 2134.1
p(3,1) = -4472.9
p(4,1) = 5310.5
p(5,1) = -3931.4
p(6,1) = 1883.4
p(7,1) = -587.03
p(8,1) = 116.87
p(9,1) = -14.249
p(10,1) = 0.99257
p(11,1) =  -0.0031176



for i=1:180
    % Based on langevin function%

    B(i)=(i-1)*0.005; %Magnetic field in Tesla
    H(i)=B(i)*795774.77; %Magnetic field in A/m
    alpha(i)=alpha_p*H(i);
    L(i)=((1/tanh(alpha_p*H(i)))-(1/(alpha_p*H(i)))); % Langevin function
    delEtaByEta(i)=0.001*78*phi*((alpha_p* H(i)*L(i))/(1+(0.5*alpha_p*H(i)*L(i))));
    Eta(i)= ((delEtaByEta(i)));
    Mag(i)=(L(i)*phi*Mb)*mu;

    % Fitted by polynomial 'y' denotes magnetisation%

    y(i) = p(1,1)*(B(i))^10 + p(2,1)*(B(i))^9 +...
        p(3,1)*(B(i))^8 + p(4,1)*(B(i))^7 +...
        p(5,1)*(B(i))^6 + p(6,1)*(B(i))^5 +...
        p(7,1)*(B(i))^4 + p(8,1)*(B(i))^3 +...
        p(9,1)*(B(i))^2 + p(10,1)*(B(i)) +...
        p(11,1);
end
figure(1)
plot(B,Eta,'-k')
hold on
figure(10)
plot(B/(4*pi*10^-7),(Eta*0.001)/(4*pi*10^-7),'-k')
hold on
figure(1)
plot(B,y,'-g')
hold on
```

```
% figure(2)
% plot(B,Mag,'-k')
% hold on

%%
%%%%%% Section 4. Magnetic Field calculation in the
    antitube %%%%%%
% this is just to check the field inside the antitube
% remove or ignore if you dont want, doesnot harm the
    code.
for i=1:100
    h(i)=(i-1)*0.000013; %Radius of antitube
    Field(i)=((4*Mr*h(i)*mu_0)/(pi*W)); %Field variation
        in the antitube, this gives an indication to
    %choose linear or saturation media model
    % Neglect it if you want, it does not harm the code
end

figure(4)
plot(2*h,Field,'*r')
%%
%%%%%% Section 5. Numerical model for calculating
    deformation of antitube and stability  %%%%%%

% Guess the value of "Dpredict" always less than "d0"
% Run the code
% Check residual, if it is less than 0.1% of initial
    volume
% if not then reduce or increase "Dpredict"
% if it is less than 0.1% of initial volume
% Check if Stability_sat is negative
% if its positive the system is stable for this flow rate
% if its negative the system is unstable for this flow
    rate

nx=100000; %finite difference points
dx=LL/(nx-1); %length between two points
Dpredict=(0.000607); % predicted diameter at the outlet
h=zeros(nx,1);        % Array for radius of antitube along
     the length
h(:,1)=Dpredict/(2); % filling array with one value, this
     is just computing step- no science
h(nx+1,1)=h(nx,1);  %Boundary condirion see notebook for
    details
h(nx+2,1)=0.00030350000001; %Predicted h(nz+2) see
    notebook for details
```

Appendix C

Imaging

C.1 X-Ray imaging

The X-Ray imaging is done using three setups depending on the resolution required

Homemade X-Ray imaging setup with a resolution of the detector as 20 μm. The setup was used for the experiments of imaging the antitube diameter in mm scale. The system is limited to radiography (2D images). The deformation images shown in Chapter 4 are also taken using this setup. The setup essentially contains a dental X-Ray source showering X-Rays over a cell placed above the detector.

The RX-Solutions EasyTom 150/160 at Institut Charles Sadron, Strasbourg, France was

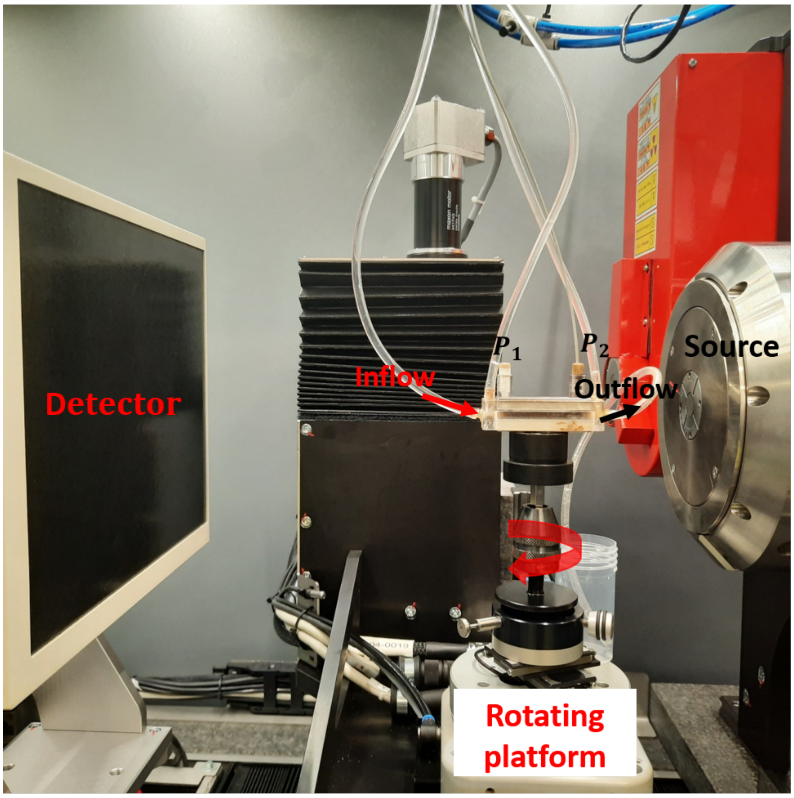

FIGURE C.1: The RX solution tomography setup with cell.

used with a resolution of the detector up to 6 μm. The setup was used for the experiments

of imaging the antitube diameter in mm scale as well as sub mm scale down to 80 μm. The system was also used for 3D tomography measurements shown in Chapter 4 and pressure drop measurement in sub-mm size antitube in Chapter 2. Fig.C.1 shows the experimental setup. The experimental cell is mounted on the rotating platform for tomography. The source showers X-Ray and the absorption contrast image is recorded using the detector.
The X-Ray Synchrotron source at the Swiss light source , Paul Scherrer Institute (PSI), villigen Switzerland was used to image antitube below 100 μm. The minimum resolution of the detector was 0.165 μm. The imaging system was also used to record tomography data for the static antitube. Fig.C.2 shows the imaging setup. The cell is mounted on the rotating

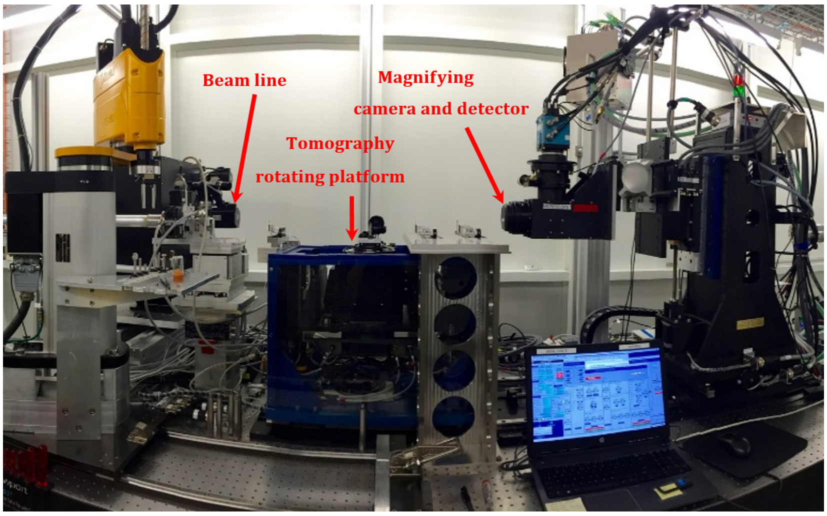

FIGURE C.2: The synchrotron tomography setup.

platform and the X-ray beam passes through the cell and microscope to the detector. Note that only static antitube imaging is done using the synchrotron source at PSI.

C.2 Optical microscopy

We used Zeiss Axiovert 200M brightfield microscope with 5X and 10X magnification. The maximum frame rate was 18 images per second. The brightfield was used to show the soft microfluidics behavior shown in Chapter 6. Along with the dynamic case, the same microscope was used to record the static equilibrium antitube diameter shown in chapter 1. The images were analyzed using Fiji and ImageJ.

Appendix D

Experimental cell

D.1 Antitube experimental cell

The experimental cell for creating an antitube depends on the size of antitube expected. Different cells used in our work are presented below

D.1.1 Cell for mm size antitube

A plastic casing with slots for magnets and the flow channel(cavity) is printed using a Form 3 3D printer from Form Labs. The minimum accuracy of the 3D printer is 25 μm. The magnets used are Nd-Fe magnets (from SUPERMAGNETMAN) with remenant magnetisation at the surface of 0.5 T. The magnets are 50 mm in length, 6 mm is width and thickness. Fig.D.1 and Fig.D.2 show the schematic and printed cell respectively.

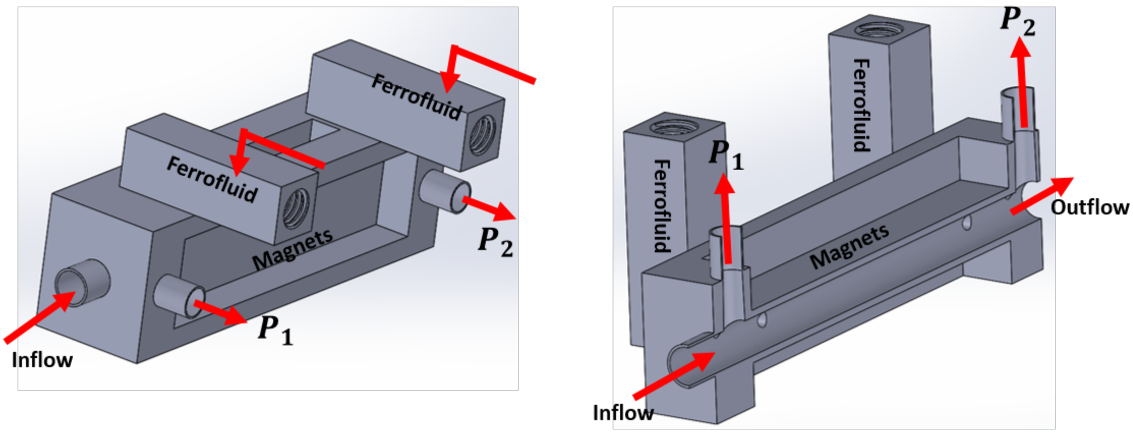

FIGURE D.1: The schematic of experimental cell for mm size antitube.

Fig.D.1 left shows the slots for magnets. There are two ferrofluid entrance, one of which is blocked if required for better control of ferrofluid volume in the cavity. $P1$ and $P2$ are the

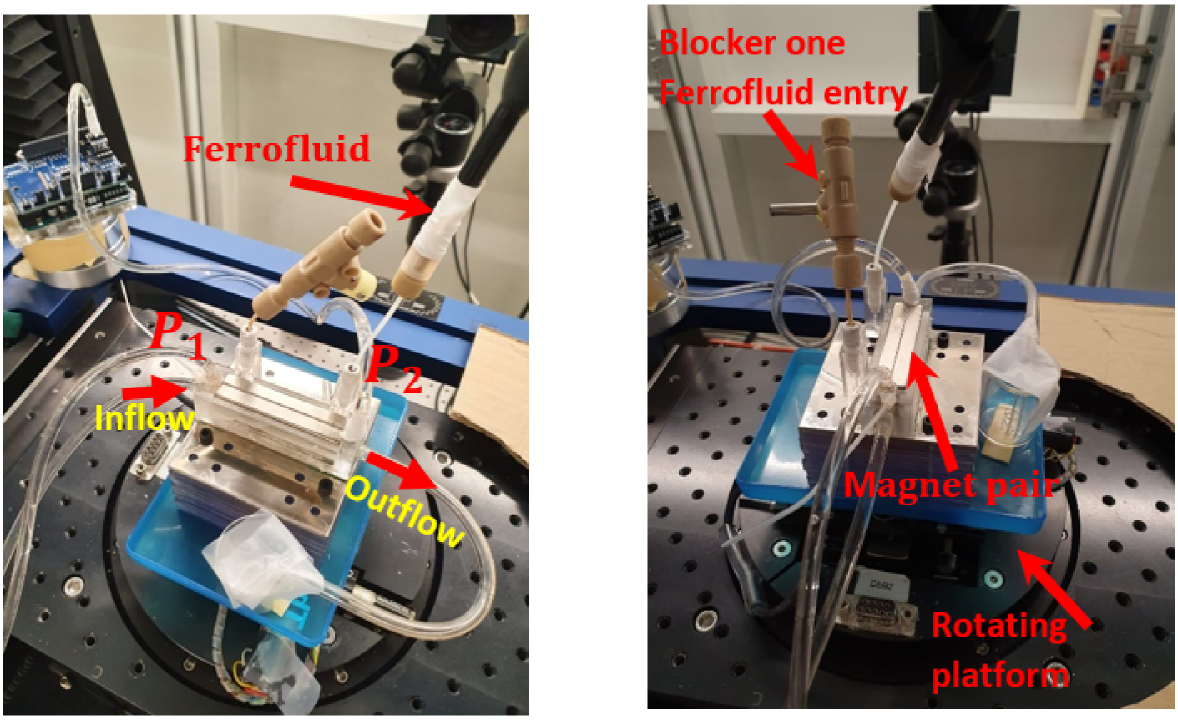

FIGURE D.2: The experimental cell for mm size antitube.

location of two pressure sensors. The inlet and outlet are for the antitube liquid. Fig.D.1 right shows a section cut. A cell mounted on the PSI experimental setup is shown in FigD.2

D.1.2 Cell for sub-mm size antitube

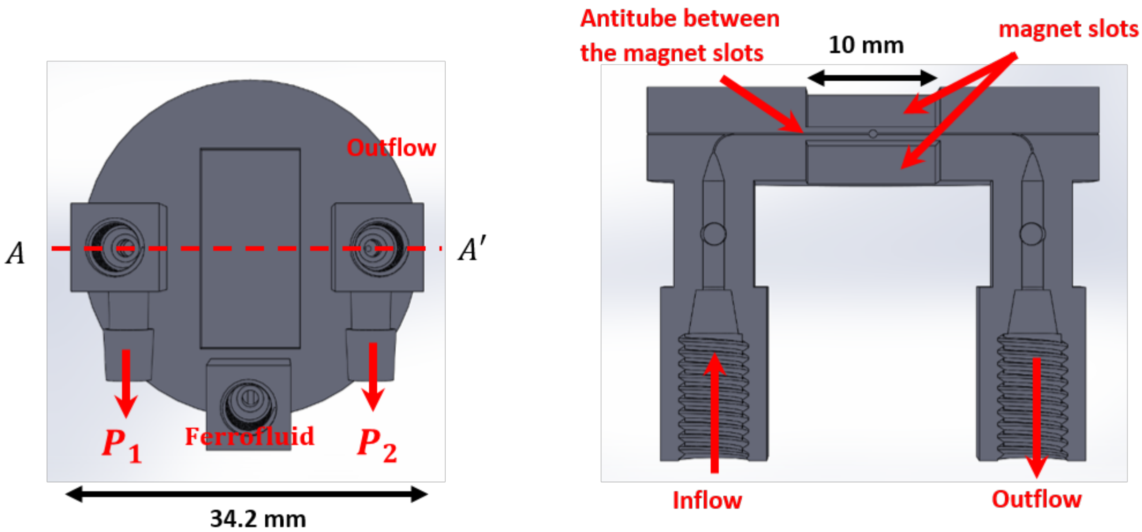

FIGURE D.3: The schematic of experimental cell for sub-mm size antitube.

A 3D printed setup suited for cube magnets of 10 mm side is used (Fig.D.3). The magnets slots are 0.9 mm apart. The cavity size is 600 micrometers. Fig.D.3 shows the design of the cell and Fig.D.4 shows the experimental cell mounted on the tomography platform (at PSI).

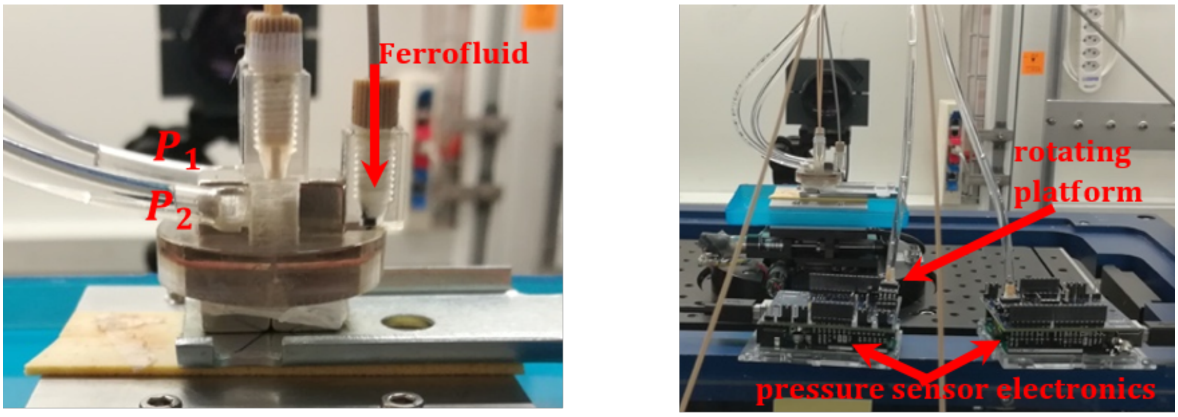

FIGURE D.4: The experimental cell for sub-mm size antitube.

Appendix E

Material properties

E.1 Viscosity

We measured the viscosity of magnetic and non-magnetic liquids using the Anton Par MCR302 viscometer. For the nonmagnetic liquid (glycerol and honey), we used the flow curve method using the parallel plates configuration. The space between the parallel plates is 1 mm. We increased the shear rate and recorded the shear stress, the slope of the curve gives the viscosity. For magnetic fluid at various given shear rate values (10 s^{-1} to 100 s^{-1}), the magnetic field is varying from 0 to 0.7 T to measure the magneto-viscosity.

Protocol for non-magnetic liquids:

- Place the liquid between the parallel plates.
- Set the parallel plates viscometer to 1 mm.
- Apply shear rate, measure shear stress.
- Plot viscosity as the slop of shear-rate and shear stress curve.

Protocol for magnetic liquids:

- Place the liquid between the parallel plates.
- Set the parallel plates viscometer to 1 mm (0.1 mm for EMG900 ferrofluid).
- Apply fixed shear rate and the linear variation of magnetic field from 0 – 0.7 T.
- Measure the shear stress as a function of increasing magnetic field.
- Plot viscosity as a function of magnetic field for various shear rate.

E.2 Interfacial tension

We measured the interfacial tension between ferrofluid and antitube liquid using a drop shape analyzer (DSA100) from KRUSS GmbH. The pendant drop method is used for the measurements, where the software fits the curvature of ferrofluid drop and uses the Young-Laplace equation to give the interfacial tension. Fig.E.1 show the variation of drop bubble size with increasing volume of the ferrofluid.

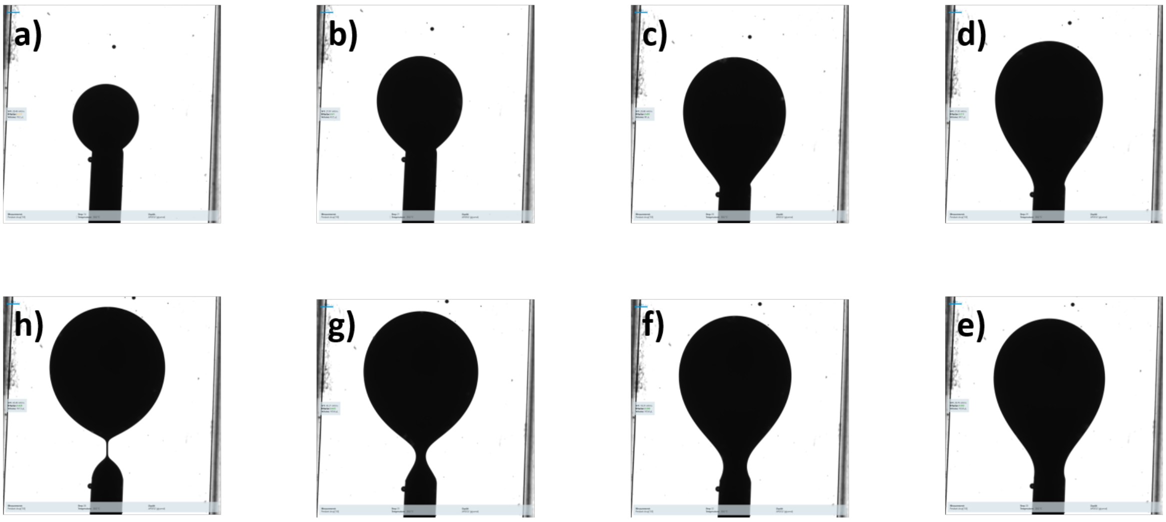

FIGURE E.1: increasing volume of inverted drop during the measurement of interfacial tension between glycerol-APG314.

Protocol:

- Fill the couette with the antitube liquid (glycerol or water).
- Make a drop of ferrofluid in the antitube liquid.
- Increase the volume of drop by steps.
- Record the surface tension.
- Finally, the drop falls/rises under gravity.

Fig.E.2 show a sample case of the variation of interfacial tension with increasing volume of the ferrofluid. Initially the measured interfacial tension increased with drop volume then after 7 steps a plateau of interfacial tension comes followed by the abrupt increase due to falling/rising of the drop from the needle. The plateau part depicts the balance between gravity and surface tension and this part is taken as surface tension with errors. Every measurement was repeated 5 times and the errors in interfacial tension reported is the standard deviation of the measured data.

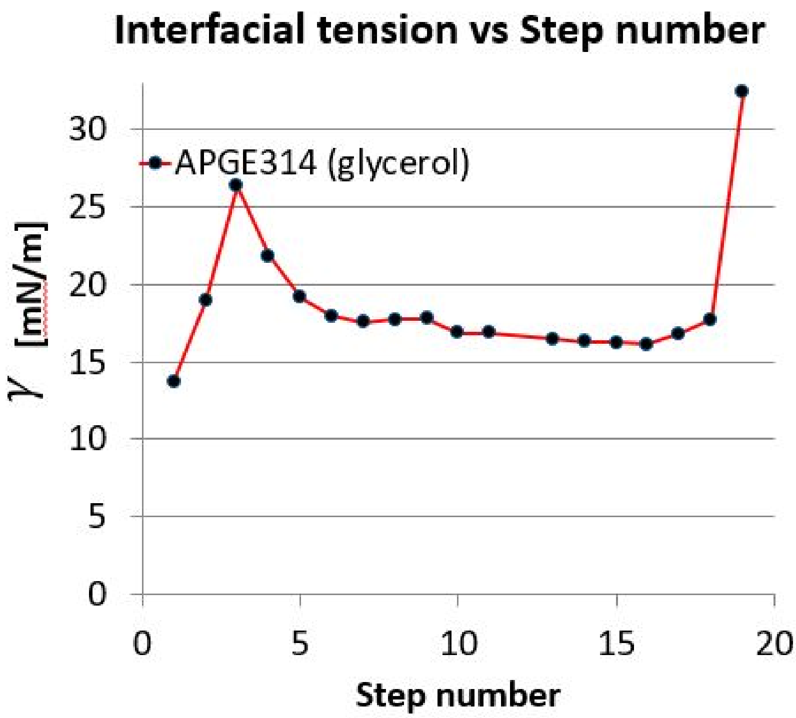

FIGURE E.2: Interfacial tension with increasing steps (drop volume).

Ferrofluid 1	Zero field viscosity (mPa.s)	Saturation magnetization (mT)	Density 2 (g/cc)	Interfacial tension
APG314	150	27.5	1.09	16.9 ± 0.84
APGE32	1200	33	1.15	28.4 ± 0.74
APG1141	5000	22	1.09	11.3 ± 0.56
EMG900	60	99	1.74	30.4 ± 0.33
EMG905	5	-	1.21	-
Biocompatible	144	-	-	-

TABLE E.1: Physical properties of ferrofluids used in the study.

E.3 Ferrofluid properties

The ferrofluid used in the experiments are commercially obtained from Ferrotech and Qfluidics. We use APG314, APGE32, APG1141, EMG905 and EMG900 ferrofluids from Ferrotech and a bio compatible ferrofluid from Qfluidics. The important properties are the M-H curve and saturation magnetization. Fig. 4.3 show the $M - H$ curve of the ferrofluid as obtained from Ferrotech. The properties of ferrofluids are listed in Tab. E.1. The interfacial tension is measured where as other quantities are provided by the manufacturer.

Arvind Arun Dev

Flow mechanics in magnetically confined liquid tubes.

Résumé

La microfluidique joue un rôle très important dans le transport de bio-fluides, allant du diagnostic médical à la simulation d'organes biologiques. La mécanique de l'écoulement dans les microcanaux est très bien expliquée par l'équation de Navier-Stokes dans la limite de petits nombres de Reynolds. Cependant, malgré des décennies de recherche, un défi majeur reste à relever : surmonter l'importante traînée visqueuse ou perte de charge qui se produit lorsque la taille du canal d'écoulement diminue. Nous présentons une nouvelle approche en créant un canal d'écoulement liquide dans un autre liquide stable (tube liquide). Le canal liquide en écoulement est encapsulé par un liquide lubrifiant composé de ferrofluide maintenu en place par des forces magnétiques. Une réduction importante de la traînée atteignant 99% est obtenue, complétée expérimentalement par la démonstration d'une grande longueur de glissement record (à l'échelle du mm). Un profil de vitesses approchant celui d'un écoulement parfait est expliqué par un nombre de Reynolds modifié. Nous montrons que la fameuse instabilité de Plateau-Rayleigh est empêchée par la présence d'un interface liquide-liquide déformable. Dans ce contexte, nous étudions la stabilité et les déformations du tube liquide en identifiant l'échelle de longueur de la déformation, dont le contrôle peut ouvrir la voie à la réalisation de dispositifs microfluidiques ultra-souples. Les propriétés uniques du tube liquide, comme la résistance visqueuse réglable, les déformations réversibles induites par l'écoulement, le rendent approprié pour l'administration de médicaments, le transport de biomatériaux, la bio-impression et comme système modèle d'écoulement dans les artères, veines et d'autres interfaces complexes. Les nouvelles possibilités offertes par les écoulements lubrifiés stabilisés par des forces magnétiques permettent de repousser les limites actuelles de la microfluidique et ouvrent ainsi de nouvelles possibilités d'applications.

Mots clés : Interface liquide-liquide, réduction de la traînée, longueur de glissement, microfluidique souple, instabilité de Plateau-Rayleigh, écoulements lubrifiés, bio-mimétisme.

Résumé en anglais

Microfluidics plays a very important role in bio-fluid transport, ranging from medical diagnostics to the simulation of biological organs. The mechanics of flow in microchannels is very well explained by the Navier-Stokes equation in the small Reynolds number limit. However, despite decades of research, a major challenge remains to overcome the significant viscous drag or pressure drop that occurs as the size of the flow channel decreases. We present a new approach by creating a liquid flow channel in another stable liquid (liquid tube). The flowing liquid channel is encapsulated by a ferrofluid lubricant held in place by magnetic forces. A significant drag reduction of up to 99% is achieved, complemented experimentally by the demonstration of a record long slip length (on a mm scale). A velocity profile approaching that of a perfect flow is explained by a modified Reynolds number. We show that the famous Plateau-Rayleigh instability is prevented by the presence of a deformable liquid-liquid interface. In this context, we study the stability and deformations of the liquid tube by identifying the length scale of the deformation, the control of which may pave the way for the realisation of ultra-flexible microfluidic devices. The unique properties of the liquid tube, such as adjustable viscous resistance, reversible flow-induced deformations, make it suitable for drug delivery, biomaterial transport, bioprinting and as a model system for flow in arteries, veins and other complex interfaces. The new possibilities offered by lubricated flows stabilized by magnetic forces push the current limits of microfluidics and thus open up new application possibilities.

Keywords: Liquid-liquid interface, drag reduction, slip length, soft microfluidics, Plateau-Rayleigh instability, lubricated flows, bio-mimicking.